Interfacing nanomechanics with multi-gated suspended carbon nanotube quantum circuits

Zur Erlangung des akademischen Grades eines

Doktors der Naturwissenschaften (Dr. rer. nat.)

von der KIT-Fakultät für Physik
des Karlsruher Instituts für Technologie (KIT)

angenommene

Dissertation

von

M.Sc. Aljoscha Auer

geboren in Heidelberg (Baden-Württemberg)

Tag der mündlichen Prüfung: 17. Mai 2024
Erster Gutachter: Prof. Dr. Wolfgang Wernsdorfer
Zweiter Gutachter: Prof. Dr. Ralph Krupke

Abstract

Carbon nanotubes (CNTs) are a unique and versatile platform for nanoelectromechanical systems (NEMS) due to their one-dimensional structure alongside a low mass density and large Young's modulus. This pushes their mechanical bending mode resonance frequencies in the range of hundreds of MHz, which is an experimentally well accessible regime and energetically comparable to the thermal energy at cryogenic temperatures. Combining their electrically tunable conduction behaviour and the large mechanical quality factor, they are suited for high sensitivity experiments acting e.g. as a mass sensor or a host for a qubit. However, their integration into complex circuits remains a challenge up to date.

In this work, we realised ultra-clean suspended CNTs that are locally tunable via multiple gate electrodes by sophisticated nanofabrication, where the CNT is integrated into a priorly fabricated metal-circuit in the last fabrication step. This is done either by chemical vapour deposition of the CNT on-chip or with a stamping process depositing a CNT grown on a separate chip onto the metal electrodes using a nano-assembly technique. The electric potential along the CNT can be modified precisely using local gates, allowing to induce up to three quantum dots in series. The coupling of these quantum dots with mechanical modes enables the realisation of complex experimental schemes making use of the adjustable electron-phonon interaction.
Besides the realisation of spin and charge qubits, mechanical qubits or phononic ground state cooling have been proposed in this type of device. Additionally, they are suitable platforms for spin-state read-out of a single-molecule magnet (SMM). SMMs can be imagined as a nanoscale magnet consisting of a single spin embedded in an organic ligand shell. They can behave as spin-qudits and the CNT could offer a controllable qudit readout using electronic transport measurements, based on magnetic flux-coupling or spin-phonon coupling.

Kurzzusammenfassung

Kohlenstoffnanoröhren (CNT) sind durch ihren eindimensionalen Aufbau sowie ihre geringe Dichte bei gleichzeitig hohem Elastizitätsmodul eine einzigartige, vielseitig anwendbare Plattform für nanoelektromechanische System (NEMS). Die strukturellen Eigenschaften sorgen für eine Frequenz der mechanischen Schwingungen im Bereich von einigen hundert MHz, was sie experimentell gut kontrollierbar macht und energetisch ähnlich zur thermischen Energie bei kryogenen Temperaturen. Die Kombination aus hoher Güte der mechanischen Schwingung und Verstimmbarkeit der Elektronenergielevel mittels elektrischer Felder macht CNTs zu einem geeigneten System für hochpräzise Messungen beispielsweise als Sensor oder Qubitplattform. Ein nach wie vor großes Problem bleibt jedoch ihre Integration in komplexere Schaltkreise.
In dieser Arbeit haben wir durch sorgfältig entwickelte Nanofabrikationsprozesse sehr saubere und frei hängende CNTs hergestellt, die durch lokale Gates elektrisch steuerbar sind. Die CNTs wurden dabei als letzter Schritt in zuvor gefertigte Nano-Schaltkreise integriert, entweder durch Gasphasenabscheidung direkt auf den Elektroden oder durch eine Stempeltechnik bei der die CNT auf einem separaten Chip gewachsen wurde und in einem Nanomontageprozess auf den Schaltkreis übertragen wird. Die lokalen Gate Elektroden erlauben eine präzise Modifikation des elektrischen Potentials und dadurch die Erzeugung von bis zu drei Quantenpunkten in Reihenschaltung in der CNT. Die Kopplung dieser Quantenpunkte and die mechanischen Schwingungsmoden eröffnet die Möglichkeit der Kontrolle der Elektron-Phonon Wechselwirkung in der CNT.
Die frei hängenden CNTs sind zusätzlich geeignete Plattformen für die Auslese des Spin-Zustandes eines Einzelmolekülmagnetens (SMM) durch Spin-Phonon-Kopplung. SMMs können einen Spin-Qudit formen und die CNT eröffnet die Möglichkeit einer kontrollierten Auslese durch Messungen der elektrischen Leifähigkeit.

Contents

1 Introduction

For decades, the semicondutcor industries' solution to ever increasing customer demands has been the miniaturisation of functional components. This gave rise to incredible technological advances in particular in silicon CMOS (complementary metal-oxide-semiconductor) fabrication following the self-fulfilling prophecy of 'Moore's law', which predicted a doubling of the transistor density every two years. However, this approach reaches its fundamental limits, when quantum effects, like leakage tunnelling currents, start to affect the device performance. Therefore, new technologies are needed, that possess an intrinsic advantage over classical electronics.
The advent of quantum computing as a concept working with completely different rules than a classical computer induced a paradigm shift and demanded a rethinking of how to perform computing. While classical computing is based on bits with two states, quantum computing is based on quantum bits (qubits) that are a superposition of two quantum states. Making use of this superposition, entanglement and interference phenomena quantum computers are theorised to require exponentially less computation steps than a classical computer for specific application cases. This opened the field for other technologies, since the physical nature of a qubit is not fixed. Qubits have been realised in industrially nanofabricated superconducting circuits [1], quantum dots in two-dimensional electron gases [2] or one-dimensional nanotubes [3, 4], a single spin in a molecule [5], optically active defects [6], trapped ions [7] and more. The different qubit designs all come with their own set of benefits and drawbacks considering scalability, tunability and fidelity. To give an example, several trapped ions are all identical which makes them somewhat easy to manipulate at the cost of low tunability, as the ions are identical and the number of different ions is limited. On the opposite end of the size spectrum are artificial atoms e.g. superconducting circuits. By means of nanofabrication superconducting circuits can be altered easily between different generations, but, due to their macroscopic size and large tunability, each superconducting circuits will have its own distinct set of parameters.

One system providing a potential trade-off of large tunability and large reproducibility are single-molecule magnets (SMMs). Single-molecule magnets feature a single giant spin typically originating from transition metals surrounded by an organic ligand shell with a strong anisotropy. The possibility of chemical synthesis allows for millions of identical molecules with electronic and binding properties tunable by chemical engineering of the central atom and the surrounding ligand shell. This chemical synthetisation of gives rise to the production of millions of identical qubits, widely tunable between generations. A frequently studied SMM is terbium (bis)phthalocyaninato ($TbPc_2$), where the central terbium ion in the crystal field is responsible for the giant spin. The terbium nuclear-spin states feature extremely long lifetimes up to years [8] and coherence times at cryogenic temperatures, due to their strong decoupling from the environment as they interact via the giant spin which in itself is well

protected by the organic ligands. However, the small size of a molecule and the strong decoupling come at the price of a significant challenge in terms of integration into other systems and spin state readout. In previous experiments, amongst others, a spin-transistor [9, 10], a spin-valve [11–13] or coupling to a mechanical motion of a carbon nanotube nanoelectromechanical systems (CNT NEMS) [14–16] have been achieved in order to readout the (nuclear-) spin state. The multilevel nuclear system allowed the realisation of a quantum digit (qudit) and the application of the Grover algorithm has been demonstrated [17].

This thesis aims to continue the work on spin-phonon coupling using CNT NEMS as a clean and versatile platform. A CNT in itself is an interesting nanoscale object based on its one-dimensionality, exceptional mechanical properties and electronic tunability rendering them well suited for NEMS-applications. CNTs have been used in many experiments such as (spin) qubits [18], ultra-high quality factor mechanical resonances [19], formation of a Wigner-crystal [20], Franck-Kondon blockade [21] and more.

CNTs can be produced in a lab without the need of high-end equipment by using chemical vapour deposition [22]. Over the years, different ways of integrating CNTs into metal circuits have been realised. The metal circuit can be patterned around the CNT lying flat on a surface and the contact is done by depositing a conductive material on top of a CNT segment [23, 24]. Similarly, the CNT can be grown on top of the metal circuit by locally depositing catalyst nanoparticles at the positions where CNTs are supposed to be integrated [25, 26]. A different approach comprises the growth on a separate chip and transferring the CNT as a last step with an assembly system onto the metal circuit fabricated prior to the assembly [27]. Each technique has its benefits and drawbacks in terms of cleanliness, contact resistance and versatility discussed in a later chapter, but for this work only the latter two approaches were used since the CNT will not be contaminated by solvents or resist this way. By suitable nanofabrication processes, a CNT suspended above several local gates able to tune the electric potential along the CNT has been realised. The integration was possible via direct growth or transfer.

The coupling of two nanoscale objects, a CNT and an SMM, still is a significant challenge. In the past, solutions containing SMMs were dropcasted on chips hosting CNTs. While this proved to be successful [14], the cost was an exposure of the CNT to the solvent inevitably contaminating the CNT with other hydrocarbons as well. To provide a cleaner method of depositing SMMs, in this work an evaporation system was remodelled in order to couple thermally evaporated SMMs to a CNT without the need of additional solvents therefore keeping the CNT clean.

The readout of the molecular spin state using the CNT can be based on a spin-valve effect [11] affecting electric transport by a magnetoresistive effect, magnetic-flux coupling in a dc-SQUID (superconducting quantum interference device) with the CNT as the superconducting weak link [24, 28] or a coupling to the mechanical modes of the CNT [14]. Spin relaxation processes require a conservation of angular momentum which forces the creation or annihilation of a phonon, which have a discrete energy spectrum in the case of CNT NEMS, resulting in selective relaxation dynamics [16] for an SMM grafted on a CNT. In case of a magnetic field that is not parallel to the easy axis of the SMM, the interaction with the magnetic moment forces a torque on the CNT that induces additional strain which shifts the mechanical resonance frequency. Mechanical resonances in a small NEMS often follow the behaviour

of a bifurcating Duffing-oscillator [29] which can cause huge signal jumps for small variations. This way, a binary readout can be realised, which was the aim of this work. However, the coupling between the molecular spin and electronic transport or the mechanical modes could not be realised and the focus shifted to the study of the, in itself, interesting system of a CNT NEMS.
In chapter 2, an introduction into the physics of CNTs in context of quantum dots and nanomechanics is provided. The chapter concludes with a description of SMMs and how the coupling to CNTs could be realised. Following this, in chapter 3 an overview of the fabrication processes as well as necessary trade-offs for the different sample types produced and measured are given. The section also contains parts on the room-temperature selection and annealing of devices to improve the interface quality. Besides room-temperature measurements, experiments were also performed at cryogenic temperatures in a setup that is presented in chapter 4. The data acquired at cryogenic temperatures, studying mechanical resonance modes as well as single and double quantum dots, is shown and discussed in chapter 5. The last chapter 6 provides a summary of the achievements and encountered problems of this thesis and gives an outlook on the future evolution of this experiment.

2 Theoretical background

This section is dedicated to the theory behind the physical phenomena observed in the experiments shown in chapter 5. Since this thesis mainly evolves around the work with carbon nanotubes, their structure, mechanical and electronical properties are introduced first. Afterwards, a section on quantum dots in general and quantum dots in carbon nanotubes in specific explains the second big aspect of this thesis. Since we used suspended carbon nanotubes, the third subsection is dedicated to the description of their mechanical resonance modes and their interplay with electronic transport. The chapter is concluded by an introducing part on single-molecule magnets and how we wanted to integrate them.

2.1 Introduction to carbon nanotubes

2.1.1 Structure and mechanical properties of carbon nanotubes

A carbon nanotube (CNT) is one of the possible allotropes of elemental carbon. In its natural form carbon consists of 99 % ^{12}C which features no nuclear spin. The electronic structure of carbon reads [He]$2s^2 2p^2$ and carbon thus has four valence electrons. Due to its ability to form stable hybridised orbitals, a small zoo of different configurations is possible. In this hybridisation the $2s$ and up to three $2p$-orbitals combine and take a tetragonal (sp^3), trigonal (sp^2) or linear (sp) shape by forming σ-bonds. While sp^3-hybridised carbon (e.g. diamond) already finds use in technical applications due to its hardness and optical properties, sp^2-hybridised carbon only received some attention with the discovery of fullerenes in the 1980s [30], carbon nanotubes in 1991 [31] and culminated in the discovery of graphene in 2004 [32]. Graphene is formed by a monolayer of sp^2-hybridised carbon forming a honeycomb-lattice, while the p_z orbitals are arranged out of plane, and form a π-binding between them. The lattice can be described by the two lattice vectors a_1 and a_2 (see figure 2.1) and thus a vector $\vec{C}$ with

$$\vec{C} = n\vec{a}_1 + m\vec{a}_2 \tag{2.1}$$

using $n, m \in \mathbb{Z}$ as chirality indices can connect any two points on the lattice. The two lattice vectors a_1 and a_2 have a length of 1.42 Å with an angle α of 60° between them. A pictorial way of looking at a CNT is to imagine it as a rolled up sheet of graphene (figure 2.1) where the chirality vector $\vec{C}$ describes the rolling direction and therefore the symmetry. Knowing the chirality vector an expression for the CNT diameter, assuming a perfect circular cross-section, can be derived:

$$d = \frac{|\vec{C}|}{\pi} = \frac{a}{\pi}\sqrt{n^2 + m^2 + nm}. \tag{2.2}$$

This is true for a small diameter CNT. In case of a larger diameter, the CNT tends to flatten [33]. If the chirality vector aligns with either one of the lattice vectors, the CNT possesses a so called *zig-zag*

symmetry. If the chirality vector has an angle of $\alpha/2$ to one of the lattice vectors, the CNT possesses an *armchair* symmetry. These symmetries can also be expressed in terms of the chirality indices n, m where a *zig-zag* symmetry has $n \neq 0$, $m = 0$ and an armchair symmetry $n = m$. All other linear combinations of n, m are called chiral nanotubes.

Similarly to the well known unique mechanical properties of diamond, graphene and carbon nanotubes

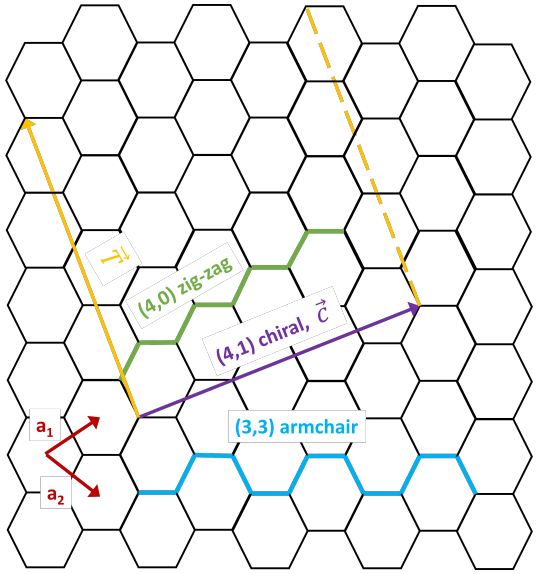

Figure 2.1: **Schematic representation of a graphene lattice and the imaginary rolling pattern of a CNT.** If a graphene lattice was to be cut along the yellow vector $\vec{T}$ and then rolled following vector $\vec{C}$ a chiral carbon nanotube with the index tuple (n, m), and in this case specifically (4,1), would be formed. The vectors $\vec{C}, \vec{T}$ are forming the unit cell. If the rolling was occurring along specific symmetry axes with either $n = m$ or $m = 0 \neq n$ the resulting nanotube is called armchair or zig-zag type.

feature a remarkably high mechanical strength. A measure to express mechanical strength is Young's modulus Y given by the ratio of tensile or compressive stress σ to the linear deformation ε. For in-plane strain, carbon nanotubes and graphene possess a Young's modulus of about 1 TPa [34] which is among the highest of any material known so far. However, carbon nanotubes are far softer in radial direction with a Young's modulus below 60 GPa that is decreasing for an increasing tube radius [35]. The reason behind this high in-plane strength can be found in the high stability σ-bonds of the hybridised sp^2 orbitals. Since carbon nanotubes also have a low density, mechanical resonances will have a comparably high resonance frequency in the hundreds of MHz range for bending modes or tens of GHz for stretching modes, which makes them readily accessible and combinable with common rf-techniques rendering them a very interesting material for nanoelectromechanical systems (NEMS).

2.1.2 Electronic properties of carbon nanotubes

When describing the electronic properties of carbon nanotubes, it is instrumental to describe the properties of graphene and then look at the occurring deviations due to the curvature and the constraints to

one dimension. As mentioned, the hybridised electrons are located in σ-bonds forming the hexagonal lattice but they do not partake in electronic transport. The electronic transport is dominated by the delocalised π- and π^*-orbitals formed by the out-of plane oriented p_z-orbitals. The π- and π^*-orbitals give rise to the valence and conduction band. Following tight-binding calculations performed for graphite, the energy dispersion was found to be [36, 37]

$$E_{\pm}(\vec{k}) = \pm t\sqrt{3 + f(\vec{k})} - t' f(\vec{k}) \tag{2.3}$$

$$f(\vec{k}) = 2\cos\left(\sqrt{3}k_y a\right) + 4\cos\left(\frac{\sqrt{3}}{2}k_y a\right)\cos\left(\frac{3}{2}k_x a\right) \tag{2.4}$$

with t and t' being the hopping energies to the nearest and next-nearest neighbours in the sublattice, respectively. Plus and minus correspond to the π^* and π band while k_x, k_y are the components in k-space. From the formula alone it is expected that the dispersion is symmetric around zero in case of $t' = 0$. In case of $t' \neq 0$ electron-hole symmetry is broken and the conduction and valence band become asymmetric [36]. A plot of the resulting band structure with hopping parameters is shown in figure 2.2. The hexagonal lattice structure still determines the symmetry in the band structure resulting

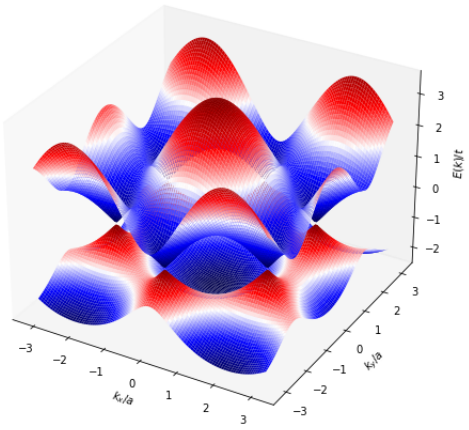

Figure 2.2: **Band structure of graphene according to eq. (2.4).** The upper and lower bands are touching at the six Dirac points. In their vicinity linear dispersion can be observed.

in six pairs of cones facing each other and forming a hexagon. The points in the band diagram where the cones are touching are called *Dirac points*. Neighbouring Dirac points cannot be connected by using reciprocal lattice vectors and are thus two different sites labelled K and K'. This results in two distinguishable electronic states called *valley*-states. Since the cones are touching at the Dirac points, graphene possesses no bandgap and the Fermi energy E_F is right between the cones and crossing the touching point. Upon expansion of eq.(2.4) around a Dirac point K using $\vec{k} = \vec{K} + \vec{q}$ in the limit of $|\vec{q}| \ll |\vec{K}|$ a linear dispersion can be observed [37]:

$$E(\vec{q}) = \pm\hbar v_F |\vec{q}| + O\left(\left|\frac{\vec{q}}{K}\right|^2\right) \tag{2.5}$$

with $\vec{q}$ as the momentum relative to the K-point and the Fermi velocity v_F given by $v_F = 3ta/2 \simeq 10^6\ ms^{-1}$. The resulting Fermi velocity is rather unusual as it does not depend on either momentum or energy [36].

As previously mentioned, a CNT can be imagined as a rolled up sheet of graphene. While a sheet of graphene can be described as a two-dimensional (2D)-crystal of infinite size in two-dimensions, a CNT possesses a one-dimensional (1D)-symmetry and thus deviations are to be expected. The transition from 2D to 1D is done with the so called *zone-folding approximation* by introducing periodic boundary conditions for the radial component $k_\perp$ which is oriented orthogonal to the nanotube symmetry axis. This results in a quantisation in the direction of the chirality vector $\vec{C}$. The values of $k_\perp$ are given by

$$\vec{k}\vec{C} = \pi d k_\perp = 2\pi l \tag{2.6}$$

with an integer l. For sufficiently long nanotubes there is no quantisation along the tube axis $\vec{T}$, i.e. $k_\parallel$ is not quantised, and electrons can move freely in this direction. This results in a modification of the band structure around the Dirac cones and eq. (2.5) can now be written as

$$E_D(k_\perp, k_\parallel) = \pm\hbar v_F \sqrt{k_\perp^2 + k_\parallel^2}. \tag{2.7}$$

The quantisation of $k_\perp$ results in the creation of one sub-band per $k_\perp$-vector (figure 2.3). If at least one of the sub-bands crosses a Dirac point, the CNT is considered to be metallic. If none is crossing, it is considered to be semiconducting due to the emerging bandgap. It was found that this can also be expressed in terms of the chiral indices [38] n, m: A CNT is metallic if $2n + m = 3l$ where l is again an integer. This condition is always fulfilled for armchair nanotubes with $n = m$ and they are thus considered to be metallic. For zig-zag nanotubes ($m = 0$) this condition is only fulfilled for $n = 3p$ and thus the majority is considered semiconducting. However, these arguments assume no influence of the curvature which can shift the Dirac cones and deviations are observed when taking the latter into account [39]. It was found that the bandgap scales with the diameter of the nanotube and approximately follows $\Delta E_{gap} = \frac{0.7}{d}$ eV with the diameter d in nm for small diameter nanotubes and a proportionality of $\propto \frac{1}{d^2}$ for larger diameters [40]. As a result, even many supposedly metallic nanotubes feature small bandgaps and are called *narrow-gap* nanotubes. Besides curvature, it was found that mechanical strain, e.g. induced by an atomic-force-microscopy- (AFM)-tip, can modify the bandgap [41].

This resulting bandgap allows for many applications in analogy to frequently used semiconductor techniques in contrast to graphene which does not have a bandgap and thus complicates applications such as transistors. With this bandgap, however, and due to the tunability of electronic states in the CNT, electric charges can be spatially confined which will be discussed in section 2.2 where quantum dots are introduced.

The (electric) conductance of a one-dimensional conductor can be expressed as the sum of all conduction channels that each contribute one quantum of conductance $G_0 = \frac{2e^2}{h}$: $G = NG_0T$ in the case of N conduction channels with perfect transmission $T = 1$ [43]. In reality, of course, some channels will be partially suppressed. In case of a scattering free CNT (i.e. its length L is smaller than the electron mean free path l) the intrinsic resistance has a lower limit of $R = \frac{1}{2G_0} \approx 6.5\,\text{k}\Omega$. The factor 2 is a result of the two different valley states, the two possible spin states are already considered in the definition of G_0.

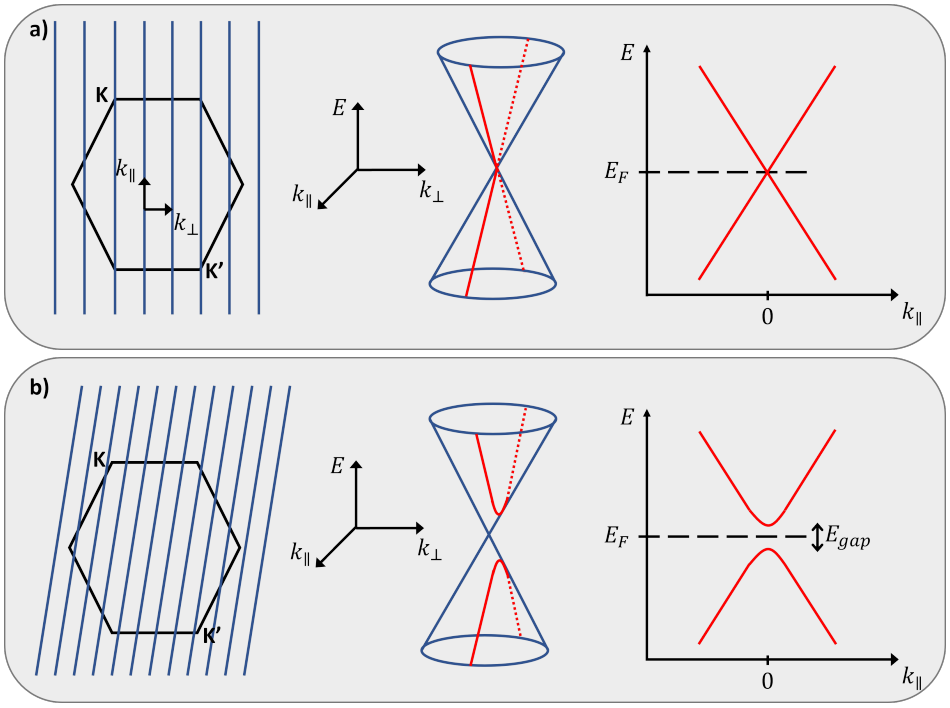

Figure 2.3: **Schematic representation of the consequences of the zone-folding approximation.** **a)** The periodic boundary conditions result in a Brillouin zone in the shape of a line. In the case of a metallic nanotube the resulting lines touch at least one Dirac point and the result is analogous to graphene zero-bandgap. **b)** If the perpendicular component $k_\perp$ is finite, as for this exemplary chiral nanotube, no Dirac point is crossed and a bandgap of energy E_{gap} emerges. Figure adapted from [42].

In real CNT devices, however, scattering as well as an interface resistance R_C between the CNT and the contacting material will result in an increased resistance [44]:

$$R \approx \frac{h}{4e^2} + \frac{h}{4e^2}\frac{L}{l_m} + 2R_C. \tag{2.8}$$

Typically, the contact resistance R_C is non-negligible and is often even the dominating contribution to the overall resistance. The next section is dedicated to this arising resistance in the form of *Schottky barriers* and how they can be understood as well as reduced.

2.1.3 Carbon nanotube - metal interface

The resistance between a carbon nanotube and a metal contact is sensitive to a few contributing factors. Generally a good electric contact occurs if there is a large orbital overlap between metal and carbon nanotube and energy levels are easily accessible. It is obvious that surface contaminations that form an intermediate layer between the CNT and the metal deteriorate the contact quality and, if not for some lucky chance, increase the contact resistance. This was observed for early devices where the nanotubes have been dispersed on pre-patterned contacts [45, 46]. The surface contaminations as well as the loose attachment resulted in a contact resistance of about 1 MΩ. Materials that have a high work function (e.g. gold, platinum) have been chosen for the contacting laye that match the high work function of CNTs ($\approx$ 4.8 eV [47]). A mismatch in the work function and the effect of Fermi-level pinning can result in the formation of Schottky barriers (figure 2.4), where an energy barrier occurs at the interface between a (semiconducting) nanotube and a metal.
In case of carbon nanotubes this barrier decays over a few nm [48] due to the point-like geometry of the contact and acts as a tunnelling barrier with a tunnelling rate depending on the temperature. The observable I-V characteristics of such a contact resemble a diode.
When contacting a carbon nanotube from the side, charge injection into the CNT may only take place by interaction with the p_z orbitals. Due to the curvature, the overlap of individual p_z-orbitals is reduced on the outside of carbon nanotubes compared to the inside and an interaction is facilitated. Typically nowadays, transition metals are being used to form the contact. Good wetting properties are desired to increase the overall contact between metal and nanotube which is given for metals like titanium or palladium while others such as aluminium or gold tend to form islands [48]. Even though titanium has even better wetting properties than palladium (i.e. stronger binding) it is typically forming non-ohmic contacts since charge is accumulating more strongly in the atomic layers of the titanium/carbon system and the interlayer region is depopulated of charge carriers. In case of palladium, excess charge is accumulated between the two layers [48].
The arguments given for side contacts hint that an increase of the contacting area will result in a decrease of the contact resistance, which also was observed for different metals [49]. Another way of contacting the CNT, which is not requiring big overlaps of carbon nanotube and metal, is an edge-contact where the dangling bonds at the end of a nanotube are covalently bonded to the contacting material. While this is readily applied for graphene [50] the application for nanotubes is not that easy due to the much smaller contacting area. Edge-contacts have been achieved by chemical binding to a

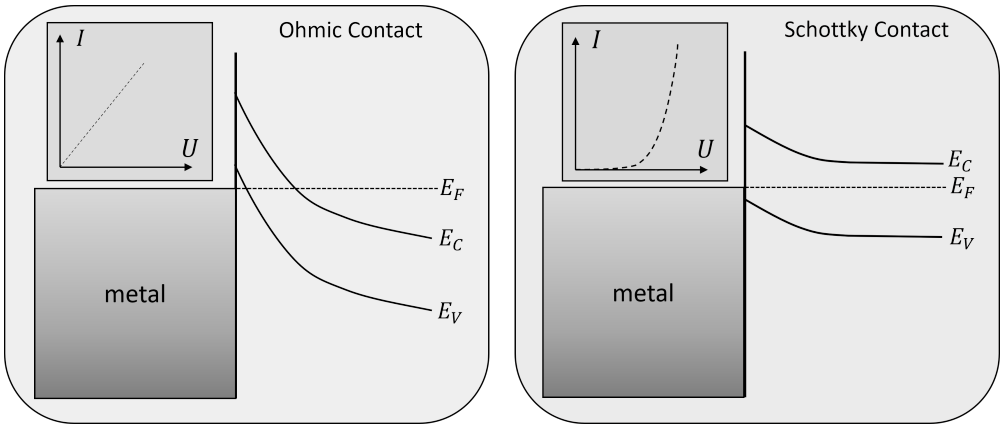

Figure 2.4: **Schematic drawing of a Schottky barrier at a semiconductor-metal interface. Left:** An ohmic contact is shown where charge carriers can traverse freely since the Fermi energy is within the carbon nanotube valence band. The inset shows the typical linear *I-V*-behaviour. **Right:** the case with an emerging Schottky barrier is shown. The inset shows an *I-V*-curve that features a barrier for low bias voltages that develops into an exponential increase. Figure adapted from [48].

metal evaporated on top of the CNT [51] and indeed they show no dependence on the overlapping length and ohmic behaviour.

2.2 Single and double quantum dots

A quantum dot (QD) is a, as the name implies, zero-dimensional system that can be created by confining a system in three dimensions. This can be achieved in various systems like a two-dimensional electron gas in a multistack-semiconductor (e.g. review [52]), a small metallic island, a single molecule magnet [9] or inside a carbon nanotube (e.g. [20, 53] or review [42]), to name a few.
Due to this confinement and the arising boundary conditions for the electron wave function, the energy states of the quantum dot only take discrete values and quantum dots are often called artificial atoms due to the similarities with electronic states in atoms. In the following, the terms electron and charge carrier are used synonymously. In reality, however, quantum dots still have a finite size that, in case of a carbon nanotube, is described by the length L due to the one-dimensionality of a carbon nanotube. This finite size gives interference conditions and the energy spacing is given by $\Delta E = \frac{h v_F}{2L}$ [42]. In a carbon nanotube, the outer boundaries confining the charge carrier may occur naturally in the form of defects or Schottky barriers but they can also be induced e.g. by tuning the electrostatic environment.
A way to visualise and realise this is by contacting one end of the carbon nanotube with a metal electrode *source*, one end with a metal electrode *drain* and position a third electrode (*gate*) in proximity and capacitively coupled to the carbon nanotube. Assuming Schottky barriers at the metal-CNT interface, the result is a spatially confined area in the CNT coupled via tunnelling barriers to the electrodes. A schematic representation of the equivalent circuit is presented in figure 2.5. For the

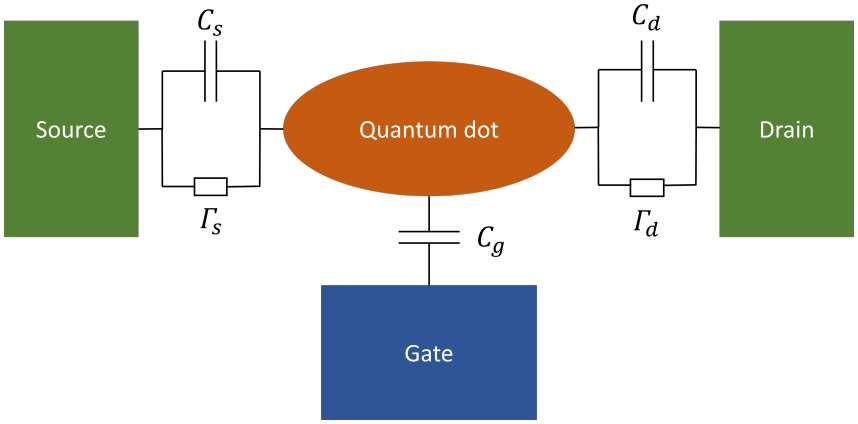

Figure 2.5: **Schematic equivalent circuit of a quantum dot coupled to two leads.** The quantum dot is coupled capacitively to source, drain and gate with the capacitances C_s, C_d and C_g. Charge carriers can hop onto the dot via tunnelling barriers with the tunnelling rate Γ_s and Γ_d.

description of this system the electrodes are assumed to be infinitely large reservoirs of electrons that are coupled to the quantum dot via a tunnelling barrier with the tunnelling rates Γ_s and Γ_d. The tunnelling rates represent the coupling between electrodes and quantum dot. They mainly depend on the overlap of the electrode and dot wavefunctions where the latter can be tuned by applying a voltage on the gate electrode. When confining electrons in a small area, the occurring physics are dominated by discrete charge effects and an additional charging energy due to Coulomb repulsion needs to be paid when adding an electron to the quantum dot. This charging energy E_C can be expressed in terms of the total capacitance C_tot given by the sum of the device capacitances: $C_\mathrm{tot} = C_\mathrm{s} + C_\mathrm{g} + C_\mathrm{d}$. Where C_s, C_g and C_d represent the capacitance to the source, gate and drain electrode, respectively. The charging energy is then $E_\mathrm{C} = \frac{e^2}{C_\mathrm{tot}}$ for an electron of charge e.

Regimes of transport at low temperatures

The type of observable phenomena is governed by the different energy scales arising from the tunnelling barriers, the energy level spacing ΔE in the quantum dot, the thermal energy and the charging energy E_C:

- **Thermal energy**: The thermal energy is given by $k_\mathrm{B}T$ and describes the internal energy that the system has available due to its temperature. Generally thermal energy leads to uncontrolled excitations and a smearing of sharp features, e.g. in electronic transport. Therefore, for many experiments on quantum dots the system is cooled down to cryogenic temperatures of $\approx 30\,\mathrm{mK}$ which corresponds to an energy of $\approx 2.6\,\mu\mathrm{eV}$, compared to $\approx 25\,\mathrm{meV}$ at ambient temperatures.

- **Coupling**: The coupling describes the interaction strength between the quantum dot and its surroundings. It directly controls the tunnelling rate which describes the rate with which charge carriers are exchanged between the source (Γ_s) and drain (Γ_d) electrodes and the quantum dot. In

general, they can vary and are determined by the electronic density of states and the wavefunction overlap.

- **Charging energy**: The charging energy E_C determines the energy it takes to add an additional charge carrier into the quantum dot due to Coulomb repulsion and depends on the total capacitance of the dot. Typically, the energy scale is in the order of meV.
- **Energy level spacing**: The energy level spacing ΔE describes the energy difference between individual energy levels in the quantum dot and arises from interference conditions due to the spatial constraint. Here, the energy scale is typically in the order of few meV.

In order to observe clear and clean quantum transport effects it is beneficial to reduce the system temperature and thereby prevent thermal fluctuations from disturbing the quantum effects. This can be achieved if the thermal energy is much smaller than the other energy scales involved:

$$k_B T \ll \Delta E, E_C, \hbar\Gamma. \tag{2.9}$$

The other major factor competing with the internal energy scales of the quantum dot are the tunnelling rates, or generally the coupling Γ. The energy $\hbar\Gamma$ expresses a finite line broadening of the levels in the dot as result of the coupling of the discrete spectrum in the dot with the continuous spectrum of the leads. Depending on the ratio of coupling to charging energy, generally three different transport regimes are distinguished:

- **Closed quantum dot regime**: $\hbar\Gamma \ll E_C$
  Here, discrete charging effects dominate the transport and features like Coulomb blockade or a single-electron transistor emerge.
- **Intermediate quantum dot**: $\hbar\Gamma \leq E_C$
  Here, charging effects and cotunnelling processes matter. Commonly observable features are higher order tunnelling processes.
- **Open quantum dot**: $\hbar\Gamma \gg E_C$
  Here, interference effects are dominating the transport behaviour. The dot behaves as a quantum analogon to Fabry-Pérot-interference.

Since the coupling Γ is directly depending on the height of the tunnelling barrier, the contact quality between the quantum dot and the leads can already determine the regime of transport. In the following, the different transport regimes as well as some of the occurring phenomena will be discussed.

2.2.1 Closed quantum dot regime

In the closed quantum dot regime the transport behaviour is predominantly determined by discrete charging effects due to a weak coupling to the leads. Typically, charge carriers pass the dot one by one in a sequential tunnelling process and the charge state of the quantum dot is well-defined since the level-spacing inside the dot is larger than the coupling and the thermal energy prohibiting the

population of energetically higher levels. After a charge carrier enters the quantum dot the additional Coulomb repulsion blocks other charge carriers from entering the quantum dot, until the first charge carrier left the dot. This regime of conductance is therefore called Coulomb blockade.
A rather simple yet widely useful model to describe electronic transport in the Coulomb blockade regime is the *constant interaction model* (CIM). In order to apply this model, two assumptions need to be made. First, all electrostatic interactions need to be describable by a total capacitance C_Σ and second, the energy level spacing in the quantum dot may not depend on the number of charge carriers in the dot but must remain constant. The amount of total energy U gained or lost when an additional charge carriers enters the quantum dot is called the chemical potential μ. It is defined by

$$\mu(N) = U(N) - U(N-1), \tag{2.10}$$

which describes the total energy difference between $N-1$ and N charge carriers inside the dot. The total energy for an occupation with N charge carriers can be calculated [54] as

$$U(N) = \frac{\left(\alpha_\mathrm{s} C_\mathrm{s} V_\mathrm{sd} - \alpha_\mathrm{d} C_\mathrm{d} V_\mathrm{sd} - C_\mathrm{g} V_\mathrm{g} - Ne\right)^2}{2C_\Sigma} + \sum_{i=1}^{N} E_i \tag{2.11}$$

with V_sd being the voltage applied between the two leads, α_i the relative voltage drop at either tunnelling barrier, C_i the individual capacitances as defined before and E_i the single particle energies depending on the confinement. For the understanding of the system, it is helpful to keep in mind that the difference in chemical potential between two occupation numbers N and $N-1$, i.e. the addition energy E_add [54], is given by the sum of charging energy and level spacing:

$$E_\mathrm{add} = \mu(N) - \mu(N-1) = E_\mathrm{C} + \Delta E(N), \tag{2.12}$$

where ΔE can even vanish in the case of degenerate levels.
In this transport regime, electrons may only traverse the dot if the levels in the dot are within the window between the chemical potential of source μ_s and drain μ_d, $\mu_\mathrm{s} - \mu_\mathrm{d} = -|e|V_\mathrm{sd}$, created by the voltage V_sd applied between source and drain electrode, i.e. $\mu_\mathrm{s} \geq \mu(N) \geq \mu_\mathrm{d}$ for any N. A simplified cartoon showing this process is shown in figure 2.6. The energy range for which transport is possible is called bias window. For this description it is generally assumed that there are available filled states in the source electrode and available empty states in the drain electrode.
If the condition $\mu_\mathrm{s} \geq \mu(N) \geq \mu_\mathrm{d}$ is not fulfilled the number of electrons within the dot remains fixed and no current will flow. This effect is called Coulomb blockade. The blockade can either be lifted by increasing the bias window (increasing V_sd) or by tuning the energy levels with a gate voltage V_g, see figure 2.6. If an additional level in the dot becomes available, an electron may hop into and later out of the dot, thereby opening the level again for the next electron to follow the same steps. This process is called single-electron tunnelling and the resulting current mainly depends on the tunnelling rates.
When measuring the current or conductance with a fixed bias voltage close to zero as a function of the applied gate voltage periodic conductance peaks, so-called Coulomb peaks, can be observed (figure 2.7). Their width is determined by the linewidth of the involved levels, applied bias voltage and thermal energy. Every peak corresponds to the situation in figure 2.6b) and the large blocked areas to

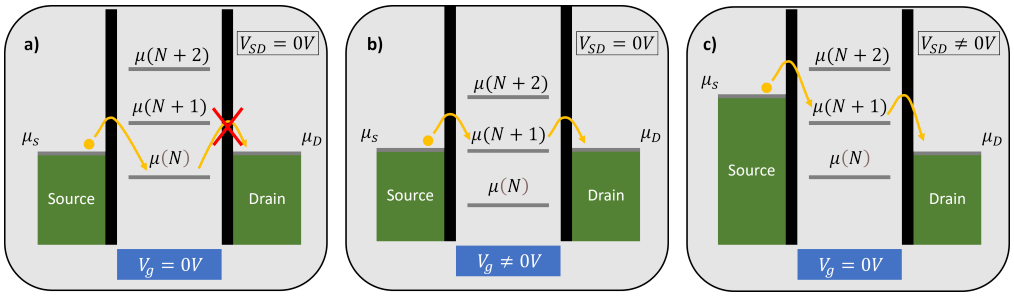

Figure 2.6: **Scheme of energy levels and transport in a quantum dot.** A source and drain electrode are connected to a quantum dot via tunnelling barriers (black bars). Yellow arrows indicate energetically favoured hopping. **a)** The electron may only hop into the dot but cannot leave it towards the drain. The total number of electrons in the dot is fixed. This situation is called Coulomb blockade. **b)** After applying a gate voltage V_g, levels are aligned and transport is possible. **c)** Applying a bias voltage V_{sd} opens a window to enable transport, even without an additional gate-voltage.

a situation as shown in figure 2.6a). If now the bias voltage is also varied, the width of the peaks is increasing. A common characterisation of quantum dot devices is a charge-stability diagram, where the conductance is measured as a function of gate- and bias voltage. Since the peaks are broadening the region of Coulomb blockade is shrinking. At some point, the peaks will overlap and there is no full blocking region anymore. In the charge stability diagram, this occurs at the tip of a diamond shaped area called *Coulomb diamond* (figure 2.7).

A charge stability diagram generally can give a good overview over the transport properties of the device under test. Coulomb diamonds in particular can give insights into the energy scales involved. Their height (zero-line to tip) is defined by the addition energy with $E_{\text{add}} = |e|V_{\text{sd}}$. Their width gives information about the gate coupling, since the charging energy is still the same. The gate lever arm α defines a ratio between bias voltage and change of gate voltage ΔV_{g} needed to achieve the same change of available charge state which can be expressed as $|e|\, V_{\text{sd}} = \alpha|e|\, \Delta V_g$. When looking at the slopes of the Coulomb diamonds, additional information about the involved capacitances of source, drain and gate can be gained. The flank on the right side of a diamond peak (towards higher gate voltage) is given by the ratio of $s_- = -C_g/C_s$ while the flank on the left side is given by $s_+ = C_g/(C_g + C_d)$. This allows for another definition of the gate lever arm $\alpha = \frac{1}{S_+ + s_-}$.

In the closed quantum dot regime transitions and features are typically sharp since coupling between different systems is generally weak. This weak coupling also implies that most processes are single-particle processes of lower order. This makes the closed quantum dot regime interesting for studies where a high resolution is required, e.g. when energy level spectroscopy is performed or for mechanical resonances with a high quality factor.

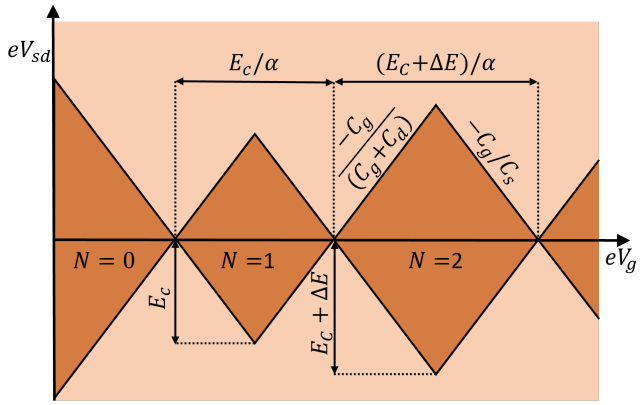

Figure 2.7: **Schematic diagram of a charge-stability map.** Plotted are the applied bias voltage V_{sd} over the applied gate voltage V_g scaled with the elemental charge e. Areas in darker red show Coulomb blockade and no conduction. This example shows spin-degeneracy and therefore every other Coulomb diamond is larger (shell-filling after two charge carriers). The height of the diamonds is determined by the addition energy $E_{add} = E_C + \Delta E$, the width by the product of addition energy and gate lever arm α. From the slopes of the Coulomb diamonds, the capacitive coupling can be determined.

2.2.2 Intermediate quantum dot regime

In the intermediate quantum dot regime we again assume the thermal energy $k_B T$ to be much smaller than the coupling $\hbar\Gamma$ and the addition energy. Now, however, coupling and electrostatic energies are about the same size with an ordering given by $\hbar\Gamma \leq E_C < \Delta E$.
In this regime higher order tunnelling processes are non-negligible and the charge state is object of quantum fluctuations. Due to Heisenberg's uncertainty principle classically forbidden energy states are available for a time $h/\delta E$ where δE is the energy difference from the Fermi energy. Within this time window an electron could, e.g. leave the dot, if another electron tunnels into the dot. The intermediate, unoccupied state that classically is not possible is called virtual state. As a result of such a process, effectively one electron has been transported through the dot. Since for this process tunnelling across two barriers is involved, its amplitude scales with the inverse square of the tunnelling barrier height (R_C). There are several different ways how such processes can manifest of which an elastic cotunnelling, an inelastic cotunnelling and a spin-flip tunnelling following [55] will be briefly explained here.
In an elastic cotunnelling process an unoccupied energy level in the dot is briefly occupied creating a virtual state (see figure 2.8A). If within this brief time t h/Γ determined by the coupling, the electron leaves this energy level towards the drain, one electron has been effectively transported. An analogous process can occur if an electron temporarily tunnels from an occupied level in the dot to the drain. If an electron from the source reoccupies the energy level in the dot during the lifetime of the virtual state, again one electron has been transported. In comparison to previously described sequential tunnelling processes the energy levels remain in their original state for most of the time, the amplitude of transport is thus lower as for aligned energy levels (resonant transport).

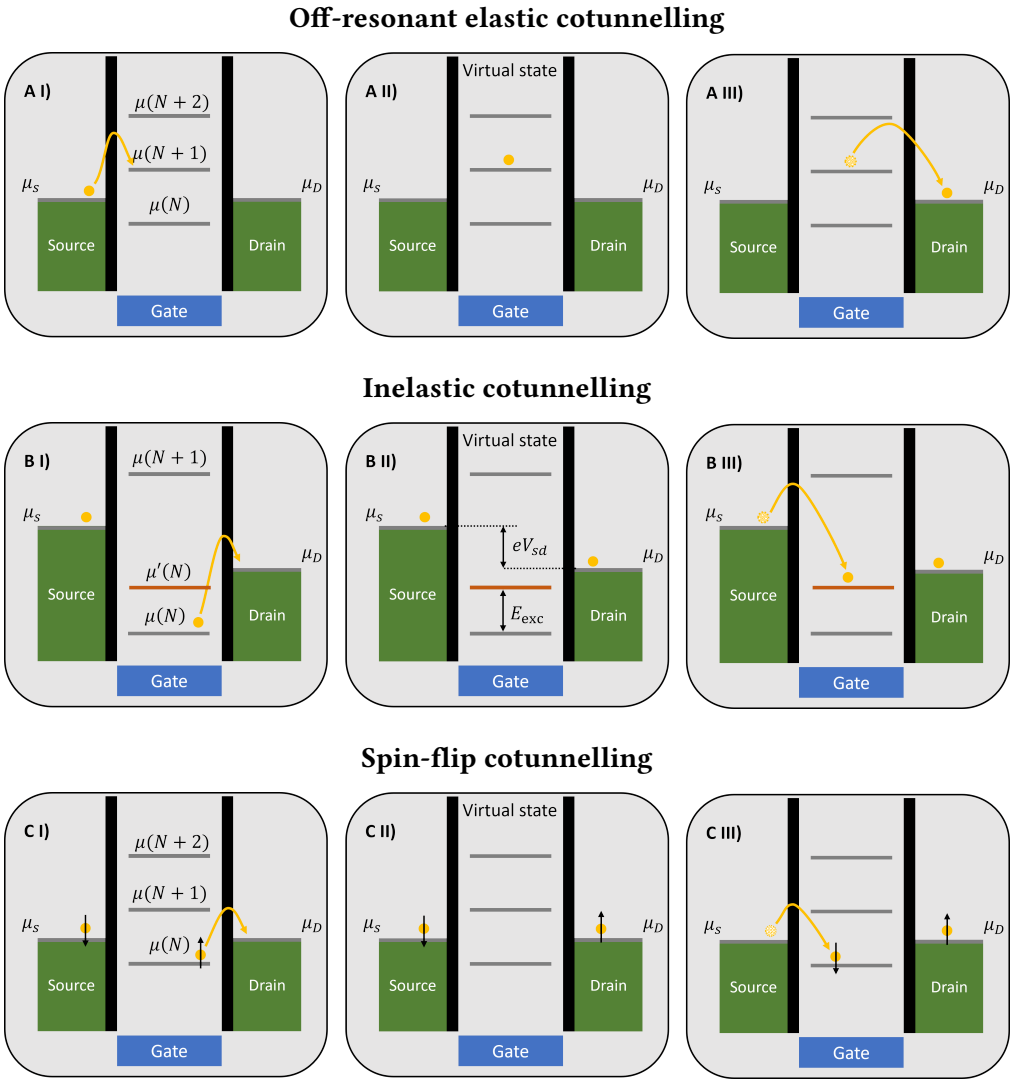

Figure 2.8: **Compilation of different cotunnelling mechanisms. A I-III:** In an exemplary elastic cotunnelling process a classically forbidden state $\mu(n+1)$ is temporarily occupied within a time given by Heisenberg uncertainty. From the temporarily occupied state, the electron can tunnel to the drain. An equivalent process for the filled state $\mu(N)$ tunnelling to the drain exists as well. **B I-III:** An exemplary inelastic cotunnelling process where a filled dot is temporarily emptied is shown. A second electron tunnels into the dot and occupies an excited state $\mu'(N)$. This occurs if the excitation energy E_{exc} matches eV_{sd}. Relaxation can happen via phonon or photon emission. **C I-III:** A spin-flip cotunnelling or Kondo effect is a special case of an elastic cotunnelling. For an odd number of electrons in the dot the spin is 1/2. An antiferromagnetic exchange coupling can lead to a spin-flip within the quantum dot if the electron in the dot tunnels to the leads and the dot is refilled with an electron of opposite spin. How these effects can manifest in a charge stability diagram is presented separately in figure 2.9.

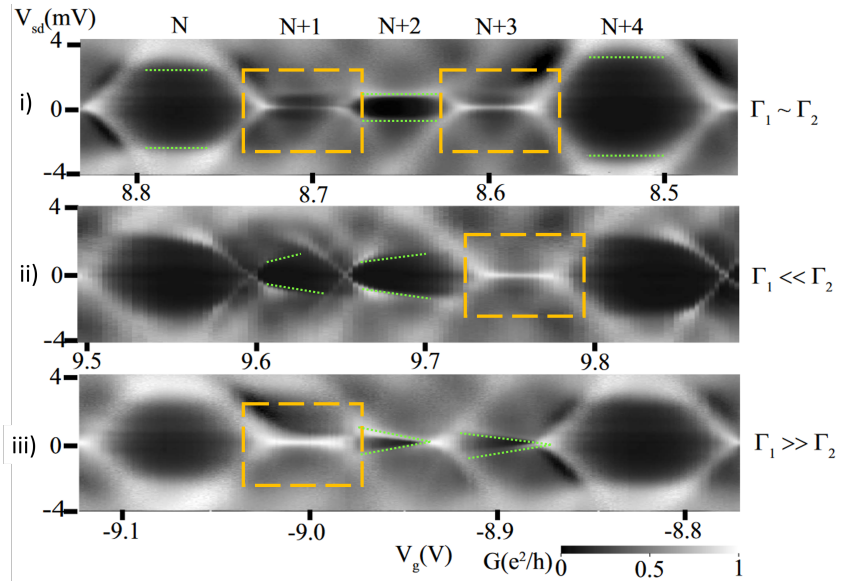

Figure 2.9: **Real data manifestation of cotunnelling effects described in figure 2.8.** The measurements **i)-iii)** show charge stability diagrams for different tuning points of the tunnelling rates through the left barrier (Γ_1) and right barrier (Γ_2). **i)**: For similar rates, inelastic cotunnelling, highlighted in green, was observed for even occupied dots and spin-flip cotunnelling (Kondo ridge) for odd occupied dots, highlighted in orange. **ii)** and **iii)**: the $N+1$ ($N+3$) Coulomb diamond shows no Kondo ridge for $\Gamma_1 \ll \Gamma_2 (\Gamma_1 \gg \Gamma_2)$ and inelastic cotunnelling ridges show a gate-dependent splitting that increases towards higher absolute gate voltages. Adapted from [56].

Inelastic cotunnelling can occur if the bias window is at least the size of the energy spacing $eV_{sd} \geq E_{exc}$. In this case, an electron can leave an occupied level in the quantum dot towards the drain creating a virtual state with an unoccupied level. If another electron from the source tunnels into the dot and occupies an excited state $\mu'(N)$ again, effectively one charge has been transported. Since this type of cotunnelling requires a certain voltage threshold to be exceeded, it is expressed in a charge stability diagram in the form of horizontal lines within a Coulomb diamond, representing a gate voltage independent opening of another conduction channel. Even in the case of an energy level within the bias window, the addition of an excited level leads to an increase in current. In a dI/dV-map, this feature can be seen as lines of conductance change parallel to the contour of the Coulomb diamonds. Studying these additional lines can thus be used as a spectroscopy tool for excited states.
So far properties like spin-state, valley-state etc. have been neglected. A third cotunnelling process takes into account antiferromagnetic exchange coupling for a quantum dot, occupied with an odd number of electrons (effective spin 1/2), to the electron bath of the leads. This gives rise to the Kondo effect. The spin-flip cotunnelling is a special form of elastic tunnelling where an electron of spin up (down) for a short time tunnels into one of the leads. During this time an electron from the opposite lead with spin down (up) can tunnel into the dot, facilitated and enhanced due to the antiferromagnetic exchange coupling. Since there is no applied bias voltage, energy is conserved in this elastic cotunnelling process but the spin in the quantum dot has flipped. In a charge stability diagram this effect manifests as a horizontal line around zero bias in quantum dots with an odd number of electrons inside. The width of the line is determined by the characteristic energy scale of the Kondo temperature T_K being on the order of 10 K for carbon nanotubes.

2.2.3 Open quantum dot regime

In the open quantum dot regime the coupling energy $\hbar\Gamma$ surpasses the charging energy E_C and the barriers confining the dot become increasingly transparent. In this regime, charge is not a good quantum number and the picture of single particle transport does not apply anymore. Interference effects take over the dominant role if the size of the quantum dot is comparable to the coherence length of the conductor. In an analogy to photons in an optical cavity, a quantum dot can act as a resonant cavity for electrons if the transport across the dot is ballistic and no defect scattering occurs. The boundaries of the cavity where the electrons scatter are formed by the tunnelling barriers. Resulting from this, an interference pattern can be observed in a charge stability diagram (see fig. 2.10). The interference pattern can be understood as a consequence of the modulation of the electron number in the dot defined by the applied voltages at bias and gate electrode. In a horizontal cut (constant bias voltage), the conductance value oscillates periodically with the applied gate voltage. It was found [23] that the energy level spacing in this regime still scales with the inverse characteristic length scale L^{-1}, analogous to what was described in the beginning of section 2.2.

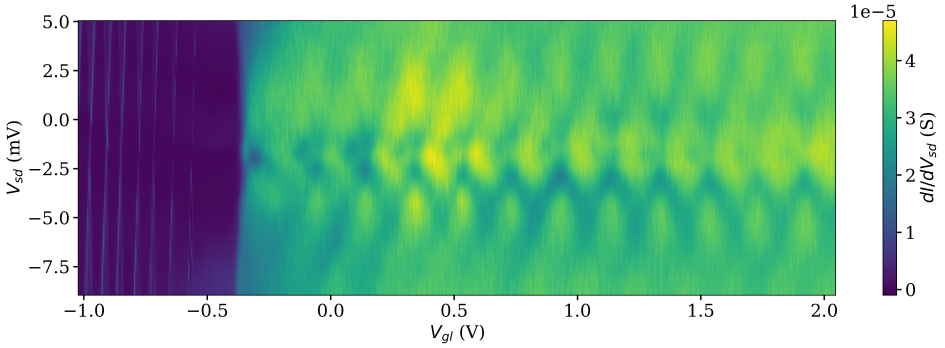

Figure 2.10: **Map of conductance as a function of applied gate voltage V_{gl} and bias voltage V_{sd}.** For gate values larger than $\approx -0.4\,\mathrm{V}$, the sample is in the open dot regime and interference patterns dominate. For lower gate voltages, the dot is in the closed dot regime and Coulomb blockade dominates. Data replotted from [57].

2.2.4 Double quantum dots

In a similar way to how confinement of charge carriers can create a single quantum dot, further confinement within the dot can cause the division into two smaller dots, a so called double quantum dot. Their arrangement can either be in parallel, i.e. they are connected to the same leads or in series, i.e. in order to pass from lead to lead the dots need to be traversed sequentially and a tunnelling barrier separates the two dots. Their physical implementation can be manifold. In gate-tunable devices, a quantum dot can be split laterally or longitudinally by applying a local electric field thereby creating an additional barrier, e.g. in two-dimensional electron gas (2DEG) semiconductor systems (e.g. [58]) or carbon nanotubes [59]. Two parallel quantum dots can for example be formed in a dc-SQUID geometry, where a quantum dot can be formed in each weak link [24].
In the following, the description will mainly focus on a series double dot, though some concepts can be equivalently applied on a parallel double dot. In order to describe this system, it is convenient to introduce an equivalent circuit (see figure 2.11) analogous to what has been done for a single quantum dot (figure 2.5). The coupling between the two individual dots is represented by a tunnelling rate Γ_m and a capacitance C_m. Each dot is coupled to one local gate electrode that allows to tune the energy levels. It is worth noting that while in general two gates can be sufficient to form a double dot, precise control can only be achieved with at least five local gates when the outermost gates tune the tunnelling barriers to the leads and the central gate the barrier in between the dots. In this five gate scenario, the gates 2 and 4 would be used to tune the energy levels of the dots.
Assuming a two gate situation and neglecting cross-capacitances, the chemical potential for the left and right dot can, in analogy to eq. 2.10, be written as

$$\mu_l = U(N_1, N_2) - U(N_1 - 1, N_2) = (N_1 - \frac{1}{2})E_{C_1} + N_2 E_{C_\mathrm{m}} - \frac{1}{\mathrm{e}}\left(C_{\mathrm{g}1}V_{\mathrm{g}1}E_{C_1} + C_{\mathrm{g}2}V_{\mathrm{g}2}E_{C_\mathrm{m}}\right), \tag{2.13}$$

$$\mu_r = U(N_1, N_2) - U(N_1, N_2 - 1) = (N_2 - \frac{1}{2})E_{C_2} + N_1 E_{C_\mathrm{m}} - \frac{1}{\mathrm{e}}\left(C_{\mathrm{g}1}V_{\mathrm{g}1}E_{C_\mathrm{m}} + C_{\mathrm{g}2}V_{\mathrm{g}2}E_{C_2}\right). \tag{2.14}$$

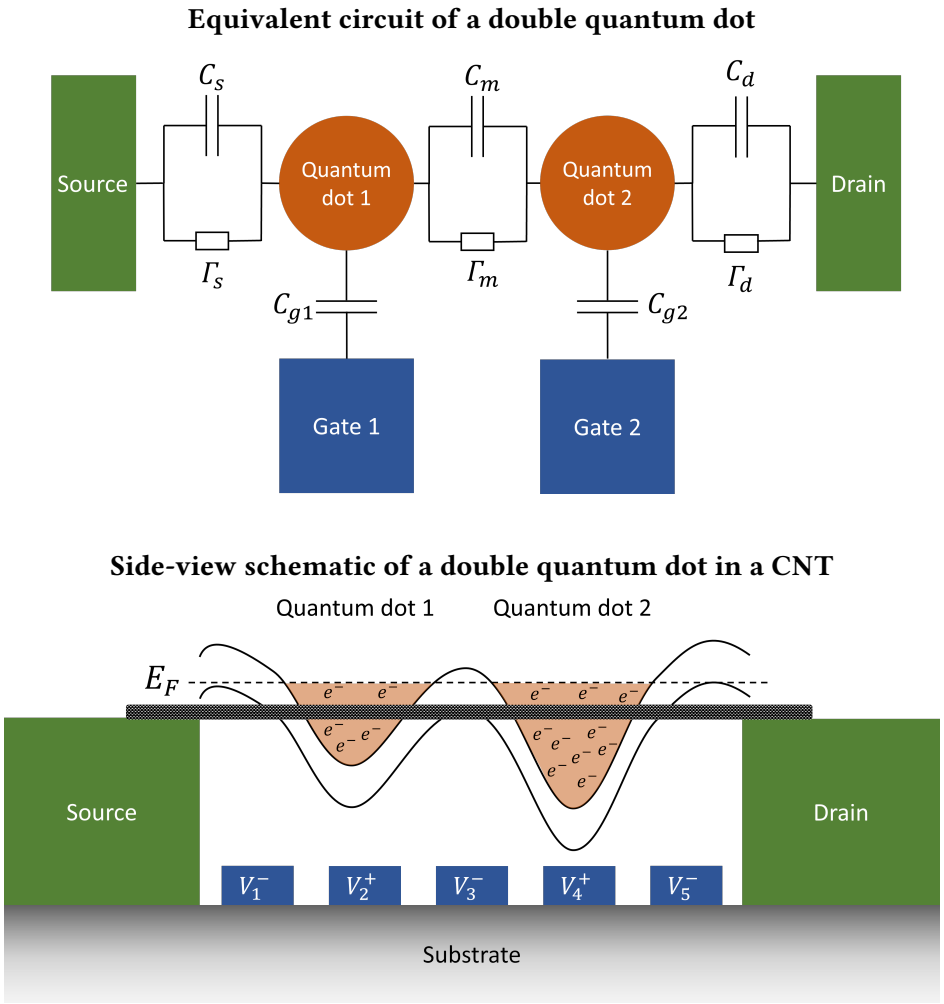

Figure 2.11: **Upper panel:** Schematic equivalent circuit of a double quantum dot with two dots in series coupled to two leads. Each dot is capacitively coupled to one local gate, cross-coupling between dot 1 and gate 2 or vice versa is neglected for this sketch. Compared to figure 2.5 the coupling Γ_m and capacitance C_m between the two dots has been introduced which describes the tunnelling from one dot to the other. **Lower panel:** Schematic side-view of an induced double quantum-dot. Gate-voltages with odd number (negative voltage) are used to tune the tunnelling barriers, gate voltages with even number (positive voltage) form the potential wells that are occupied by a finite number of electrons.

Here, the charging energies E_{C_1} and E_{C_2}, the total capacitances C_1 and C_2 for each dot, as well as the coupling energy between the dots E_{C_m}, i.e. the energy change in one dot if an electron is added to the other dot, have been introduced. Their values can be calculated as

$$C_1 = C_\mathrm{s} + C_\mathrm{g1} + C_\mathrm{m}, \qquad C_2 = C_\mathrm{d} + C_\mathrm{g2} + C_\mathrm{m} \tag{2.15}$$

$$E_{C_1} = \frac{e^2}{C_1}\left(\frac{1}{1-\frac{C_\mathrm{m}}{C_1 C_2}}\right), \qquad E_{C_2} = \frac{e^2}{C_2}\left(\frac{1}{1-\frac{C_\mathrm{m}}{C_1 C_2}}\right) \tag{2.16}$$

$$E_{C_\mathrm{m}} = \frac{e^2}{C_\mathrm{m}}\left(\frac{1}{\frac{C_1 C_2}{C_\mathrm{m}^2}-1}\right). \tag{2.17}$$

The interdot capacitance C_m is a convenient quantity to express different coupling regimes between the two quantum dots. Typically, three different regimes are distinguished (see figure 2.12). In the uncoupled regime the coupling $C_\mathrm{m} \to 0$ vanishes and the two dots behave fully independently and are charged individually. In the weak coupling regime where $C_\mathrm{m} > 0$, there is a small exchange between the two individual dots, i.e. dot 1 is slightly affected if dot 2 is tuned. In the strong coupling regime where $C_\mathrm{m} \to C_{1/2}$ the dots are so strongly coupled that they cannot be considered independently anymore but are rather one single big dot. These regimes are nicely visible when measuring the conductance as a function of applied gate voltages V_{g1} and V_{g2} for a fixed small bias voltage (figure 2.12).
In the uncoupled regime tuning one gate voltage only affects the occupation of one quantum dot which is expressed in terms of orthogonal lines of conductance that form a rectangular grid. In the strongly coupled case, the lines of conductance are diagonal, which is the expected pattern for a single dot since in this case both gate voltages tune the occupation in both dots. It is worth mentioning, that a V_sd-V_g-map probes a vertical or horizontal cut of a gate-gate-map as a function of applied bias. Therefore, the size of the areas with stable charge occupation correspond to the width of arising Coulomb diamonds.
The most realistic case is the case of weakly coupled dots where the transition between the two stable charge states can be observed and the voltage areas of stable occupation form a honeycomb pattern. What previously was a quadruple point in the uncoupled regime (the corners of the charge-stable domain) is split into two triple points (figure 2.12(d)), where three charging domains touch. The spacing of the splitting is given by the coupling energy E_{C_m}. The splitting can be explained by the existence of two transport processes, one constituting of electrons passing the two dots, one constituting of holes in the opposite direction. When a finite bias voltage is applied these points of conductance expand to bias triangles. Similarly to how excited states can be spectroscopically studied in a single quantum dot, their presence leads to a substructure within the bias triangles [61–63] as all states within the bias window contribute to the conductance.

2.3 Quantum dots and qubits in carbon nanotubes

By their very nature, carbon nanotubes are one-dimensional systems with tunable electronic energy levels and possible potential barriers at their interface to the environment. Since they can feature ballistic transport of charge carriers for lengths up to 1 µm [64] the latter stay coherent for typical device

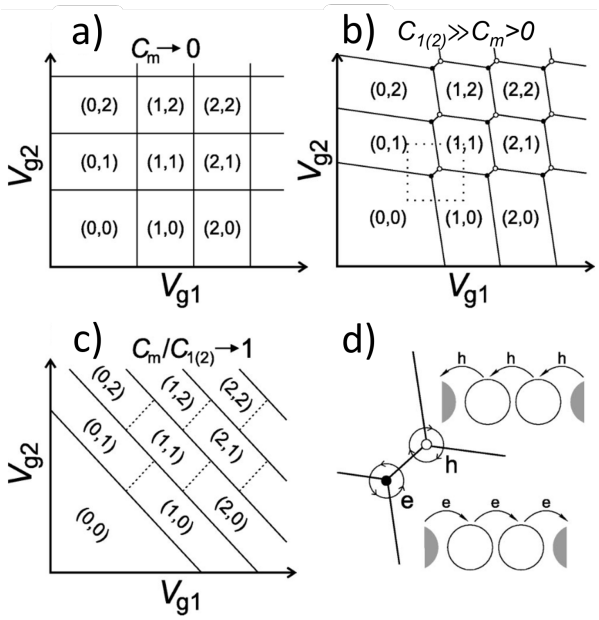

Figure 2.12: **Scheme of a charge stability diagram of a double quantum dot.** Shown are diagrams in the **a)** uncoupled regime, **b)** the weakly coupled regime and **c)** the strongly coupled regime. Large white areas feature a stable charge occupation of (N_1, N_2). In the weakly coupled regime, the intersection points are split into two triple points. A zoom in on the dashed area in **b)** is shown in **d)**, where (○) indicates a hole-transport process and (●) an electron process. Taken and adapted from [60].

dimensions. Therefore, a basic quantum dot can be formed by merely putting contacting electrodes to the carbon nanotube, which effectively confines the electrons in the one-dimensional tube due to arising Schottky barriers (see sec. 2.1.3). Further constrictions can be caused by defects or adsorbates. A quantum dot in a carbon nanotube features all of the general effects observable in quantum dots as described before, in addition to features that arise from the internal physics of carbon nanotubes such as spin-valley effects or a potential influence of mechanical vibrations.

2.3.1 Spin-orbit and valley effects

In section 2.1.2 we introduced the electronic properties of CNTs and their spin- and valley degrees of freedom. This results in general in a four-fold (2x spin, 2x valley) degeneracy in absence of a magnetic field for each level defined by longitudinal confinement. The valley states resulting from the K and K' Dirac cones are a well usable quantum number since they are well separated in momentum space. Their manifestation can be imagined as electrons circling the circumference of the carbon nanotube clockwise or counter-clockwise. Due to structurally defined strong transversal confinement, the next set of Dirac cones is energetically far away (>100 meV). The strong separation in momentum space of K and K' valleys can be overcome by scattering, due to disorder. This scattering leads to a mixing of K and K' states and lifts the degeneracy by a mixing energy $\Delta_{K,K'}$. The application of a magnetic field B results in a shift of the valley energy levels and allows the assignment of an orbital magnetic moment μ_{orb} given by [42]

$$\mu_{\mathrm{orb}} = \frac{\partial E}{\partial B_{\parallel}} = \frac{ed}{4\hbar}\left|\frac{\partial E_{\mathrm{Dirac}}(k_{\perp}, k_{\parallel}}{\partial k_{\parallel}}\right|, \tag{2.18}$$

with the two-dimensional energy profile $E_{\mathrm{Dirac}}(k_{\perp}, k_{\parallel}) = \pm\hbar v_{\mathrm{F}}\sqrt{k_{\parallel}^2 + k_{\perp}^2}$ of the Dirac cones. For low energy electrons (small $k_{\parallel}$), this reduces to

$$\mu_{\mathrm{orb}} = \frac{edv_{\mathrm{F}}}{4}. \tag{2.19}$$

The orientation of this magnetic moment points along the carbon nanotube axis.
Additionally, spin-orbit coupling occurs in carbon nanotubes with an amplitude that is far higher than what might be expected when looking at the low atomic-number and the resulting small value for graphene where $\Delta_{\mathrm{SO}} \approx 50\,\mu\mathrm{eV}$ [65]. However,significant spin-orbit coupling has been predicted [66] for carbon nanotubes due to curvature induced effects that lead to a breaking of spatial inversion symmetry. Indeed, values up to 3.4 meV have been measured [67]. In the picture of figure 2.3, the predicted spin orbit coupling results in a horizontal shift of the Dirac cones. Due to the curvature, a radial electric field is induced which results in a Rashba-like coupling to the $k_{\parallel}$-component of the electrons. This effect breaks the electron-hole symmetry [68]. In perturbation theory calculations it was found that higher order terms result in a Zeeman-type effect that can be understood as a vertical shift of the Dirac cones [69]. The overall spin orbit coupling is the combination of the two described effects and also depends on the filling of individual shells [70] as well as the exact local environment, i.e. chirality and curvature/diameter.
The introduced spin orbit coupling features a twofold symmetry in zero magnetic field in addition to

the fourfold symmetry introduced earlier. The resulting pattern for Coulomb diamonds was shown in figure 2.7, where the first dot ($N = 0$) and third dot ($N = 2$) are larger than the other two, with the $N = 0$ dot being even larger due to shell-filling of both spin and valley.

2.3.2 Charge and spin qubits in carbon nanotubes

A qubit is the quantum equivalent of the classical bit used to store (quantum) information. It is realised as a two-level quantum system where the two levels define the ground and excited state. In contrast to classical systems where the bit is either in the ground or excited state, in a quantum system the qubit is a superposition of ground and excited state. Among the many realisation possibilities, qubits where the information is encoded in the charge or spin state of the system have been realised in carbon nanotubes [3, 4, 71] and a mechanical qubit has been proposed [72].

Charge qubit in a carbon nanotube

In carbon nanotube double quantum dots a charge qubit has been realised where the information is encoded in the occupation of the two dots [3]. Penfold et al. found that, depending on the applied detuning, the energy levels for the (1,0) and (0,1) occupation shift and can hybridise for specific detuning values. At the hybridisation point, typically for zero detuning, the energy spacing is given by $2t_c$ where t_c is the tunnel coupling between the two dots. Here, the localisation is minimised. The readout was done by measuring the phase of a resonant electric circuit that is sensitive to the quantum capacitance of the double dot system. This capacitance is maximised if the system is in the ground state and minimised in the excited state. Their measured relaxation time T_1 was 48 ns and a coherence time T_2^* of 5 ns. They attribute these rather small time scales to charge noise and dot-lead coupling. Since they were measuring a carbon nanotube on substrate, the charge noise which is often caused by two-level systems in amorphous oxides or adsorbates is expected to be much higher than for a suspended carbon nanotube. Another approach to read out such a system could involve a charge sensor such as a second quantum dot in the proximity that features a conductivity depending on the occupation of the double dot system. Thus, by reading out the change of conductance in the sensing dot the charge state can be retrieved.

Introduction to spin qubits

Besides storing the quantum information in the charge state, a storage of information in the spin and valley state has been achieved as well for carbon nanotubes [4]. Storing information in the spin state typically results in much longer relaxation and decoherence times because a single spin is much less coupled to the environment than a single charge. At the same time, this decoupling from the environment comes at the price of a more challenging manipulation and readout since the spin is so well decoupled. One possibility to overcome this, is to encode the spin state coherently in another physical property like a charge state or looking at two-particle spin states where an effective exchange coupling can serve as a handle as described in the case of Pauli blockade (see following sections).

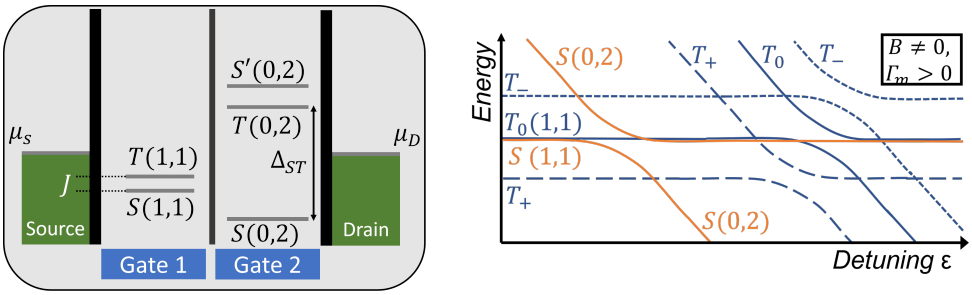

Figure 2.13: **Sketch of the singlet and triplet energy levels for two electrons in a double dot. Left:** Chemical potential levels for a double dot system with one electron in the right dot and an arbitrary gate tuning. The singlet states form the energetical ground state and are separated from the triplet states by the singlet-triplet splitting Δ_{ST} in the (0,2) case and an effective exchange coupling J for the (1,1) case. **Right:** For the case of an applied magnetic field, the triplet states split and form parallel lines when tracking the energy levels as a function of the detuning of the dots ε. At crossing points of same-spin configurations, the states hybridise for a finite coupling Γ_m and their splitting is given by $2\sqrt{2}\hbar\Gamma_m$.

Singlet and triplet states in a CNT double quantum dot

It is a well known fact that fermions need to follow selection rules when undergoing state transitions and that two different fermions may not be in the exact same spin and orbital state (Pauli-exclusion principle). Here, we first introduce spin states in a double quantum dot. Starting from this, we explain an occurring Pauli blockade, i.e. transport blocked by the Pauli exclusion principle, in a generic quantum dot according to [54] and mention the special case for carbon nanotubes where valley-states create additional rules and possibilities from this. When a second dot is introduced we need to distinguish the case of (0,2) (or (2,0), but we reduce it to the first) occupation which behaves like a single quantum dot and the (1,1) occupation for which we get the singlet state $S(1,1) = \frac{1}{\sqrt{2}}(|\uparrow_1\downarrow_2\rangle - |\downarrow_1\uparrow_2\rangle)$ and the three triplet states $T_+ = |\uparrow_1\uparrow_2\rangle$, $T_0 = \frac{1}{\sqrt{2}}(|\uparrow_1\downarrow_2\rangle + |\downarrow_1\uparrow_2\rangle)$ and $T_- = |\downarrow_1\downarrow_2\rangle$. The subscript denotes the location of the electron. Here, the energy difference J between the singlet ground state and the triplet states depends on the tunnel coupling Γ_m and is therefore gate-tunable and the charging energy E_C. The commonly used quantity is the detuning ε which describes the relative energy level shift for the two quantum dots. The energy shift J is often small compared to the singlet-triplet splitting Δ_{ST}, resulting in almost degenerate $S(1,1)$ and $T(1,1)$ states. The first excited singlet state $S'(0,2)$ is energetically higher than the triplet states and therefore does not contribute in most cases.

If the tunnel coupling is finite the $(1,1)$ and $(0,2)$ states hybridise and an avoided crossing will form with a splitting given by $2\sqrt{2}\hbar\Gamma_m$. Since interdot tunnelling preserves spin, the singlet state $S(1,1)$ (triplet state $T(1,1)$) may only couple to $S(0,2)$ ($T(0,2)$). Due to the singlet-triplet splitting the singlet and triplet states therefore hybridise at different detuning values (cf. fig 2.13). This distance between the avoided crossings allows it to control whether singlet or triplet states are hybridised by simply controlling the detuning. If the system is tuned to a hybridised singlet states, the electron charge state is of the form of $\frac{1}{\sqrt{2}}[|(1,1)\rangle + |(0,2)\rangle]$ for a spin singlet, but in the charge state $[|(1,1)\rangle]$ for a spin

triplet. This difference in the average charge distribution allows for the readout of the spin-state by charge sensing [73, 74], similar to a charge qubit.

Pauli blockade

The aforementioned conservation of spin does not only have implications on the charge state but can also affect the transport properties of a double dot system and can lead to current rectification [54, 75, 76]. This rectification is called spin blockade or Pauli-blockade, since transport can be blocked depending on the spin state.
A scheme depicting the mechanism of Pauli blockade is given in figure 2.14. Here, the double dot is tuned to the triplet point (0,1)/(0,2)/(1,1). Disregarding spin, transport at this point can happen in both directions, i.e. from right to left $(0,1) \rightarrow (0,2) \rightarrow (1,1) \rightarrow (0,1)$ and left to right $(0,1) \rightarrow (1,1) \rightarrow (0,2) \rightarrow (0,1)$ as is indicated by the arrows turning clockwise and counterclockwise in figure 2.14. This way, the right dot always contains at least one electron. Assuming the right to left process (i.e. negative bias) and an electron of spin up in the right dot, due to Pauli exclusion only an electron with spin down can tunnel from the lead into the dot and form the $S(0,2)$ singlet state. From this state either electron can tunnel into the left dot and subsequently to the left lead. In the case of positive bias (i.e. left to right process), however, no spin selectivity is enforced on the electron entering the left dot from the lead. When an electron enters the left dot, the resulting hybridised state can now be either a singlet state $S(1,1)$, in which case the electron from the left may also move to the right dot to form the $S(0,2)$ state, or triplet state $T(1,1)$ for which the electron on the left dot may not tunnel into the right dot as the $T(0,2)$ triplet state is energetically unavailable. In the latter case, the system will be stuck in the $T(1,1)$ state, until spin relaxation transforms the system to a $S(1,1)$ state. This spin relaxation time can be quite large, reducing the current in this bias direction far below the value for the opposite direction causing a current rectification.

Singlet-triplet qubit

The latter can be used in case of a singlet-triplet qubit where the singlet $S(1,1)$ and triplet $T_0(1,1)$ state serves as ground and excited states if T_+ and T_- are energetically detuned by a magnetic field. If the system is initialised in the two (1,1) states, the readout can be done by changing the detuning to a point where the $S(1,1)$ and $S(0,2)$ states hybridise while the $T(1,1)$ remains unchanged. This change of charge state caused by the spin state is then read by a close-by charges sensor (quantum dot, quantum point contact, electric resonator...). This type of qubit was mainly used in III-V semiconductors such as GaAs but elements of the IV-group in the periodic system of elements attract interest due to their natural low abundance of nuclear spins (e.g. 1% ^{13}C in natural carbon) which should increase coherence times due to reduced spin-spin interactions.

Spin-valley supersinglet and supertriplet states in carbon nanotubes

As mentioned before, the situation is ever more complex for the case of carbon nanotubes where electrons possess a valley degree of freedom in addition to the spin. The presence of spin and valley

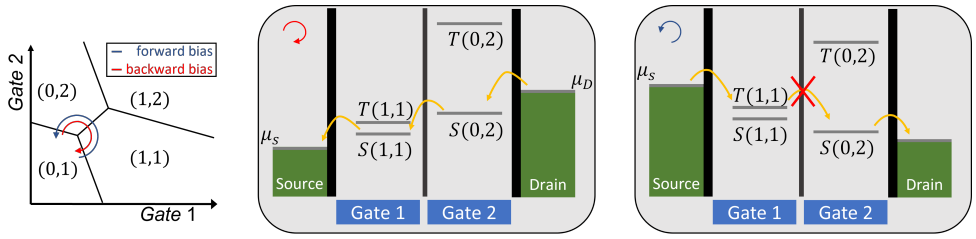

Figure 2.14: **Schematic representation of current rectification due to Pauli blockade. Left:** When a double dot is tuned to the triplet point (0,1)/(1,1)/(0,2) transport is generally possible in both directions, depending on the polarity of the applied bias voltage. **Middle:** in the backwards biased scenario an electron may tunnel into the right dot from the right lead, occupying a singlet state. When tunnelling into the left dot it can only enter the $S(1,1)$ singlet state, since $T(1,1)$ is forbidden by Pauli exclusion. From the $S(1,1)$ state it may leave the double dot towards the left lead, thus transport is allowed. **Right:** in the forwards biased case an electron from the left dot may enter the singlet $S(1,1)$ or the triplet $T(1,1)$ state. If it is int he singlet state it may tunnel into the right dot and subsequently enter the right lead. If it is in the triplet state, a transition into the singlet state $S(0,2)$ is forbidden by Pauli exclusion. The system first needs to relax from the triplet to the singlet state with a time T_1 which can be milliseconds [54], before this blockade is lifted

states result in a fourfold degeneracy for each energy level in the dot which has some implications on the Pauli blockade discussed before as will be very briefly introduced now. In analogy to the singlet states in a regular quantum dot, it is possible to define *supersinglet* states that have a combined spin-valley wave function that is antisymmetric under particle exchange [77]. The *supertriplet* states are symmetric under particle exchange. This results in a splitting into six supersinglet $(0,2)$ and ten supertriplet (0,2) states whereas the latter are energetically well separated from the first by an energy analogous to the singlet-triplet splitting caused by the orbital part of the wavefunction [68]. A splitting within the multiplet's sublevels arises from the Zeeman effect for spin and orbital part as well as spin-orbit coupling. For the (1,1) occupation the same splitting into six supersinglets and ten supertriplets is observed and hybridisation between states is only possible between (0,2) and (1,1) supersinglet states. A system in the supertriplet (1,1) state is considered blocking since it requires higher orbital effects to transition into the supertriplet (0,2) state or a decay into a supersinglet (1,1) state via spin flip or change of the valley state. Therefore, the analogy to Pauli-blockade still holds but a detailed description is much more involved than what is meaningful for this thesis.

Hybrid qubit in a carbon nanotube

Laird et al [4] used entangled spin-valley states in a carbon nanotube that featured a bend and a double dot in the spatially different aligned sections of the carbon nanotube. As a result, the effective magnetic field parallel and perpendicular to the carbon nanotube changed between the two dots. In an electrically driven spin resonance they applied an electric ac-signal and induced interdot transitions. For the hopping electron, the angle of the effective magnetic field changes periodically in time and

the qubit with an energy splitting $\Delta E = g_s \mu_B |B_{\text{eff}}|$ can be driven at a frequency $f = \Delta E/h$. This qubit also uses spin-valley blockade for the readout since it only allows for a small leakage current in the blocked state that depends on the decay time of the blocking state which is determined by tunnelling events that do not conserve spin or valley, such as disorder in combination with spin-orbit coupling [4]. Since the decay rate is dependent on the superposition of spin and valley states that differ for the ground and excited state of the qubit, the leakage current is sensitive to state flipping events. For this qubit they found a decoherence time of 65 ns determined by Hahn spin-echo and a T_1 of 2.5 µs which was significantly higher than what was observed for the charge qubit described before, but at the same time showed that a partial suspension and using spin as the storage for quantum information is not sufficient to reach the large T_1-times in the seconds range and coherence times in the ms-range observed in industrially manufactured semiconducting qubits [78].

2.4 Carbon nanotubes as nanomechanical resonators

In section 2.1.1 the unique combination of structural properties of carbon nanotubes have been introduced. In this section, an introduction into the field of nano- and microelectromechanical systems (NEMS and MEMS) and especially for the use-case of carbon nanotubes, will be given. Out of the different possible vibration modes, the focus will lie on transversal modes and to a smaller degree longitudinal vibrations whereas radial breathing and twisting modes will only be briefly introduced.

2.4.1 General aspects of nanoelectromechanical systems

This general introduction loosely follows the reviews [79, 80] as well as the PhD thesis by Sazonova [81] that, although not very recent, still give a nice general approach on the field. Electromechanical systems are at their very core systems in which a mechanical motion can be converted into an electrical signal and vice versa. Often a mechanical resonance is used that can be stimulated with an electric signal and its change of state back-converted or transduced to an electric signal. The mechanical resonator is mostly described by its two core parameters: The resonance frequency ω and the quality factor Q which is a measure of internal losses as introduced in section 2.4.2.
There is a multitude of physical realisations of NEMS such as drum resonators in graphene [82, 83] or other 2D-materials [84, 85], doubly clamped beams in various materials [86–88], nanowires [89, 90] and even 3-D printed [91] structures, where the citations serve as examples and only show a fraction of all devices and experiments. In the further description of section 2.4.3, the focus will be on flexural modes and in particular on the system of a beam fixed on both ends.
NEMS are the consequence of miniaturisation of MEMS that require different approaches for nanofabrication and more sensitive transducing techniques suited for the small dimensions. While MEMS with their micron dimensions are often fabricated in bulk micromachining processes, the processes used for NEMS are more seen as surface nanomachining [80]. MEMS are used for decades in technology to serve many different tasks like regulating current, tuning optics, switches etc., but they can not reach some of the application possibilities for NEMS due to their low active mass, rather high resonance frequency, high local sensitivity and other features that follow as a consequence of their small size like

a small heat capacity. This gives rise to plenty of possible experiments like single particle sensing [80, 86], generation of quantum states of mechanical motion [92, 93] and more.
When downscaling a system, the fundamental question arises at which point continuum mechanics fails to describe the system properly and atomistic or quantum effects need to be considered. In calculations it was found that this limit is reached for dimensions in the order of few tens of lattice constants [94, 95], meaning that classical beam mechanics can still describe systems down to tens of nanometres. Another consequence of the small size is the increase in surface-to-volume ratio which puts more emphasis on surface effects and properties than for a MEMS of similar geometry resulting in additional demands on nanofabrication processes.
Following this introduction, the classical harmonic damped oscillator will be introduced as the basic description of a NEMS (section 2.4.2) to introduce some basic properties often used later on. For this we assume to use the resonator in a linear regime of small displacement. For a larger displacement nonlinear effects alter the behaviour and lead to deviations in the resonance behaviour where one particular effect will be discussed in section 2.4.4. Since later presented measurements have been performed on carbon nanotubes that can be described as a doubly clamped beam as a first approximation an introduction to the mechanical modes of a doubly clamped beam is given (section 2.4.3). This section will conclude with the description of electron-phonon interplay observable in NEMS, resulting in interesting effects like Franck-Condon blockade [21, 96](section 2.4.8) or single-electron tunnelling induced reduction of the quality factor [97](section 2.4.7).

2.4.2 Description as classical damped harmonic oscillator

Classically a doubly clamped beam can be described as a weakly driven harmonic oscillator affected by a damping term. The solution of the differential equation for such a system oscillating along the z-axis using a point mass m, a spring constant k, the resonance frequency $\omega_0 = \sqrt{\frac{k}{m}}$, $\dot{z}$ a derivative in time, z' a spatial derivative, a sinusoidal force F_0 with frequency ω, a damping factor b, the amplitude z_o and the phase ϕ is given by

$$z(t) = \frac{F_0/m}{\sqrt{(\omega_0^2 - \omega^2)^2 + 4\omega^2\beta^2}} \cos(\omega t - \phi) \tag{2.20}$$

$$\phi = \arctan\left(\frac{\omega_0^2 - \omega^2}{2\omega\beta}\right) \tag{2.21}$$

with the introduced notation of $\beta = b/(2m)$. In figure 2.15 the response of a resonating system upon driving with varying frequency for both the amplitude of the oscillation as well as its phase is plotted. We can see that the phase undergoes a clear phase shift from 0, i.e. the system follows the drive for slower frequencies, to π for frequencies higher than the resonance frequency ω_0. At resonance $\omega_0 = \omega$, the system trails the applied drive with a phase of $\pi/2$. The amplitude response features a Lorentzian shape with its maximum at resonance. The width of the resonance is determined by the damping and described by the quality factor Q, which is defined as

$$Q = 2\pi \left(\frac{\text{Total oscillation energy}}{\text{Energy loss per period}}\right). \tag{2.22}$$

For small attenuation the quality factor is often determined by $Q = \omega_0/(\Delta\omega)$ where $\Delta\omega$ describes the full-width at half maximum (FWHM) of the resonance. If the parameters of the system are known, it can also be calculated by $Q = \omega_0/(2\beta)$. The energy loss per period can be composed of distinct contributions like the internal losses in the system (damping) and other losses e.g. into the read-out or excitation lines (coupling). They add up inversely $Q_{\text{tot}} = \sum_i \frac{1}{Q_i}$ and therefore the channel with the highest loss dominates the overall quality factor.

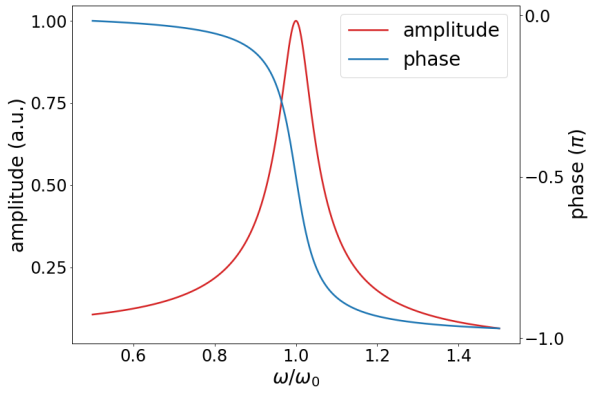

Figure 2.15: **Plot of the frequency dependence of amplitude and phase for a driven harmonic oscillator in the case of weak damping.** The resonance occurs at $\omega = \omega_0$ and results in a peak in amplitude and a phase-shift. The quality factor Q can be determined from the FWHM of the resonance.

2.4.3 Mechanics of a doubly clamped beam

While the previous introduction of a damped and driven harmonic oscillator describes an ideal mechanical resonator, many of the necessary assumptions do not hold in reality. Within this thesis the mechanical vibrations of carbon nanotubes fixed on each end on a metal electrode have been studied. Due to their dimensions, especially their large aspect ratio, their longitudinal and transversal vibration modes can be described using beam mechanics. The summary given here follows the work of [81, 98, 99]

For this more realistic description of a transversal mode of a vibrating carbon nanotube we imagine a beam clamped on both ends as depicted in figure 2.16. The beam has the dimensions of width(w) x height (h) x length(l) where the beam axis is parallel to x and the z-direction is perpendicular to the beam (and later directed towards a gate). For the sake of simplicity and since it is a valid assumption for carbon nanotubes with a round cross-section, width and height are assumed to be identical, thus reducing the problem to two dimensions x and z. Taking into account the elasticity E and the residual tension T_0, the potential elastic energy is given by [98]

$$U = \frac{1}{2}\int_0^l \left(EIz''^2 + T_0 + \left(\frac{EA}{2l}\int_0^l z'^2 dx \right) z'^2 \right) dx \tag{2.23}$$

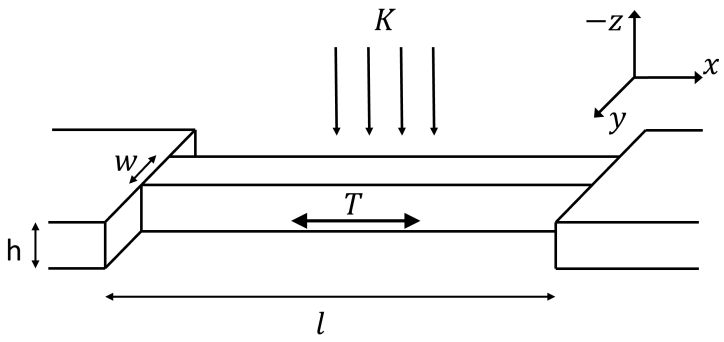

Figure 2.16: **Sketch of a doubly clamped beam.** The beam has the dimensions $w \times h \times l$ and a cross-section A. A constant force K is applied along the z-axis and the beam has the internal tension T.

with the cross-section area of the beam A, the moment of inertia I and the flexural modulus E. The first term in the integral contains the *flexural rigidity* (EI) which is defined as the force required to bend a beam by one unit of curvature, following Euler-Bernoulli beam theory, and describes the energy contained within the flexural motion. The second and third term describe the energy in the beam due to tension using residual tension and the *axial rigidity* (EA) which is the force required to create one unit of stress inside the beam. In the limit of small deformation the curvature κ of the beam can be approximated by z'' and the strain ε within the beam by $\frac{1}{2}z'^2$. Using these reformulations, equation (2.23) simplifies to

$$U = \frac{1}{2}\int_0^l \left(EI\kappa^2 + T_0 + EA\varepsilon^2\right) dx. \tag{2.24}$$

Since in our experiments a static electric field acts on the carbon nanotube, a constant, downwards acting force K applied along the beam, is added:

$$U = \frac{1}{2}\int_0^l \left(EI\kappa^2 + T_0 + EA\varepsilon^2 + Kz\right) dx. \tag{2.25}$$

In order to get some meaningful statements from this we calculate the minimum energy. This results in the equation

$$EI\kappa'' - T_0 z'' - EA(\varepsilon z)'' - K = 0 \tag{2.26}$$

and upon resubstituting κ and ε as well as introducing the total tension $T = T_0 + \frac{EA}{2l}\int_0^L z'^2$

$$EIz'''' - Tz'' - K = 0, \tag{2.27}$$

which is essentially a quadratic equation that can be solved in two different limits, i.e. two different ratios of tension to flexural rigidity, that will be discussed in the following.

The bending limit

In the bending limit, the bending term corresponding to the flexural rigidity is much larger than the tension $EI/l^2 \gg T$. In analogy to classical mechanics we can replace the constant force K with $\mu\ddot{z}$,

where μ is the mass density and $\ddot{z}$ is an acceleration in direction of the force. Doing this and neglecting the tension term in equation(2.27), we get a wave equation

$$\mu\ddot{z} = EIz'''' \tag{2.28}$$

for which the standard solution is given by $z = z_0(x)\cos(\omega t + \phi)$ with ω as the oscillation frequency.The boundary conditions require that $z(0) = z(l) = 0$ and $z'(0) = z'(l) = 0$, i.e. the beam is firmly fixed and does not move at its fixation points. Plugging in the boundary conditions yields the resonance frequencies ω_n of the system [81] to

$$\omega_n = \left(\frac{\beta_n}{l}\right)^2 \sqrt{\frac{EI}{\mu}} \tag{2.29}$$

where the β_n are given by $\beta_n = k_n l$ and can be determined using

$$\cos(k_n l)\cosh(k_n l) = 1. \tag{2.30}$$

On a sidenote, it is worth mentioning that the calculation works analogous for a cantilever geometry with the only difference in the calculation (arising from different boundary conditions) in the end is the condition $\cos(k_n l)\cosh(k_n l) = -1$, thus resulting in differently spaced β_n.

The tension limit

In the tension limit the tension dominates over the flexural rigidity and hence $T \gg EI/l^2$. Neglecting the flexural term in equation (2.27) we find that

$$Tz'' + K = 0. \tag{2.31}$$

which is solved by a standard wave

$$z = z_0 \cos(kx)\cos(\omega t + \phi) \tag{2.32}$$

in case of the described doubly clamped beam. From this equation we find the resonance frequencies to be

$$\omega = \frac{\pi}{l}\sqrt{\frac{T}{\mu}} \tag{2.33}$$

which corresponds to the common string vibration as is e.g. observed in a guitar.

Intermediate or catenary range

If neither tension nor flexural rigidity dominate, which is the case most of the time for real devices, both contributions need to be taken into account which leads to second order corrections. Sapmaz et al [100] calculated these corrections to be:

$$\omega = \frac{22.4}{l^2}\sqrt{\frac{EI}{\mu}} + 0.28T\sqrt{\frac{1}{\mu EI}}, \qquad T \ll EI/l^2 \tag{2.34}$$

$$\omega = \frac{\pi}{l}\sqrt{\frac{T}{\mu}} + \frac{2\pi}{l^2}\sqrt{\frac{EI}{\mu}}; \qquad T \gg EI/l^2 \tag{2.35}$$

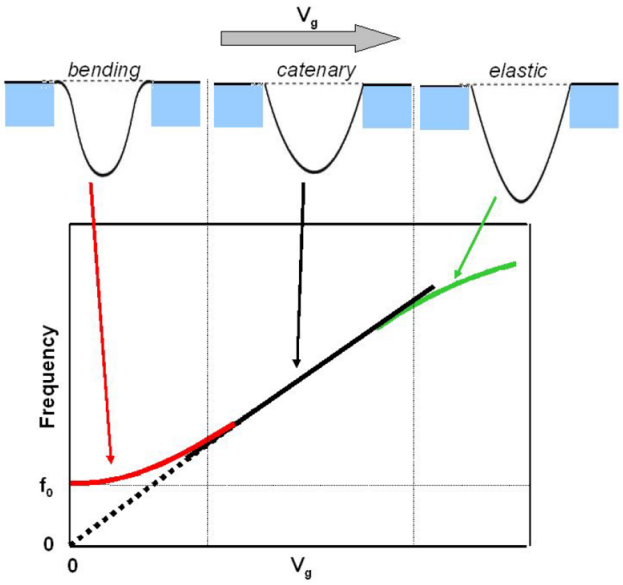

Figure 2.17: **Qualitatively predicted dispersion for a carbon nanotube NEMS.** For low gate voltages (V_g the resonance frequency depends quadratically on the gate voltage before transitioning into a linear regime in the intermediate range and finally features an exponent <1 in the tension limit. Figure taken from [81].

For NEMS like the ones used within this thesis, the amount of induced tension can be tuned by applying a static electric field effectively pulling on the resonator. The transition from bending limit to the intermediate range and lastly to the tension limit is shown qualitatively in figure 2.17 Our devices typically were in the bending limit during measurements and showed a quadratic dependence on the applied electric field.

2.4.4 Duffing oscillator

In the description of the previous chapters it was assumed that the displacement is small and that the resonator follows Hooke's law where the restoring force is linear to the displacement. The latter is not necessarily the case however, when the displacement becomes larger and the vibration leads to an elongation of the resonator inducing additional tension. The case of a cubic restoring force results in an equation of motion of the type of

$$m\ddot{z}(t) + b\dot{z}(t) + kz(t) + \alpha z^3 = F_0 \cos(\omega t) \tag{2.36}$$

which extends equation (2.21) by the cubic αz^3 term, where α is a system specific parameter describing the nonlinear restoring force. Such a system is called a *Duffing oscillator*. In figure 2.18 resonance curves at different powers are shown. It is evident how the Lorentzian shape of a resonance curve is restored for low powers whereas for higher powers the resonance peak is "bent" to either side. This amplitude at which the peak starts to shift is the critical amplitude a_c. Interestingly, we could observe a dragging of the peak towards higher or lower frequencies in different vibration modes of one suspended carbon nanotube device (see sec. 5.4.3). If the driving power is increased even further, the system can reach

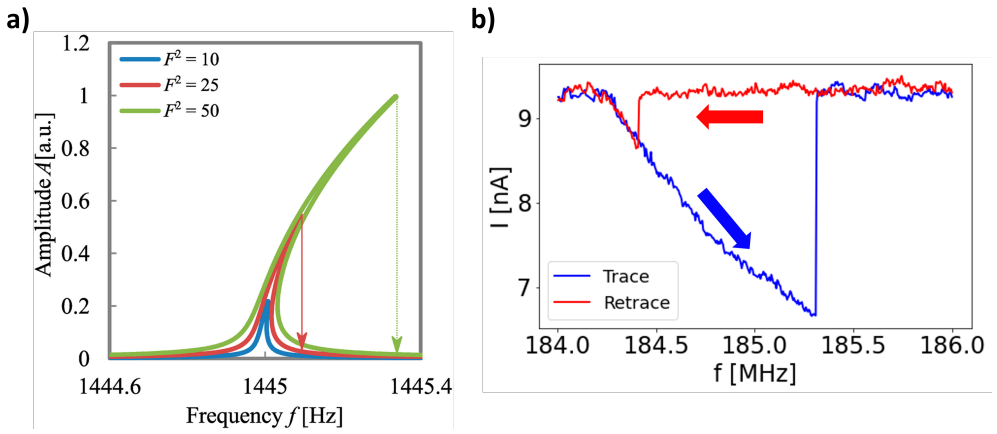

Figure 2.18: **Power and sweeping direction dependence of a Duffing oscillator with positive α. a)**For an increasing driving power F, the resonance shape deviates more and more from a Lorentzian shape (blue) towards a strongly distorted resonance shape. During an actual measurement, the amplitude measured would jump at the positions indicated by the arrows for an upwards directed frequency sweep. Figure **a)** taken from [101]. **b)** When comparing trace (upwards sweep) and retrace (downwards sweep) of a measured resonance, the full width of the bistable regime becomes obvious. During the trace the system follows the high amplitude branch until the sudden drop while it remains in the low branch during the retrace until it reaches the resonance base.

a regime, where there is more than one solution (state) for a given driving frequency. Of the three possible solutions only two are observable: the one on the upper branch (i.e. the highest amplitude) and on the lower branch (lowest amplitude) while the intermediate one is not stable. This resonance shape gives rise to hysteretic behaviour since the direction of the frequency sweep determines the observed resonance shape. In figure 2.18b), a resonance is shown for a sweep in both directions. The vertical jump occurs at positions where a discontinuity of amplitude is observable upon changing the frequency. This discontinuity could allow for some very sensitive measurements, since a small change of resonance frequency (e.g. induced by a change of charge/magnetic state) can result in a sudden and strong change of amplitude.

Postma et al. [29] performed calculations for a doubly clamped beam and derived the critical amplitude from equation (2.36). Upon rewriting the loss factor b as $b = \frac{\omega_0}{Qm}$, k as $k = \frac{\omega_0^2}{m}$ as well as assuming a freely vibrating beam, they found the (slightly overestimated) resonance frequency and Duffing parameter α/m to be

$$\omega_0 = \left(\frac{2\pi}{l}\right)^2 \sqrt{\frac{EI}{3\mu}\left(1 + \left(\frac{l}{2\pi}\right)^2 \frac{T_0}{EI}\right)} \tag{2.37}$$

$$\alpha/m = \frac{E}{18\rho}\left(\frac{2\pi}{l}\right)^4. \tag{2.38}$$

From this they calculated the critical amplitude a_c to be given by

$$a_c = \frac{\omega_0 l^2}{\pi^2}\sqrt{\frac{\sqrt{3}\rho}{EQ}} \tag{2.39}$$

using the mass density ρ.

2.4.5 Introduction to carbon nanotubes as a mechanical resonator

As described in more detail in section 2.1.1, carbon nanotubes are hollow cylinders with a very large aspect ratio between length and diameter. Due to their low mass density and strong chemical bonds, large resonance frequencies are expected in the different possible resonance modes. This section is dedicated to introducing the different occurring resonance modes while showing their significance for applications.
We previously introduced a double clamped beam as a reference system to describe some mechanical modes in carbon nanotubes and thus transversal *bending* modes are the first mechanical mode mentioned. Here, a displacement occurs orthogonally to the nanotube axis leading to a displacement typically in the pm-range. Obviously, for this mode to occur the carbon nanotube needs to be suspended since it is otherwise fixed by van der Waals forces on the substrate. These modes have been studied (e.g. [97, 102–106]) and used for detection, e.g. for mass sensing [107, 108] or spin states [14]. The principles of measurements using bending modes are presented in section 2.4.6.
The carbon nanotube may also experience a displacement of its centre of mass along its symmetry axis which results in an oscillation along this axis. These modes are *stretching* modes since the nanotube stretches and contracts along its axis. The endpoints are typically defined by the contacts where the nanotube is not suspended anymore. These stretching modes couplestrongly to electron tunnelling and thus create additional features in transport measurements. The influence of this electron-phonon coupling has been studied in the past [21, 96] and will be presented in section 2.4.8. Closely related are twisting modes, where parts of the nanotube rotate around the symmetry axis in a point symmetric fashion. Their coupling to electrons is weaker and they are thus less studied experimentally. Theoretically, however, it has been predicted that twisting modes can induce an ac-spin-current mediated by spin-rotation coupling [109].
Due to their hollow cylindric structure carbon nanotubes also express modes of mechanical motion in radial direction, i.e. an expansion and contraction, called *radial breathing mode* or *RBM*. These modes do not depend on the nanotube length but on the chirality. RBM can be measured in Raman spectroscopy and allow to identify the chirality by measuring the Raman shift (see e.g. [110]), since it is unique for each chirality. Additionally, it is possible to classify carbon nanotubes by their chirality (see e.g. review [111]) which can be helpful when targeting specific properties.

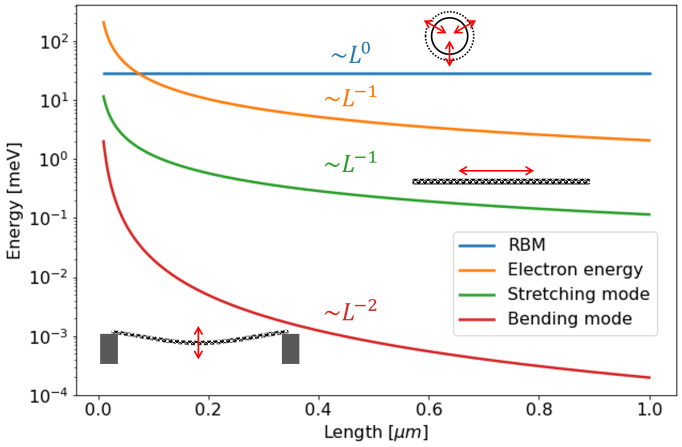

Figure 2.19: **Comparison of different mechanical resonator modes and electronic level spacing in a quantum dot as a function of the carbon nanotube length** L**.** Since radial breathing modes (RBM) only express movement along the radial axis, their resonance frequency only depends on the chirality of the carbon nanotube but not on its length. The electronic energy (see sec. 2.2) and longitudinal stretching modes (LSM) express a L^{-1} dependence equivalent to a classical standing wave. Bending modes, here in the bending limit, feature a L^{-2} dependence in analogy to the double clamped beam but in general possess much lower energies/frequencies (4 µeV≈1 GHz) as the other resonance modes.

2.4.6 Detection of transversal mechanical resonances in carbon nanotubes

Current rectification

In 2009, Huettel et al. [103] and Steele et al. [97] introduced a mechanism using the nonlinear gate dependence of the electronic conductance in carbon nanotubes that allows to both actuate the carbon nanotube as well as detect the mechanical resonance [97, 103].

The ensuing description follows the arguments given in [103]. Upon driving the mechanical oscillation of the carbon nanotube with electromagnetic waves, sent via a local antenna in the proximity or a local gate (see figure 2.20), the motion amplitude changes as depicted in figure 2.15 depending on the frequency of the incident radiation. When driving the system at its resonance frequency f_r, it oscillates with an amplitude $u(t) = u_0 \cos 2\pi f_r t$. Since part of this motion happens out of plane (with respect to the device surface, here z-axis) the distance to the gate and therefore the capacitance to the gate C_g is modulated periodically with $\delta C_g = \frac{\partial C_g}{\partial u} \cdot u$. This capacitance change results in a change of the induced charge $q_c = C_g V_g$ in the carbon nanotube and behaves like an effective oscillating gate voltage given by $\frac{\delta C_g}{C_g} = \frac{\delta V_g}{V_g}$ with $\delta V_g = V_g^{ac,eff} \cos 2\pi f t$.

The electrostatic attraction between the charge in the dot q_c and the gate causes an electrostatic downward force approximated by [102]

$$F_{el} = \frac{1}{2} C_g' \left(V_g^{DC}\right)^2 \approx \frac{1}{2} C_g' V_g^{DC} \left(V_g^{DC} + 2\delta V_g\right) \tag{2.40}$$

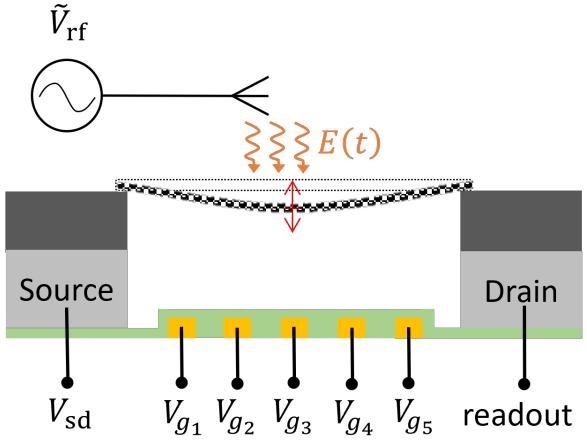

Figure 2.20: **Sketch of the measurement setup used in a current rectification technique setup, based on [97].** The carbon nanotube is suspended between two electrodes and gate controlled via local gate voltages $V_{\mathrm{g}i}$. A bias voltage V_{sd} is applied across the carbon nanotube while a local antenna sends an oscillating electric signal V_{rf}. The nanotube movement is indicated with small red arrows.

where the oscillating change is assumed to be small compared to the DC-voltage on the gate and $C_{\mathrm{g}}^{'} = dC_{\mathrm{g}}/dz$ is the derivative of the capacitance as a function of the distance between nanotube and gate.

For many measurements we used a setup similar to [103], using an antenna to send in rf-signals. Our measurement bandwidth (kHz-range) for the current is much smaller than the occurring mechanical resonance frequencies (MHz to GHz range) and thus only time-averaged current can be measured. This time averaged current $\bar{I}$ can be calculated in a Taylor-expansion of $I(V_{\mathrm{g}} + \delta V_{\mathrm{g}})$ around $\delta V_{\mathrm{g}} = 0$. It can be expressed as:

$$\bar{I}(u_0, V_{\mathrm{g}}) = I(V_{\mathrm{g}}) + \frac{u_0^2}{4}\left(\frac{V_{\mathrm{g}}}{C_{\mathrm{g}}}\frac{\partial C_{\mathrm{g}}}{\partial u}\right)^2 \frac{\partial^2 I}{\partial V_{\mathrm{g}}^2} + O(u^4) \tag{2.41}$$

where higher order terms are omitted. Interestingly, due to the averaging, this deviation from the static current $I(V_{\mathrm{g}})$ induced by the mechanical motion depends only on the local curvature $\frac{\partial^2 I}{\partial V_{\mathrm{g}}^2}$ of the static current and not on the first derivative. One necessity for a strong signal are thus sharp gate-dependent conductance changes that require cryogenic temperatures to avoid smearing out due to a large thermal energy. When looking at Coulomb peaks occurring in the Coulomb blockade regime (see section 2.2.1), the sign of the curvature changes twice. On the flanks of the peak, the local curvature is positive and the current observed at resonance is thus larger resulting in a current peak, while the curvature near the maximum of the Coulomb Peak is negative and the resonance frequency thus results in a current minimum.

Carbon nanotubes as a frequency mixer

In the works of Sazonova [81, 102] a mixing technique [112–114] was used, where the carbon nanotube acts as a frequency mixer. The following description follows these publications. In general, a mixing technique uses nonlinear conductance behaviour of an electric component (e.g. a diode) to mix two incoming frequencies f_0 and f_1 to two outgoing frequencies $f_0 \pm f_1$. Since current is given classically by $I = GV$ an oscillating conductance and oscillating applied bias voltage can mix their frequencies and create a current signal at the sum and difference of the incident frequencies. As introduced an applied oscillating gate voltage leads to a change of the induced charge $\delta q_c = \delta(C_G V_G)$ due to a transistor like gating effect and mechanical oscillation. The latter is of course the strongest at resonance.
A second oscillating signal is applied on the source electrode δV_{sd}. The resulting current is measured at the frequency difference $\Delta f = |f(\delta V_g) - f(\delta V_{sd})|$ of the frequencies applied at the gate and the source electrode since the sum of the two frequencies is far beyond the measurement bandwidth. The resulting lock-in current depends on the amplitude of the applied voltages and the transconductance $\frac{dG}{dV_g}$, which carries the mechanical information. An expression for the current can be derived from the fluctuating control charge and can be expressed as

$$\delta I_{\Delta f} = \delta G \delta V_{sd} = \frac{1}{\sqrt{8}} \frac{dG}{dV_g} \left(\delta V_g + V_g^{DC} \frac{\delta C_g}{C_g} \right) \delta V_{sd}. \tag{2.42}$$

In contrast to the previous technique of current rectification, here on first approximation the current depends only on the first derivative with respect to the displacement. When analysing the resulting signal, typically information can be retained by fitting a Lorentzian function to the measured data [81]. In case of larger amplitudes, however, where the Duffing-behaviour takes over the overall lineshape of the resonator, this evaluation becomes increasingly inaccurate. The contribution of both the mechanical part as well as the electrical part, however, can also be obtained by data analysis if both contributions are well above the noise level [115].
Building on this approach, the group of A. Bachtold developed a different readout scheme [106, 116], based on work on quantum point contacts [117, 118], still relying on the mixing inside a carbon nanotube but without the small bandwidth limitation due to the inherent RC-lowpass behaviour of CNT-circuits. Again, an applied oscillating voltage V_{sd} at the bias with the frequency f_{sd} results in a detectable current whose modulations are the result of capacitively transduced displacement modulations. Here, the electron-vibration coupling does not only create backaction but is also giving means to detect vibrations [106]. At the output an RLC-tank circuit with resonance frequency $\omega_{RLC} = 2\pi f_{RLC}$ limits the output frequency range and matches the impedance at resonance [119]. The frequencies are chosen such that $f_{sd} = f_{res} \pm f_{RLC}$. If $f_{sd}, f_{res} \gg f_{RLC}$ only electrons that took part in a mixing event possibly posses the right frequency to pass the RLC-circuit. The current modulation δI depends on the amplitude modulation δz with

$$\delta I = \beta \delta z \tag{2.43}$$

where β is given by

$$\beta = \frac{1}{2} V_{sd}^{ac} \frac{C_g'}{C_g} \frac{dG_{diff}}{dV_g} V_g. \tag{2.44}$$

A typical measurement consists of measuring the current noise density to quantify the variance of the current I_{res}^2 at the RLC-circuit resonance frequency [106]. By measuring the current noise at f_{RLC}, the displacement noise can be retrieved. From the displacement noise, thermal vibrations can be detected [106]. Since the measurement involves analysing noise that strongly depends on thermal energy, the signal amplitude is depending on the temperature. Using the equipartition theorem, the occupation number n can be approximated:

$$n = \frac{k_{\mathrm{B}} T_{\mathrm{vib}}}{\hbar \omega_0} - \frac{1}{2}. \tag{2.45}$$

The big advantage of this technique is the absence of a direct drive on the mechanical resonance which influences the occupation number of the vibrational state by excitation.

2.4.7 Electron tunnelling induced modifications of mechanical bending modes

In the previous section we discussed how mechanical bending vibrations alter the conductance and how these effects can be used to detect the mechanical oscillations. Since backaction works both ways, this section is dedicated to the influence of single electron tunnelling (SET) on the properties of transversal mechanical bending modes and in particular how resonance frequency and quality factor change when traversing a Coulomb peak in conductance. In order to describe this effect, we assume SET to be an external perturbation as introduced in [97, 104] and reuse their model and some experimental data for illustration.

Electrostatic-mechanical coupling

As a first step we need to quantify the electrostatic force on the quantum dot consisting of the gate voltage V_{g} and the potential on the dot V_{dot} with $V_{\mathrm{dot}} \ll V_{\mathrm{g}}$. It was found [104] that the electric force can be described

$$F_{\mathrm{el}} = \frac{1}{2} C_{\mathrm{g}}^{'} \left(V_{\mathrm{g}}^{\mathrm{DC}} - V_{\mathrm{dot}} \right)^2 \approx \frac{1}{2} C_{\mathrm{g}}^{'} \left(V_{\mathrm{g}}^{\mathrm{DC}})^2 - 2 V_{\mathrm{g}}^{\mathrm{DC}} V_{\mathrm{dot}} \right) + O(V_{\mathrm{dot}}^2) \tag{2.46}$$

and an expression given for the electrostatic potential V_{dot}

$$V_{\mathrm{dot}} = \frac{-Pe}{C_{\mathrm{dot}}} + \frac{C_{\mathrm{g}} V_{\mathrm{g}}^{\mathrm{DC}}}{C_{\mathrm{dot}}} = \frac{q_{\mathrm{dot}}}{C_{\mathrm{dot}}} + \frac{q_{\mathrm{c}}}{C_{\mathrm{dot}}} \tag{2.47}$$

where we reused the control charge $q_{\mathrm{c}} = C_{\mathrm{g}} V_{\mathrm{g}}^{\mathrm{DC}}$ and the average occupation of the energy level responsible for transport $q_{\mathrm{dot}} = -Pe$ with the occupation probability P. Looking at equation (2.46), the first term can be identified to be a static contribution independent of tunnelling processes while the second term depends on the dynamic of electrons within the dot. Plugging in eq. (2.47) into eq.2.46 we can rewrite the influential electrodynamic contribution to

$$F = -\frac{C_{\mathrm{g}}^{'} V_{\mathrm{g}}^{\mathrm{DC}}}{C_{\mathrm{dot}}} (q_{\mathrm{dot}} - q_{\mathrm{c}}). \tag{2.48}$$

At this point it is already apparent, that the resonance frequency depends on the occupation of the quantum dot since the strain inducing force $F \propto q_{\mathrm{dot}}$ directly depends on the charge on the dot.

Tunnelling-induced spring constant softening

The just established dependence of the electrostatic force F on the dot charge q_{dot} has further implications when we move from a static case to a scenario with transport across the dot. The dot charge directly depends on the occupation probability

$$\delta q_{\mathrm{dot}} = e\delta P = e\frac{dP}{dq_{\mathrm{c}}}\delta q_{\mathrm{c}}. \tag{2.49}$$

which is given by the conductance and the tunnelling rate Γ in the closed quantum dot regime [120]:

$$G = \frac{dP}{dq_{\mathrm{c}}} eC_{\mathrm{dot}}\frac{\Gamma}{2}. \tag{2.50}$$

Combining eq. (2.49) with eq. (2.50) and solving for q_{dot} yields

$$q_{\mathrm{dot}} = \delta q_{\mathrm{c}}\frac{2G}{\Gamma C_{\mathrm{dot}}}. \tag{2.51}$$

This link between conductance and dot charge has implications on the mechanical behaviour of the oscillator. The oscillator vibrates with

$$\delta z = \delta z_0 e^{i2\pi f t} \tag{2.52}$$

where δz_0 is the amplitude of its motion and f its frequency. This movement in the electric gate field, assuming small δz_0 to avoid bifurcation, leads to an oscillating capacitance δC_{g}, resulting in an oscillating control charge q_{c} and therefore also an oscillating quantum dot charge q_{dot}:

$$\delta C_{\mathrm{g}} = C_{\mathrm{g}}^{'}\delta z = C_{\mathrm{g}}^{'}\delta z_0 e^{i2\pi f t} \tag{2.53}$$

$$\delta q_{\mathrm{c}} = \delta C_{\mathrm{g}} V_{\mathrm{g}}^{\mathrm{DC}} \tag{2.54}$$

$$\tag{2.55}$$

At this point, it is worthwhile noting, that the quantum dot charge q_{dot} follows the quantised control charge q_{c} and thus in an idealised scenario of zero temperature and zero bias the two charges would show a staircase dependence since δq_{c} is an integer. In reality, however, finite temperature (i.e. thermal activation) and bias voltage result in a smearing out and a continuous dependence of the two.
Using these findings and plugging eq. (2.54) and eq. (2.51) into eq. (2.48) for the case of changing charges we get

$$\delta F = -\frac{C_{\mathrm{g}'}V_{\mathrm{g}}^{\mathrm{DC}}}{C_{\mathrm{dot}}}(\delta q_{\mathrm{dot}} - \delta q_{\mathrm{c}}) = \frac{(C_{\mathrm{g}}^{'}V_{\mathrm{g}}^{\mathrm{DC}})^2}{C_{\mathrm{dot}}}\left(\frac{2G}{\Gamma C_{\mathrm{dot}}} - 1\right)\delta z_0 e^{i2\pi f t} \tag{2.56}$$

which predicts a change of force for different conductance and tunnelling rate. Considering the dependence of the force on the displacement δz given by $\delta F = \delta k \delta z$ we find a spring constant k and therefore get an expression for the change of resonance frequency δf using $\frac{2\delta f}{f_0} = \frac{\delta k}{k}$

$$\delta f = -\frac{f_0}{2}\frac{(C_{\mathrm{g}}^{'}V_g)^2}{kC_{\mathrm{dot}}}\left(\frac{2G}{\Gamma C_{\mathrm{dot}}} - 1\right). \tag{2.57}$$

This finding predicts a direct dependence of the resonance frequency on the conductance via the quantum dot. As a consequence a spring constant softening, i.e. a reduction of the resonance frequency, is expected in regions with large conductance such as Coulomb peaks. While this effect has also been measured in this thesis, for demonstration purposes the cleaner data acquired by Steele et al. [97] using a current rectification technique are presented here.

In figure 2.21, the behaviour of one mechanical resonance as a function of gate voltage when crossing

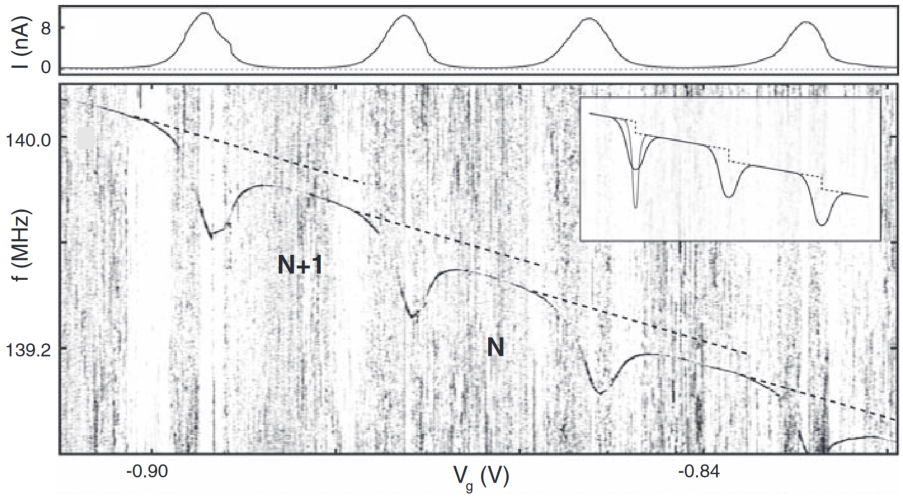

Figure 2.21: **Mechanical resonance measured as a function of gate voltage across four Coulomb peaks.** In the **upper panel**, the current measured by a rectification technique is shown as a function of gate voltage and expresses Coulomb peaks. The **lower panel** plots the normalised absolute difference to the conductance at resonance after subtracting the off-resonant average of each trace (thus resonance is always appearing dark). The jump in resonance frequency towards lower gate voltages after addition of another hole as well as the dip in the resonance frequency on a Coulomb peak are nicely visible. The inset shows the difference between a higher (dark grey) and lower (light grey) bias voltage measurement. Figure adapted from [97].

four Coulomb peaks is shown. The overall trend of increasing resonance frequency towards higher gate voltages follows the expected V_g^2-dependence. Even though it looks like there is a small shift in gate voltage between the measured Coulomb peaks and the observed frequency dips, the clear correlation expected from the previous derivation is apparent.

Influence of electron dynamics on the mechanical quality factor

Besides the appearing change of the resonance frequency, single electron tunnelling can also affect the quality factor, i.e. the losses, within the mechanical oscillator. Due to the oscillations of the carbon nanotube, the charge in the dot oscillates with δq_{dot} as well and this change of charge needs to flow via the tunnelling barriers at the leads with the current [104]

$$\delta I_{\mathrm{dot}} = 2\pi f \delta q_{\mathrm{dot}} = 2\pi f e \frac{2G}{\Gamma C_{\mathrm{dot}}} \delta q_{\mathrm{c}} = 2\pi f e \frac{2G}{\Gamma C_{\mathrm{dot}}} C_{\mathrm{g}'} V_{\mathrm{g}}^{\mathrm{DC}} \delta z_0 e^{i\pi f t} \tag{2.58}$$

where we used previously defined relations to the control charge (eq. (2.49)) and the conductance in the Coulomb blockade regime (eq. (2.50)). Once we know the current we can determine the energy loss E_{diss} per oscillation based on Ohm's law

$$E_{\mathrm{diss}} = \int_0^{1/L} \frac{1}{G}\delta I_{\mathrm{dot}}^2 dt = \frac{4\pi^2 f}{G}\left(\frac{2G}{\Gamma C_{\mathrm{dot}}} C_{\mathrm{g}'} V_{\mathrm{g}}^{\mathrm{DC}} \delta z_0\right)^2 \tag{2.59}$$

which is thus proportional to the conductance and the square of the motion amplitude. When we consider the total energy stored in the mechanical state $E_{\mathrm{tot}} = \frac{1}{2}k\delta z_0^2$ we can derive an expression for the quality factor Q using its definition in equation (2.22)

$$Q = \frac{2\pi E_{\mathrm{tot}}}{E_{\mathrm{diss}}} = \frac{1}{2\pi f}\frac{k}{GC_{\mathrm{g}}'^2}\left(\frac{\Gamma C_{\mathrm{dot}}}{2V_{\mathrm{g}}^{\mathrm{DC}}}\right)^2 . \tag{2.60}$$

The quality factor of the mechanical resonance therefore also depends on the conductance and is thus expected to decrease when crossing a Coulomb peak. Since the clear connection between electron tunnelling and the mechanical properties has been established, this seems like a reasonable result that higher conductance, i.e. higher current, leads to higher losses that are even higher in stronger electric fields. Since the total energy is determined purely by the vibration amplitude, it should be affected less. The clear change of quality factor for regions with different conductance is shown in figure 2.22 . When comparing the resonance shape at different positions on the Coulomb peak for low driving powers, a transition from a bifurcating area with a high quality factor (orange circle in figure 2.22) to a regime with lower quality factor (green circle) but a more Lorentzian-looking resonance shape can be observed. Since the dissipated energy generally depends on the current, an applied bias voltage should result in increased losses as well [97], even though it does not directly appear in the formula.

Duffing parameter modification due to electron tunnelling

When the driving power is increased bifurcation can be observed all across the Coulomb peak (figure 2.22 c)+d)). Interestingly, the sign of the Duffing parameter is changing in a similar manner to the observed current change of a mechanical resonance when crossing a Coulomb peak.
For higher driving powers also the amplitude of the oscillation or displacement of the oscillator is increased. This results in a deviation from Hooke's law and we replace the spring constant k with a modified constant $k' = k + \alpha x^2$ that takes the high amplitude motion into account. This means that the parameter α represents an effective spring constant softening (hardening) for $\alpha < 0$ ($\alpha > 0$) and also determines the bifurcation direction towards low (high) frequencies [97]. It can be calculated directly as the third derivative of the force d^3F/dz^3 and thus, neglecting d^2C/dz^2 terms

$$\alpha = -\frac{d^3F}{dz^3} = \frac{d(\delta k)}{dz^2} = V_{\mathrm{g}}^2\left(\frac{dC}{dz}\right)^2 \frac{d^2(\delta k)}{d^2 q_{\mathrm{c}}} \tag{2.61}$$

the Duffing parameter α follows the curvature of δk which can be directly retrieved from the measured gate voltage dependence of the resonance frequency. This dependence on the curvature also explains that the sign of Duffing parameter changes at the inflection points of the measured frequency dip.

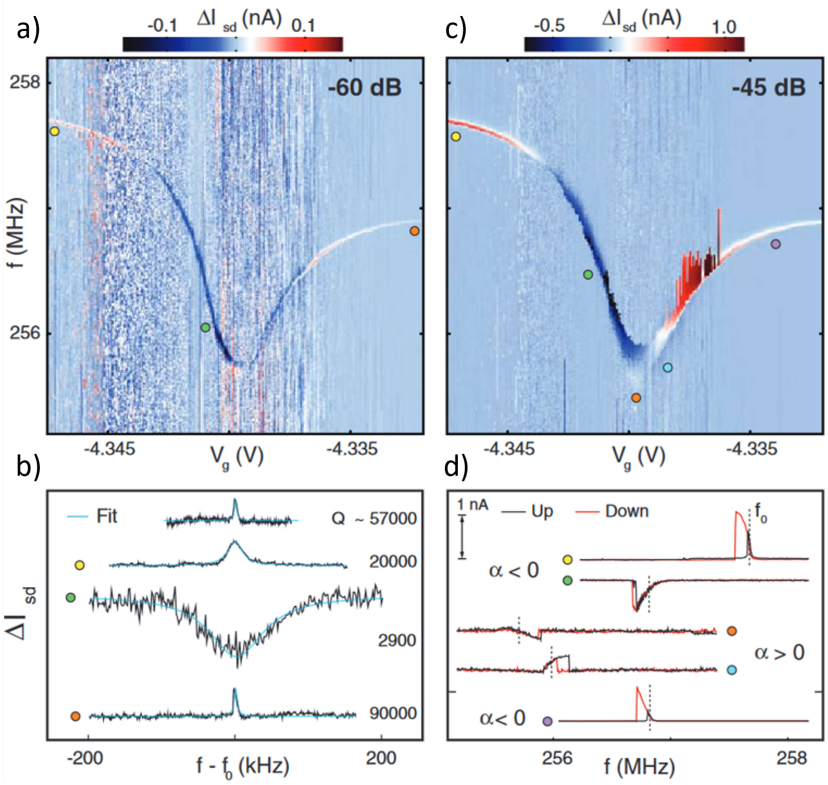

Figure 2.22: **Response of the mechanical resonance upon crossing a Coulomb peak for different driving powers.** For low driving powers **a) + b)** both bifurcating and linear behaviour can be observed. The quality factor differs strongly (up to factor of ≈ 30) with the relative position on a Coulomb peak. For higher driving powers **c) + d)** the nonlinearity and bifurcation becomes more expressed. The Duffing constant α changes sign while crossing the Coulomb peak. Figure taken with minor adaptions from [97].

2.4.8 Longitudinal stretching modes in carbon nanotubes

The discussion of mechanical vibration modes in carbon nanotubes so far has been focused on the bending modes and how they affect electronic transport. This section, however, is dedicated to longitudinal stretching modes. In contrast to bending modes, the stretching modes feature an active movement along the axis of electronic transport which results in a more direct backaction. However, their detection with previously introduced measurement technqiues is not possible since there is no movement along the electric field gradient of the gates. The energies of these modes are typically well within the measurement window of a usual transport measurement and allow an approximation of the suspended nanotube length. Due to their somewhat large energy, at least far larger than bending modes with $\approx 1\,\mu$eV, in the range of hundreds of μeV they are thermally mostly unoccupied at cryogenic temperatures where the thermal energy $k_\mathrm{B}T$ at 50 mK is $\approx$4.3 μeV and are thus close to their quantum mechanical ground state. Based on the Franck-Condon-principle [121, 122] of taking into account vibrational states for electronic transitions in molecules, single-electron tunnelling events in carbon nanotubes can induce a longitudinal displacement which is called a longitudinal stretching mode [21, 96].

The degree of interaction between electronic and vibronic states is quantified by the electron-phonon-coupling $g = \frac{1}{2}\left(\frac{x}{x_0}\right)^2$ (or electron-vibron coupling) where x is the classical displacement length and $x_0 = \sqrt{\hbar/m\omega}$ the quantum mechanical oscillator length or, alternatively g can be expressed less general as $g = \frac{F^2}{\hbar m\omega}$ [96]. For larger scale NEMS that express bulk-like characteristics g is typically very small $g \ll 1$. In contrast, for suspended carbon nanotubes values in the order of $g \approx 1$ [96] or higher ($\langle g\rangle \approx 3.3$) [21] have been reported. Generally, the absolute value for the electron-phonon coupling is strongly dependent on the sample characteristics. In particular the length and radius of the carbon nanotube as well as the position of the induced quantum dot, defects and strain in the carbon nanotube can have strong effects [123].

According to the Franck-Condon-model single-electron tunnelling can induce a longitudinal displacement and thus a shift of the equilibrium position of the oscillator. By rewriting the definition for the electron-phonon g this displacement x can be calculated with

$$x = \sqrt{2g}x_0 \tag{2.62}$$

Mariani et al. [123] derived an expression for g based on an extended Anderson-Holstein model which depends inversely on the carbon nanotube's circumference. The interested reader is directed to this publication to for more information on coupling mechanisms as well as the electron-phonon coupling of other vibration modes. In the following two sections, the influence of the electron-phonon-coupling via stretching modes on the transport properties of a nanotube in the regimes of weak/intermediate($g \leq 1$) and strong ($g > 1$) coupling will be discussed.

Intermediate electron-phonon-coupling $g \leq 1$

Since the tunnelling of an additional electron into the quantum dot can induce a displacement, a nice visualisation of the influence on transition probabilities is a plot of the corresponding vibron potentials

and their associated shift accompanying the displacement of the oscillator (figure 2.23a),b)). For very weak electron-phonon coupling $g \ll 1$, the potential shift is vanishing and (vibronic) ground-state to ground-state transitions from the N to $N+1$ electron configurations are strongly favoured. Additionally, the ground state is orthogonal to most higher vibronic states and transitions into the latter are thus suppressed.
When the electron-vibron coupling is larger and in the range of $g \leq 1$, the shift in the vibron potential is non-negligible and transitions from ground-state to ground-state as well as ground-state to excited-states are allowed. If a process takes place that results in an excited state, the system's behaviour is determined by the vibronic relaxation rate γ and the tunnelling rate to leave the quantum dot Γ. If the relaxation rate is larger than the tunnelling $\gamma \gg \Gamma$ excitations are decaying before an electron can leave the dot and thus transport is blocked. If $\gamma \ll \Gamma$ the electron can leave the dot and transport is occurring. These excited processes result in bands of high transport in parallel to the edges of a Coulomb-diamond with an equidistant spacing given by the energy difference ΔE_{vib} of the vibronic states (figure 2.23e). This energy difference can be calculated to

$$\frac{\Delta E_{\mathrm{vib}}}{L} = \frac{nh}{L}\sqrt{\frac{Y}{\rho_m}} \approx \frac{110\,\mu\mathrm{eV}}{L\,(\mu\mathrm{m})} \tag{2.63}$$

where Y =1 TPa is the Young's modulus of a carbon nanotube, ρ_m =1.3 g cm^{-3} its mass density, L its length and n the quantum number of the vibrational state [96]. This L^{-1}-dependence is analogous to the level spacing of the electronic spaces but with absolute values that are smaller by about one order of magnitude [96].
By measuring these phononic conduction sidebands an approximation on the electron-phonon coupling is possible by considering the differential conductance at the gate voltage associated to the Coulomb diamond tip [21]. If the phonons are in equilibrium, the Franck-Condon-theory predicts a relation of

$$\left(\frac{dI}{dV_{\mathrm{sd}}}\right)_n^{\max} \propto \frac{e^{-g}g^n}{n!} \tag{2.64}$$

and thus gives the means to determine the electron-phonon coupling by fitting eq. (2.64) and thus the nanotube diameter/circumference.

Strong coupling regime $g > 1$: Franck-Condon-blockade

In case of very strong electron-phonon coupling $g \gg 1$, the resulting shift of the vibron potential is big enough to suppress ground-state to ground-state transitions (see figure 2.23c). This effective blocking of low bias transitions (higher vibrational state require higher bias) due to the reduced wavefunction overlap of the ground-state wavefunctions is called Franck-Condon-blockade which results in a decreased conductance for small bias voltages V_{sd}. Additionally, tunnelling via higher excited states is enhanced due to the stronger overlap of the $N-$electron vibronic ground-state with the $N+1-$electron excited states [21].

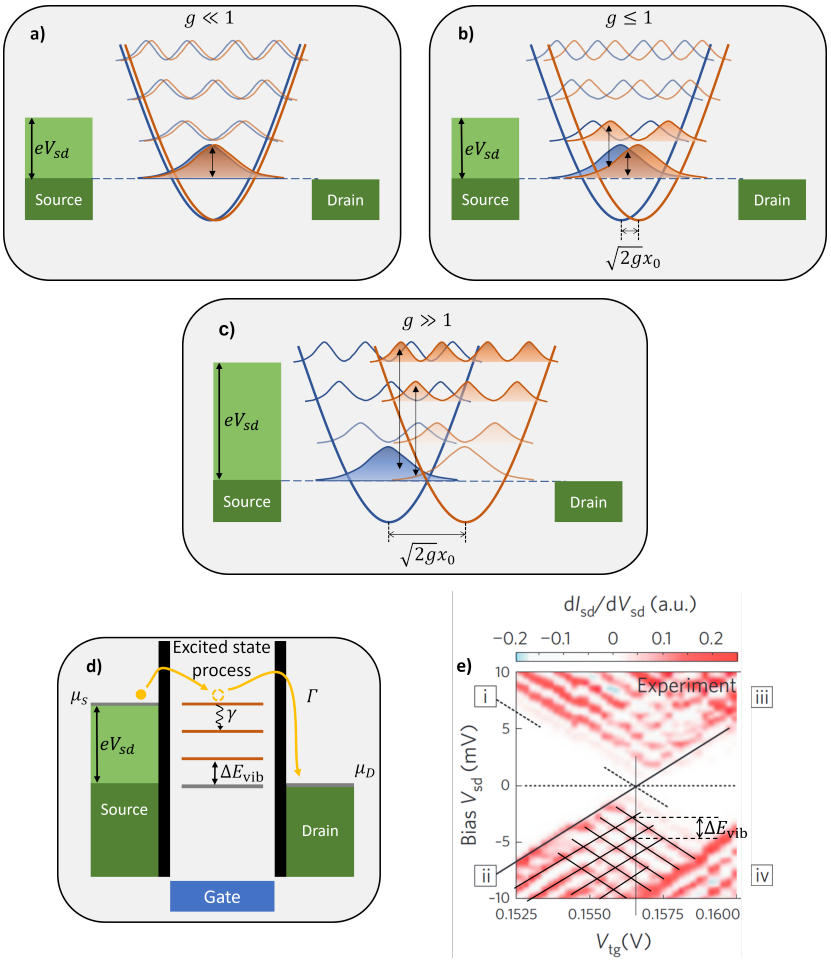

Figure 2.23: **Influence of electron-phonon coupling for different coupling strengths. a), b):** Schematic representation of the vibron-potential shift induced by single-electron tunnelling. The colour saturation is indicating the probability of transitions into the respective state. For weak electron-phonon coupling $g \ll 1$ **a)** the parabolic vibronic potential is shifted only by a small amount between the state for $N-$electrons (blue) compared to $N+1-$electrons (orange). Transport is dominated by ground-state(GS) to GS transitions, indicated by the black vertical arrow, since the GS is orthogonal to higher vibronic states. For an intermediately strong coupling $g \leq 1$, the vibronic potential is visibly shifted by a distance $x = \sqrt{2g}x_0$. Now, besides GS to GS transitions also transitions into low lying excited vibronic states are enabled. **c)** A large electron-phonon coupling $g \gg 1$ results in a large shift of the vibronic potential effectively blocking GS to GS transitions while increasing the likelihood of transitions into excited states. The energy level diagram **d)** shows the equidistant vibronic states that give rise to additional conductance, depending on the relaxation rate γ and the tunnelling rate Γ. Conduction via excited states appear as bands running parallel to the edge of Coulomb diamonds **e)**, taken from [21]). In the negative bias range, these bands have been highlighted by black lines. Measuring their energy spacing as well as their conductance allows to determine the carbon nanotube length, the electron-phonon coupling as well as the carbon nanotube diameter. In the low bias voltage range, conduction is strongly reduced since ground-state transitions are suppressed. The shift in gate-voltage is not attributed to phononic effects but an asymmetric coupling to the leads [124].

2.5 Introduction to single-molecule magnets

2.5.1 General introduction into single-molecule magnets

To conclude this introduction into the physical background, an introduction into single-molecule magnets (SMM) and how they can couple to carbon nanotubes will be given. For a more thorough treatment and description, books such as [125] are recommended to the interested reader.
Magnetism is a phenomenon mostly observed as a collective effect of of many interacting spins in a material, compensating or supplementing each other, that can cause forces on the macroscopic scale. Starting from a bulk magnet on the cm-scale consisting a multitude of magnetic domains (i.e. areas of aligned spins), downscaling in material size causes a reduction in the number of magnetic domains.Eventually, below a certain length scale, known as exchange length [126] that is commonly in the nanometer range, a particle is allowed to have only a single domain. For a single domain nanoparticle, the magnetism is simply explained using a large macroscopic spin. However, the description of the system does not really lead to single spin physics as a single domain still consists of a large number of interacting spins.
When decreasing the size even further eventually a regime can be reached where only a single spin forms the sole magnet. This single spin can originate from a single atom or electron, a defect, but also from a single molecule featuring a single large spin. Specially in the latter case, due to a large size of the molecule and an isolated magnetic core, often an ensemble of molecules also exhibits single molecule properties due to very low inter molecular interaction. With a single molecular spin being the building block in such systems, they are called single-molecule magnets (SMM).
Starting from the 1980s [127], SMMs have been synthesised and their properties studied, since predictions of a strong Jahn-Teller-effect [127] (i.e. lifting of degeneracy of electronic states due to an electric ligand-field) promised interesting findings. Since they can be synthesised chemically, it is possible to create a multitude of identical copies of the desired SMM. They can form van-der-Waals crystals, where the magnetic properties closely resemble the properties of a single molecule since it is a single crystal formed from identical building blocks. Their structure is commonly composed of one or more magnetic ions in the centre bonded to organic ligands forming a shell around the magnetic core. Frequently studied examples are the Mn_{12}-O-acetate complex $[Mn_{12}(CH_3COO)_{16}(H_2O)_4O_{12}](H_2O)$ [128–132] composed of twelve manganese ions (Mn(III)/Mn(IV)) forming a giant spin with $S = 10$ in a shell of acetate-chains (see figure 2.24) or terbium(III) bis(phthalocyaninato) ($TbPc_2$) [9–14, 17] complexes where a central magnetic atom of the lanthanide terbium provides the spin of interest and is encapsulated by Pc-plains from top and bottom. In case of the latter, which was used in this thesis, the magnetism is described by the sole magnetic core, i.e. the total angular momentum J of the single Tb^{3+} ion.
The organic ligand shell surrounding the magnetic core mainly serves two purposes. On one hand, the organic shell couples to the exterior and is responsible for binding to surfaces or intermolecular binding. Since SMMs are chemically synthesised, the organic shell can be modified in a way to enhance its performance depending on the application. On the other hand, it is encapsulating the magnetic core and thus screens it from the environment. This screening is both a curse and a blessing, since it reduces

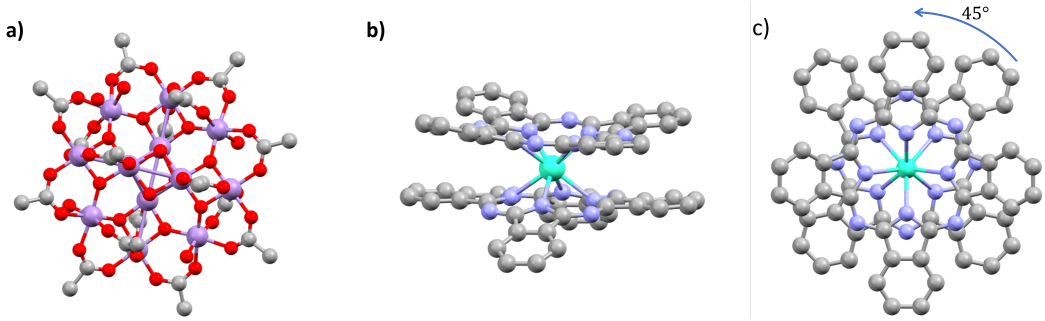

Figure 2.24: **Ball-and-stick representation of two exemplary single-molecule magnets.** The Mn_{12}-acetate complex **a)** features a core of 12 manganese ions with Mn^{+4} (central 4) or Mn^{+3} (8 outer ones) ionisation state that give an $S = 10$ spin ground state. The $TbPc_2$ molecule **b)** hosts a central Tb^{3+} ion with $J = 6$ ground state and a C_4 point group symmetry. In a top-view **c)**, the twisting angle between the two planes becomes visible. Structures generated using the software Mercury by the Cambridge Crystallographic Data Centre, hydrogen omitted. Colour code: Carbon(grey), Oxygen (red), manganese (purple), nitrogen(blue) and terbium(cyan).

disturbing interference from the outside resulting in very long spin-relaxation times [8], especially at low temperatures, but at the same time makes addressing the individual spin in a controlled way rather difficult as it is so well decoupled from the exterior.
In the following, $TbPc_2$ will be used as an exemplary representative of the SMM family to explain why spin and nuclear spin in SMM are desirable physical properties for quantum applications by explaining its electronic structure as well as the physics of spin-relaxation processes alongside the implication of conservation laws.

2.5.2 $TbPc_2$ as a model single-molecule magnet

Structure and electronic properties

As shortly introduced in the previous section, $TbPc_2$ consists of a central Tb^{3+}-ion acting as the magnetic core and organic bisphthalocyaninato ligands, arranged roughly in two parallel planes sandwiching the magnetic core (ref. figure 2.24b)). Each plane consists of four identical segments forming the characteristic wing-like looking aromatic hydrocarbons. The terbium ion is arranged in a fourfold symmetric configuration between the planes, where the inner four nitrogen atoms in the inner aromatic ring bind it in an elevated position above their centre of mass (ref. figure 2.24b)). The two Pc-planes are rotated with respect to each other by an angle of 45° (figure 2.24c)) forming an encapsulating shell around the central terbium ion.
The structural feature standing out is the terbium ion, which also mainly determines the electronic properties of $TbPc_2$. A Tb^{3+}-ion possesses an electronic configuration of $[Xe]4f^8$ stating that the eight electrons in the outermost shell dominate its behaviour. The eight electrons fill the seven 4f-orbitals following Hund's rules resulting in a total angular momentum $J = L + S = 6$. Following Hund's rule for

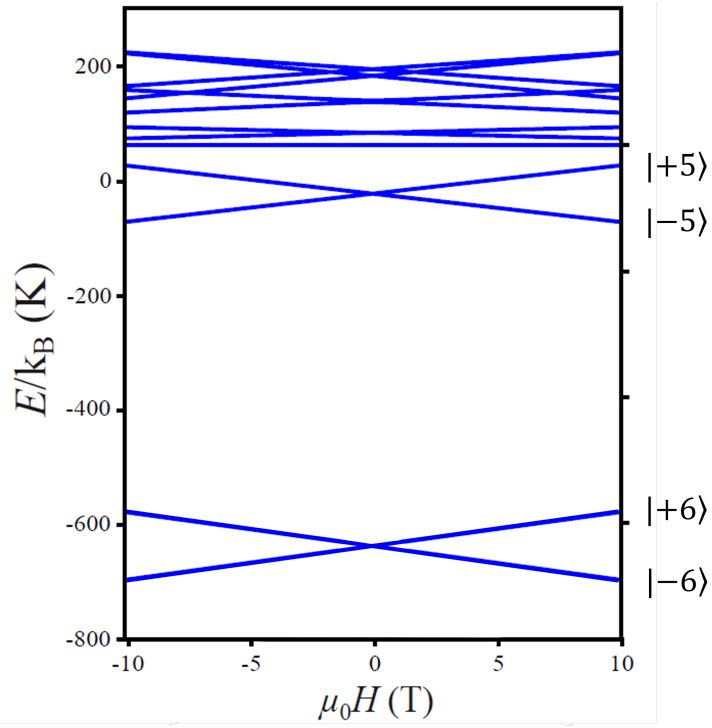

Figure 2.25: **Zeeman diagram for $TbPc_2$ showing the ligand field effect splitting the J-states as well as the magnetic field effect.** Based on [136].

more than half filled shells, the ground state is $J = 6$ with a degeneracy of $2J + 1 = 13$. Lanthanide ions feature a strong spin-orbit interaction and the first excited state $J = 5$ is split by 250 meV≃2900 K [133, 134]. Since most experiments are performed at temperatures way below this, e.g. millikelvin for this thesis, it is safe to assume excited states negligible and limit the discussion to the $J = 6$ ground state. The energy levels of the terbium ions are further modified when the influence of the organic ligands are taken into account. For the C_4 point group symmetry in a XPc_2-molecule (X= rare earth ion) arising from the 45° rotation between the upper and lower Pc-plane, the ligand field parameters have been calculated [135] and applied to measured data [136]. The ligand field Hamiltonian reads

$$\mathcal{H}_{lf} = \sum_{n=1}^{3} B_{2n}^0 O_{2n}^0 + B_4^4 O_4^4 \tag{2.65}$$

with the Stevens operators O_j^k and the associated coefficients A_j^k. The three summed terms (O_{2n}^0) describe the uniaxial anisotropies, while the O_4^4 describes a transverse field interaction that also plays a role in the anisotropy in three dimensions. Some of these terms contain contributions proportional to J_z and thus lead to an additional modification of the magnetic quantum number m_J. This additional contribution causes a splitting between the ground state $m_J = \pm 6$ and the first excited state $m_J = \pm 5$ of ≈ 600 K (ref. figure 2.25). For experiments at cryogenic temperatures this excludes thermal occupation of the first excited state and the system behaves like an Ising-spin [137] with $m_J = \pm 6$. The transverse contribution described by the O_4^4-term causes an additional small splitting of 1.05 µK [136] lifting the degeneracy between the two ground state levels, though the thermal energy in our experiments is high

enough to effectively have equal occupation. This situation of two energetically almost equivalent states separated by an energy barrier is called *magnetic bistability* [128].

Spin-relaxation mechanisms

In figure 2.26a), the energy level scheme of the m_J-states is shown with qualitatively accurate level spacing. The bistable situation occurs between the $m_J = 6$ and $m_J = -6$ states separated by a large barrier and the remaining states. In order to change from $m_J = 6$ to $m_J = -6$ or vice versa a series of thermally activated processes is necessary to overcome the barrier. As a consequence of this, relaxation times can reach extremely high values at low temperatures up to years [8]. Nonetheless, non-thermal relaxation paths consisting of quantum tunnelling of magnetisation (QTM) (see fig. 2.26) a tunnelling of the magnetic moment through the energy barrier have been observed [138–141]. This process is refered to as *quantum tunnelling of magnetisation* (QTM) (see figure 2.26a)).
Since the described electronic states and interactions originate from spins, a Zeeman effect taking place is to be expected. The Zeeman contribution to the electron Hamiltonian is given by

$$\mathcal{H}_{\mathrm{Z,e}} = g_{\mathrm{L}} \mu_{\mathrm{B}} J_z B_z \tag{2.66}$$

with the Bohr magneton μ_{B} and the Landé-factor g_{L} for terbium. The index z corresponds to the easy axis of the molecule. Therefore, an applied magnetic field causes a linear Zeeman-splitting of the m_J-states (ref. figure 2.25). This splitting of the energy states also opens another spin-relaxation path as now direct phonon processes offer an additional path to relaxate. Energy and angular momentum need to be conserved in the relaxation process which can lead to interesting selective behaviour, especially if the phononic density of states is discrete as it is the case for a molecule grafted on a carbon nanotubes [14, 16, 99]. Higher order phonon processes like the Orbach- or Raman-process offer other relaxation paths via phonons but lose importance at low temperatures due to the temperature dependence of their relaxation times [142]

$$\frac{1}{\tau_{\mathrm{Orbach}}} \propto \frac{1}{\exp E'/k_{\mathrm{B}}T - 1} \tag{2.67}$$

and

$$\frac{1}{\tau_{\mathrm{Raman}}} \propto T^7. \tag{2.68}$$

Using the Zeeman splitting while assuming a single giant spin quantised in z-direction and neglecting transversal components of the anisotropy, m-states are described by a Hamiltonian [125]

$$\mathcal{H} = -Dm^2 - g\mu_{\mathrm{B}} m B_z \tag{2.69}$$

with a magnetic field B_z applied along the z-axis and the anisotropy constant D again for the z-axis. Two states m and m' align energetically if

$$B_z = -\frac{(m + m')D}{g\mu_{\mathrm{B}}} \tag{2.70}$$

and thus the levels cross for discrete magnetic field values. As mentioned, the transverse terms from eq. (2.65) can transform this crossing into an avoided level crossing by creating a small waveform

overlap causing the eigenstates of the system's Hamiltonian to be composed of linear combinations. In the avoided level crossing situation, the two energy levels are separated by a tunnel splitting $\Delta_{m,m'}$, allowing for resonant quantum tunnelling. A spin initialised in either of the states can oscillate coherently between the states at resonant conditions with an oscillating frequency $\omega_{m,m'} = \frac{\Delta_{m,m'}}{2\hbar}$. The tunnelling between the states only happens in a certain range of magnetic field given by

$$\delta H = \frac{\Delta_{m,m'}}{g\mu_B\mu_0|m - m'|} \tag{2.71}$$

which is also referred to as the bare tunnel width. As always in real experiments, the tunnel width can be broadened by interactions with the environment influencing the coherent tunnelling.

In order to describe the dynamics of a transition upon sweeping one parameter of the system and thus

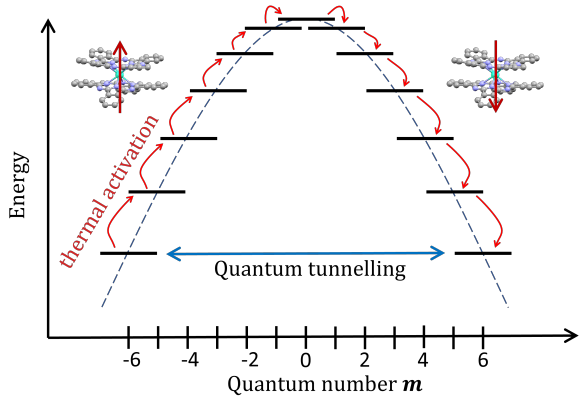

(a) Energy level scheme for a $J = 6$ SMM.

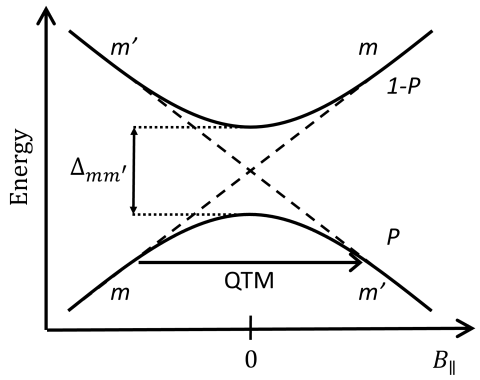

(b) Avoided level crossing and Landau-Zener transition.

Figure 2.26: **Quantum tunnelling of magnetisation (QTM) in an exemplary SMM. a)** In zero field, the energy levels are symmetric and transitions from $J = -6$ to $J = +6$ are possible by QTM or via thermally activated processes. Based on [143]. **b)** When sweeping the magnetic field parallel to the easy-axis, the SMM approaches the avoided level crossing in state m. With a probability P it can tunnel into the m' state. The tunnelling probability depends on the energy gap and the sweeping rate.

traversing an avoided level crossing Landau [144], Zener [145], Stückelberg [146] and Majorana [147] developed a formula for the probability of a diabatic transition as sketched in figure 2.26b), which can be applied for QTM. Nowadays it is often referred to as the *Landau-Zener* model and offers an expression for the tunnelling probability P which can be expressed as

$$P_{LZ} = 1 - \exp\left(-\pi\omega\frac{\delta H}{dH/dt}\right) = 1 - \exp\left(-\alpha\frac{\Delta^2}{dH/dt}\right) \tag{2.72}$$

where we reused previous definitions of tunnel width and oscillation frequency and introduced the field sweep rate dH/dt and a proportionality factor α containing the constants. It states that QTM will almost certainly happen in case of adiabatic sweeping (i.e. $dH/dt \longrightarrow 0$) or very large tunnel splitting. When increasing the sweeping rate, the tunnelling probability decreases exponentially and will eventually vanish for very large sweep rates.

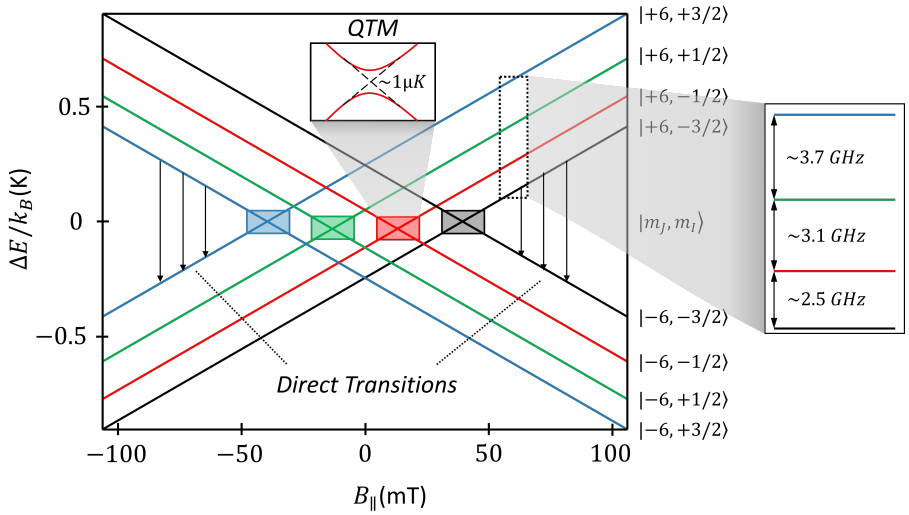

Figure 2.27: **Zeeman-diagram of the nuclear spin states of a molecule in the subspace $m_J = \pm 6$ with spin-relaxation processes,** redrawn qualitatively after [136]. For small magnetic fields quantum tunnelling of magnetisation (QTM) occurring at avoided level crossings (inset) allows for spin-relaxation. At larger magnetic fields, QTM is not possible anymore and spin relaxation is happening via direct processes. The second inset on the right shows the energy level spacing between the individual nuclear spin states.

Nuclear spin of Tb

Since terbium is composed solely of the isotope ^{159}Tb with a nuclear spin $I = 3/2$, the four possible nuclear spin states need to be taken into account as well. They feature an additional Zeeman-effect

$$\mathcal{H}_{\mathrm{Z,n}} = g_{\mathrm{I}} \mu_{\mathrm{N}} I_z B_z \tag{2.73}$$

where we used the g-factor of the nucleus g_{I} and the nuclear magneton μ_{N}. As a result, the $m_J = 6$ ground state is split for the four nuclear spin-states (see figure 2.27). The energy splitting between the nuclear spin states due to the hyperfine coupling together with a nuclear quadrupole interaction is non-linear, which opens the possibility to drive individual transitions selectively. The Zeeman splitting results in four avoided level crossings at different applied magnetic fields with a tunnel splitting Δ of about 1 μK.

In the previous section, spin relaxation processes were described while neglecting the nuclear spin. Since the flip of the electron spin conserves the nuclear spin this was a valid assumption. Taking nuclear spin states into account, the magnetic field value for which QTM can occur shifts due to the hyperfine coupling. As a consequence, in applications the nuclear spin-state can be read-out by measuring the magnetic field value at which QTM between the electronic spin doublet occurs. This technique was applied e.g. to a spin-transistor, where a spin-flip resulted in a measurable change of conductance [9, 10, 17, 148] (see figure 2.28). By sweeping the magnetic field, the current nuclear spin-state could be detected with a fidelity of 69% [9]. The sensitivity of the conductance to the terbium spin state arises from an exchange coupling between the terbium spin and the π-orbitals in the Pc-ligands that

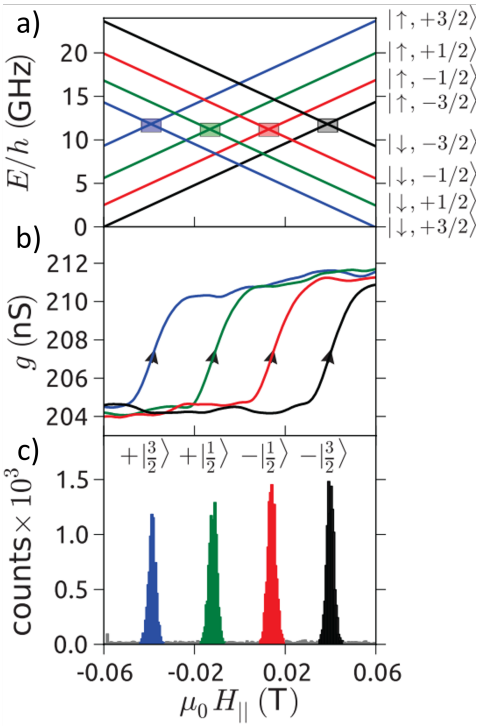

Figure 2.28: **Nuclear spin readout of the terbium ion in $TbPc_2$ in a spin-transistor. a)** A Zeeman-diagram shows the avoided level crossings where QTM may occur. **b)** Upon sweeping the magnetic field, the conductance changes when the spin undergoes QTM. The magnetic field value at which this occurs depends on the nuclear spin state. **c)** histogram of the measured switching fields, where each peak corresponds to a nuclear spin state. Figure extracted with slight adaptations from [10].

act as the readout quantum dot in the confined arrangement of a single molecule spin transisitor. By coherently applying electric pulses to the nuclear spin coupling via the ac-Stark-effect, a manipulation of terbium nuclear spin was possible. This qudit structure has been used to implement basic quantum algorithms including Rabi, Ramsey measurements yielding decoherence times upto 100 muS. Moreover, even Grover's algorithm has been demonstrated [17].

2.5.3 Readout of single molecule magnets with a carbon nanotube

Due to their exceptional mechanical properties and integrability into electronic circuits as well as their small radial size matching the dimensions of SMM, carbon nanotubes are an interesting candidate for sensitive magnetometers with different coupling mechanisms proposed such as magnetic flux, mechanical or electronic coupling [143].
As introduced in section 2.3, it is easily possible to create one or more quantum dots in a carbon nanotube, either by electric field tuning or by simply using Schottky barriers at the metal interface. In this transistor like configuration, the conductance of the carbon nanotube is very sensitive on local perturbations. It has been shown [11–13] that it is possible to both manipulate and read-out

the spin-state of the SMM via a current driven through the carbon nanotube. Similar to the spin transistor described before where the quantum dot was formed in the organic ligands, the conductance is sensitive to magnetisation reversal and thus a spin-flip is observable. By putting two molecules on different positions on one carbon nanotube it was possible to create a molecular spin-valve [11–13] based on magnetoresistive effects that reduce the current for antiparallel spin orientation.

DC-SQUID detection

Further, it is possible to couple the spin of an SMM to a carbon nanotube via the aforementioned magnetic flux coupling. A carbon nanotube can serve as the weak link in a dc-SQUID [24, 28] magnetometer where the SMM is grafted onto the carbon nanotube. Due to the very small crosssection of about 1 nm^2 which is about the same size as a typical SMM, very good flux coupling is expected. Since a lanthanide bisphthalocyaninato complex (LnPc_2) causes a magnetic flux of $\approx 10^{-4}\,\Phi_0$ [24], where $\Phi_0 = \frac{h}{2e}$ is a flux quantum, and the sensitivity of a nano-SQUID is approximated to be $\approx 10^{-5}\,\Phi_0$ a situation is created where the molecule's magnetic flux is measurable.

Magnetometry via mechanical stress sensing

Lastly, it has been shown that the spin of the single-molecule magnet can be coupled to mechanical motion of a carbon nanotube via spin-phonon coupling [14–16]. Using carbon nanotubes functionalised with single-molecule magnets have been proposed as sensitive magnetometres by Lassagne et al. [149] where the single-molecule magnet is grafted onto a suspended carbon nanotube (see figure 2.29). Applying a magnetic field $\vec{H}$ misaligned with the magnetic moment $\vec{m}$ of the SMM induces a torque $\vec{\Gamma} = \vec{m} \times \vec{H} = g\mu_\mathrm{B}\mu_0/\hbar\,\vec{J} \times \vec{H}$ causing a rotation towards the magnetic field direction causing the SMM to rotate in order to minimise the magnetic anisotropy energy resulting in a bending of the carbon nanotube [149], as illustrated in figure 2.29. The bending causes an additional tension in the carbon nanotube shifting the resonance frequency. The frequency shift depends on the position of the SMM along the CNT of length L and is not maximum when the SMM is attached to the centre ($L/2$) since this favours the shape of the first harmonic, but when the SMM is attached at $L/4$ [149]. Given high quality factors for the mechanical resonance, the sensitivity is ultimately limited by the frequency noise due to thermal fluctuations [150] given by

$$\delta f_\mathrm{th} = \frac{1}{2\pi}\sqrt{BW\frac{2\pi f_0}{Q}\frac{k_\mathrm{B}T}{kz_0^2}} \tag{2.74}$$

with the measurement bandwidth BW, the resonance frequency f_0, the quality factor Q, the spring constant k and the amplitude of motion z_0 [149]. Plugging in experimental values obtained in [103] of $f_0 \approx 50\,\mathrm{MHz}$, $k \approx 10^{-4}\,\mathrm{Nm}^{-1}$ for a length of $L \approx 1\,\mu\mathrm{m}$, they found it was possible to reach the limit of $1\mu_\mathrm{B}$ at low temperatures and few hundred μ_B at room temperature [149].

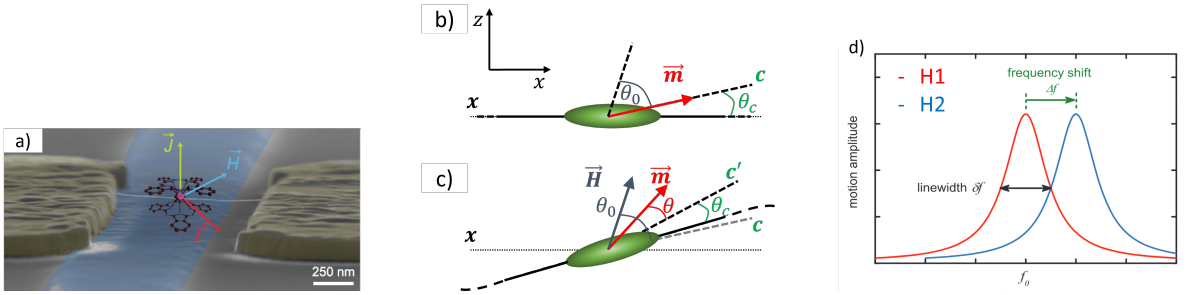

(a) SEM micrograph of CNT NEMS with stylised grafted SMM.

(b) Sketch of the CNT deformation due to applied magnetic-field.

(c) Schematic resonance frequency shift with applied magnetic field.

Figure 2.29: **CNT NEMS acting as magnetometre. a)** SEM micrograph with a SMM grafted onto a suspended CNT. Arrows are indicating the magnetic field $\vec{H}$, the SMM total angular momentum $\vec{J}$ and the acting torque $\vec{\Gamma}$. Figure taken from [15]. **b)+c)** Sketch of the acting forces and relevant angles of an SMM (Stoner-Wohlfahrth model) attached to a CNT without **b)** and with **c)** magnetic field. In case of an applied magnetic field **c)**, the SMM rotates due to a different orientation of the magnetic moment $\vec{m}$ and bends the CNT (here in black). Adapted from [149]. **d)** Schematic of the resulting frequency shift with an applied magnetic field due to the induced additional tension in the CNT. Adapted from [15].

Bi-stable mechanical resonance as digital amplifier

Ganzhorn et al. [15] proposed a readout mechanism making use of the bistability of carbon nanotubes around their mechanical resonance at higher driving powers. When a carbon nanotube is prepared in a state close to the peak of the Duffing resonance peak, small changes of the resonance frequency can result in a very strong signal due to the bistable situation (figure 2.30). Since the difference, e.g. in conductance, between the two bistable states can be huge [15, 97, 103, 107, 116], the expected signal-to-noise-ratio (SNR) is large. This mechanism is mostly suited for single event measurements, like a spin-flip or magnetisation reversal, as the resulting state is typically only weakly sensitive towards small changes of the resonance frequency induced by strain.

Quantum Einstein-de-Haas effect for nuclear-spin readout

When discussing spin relaxation mechanisms special emphasis was put on conservation of energy and angular momentum when the giant spin of an SMM flips. For an SMM grafted onto a suspended CNT, the only system that can compensate the difference in angular momentum and energy is the CNT it is attached to. As discussed in section 2.4.5, carbon nanotubes do not have a continuous spectrum of available mechanical modes but rather a discrete set of modes at energies specific to the CNT geometry and its environment. Upon sweeping a magnetic field parallel to the easy axis of an SMM attached to a CNT, Ganzhorn et al. [16] found that the SMM undergoes a magnetisation reversal, measurable as a conductance jump, in 100% of the sweeps for magnetic field values of 70-170 mT for upwards

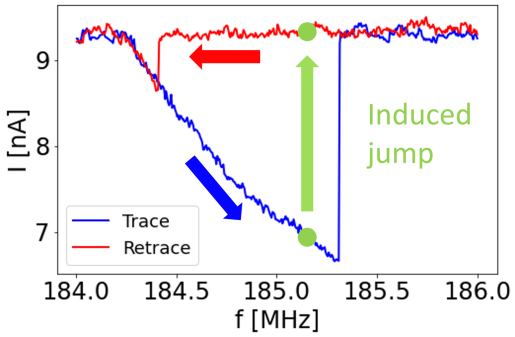

Figure 2.30: **Schematic of a spin-reversal readout using the mechanical bistability of a CNT mechanical resonator.** When the CNT is prepared in a state in the bistable region (green dot), perturbations like a magnetisation reversal or a magnetic field can induce a jump resulting in a large signal-to-noise-ratio.

sweep direction bunched around four distinct values but never around zero. This matches the energy scale of longitudinal vibration modes (sec. 2.4.8) of about 1 K, which is way above the tunnel splitting of 1 µK at the avoided level crossing and thus cannot be QTM but must rather be attributed to a direct process as depicted in figure 2.27. The same can be said for the energies of bending modes and radial breathing modes, though no direct transitions have been observed at their respective energy scale. At low temperatures of about 20 mK and moderate magnetic field sweep velocities ($\approx 100\,\mathrm{mT\,s^{-1}}$, magnetisation reversal occurs mainly around four discrete field values [16], visible as four peaks in a histogram in figure 2.31 indicating that the electron spin flip for the four different nuclear spin states are observed. The average initial nuclear spin occupation can be determined by comparing the peaks within the histogram since they can be attributed to the four nuclear spin-states. For slow magnetic sweeping speeds, the system has enough time to relaxate into its nuclear spin ground state and therefore mostly transitions at smaller field values are measured. At higher temperatures, the four peaks start to smear out and cannot be distinguished properly anymore.
These experiments showed, that carbon nanotubes are a versatile platform that can interact with Single-molecule magnets in different ways that can be adjusted for the application case. They have proven to be able to non-destructively read-out the nuclear spin state of the central terbium-ion while offering a way to integrate SMMs into nano-circuits. How such circuits can be fabricated, which challenges need to overcome and how potential devices could look like, is the subject of the next chapter.

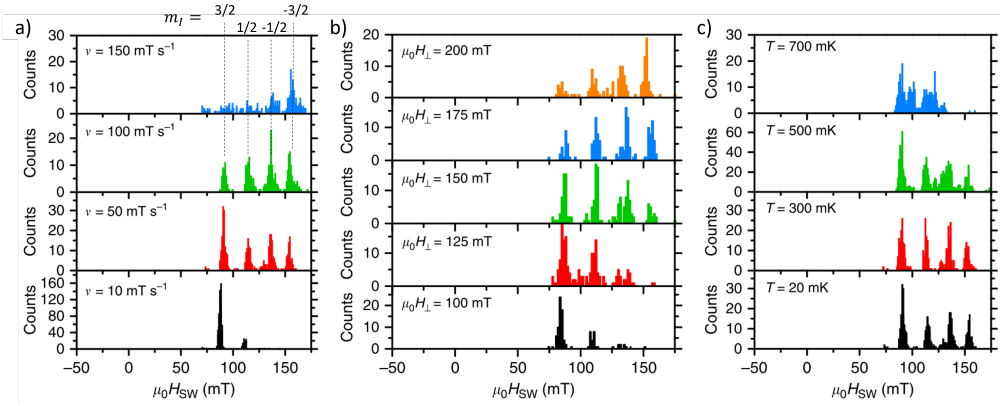

Figure 2.31: **Magnetisation reversal histograms for $TbPc_2$ attached to a CNT NEMS for different magnetic field sweep rates a), transverse magnetic field b) and temperatures c).** The four distinct peaks in most histograms can be attributed to the four nuclear spin states of the central terbium-ion. Figure extracted with adaptations from [16].

3 Fabrication

In this chapter, the fabrication of the devices measured within the frame of this thesis will be presented. The purpose of this chapter is to discuss the individual steps, the problems we encountered and how we were tackling them. A detailed list of process parameters and values can be found in section 6. At first, the design and fabrication scheme for the nano-structured metal-circuits of the two different carbon nanotube integration techniques, the '*top-growth*' and the '*stamping*' technique, will be introductory presented (section 3.1). Following up on this in section 3.2, the fabrication techniques used for the production of said circuits will be reviewed. The bulk of this chapter is composed of a detailed review of the two carbon nanotube integration techniques used in this thesis in section 3.3, pointing out their similarities and differences as well as weighing their benefits and drawbacks. As a last step, the deposition of single-molecule magnets using an evaporation technique as well as an attempt to verify their integrity are shown in section 3.4.

3.1 Circuit designs and fabrication scheme

In this section the design and fabrication layout of some of the devices are presented. A list of steps will be given for both 'top-growth' and 'stamping' samples. The fabrication techniques themselves as well as some of the occurring problems are discussed in the later section 3.2.

3.1.1 Layout of the metal-circuit for 'top-growth' procedure

Since this project evolves around suspended carbon nanotubes, their mechanical modes, double quantum dots and a potential coupling to single-molecule magnets we wanted to build a circuit containing a suspended carbon nanotube with several local gates to tune the electric potential landscape. The layout and an electron microscope picture of one device are given in figure 3.1. The exact parameters for the fabrication are given in appendix 6. Here, a list of steps (table 3.1) for the top-growth process together with an explanation on why the process was designed this way is given. The first constraint to keep in mind is that the growth process forces harsh conditions (≈800 °C in an atmosphere of CH_4 and H_2, see section 3.3.1) onto the circuit. This severely limits the usable range of materials as some commonly used materials will either melt (e.g. Al [151]), become diffusive (e.g. Au [152]) or chemically react with the gases (e.g. Nb [153]). While it is still possible to use them for non-functional structures such as markers, no functional structure can be made from them, making it harder to, for example, build superconducting circuits.

We start off the fabrication by cleaning a commercially bought p-doped (i.e. doping with boron) (100)Si-chip with a size of 15x15 or 20x20 mm^2 cut from a 4-inch wafer grown in a Czochralski-process

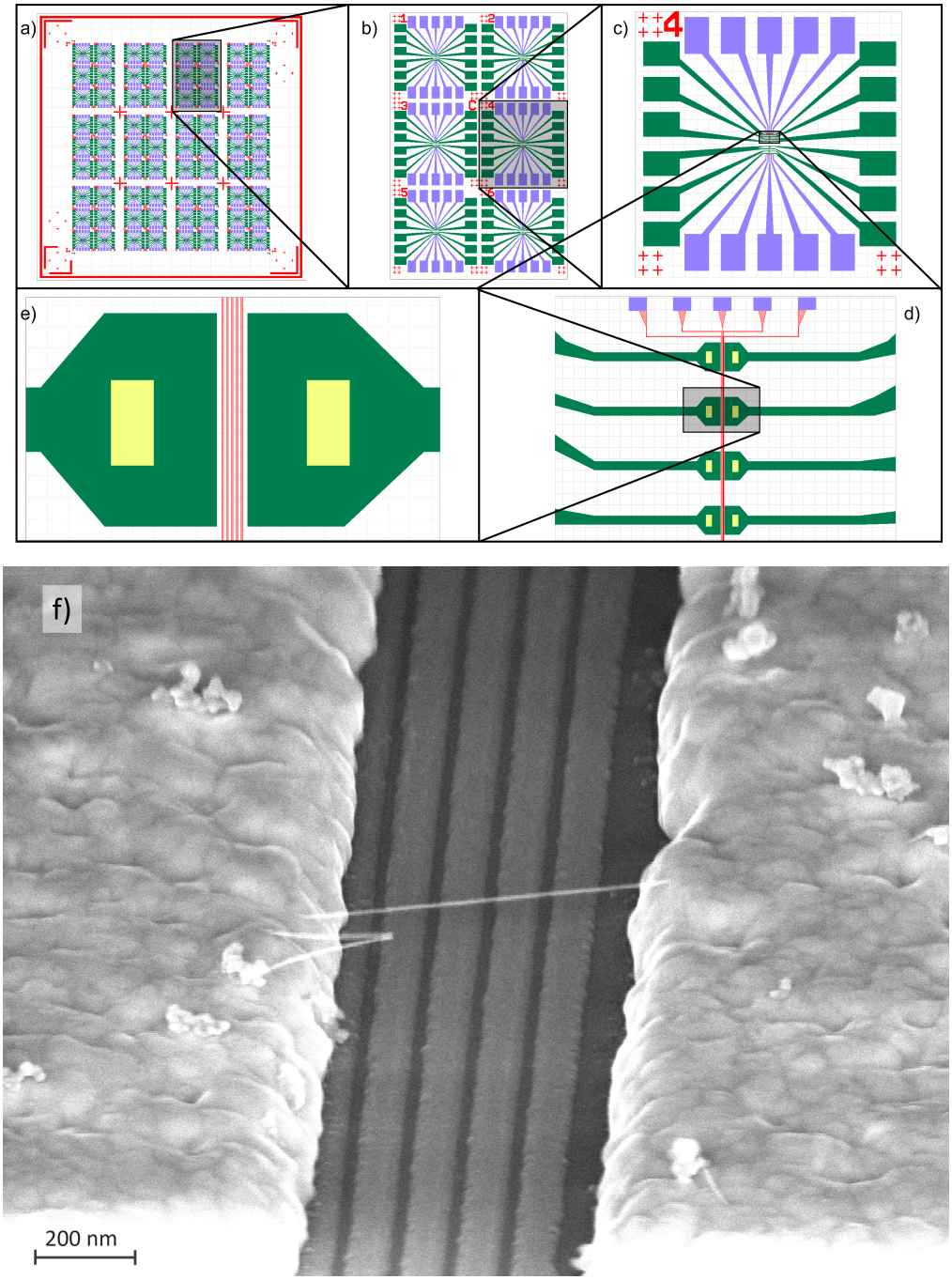

Figure 3.1: **Full layout of a chip used for top-growth circuits a).** Large red areas are alignment markers for orientation. A single chiplet **b)** is divided into 6 identical pieces **c)**, split in two parts of four devices each **d)** with shared five local gates (e-beam part is coloured red, optical part is coloured purple). The contact electrodes coloured dark green are made in a combined e-beam/optical lithography step. The catalyst islands coloured yellow are located symmetrically around the gap **e)** and serve as starting points for CNT growth. An SEM micrograph **f)** shows an actually measured device with four fully functional gates. The gate on the left was partially screened due to imperfect alignment.

Step 1: Alignment markers	Optical Lithography	5 nm titanium, 40 nm gold
Step 2: Local gates	E-beam Lithography	3 nm titanium, 7 nm molybdenum or platinum
Step 3: Gate bondpads	Optical Lithography	5 nm titanium, 70 nm platinum
Step 4: Insulating Oxide	Atomic layer deposition	10-15 nm aluminium oxide
Step 5: Contact Electrodes and bondpads	E-beam and Optical Lithography	5 nm titanium, 70 nm molybdenum, 70 nm platinum
Step 6: Catalyst windows	E-Beam lithography	nanoparticle deposition (rf. section 3.3.1)

Table 3.1: **List of the nanofabrication steps for the fabrication of top-growth samples.** Details including used resist, parameters, reactants etc. can be accessed in section 6.

and a thickness of about 525 µm, resulting in a resistivity of 1-5 mΩ cm. The surface of this chip features a 290 nm thick layer of amorphous, insulating SiO_2[1] produced in a dry oxidation process. The p-doping creates a conductive substrate that allows us to use the substrate as a global backgate or ground plane. The dry oxidation technique typically results in thinner, but cleaner SiO_2 layers whereas the wet oxidation process can create thicker layers with more impurities but at the same time created problems in combination with chemical vapour deposition processes [99] due to strain. Despite the harsh conditions hinted at before, we still used gold as the material for the alignment markers (step 1) fabricated in an optical lithography step since it is easy to handle and provides great contrast for e-beam lithography. At the time of the CVD process, the markers are not needed any longer and damage to them is no concern. We mainly used crosses with a feature size of few micrometre or rectangles arranged in a vernier caliper working principle to align individual optical lithography steps. For the alignment of e-beam lithography steps, more crosses close to the structures to be written were patterned. How a lithography process works is described in section 3.2.1. The achieved alignment accuracies were in the order of 1 µm for optical alignment and below 100 nm for e-beam alignment.
Since the CNT mustn't touch the local gates even for applied electric fields it is essential to put some distance between gates and the CNT. This means that the contacting electrodes need to be manufactured much higher than the local gates. We thus chose a height of 10-15 nm for the local gates to ensure an uninterrupted film even if Volmer-Weber-growth (i.e. growth predominantly in islands instead of layer by layer) is predominant but still stay reasonably thin. We were aiming to have five local gates which we need to bring below the suspended CNT section whose length is limited due to the CNT growth and the contacting electrode height as the CNT will have some slack. We aimed for a

[1] Siegert Wafer, Charlottenburger Allee 7, 52068 Aachen

ratio of suspended length:suspension height of 5:1, which proved to be enough for CNTs that were growing roughly orthogonal to the local gates. Additionally some leeway for alignment inaccuracies was given between gates and contacts to avoid overlapping. Taking all of this into account we chose a gate width of about 50 nm with a spacing of about 60 nm and 100 nm of leeway resulting in a high yield percentage of functional structures. Since typically gates were shared between 4 contact pairs 3.1d) these gate lines were rather long (35 µm, aspect ratio of more than 500:1), hence sometimes cuts could not be avoided. As a consequence of the thin film thickness, microbonding directly on it is not feasible. Thus, we were fabricating bondpads and lines leading to the local gates using optical lithography. We chose a rather large thickness of about 70 nm to facilitate microbonding even in the presence of additional insulating layers on top.
Since the growth of CNTs is a non-deterministic process (see section 3.3.1) we globally covered all structures fabricated up to this point in an oxide layer to avoid shorting lines electrically. As a first test, we evaporated aluminium with a low rate of about $0.02\,\mathrm{nm\,s^{-1}}$ in an oxygen atmosphere of about 1×10^{-3} mbar to create aluminiumoxide. The created oxide proved to be insulating after evaporation and further lithography steps but unfortunately was conducting after exposing the device to CVD growth conditions (as described in section3.3.1). We blame this on an impure oxide that formed conduction channels after "annealing" at high temperatures. Therefore, we created a cleaner oxide using atomic layer deposition (ALD). The details of an ALD process are presented in section 3.2.3. At this point it suffices to say that the ALD process resulted in nicely insulating layers that survived CVD-conditions and no leakage occurred for devices without other obvious flaws such as molten gates or a partially broken substrate.
The next fabrication step consisted of creating the electrodes that are supposed to form the contact to the carbon nanotube. We used an approach where we combined optical and e-beam lithography to reduce the number of necessary lithography steps and evaporations. The combination of the two lithographies (writing and developing) worked out nicely. Still, this step proved to be the most challenging one, as is discussed in detail in 3.2.2. In short, excessive heating during the evaporation caused the film to curl after the evaporation, hard baked or burned parts of the resist and resulted in broken structures. In the end, we fabricated electrodes about 750 nm apart with a height between 150-200 nm with a platinum top layer for a good electric contact to the CNT [26].
When all these individual lithography steps worked out, the resist for the last lithography step needed to define starting areas for the carbon nanotube growth (cf. section 3.3.1) was spincoated. The chip was then diced into sections of approximately $2.5 \times 3.5\,\mathrm{mm^2}$ to be used in the CNT growth, such that every chiplet labelled by a letter (figure 3.1b) can be treated on its own. Overall each single chip consists of 12 chiplets (letters "A"-"L") that consist of 6 identical fields with 8 devices each. Thus a total of 12*6*8=576 devices are fabricated on each single chip necessitating some post-selection (cf. section 3.3.3) since not each and every one of the devices can be cooled down and measured.

3.1.2 Layout of the metal-circuit for the 'stamping' technique

The stamping technique requires some spatial freedom to manoeuvre the cantilever chip in order to position the CNT at its designated spot. Therefore, it is necessary to etch parts of the substrate to enable

Step 1: Alignment markers	Optical Lithography	4 nm titanium, 40 nm gold
Step 2: Local gates	E-beam Lithography	3 nm titanium, 8 nm aluminium
Step 3: Contact Electrodes	E-beam Lithography	5 nm titanium, 100 nm aluminium, 10 nm palladium
Step 4: Trenches	Optical lithography	Reactive-ion etching using CHF_3, Ar, SF_6,C_4F_8

Table 3.2: **List of the nanofabrication steps for the fabrication of stamping-transfer samples.** Further details including used resist, parameters, reactants etc. can be accessed in section 6.

vertical movement. Since the CNTs are not grown directly on the chip anymore, the structures on the chip are never exposed to the violent CVD conditions allowing us to use metals such as aluminium, gold and titanium also for functional structures. This is an obvious simplification that also allows for the easy introduction of common superconductors like the mentioned aluminium.

The fabrication scheme follows a similar pattern (cf. table 3.2), consisting of alignment markers of gold in the first optical lithography step with the difference that in this case the bond pads as well as the lines leading to the functional part of the circuit are patterned as well, since there is no later fabrication step, e.g. CNT growth, that is going to harm them. We are using a universal layout consisting of 24 dc-lines that allows for a flexible design of e-beam patterned structures in the centre of the chip (figure 3.2). As a next step the local gates are fabricated in an e-beam lithography step with a thickness of 10-20 nm. A reasonably large overlapping area with the leads leading from the bondpads to the nano-circuit was chosen such that there is a high chance of a proper electric contact. Since the gates are thinner than the optical lines they are supposed to overlap with, the connection will sometimes be interrupted since the metal film can be discontinuous at the edges. To enhance the chances of successful connection, it can be helpful to envelop the optically patterned structure on at least 3 sides to avoid detrimental effects of a small angle during the evaporation. Typically, the gates were made from a stack of titanium and aluminium which offers the advantage of a native insulating oxide layer forming at the surface helping to prevent electrical shorts.

Once the gates are on the chip, the contacting electrodes are fabricated and, analogously to top-growth chips, they are fabricated a fair bit higher ($\approx$ 110 nm) than the local gates. The reasoning is again to enable the CNT to be suspended by having enough distance between the CNT and the substrate. The exact material stack for this technique differed widely between individual devices, but typically was in the format of titanium-metal-palladium since palladium as a contacting material is known to be able to result in a low-ohmic interface resistance (e.g. [154]) which is attributed to the small work-function mismatch to CNTs and titanium behaves nicely as an adhesion layer.

For this, we patterned an etching mask using optical lithography before etching the SiO_2 and Si in a reactive-ion etching process. To etch the 290 nm SiO_2 surface, a mixture of CHF_3/Ar/O_2 was used

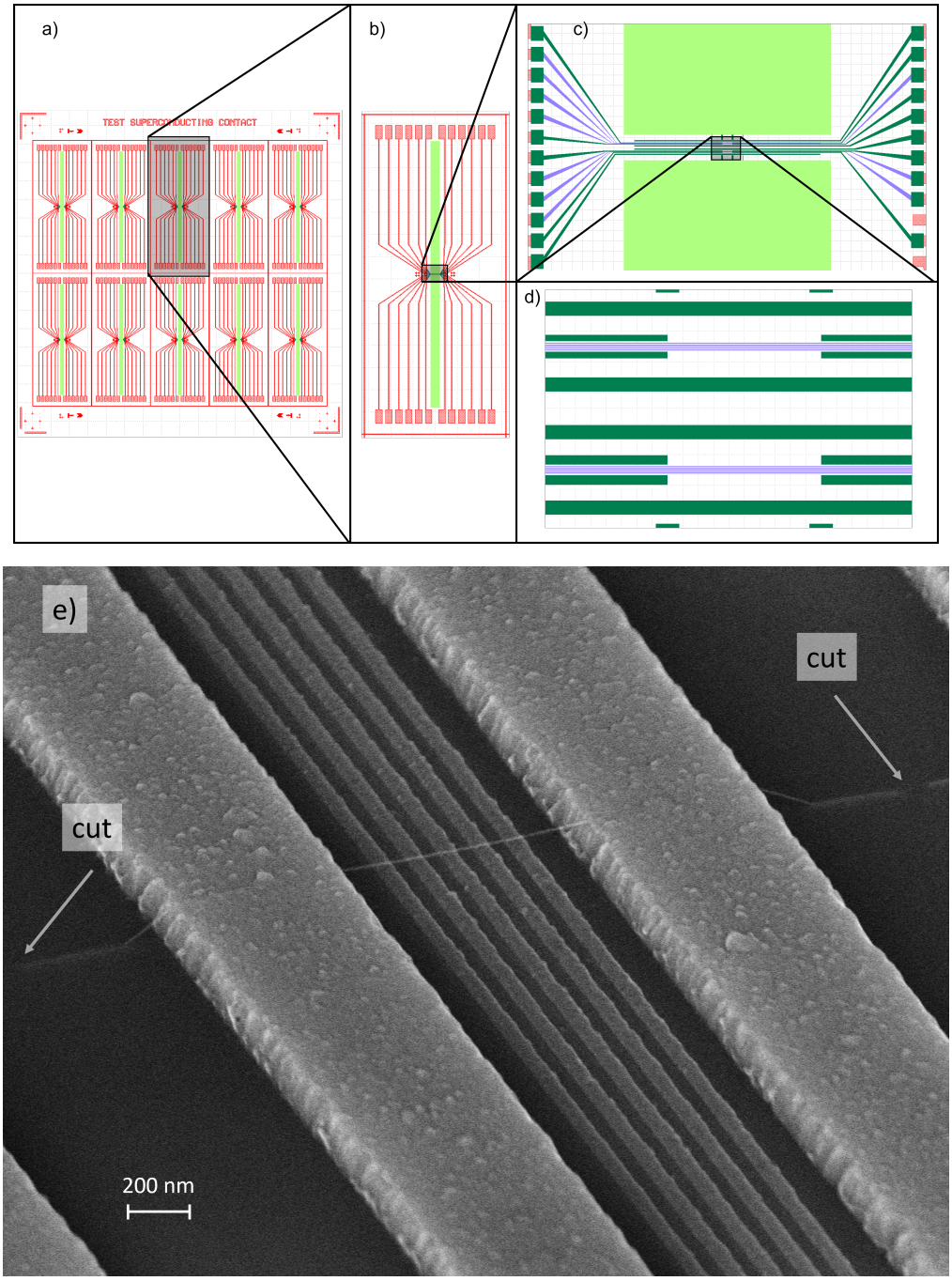

Figure 3.2: **Full layout of a fabricated chip for the stamping transfer technique a).** After etching trenches (in light green), the chip will be cut in 10 chiplets **b)** with shared optical designs (in red) and differing e-beam written structures in the centre (gates in purple, contacts in dark green). Here, a layout for four double quantum dot circuits is shown **c)** and **d)**. In a fabricated and measured device it is nicely visible on an SEM micrograph **e)** where the CNT was cut and how it is suspended between the two contacts

while for etching the main depth of the trench ($\approx 10 - 20\,\mu m$) a Bosch-like process was the technique of choice. Here, the etching was performed by cycling two different etchants where SF_6 was used to etch the substrate, while C_4F_8 was used to passivate the sidewalls between the etching steps to protect them from further etching. This procedure is particularly useful for deep etching recipes since the etching process is not perfectly anisotropic and thus the sides would be slowly etched away resulting in non-vertical walls and an uncontrolled broadening of the etched structure.
Once the trench is etched the metal-circuit fabrication of these devices is complete and the CNT needs to be integrated as a last step. The integration via the stamping technique is discussed in section 3.3.4.

3.2 Nanofabrication techniques

To observe any of the physics discussed in previous chapters an electric circuit is needed. We were fabricating every nanostructure using the facilities available at KIT in the 'Physikalisches Institut'[2], the Center for Functional Nanosctructures[3] and the Institute for Nanotechnology[4]. The processing scheme for the devices has been shown in section 3.1. Here, an introduction into nanofabrication techniques is given. In order to shape the metal structures, two different general principles can be applied: Either material is added locally by evaporation or sputtering or material is added globally and then removed locally by wet or dry etching. Both ways require the possibility to manipulate the surface on a scale down to nm-dimensions. The most common way of doing so is by using lithography techniques which will be discussed in the following.

3.2.1 Photo- and e-beam-lithography

In general in a lithography (greek: *lithos*=stone, *gràphein*=to write) step a sacrificial layer will be applied to the substrate, then a part of this layer is altered locally and removed. We were using two similar techniques to structure our circuits: photo lithography and e-beam lithography. Here, an organic resist that is sensitive to irradiation with either electrons or photons of a certain energy is deposited onto the substrate. Several techniques exist for this application such as spray covering or using a rotating disc. For reproducibility it is important to be able to reliably realise a certain thickness with a homogeneous surface across the full substrate. To realise this, using spray covering requires a sophisticated approach where mechanisation helps a lot and is therefore mostly an industrial application. We were using the rotating disc technique called spincoating. Here, the substrate is fixed on a disc via vacuum pumping and the resist of choice can be cast onto it. Then, the disc starts to rotate with typical frequencies between 1000 and 10000 rpm. The resulting centrifugal force pushes the resist away from the centre while cohesion and adhesion guarantee a thin layer to remain. By tuning rotation speed (spinning parameter) and cohesion (resist parameter), the resulting thickness can be tuned.
After application to the substrate, the solvent of the resist is evaporated by heating above its evaporation temperature. Depending on the chosen resist this so called baking can also change the sensitivity

[2] Physikalisches Institut, Wolfgang-Gaede-Str. 1, 76131 Karlsruhe, Germany
[3] Center for Functional Nanostructures, Wolfgang-Gaede-Str. 1a, 76131 Karlsruhe, Germany
[4] Institute of Nanotechnology, Hermann-von-Helmholtz-Platz 1, 76344 Eggenstein-Leopoldshafen

towards later exposure, i.e. the amount of incident radiation necessary to sufficiently alter the resist. It is necessary to avoid surpassing the decomposition temperature of the resist where irreversible chemical changes deprive the resist of its functionality. If another layer of resist is supposed to be spincoated on top of the first one it is highly advisable to check their compatibility, e.g. making sure that the later applied resist does not dissolve the previous one or react chemically in undesired fashion. Additional resist layers may be necessary when either a high thickness is required, as might be necessary for etching processes where the resist can be attacked as well, thick metal film deposition, or when a specific resist profile like an undercut structure (figure 3.3) is desired. The latter leads to spatially separated resist and metal film resulting in a facilitated lift-off (as described in section 3.2.2 and shown in figure 3.3).

The exposure of the device, i.e. the process that manipulates the resist, was either performed by NSL-employees in the form of electron beam lithography[5] or by ourselves as photo lithography using a Hg-Xe gas lamp [6]. In the first case an electron beam with acceleration voltages of 50 kV scanned the sample and locally altered the resist. In our case, for e-beam lithography, PMMA (poly[methyl metacrylate]) was used primarily where the incident electron beam causes a breaking of chemical bonds between monomers in the polymer effectively reducing the polymer chain length. The typical quantity used to describe the deposited energy is the so called dose given in units of $\mu C/cm^2$. It is intuitively clear that the dose needs to be large enough to alter the resist strong enough as it otherwise will not be removed in the following development step. On the higher end of the dose spectrum things depend more on the specific resist as some are not too sensitive on large doses while others, like PMMA, tend to form crosslinks that make it insensitive to typical development [155, 156].

During the development step, the resist is submerged in a solvent that only dissolves the chemically changed parts of the resist but leaves the non-exposed parts unaffected or vice versa. In reality, the chosen solvent, the developer, will also attack the remaining resist. It is therefore necessary to adjust the development time to make sure that everything that is supposed to be removed is removed, but the remaining structures are only weakly affected. Appropriate choice of developer, temperature, development time and technique, i.e. a reproducible way of applying the developer to the resist, greatly improves the result and reproducibility. If only the exposed part is removed, the process is called positive lithography and if only the exposed part remains it is called negative lithography. Since some of the incident photons and electrons during the exposure are scattered and absorbed upon hitting the resist, the development typically does not lead to vertical walls but a certain inclination outlining the scattering cone, beam shape and absorption profile can be observed [157]. This effect can be enhanced by stacking different layers of resist that are unequally sensitive to the exposure and development process as described before. Once this mask for the following structure was prepared we continued with a metal evaporation or etching step to shape the device in the form of the desired structure. It should be noted that in order to positionally match different lithography steps some alignment procedure is required. Our procedure revolved around evaporating specific marker structures during the first lithography step and then realigning the to be written structures with respect to these markers.

[5] used machine: JEOL JBX-5500, scanning electron microscope

[6] used machine: SÜSS Manual Mask Aligner, MA6 Rev03

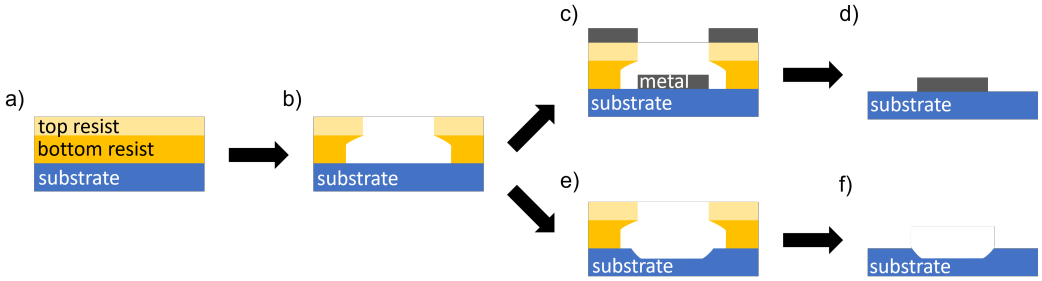

Figure 3.3: **Scheme of a lithography using a double-layer of resist.** Two layers of different resists are coated onto a substrate **a)** and exposed and developed **b)**. Then either a metal thin film is evaporated **c)** and the remaining resist plus undesired metal removed **d)** or parts of the substrate are etched **e)** and the resist removed afterwards **f)**.

Design-wise, as mentioned, we either used crosses or rectangles arranged in the working principle of a vernier caliper giving us a typical accuracy of less than 1 µm for optical lithography and ≤ 100 nm for e-beam lithography.

3.2.2 Metal-evaporation and thin-film growth

In this section some of the principles behind thin film growth and metal deposition will be discussed since they made up a large part of our fabrication process and were responsible for many of the problems we encountered. There are several ways of getting a metal film onto a substrate such as electroplating, electron-beam or Focused-ion-beam-assisted deposition (e.g. for platinum [158]), atomic layer deposition (e.g. for aluminium [159]), magnetron sputtering and thermal evaporation of which only the latter two will be discussed here. Both techniques, however, are working in a different pressure regime inside the vacuum chamber that changes their preferred application area.
The pressure during a sputtering process is typically in the order of 1×10^{-3} mbar due to the necessary ionised atoms that are accelerated onto the target and eject atoms from the target material, which then travel to the substrate where they are deposited. In order to determine the rate with which material is deposited, typically an oscillating quartz crystal is put in proximity to the substrate. If metal is deposited onto the oscillating quartz its resonance frequency is decreasing due to the additional mass. If the density is known, the thickness can be calculated. Since the deposition rate at the quartz is not necessarily exactly the same as on the substrate, a tooling factor is set that compensates for the differing rates. Due to the comparably high pressure the mean free path is only in the order of tens of centimetres so a non negligible amount of atoms will scatter and not reach the surface vertically. While this is no problem if the full surface of the substrate is to be covered, it can cause issues if there is a resist mask on top of the substrate and part of the target material is deposited on the sidewalls of the resist stack. In this case the resist can be encapsulated in the metal film making it harder to remove and additional metal may remain on the structures in the form of fences (Fig. 3.4). A metal fence is a thin wall of metal attached to the edges of the top of the written structure and can be as high as the resist stack. These fences can be detrimental when trying to connect another structure onto this one,

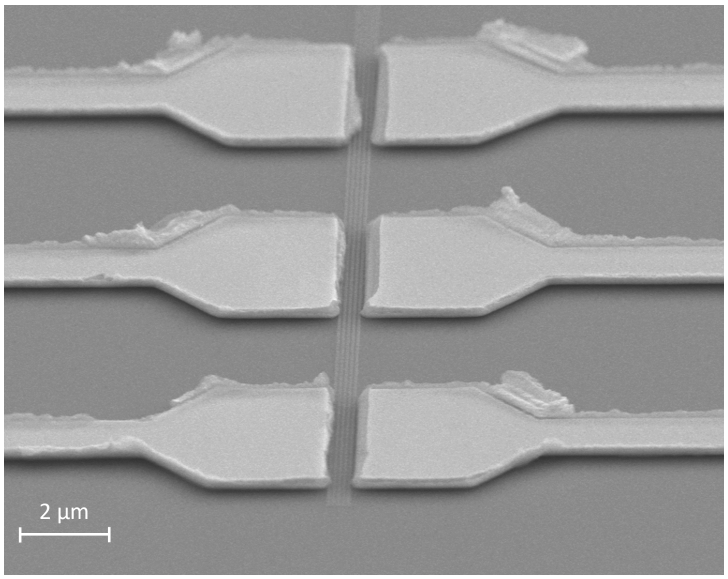

Figure 3.4: **Scanning electron micrograph of nanofabricated local gates and contact electrodes.** The contact electrodes show clear and high fences, most likely due to material evaporated on the sidewalls of the resist connected to the structure.

since the local resist stack can be strongly affected, the overlap reduced or it can even act as a shadow mask in the case of an evaporation under an inclined angle with respect to the surface normal. For the stamping technique (see section 3.3.4) to transfer nanotubes onto a fully fabricated chip these fences also locally alter the interface conditions possibly changing the quality and behaviour, for the better or the worse, of the CNT-metal contact.

The technique we used for all metal structures shown in this thesis is thermal evaporation. For this, the desired material is heated up to a temperature where the vapour pressure is high enough that atoms are evaporated into the gas phase and travel through the vacuum chamber. Typical chamber pressures in such an evaporation procedure are in the order of 1×10^{-7} mbar or lower. The mean free path in this pressure range is in the order of a few hundred metres or higher and atoms traverse the chamber mostly without scattering since the distance between target and substrate is about 30-40 cm. As described before, the deposition rate is measured with an oscillating quartz in proximity to the sample.

In contrast to the sputtering technique where the ejection of atoms into the gas phase is created by collision cascade, the ejection via thermal energy can lead to problems. It is obvious that different materials with different melting points will have different vapour pressures at the same temperature. As a result, in some compounds such as alloys, the components will not necessarily deposit with the same rate as the vapour pressure at the target is the sum of the partial pressures of the components [160] limiting the range of materials for which thermal evaporation is applicable. Also, high melting points materials are trickier to handle since a crucible material is necessary that can sustain the required high temperatures without melting or breaking. Alloy formation can lead to problems as well, e.g. when evaporating niobium in a tungsten crucible. Thermal radiation can also have detrimental effects

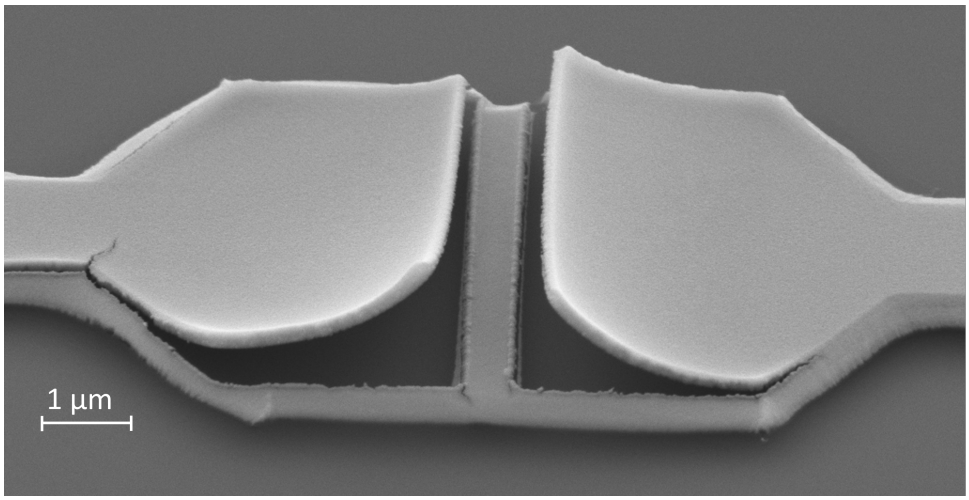

Figure 3.5: **SEM-image of an evaporated metal film after a lift-off process.** Internal stresses were strong enough to rip parts of the film from the substrate making it curl. The effect was the strongest at the widest parts of the structures.

both on the chamber pressure (e.g. degassing of surfaces) as well as the resist. Since the resist can be damaged by deposited energy due to heat radiation as well, a trade-off between evaporation time, incoming heat flux and cooling power is required. The evaporation rate increases exponentially with temperature while the radiative heat increases with T^4. Higher evaporation rate, means a shorter evaporation time and thus shorter heat exposure at a higher heating rate, shifting the equilibrium temperature to a higher value which is not necessarily reached during the evaporation process. Ideal parameters are thus very dependent on setup and application

Since an evaporation growth process cannot lead to a perfect film and the heating during the evaporation causes thermal expansion/contraction when removing the sample afterwards, residual stress is unavoidable. This stress can be significant reaching several hundred MPa or more [161]. As a consequence an adhesive layer in between substrate and desired metal film may be necessary to make sure that the metal film remains in place. Otherwise, if for example the thermal expansion coefficients do not match, the metal film might curl, ruining the circuit (Fig. 3.5). One peculiar example of a tricky evaporation was the evaporation of the contacting electrodes for the top-growth process.

Evaporation of contact electrodes using molybdenum

The most obvious requirements for this step in the fabrication are a rather large film height of about 150 nm or more as well as temperature resilient materials that also need to form a low-ohmic contact to CNTs. In the past, platinum has proven to be a well suited material for this purpose [26, 162]. However, when fabricating thick platinum films at room temperature, we ran into problems of films peeling off (figure 3.5) due to large strain most likely due to the strong mismatch of thermal expansion coefficients ($\alpha_{\mathrm{Pt}} \approx 10^{-5}\,\mathrm{K}^{-1}$ [163], $\alpha_{\mathrm{SiO_2}} \approx 0.55 \cdot 10^{-6}\,\mathrm{K}^{-1}$ [164], $\alpha_{\mathrm{Si}} \approx 2.6 \cdot 10^{-6}\,\mathrm{K}^{-1}$ [165]), especially at the metal/oxide interface. We could reduce this problem with the choice of a proper adhesive layer of

titanium that is forming chemical bonds with the oxide and provides a good interface for the metal and using an intermediate layer of molybdenum. Molybdenum offers the advantage of being thermally and chemically resilient and provides an intermediate thermal expansion coefficient ($\alpha_{\mathrm{Mo}} \approx 5 \cdot 10^{-6}\,\mathrm{K}^{-1}$ [166] while still being a good thermal and electric conductor. However, the high melting point and low vapour pressure also complicate the thermal evaporation of molybdenum.

As described previously, thermal evaporation of metals offers a heating trade-off and molybdenum

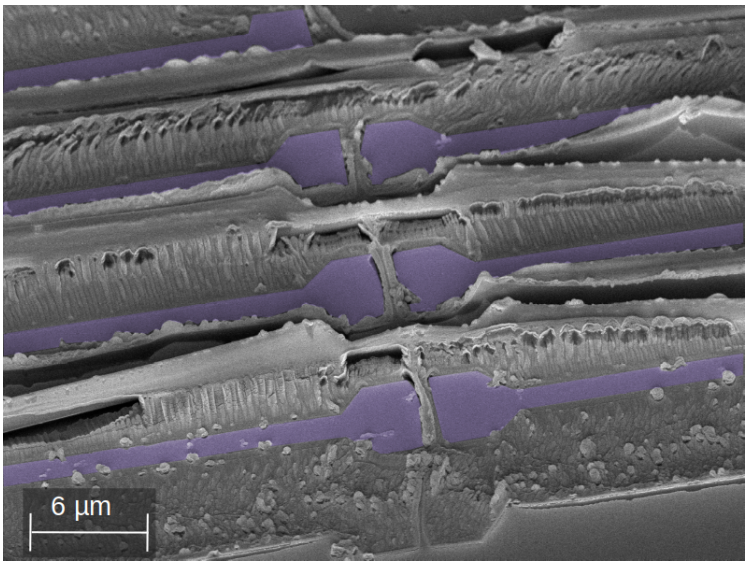

Figure 3.6: **Scanning electron micrograph of the contact electrode lithography before the lift-off.** The highlighted patterned structures are still easily identifiable despite the apparent merging with the surrounding resist due to the overheating in the evaporation chamber during molybdenum evaporation. Post lift-off the structures were electrically shorted and unusable.

evaporation induces a lot of heat in the sample making it easy to destroy the resist and therefore ruin the lithography (figure 3.6). We therefore developed a routine that reduces the heating of the sample by evaporating in steps of a few nanometers using a rather low rate of about $0.05\,\mathrm{nm\,s^{-1}}$ followed by a 90 s break with closed sample shutter protecting the sample from the radiative heat. Additionally, the sample holder was cooled to −80 °C by circulating cryogenic N_2 gas. This way, the resist was less damaged and the lithography worked out nicely more often. Towards the end, we additionally cooled the walls of the evaporation chamber by filling liquid nitrogen into an installed tank. Cold chamber walls decrease the pressure due to reduced degassing and potentially cryo-pumping. Additionally, cold walls make a radiative cooling of the sample more efficient thereby decreasing the heatload on the sample which benefits the resist as well. Taking all factors into account, we mostly used a metal stack of 5 nm Ti, 70 nm Mo and 70 nm Pt as a trade-off of evaporation time, stability, resistivity and cost.

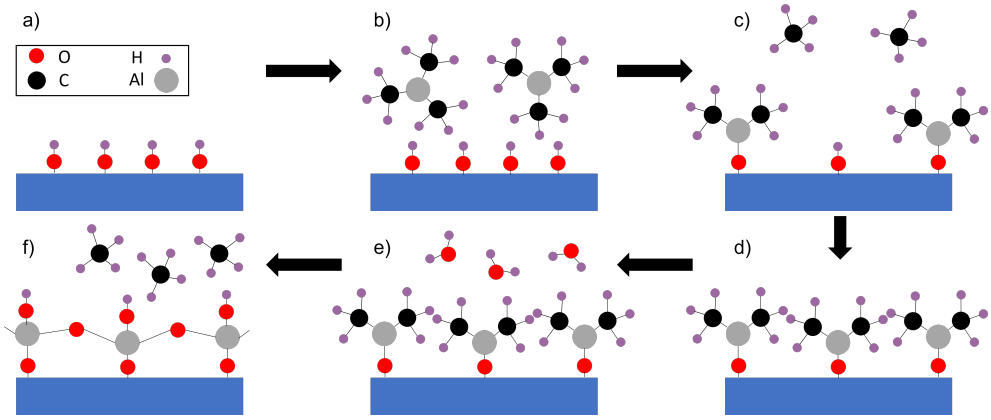

Figure 3.7: **Simplified scheme of an ALD process for the formation of Al_2O_3 thin films shown in a two dimensionsal cross-section.** **a)** Upon entering the process chamber, the surface sample is saturated by hydroxyl groups. **b)** When TMA is introduced to the chamber it **c)** reacts with the hydroxyl groups under methane formation **d)** covering the surface with DMA. **e)** The chamber is now filled with H_2O **f)** replacing the methyl groups attached to the central aluminium atom with hydroxyl groups under methane formation. This way, the surface is again terminated with hydroxyl groups and the cycle can start again.

3.2.3 Atomic layer deposition

In this deposition technique a thin film is deposited atomic layer for atomic layer using cycles of different precursor gases until the desired thickness is reached. We either used Al_2O_3 or HfO_2 as the insulating material of choice. Processes for creating Al_2O_3 have been more established in our lab and were thus used most of the time. However, we also fabricated a few samples with HfO_2 since the higher dielectric constant ($\kappa_{Al_2O_3} \approx 6-8$ [167], $\kappa_{HfO_2} \approx 18-20$ [168]) was attractive to us since it increases the capacitive coupling between local gate and CNT, even though fabrication issues for similar circuits on top of HfO_2 have been reported in the past [99]. In the following a process for Al_2O_3 is described exemplary. The surface of our chips was typically terminated by hydroxyl groups formed by residual water vapour in the air. The ALD process we used involved an oxygen plasma or ozone surface cleaning step followed by cycles of trimethylaluminium (TMA, $Al(CH_3)_3$) and water vapour (H_2O) at a temperature of 250 °C (see figure 3.7). In non-chemical terms, the hydrogen in the hydroxyl group is replaced by a Dimethylaluminium (DMA) under methane (CH_4) formation. Afterwards the chamber is flushed with an inert gas before H_2O is used as a reactive gas in the second step. In this step, hydroxyl groups replace methyl groups while forming methane rendering the surface termination as it was before the first step enabling a cycling of the steps. Generally for us, 10 steps resulted in thickness of ≈1 nm. To ensure that all local gate lines are completely covered with an oxide layer we chose thicknesses between 10 and 15 nm, matching or surpassing the local gate height.

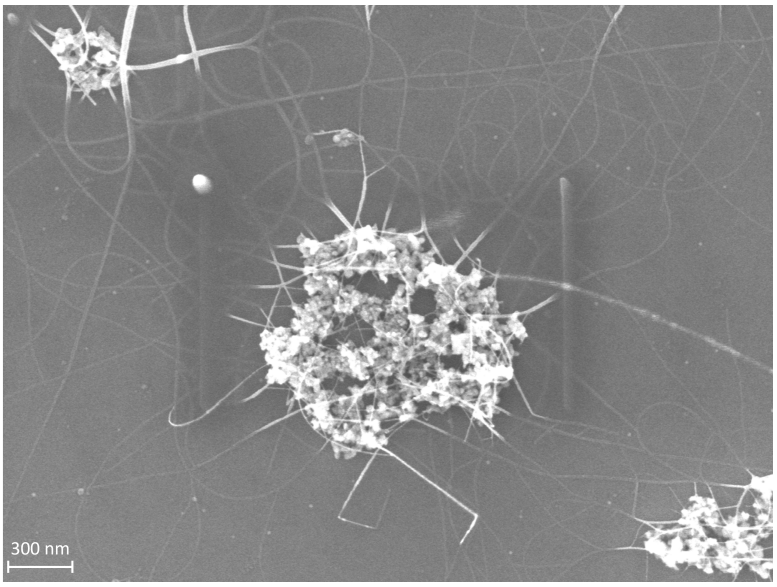

Figure 3.8: **SEM picture of clusters of catalyst nanoparticles on an SiO_2 surface.** Mainly visible are the matrix of Al_2O_3 forming clusters as well as many CNTs emerging from this cluster and forming a network. The exaggerated diameter of the CNTs is an artifact of the imaging technique (charging, hydrocarbon deposition).

3.3 Integrating carbon nanotubes into metal circuits

After discussing the fabrication of the metal circuit of the devices, the integration of the centrepiece of these circuits, the CNT, is the last step in the creation of the functional circuits. Within the frame of this thesis, two techniques, the so called top-growth and the stamping, have been used. In the following a comparison between the two techniques will be given, some (dis)advantages discussed and details on how we applied these techniques presented.

3.3.1 Carbon nanotube growth

The main feature of the top-growth procedure is described in the name itself, as in this technique the CNTs are grown directly on top, i.e. on the site where they are later used, of the metal circuit. Historically, different techniques for the creation of carbon nanotubes have been established such as laser ablation [169], plasma arc ablation [170] and the technique we used which is the chemical vapour deposition [22, 171, 172]. In this technique a catalyst is locally applied that serves as an activation centre where the carbon nanotube growth is taking place.

Catalyst preparation and deposition

For the top growth process the catalyst solution should only be applied locally on predefined positions on the circuit. Since the required alignment precision is about 1 µm and the feature size is in the same order of magnitude we chose to use e-beam lithography to be able to reliably pattern a resist in the shape and on the position we want it to be (figure 3.1e)). To facilitate the lift-off we used a double-layer

of PMMA to achieve a thick resist film spatially separating the nanoparticles on top of the resist and the substrate surface. Our standard lift-off recipes for metal evaporation typically involve ultrasonication which greatly helps getting rid of metal leftovers loosely attached to the circuit and can thus not be applied for this step as otherwise the nanoparticles will move on the surface or be removed since they are also only loosely attached at this point. Thus, we used a series of beakers (3 times acetone, 1 time isopropanol) to remove the resist. In the first two beakers the sample is submerged into acetone for 5 seconds while constantly stirring to remove the uppermost parts of the resist and get rid of nanoparticles attached to it. To further reduce redeposition, the sample can be held upside down to have the help of gravity. In the third beaker the sample is stirred for 6 minutes before being cleaned in IPA and dried by an N_2-gun to remove the solvent. Using this technique there is typically very little catalyst outside of the pre-defined windows.
The last step before the actual growth itself consists of a surface cleaning of the circuit and catalyst since there are always some organic residues after using any lithography technique. Therefore, we applied an oxygen plasma to the sample in a plasma asher[7] to burn away any organic residues on the surface. The isotropic plasma in the chamber offers the advantage of mainly chemical etching processes and only very little physical etching so the structures are barely damaged by this. In the past, this plasma cleaning and activation of the resist has shown to improve the activity of the deposited catalyst [172, 173].

Chemical vapour deposition

Generally, chemical vapour deposition (CVD) is a process to deposit thin films or create small quantities of a specific material on top of a substrate. It involves precursor gases that decompose in the vicinity of the substrate or chemically react with it forming the desired compound. Since there can be volatile side-products and a continuous feed of fresh precursor gas can be beneficial by replenishing the feed stock this process is often performed in a chamber with a continuous gas flow. The temperature in the process chamber is a crucial parameter as it greatly influences chemical reactions and dissociation of precursor gases.
The process we use for the formation of CNTs involved the precursor gases H_2 and CH_4 and temperatures inside the reaction chamber of 750-900 °C. Our reaction chamber consists of a 2.5 cm diameter quartzglass tube with a scroll pump on one end and three mass-flow controllers (for H_2, CH_4, and Ar) on the other end. A section of about 30 cm of the tube is placed in a hinged oven with a heating zone of about 15 cm which we use to create the required temperatures (see figure 3.9). The samples are located on a quartz crystal arm we can move along the tube axis to move the samples into and out of the oven at any point in time. The catalytic growth process can be described following the vapour-liquid-solid model (VLS). When the process gases reach the interior of the oven, the high temperature combined with the catalyst particles at the surface lead to a decomposition of CH_4 into hydrogen and carbon radicals. While the unsupported decomposition of methane needs temperatures above 1200 °C, the usage of catalyst lowers it into an accessible range [174]. At these elevated temperatures, the surface of the nanoparticles is molten and the carbon radicals can diffuse into it while the hydrogen exits the

[7] Niederdruckplasmaanlage; Type: Nano, Diener electronic GmbH +Co. KG

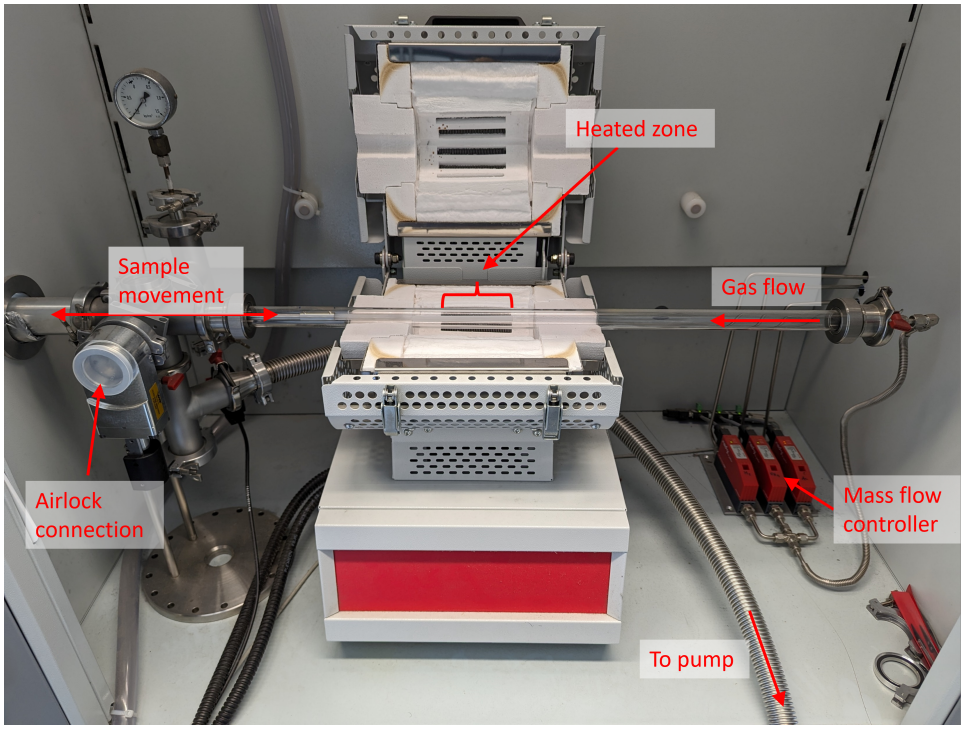

Figure 3.9: **Photograph of the hinged oven used for the CVD-process to grow CNTs.** The gas flow is regulated by mass-flow controllers on the right side, attached to the left side is a pump. On the cross on the left side of the pictures samples can be loaded from the top and unloaded via an attachable airlock. A movable arm made of quartz (barely visible) allows the movement of the samples in and out of the oven. For safety reasons, the heated oven with flammable gases is located inside a fume hood.

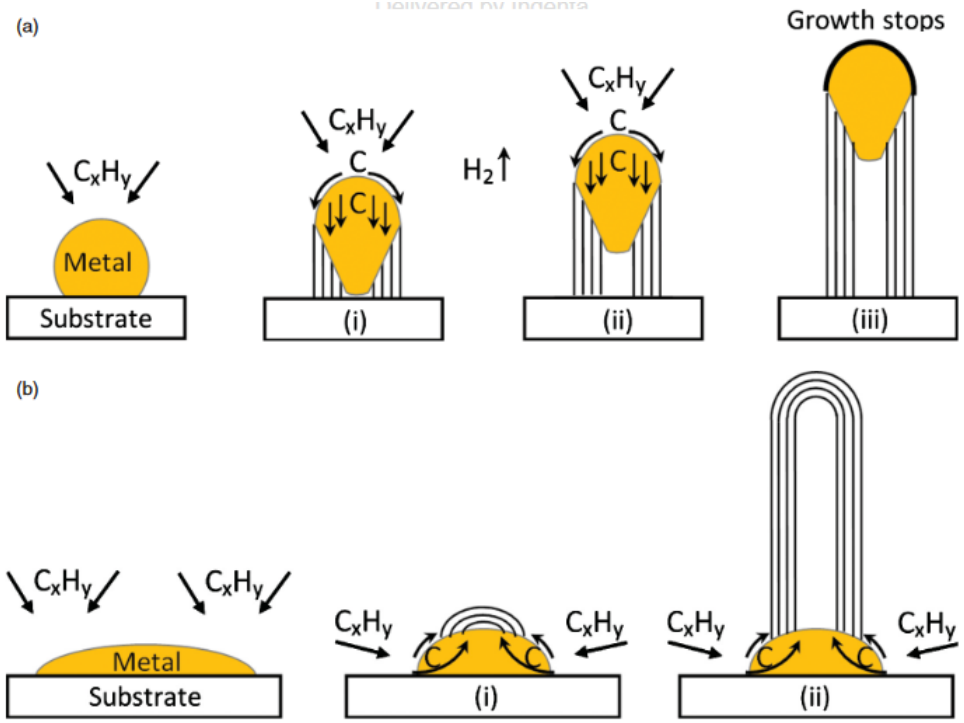

Figure 3.10: **Scheme for the two widely accepted growth modes for carbon nanotubes in a CVD process, taken from [22]. a)** tip-growth model where the catalyst nanoparticle is lifted and hovering while the nanotube grows at the top moving the nanoparticle with it. **b)** base-growth model where the catalyst nanoparticle remains on the substrate and the carbon nanotube is being pushed out of the catalyst.

furnace with the gas flow. When the carbon solubility limit is reached, parts of the carbon start to crystallise on the surface of the nanoparticle. The exact process that is going on is still up for debate but two modes are generally accepted as depicted in figure 3.10. The description follows the arguments given in [22]. In the tip-growth mode the interaction between catalyst and surface is weak and the carbon crystallises on the sides of the nanoparticle. Fresh carbon enters from the top and diffuses to the sides where it crystallises and pushes the nanoparticle upwards, away from the substrate. The crystallisation happens without dangling bonds and is energetically stable. The growth process is terminated when the carbon gradient in the particle vanishes, which can happen if a carbon cap is screening the nanoparticle. In an alternative growth mode, the substrate-catalyst interaction is strong and the nanoparticle remains on the surface. In this case, carbon enters the catalyst on the sides and bottom and diffuses towards the upper centre. The crystallisation occurs on the upper central areas and starts by forming a hemisphere which is subsequently pushed out of the nanoparticle. In analogy to the previous mode, growth is terminated when a carbon cap screens the catalyst particle, or when the tube can not be pushed out further meaning no crystallisation occurs and the carbon gradient breaks down.

By adjusting different parameters of CNT growth, such as temperature, gas flow, precursor gases, cata-

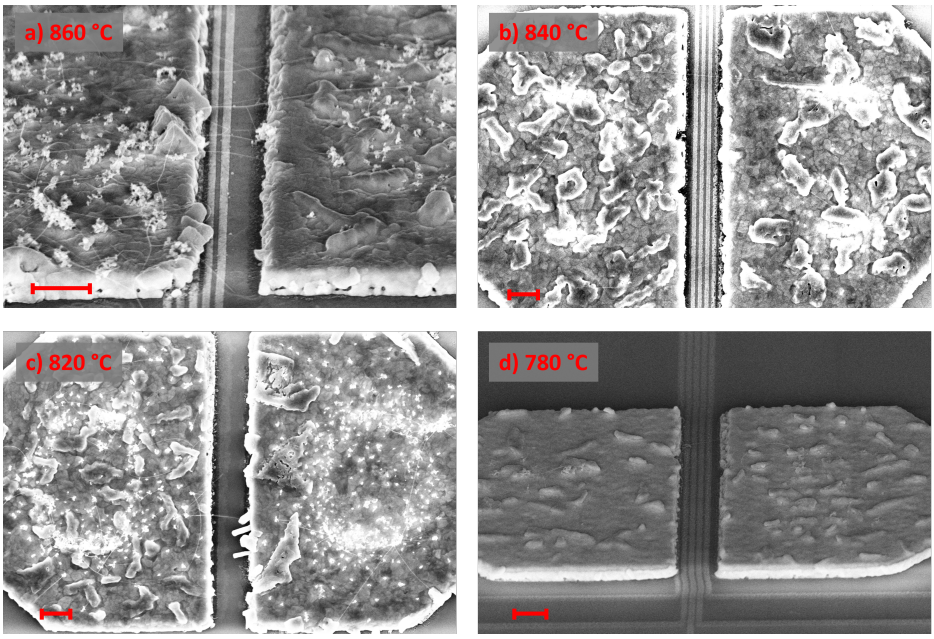

Figure 3.11: **Comparison of scanning electron microscopy (SEM) micrographs for the same metal stack but different CVD-temperatures. a)** and **d)** offer a tilted view, **b)** and **c)** show a top down view. All images were taken on individual pieces of a single chip that have seen different CVD growth temperatures. A clear trend to a less deformed surface and less CNTs is visible with decreasing temperature.

lyst material and size etc. the results obtained from CNT growth can be tuned to fit the requirements the best.

3.3.2 Top-growth procedure

As aforementioned, the strongest concern for us when it comes to growing CNTs directly on the metal circuit were the high temperatures involved in the CVD-process that could negatively affect our samples. A comparison of the metal film surface for different growth temperatures can be seen in figure 3.11. Unsurprisingly the film is stronger affected, when the temperature during the growth process is higher. The surface before each growth was smooth but appeared wavy with a significant amplitude after the growth for some devices. For other materials parts of the material film were ejected at high growth temperature while the film stayed intact for lower temperatures. Even though this might not necessarily be detrimental for the CNT-metal contact quality, as higher temperatures can lead to metal-carbide formations that show low-resistance [51], the reproducibility and cleanliness of the samples suffers. In addition, the density, i.e. the number of nanotubes connecting source and drain electrodes, was too high at these temperatures and we frequently saw two or more CNTs per junction in SEM imaging (fig. 3.11a)). Compared to previous work [68, 99] on similar devices it is apparent that we had a higher yield when using similar parameters and had to reduce the number of CNTs per junction. The logical consequence to both issues for us was to reduce the heatload the

sample is exposed to. In order to do so, we first reduced the growth temperature and in addition tested the impact of using a "hot-load" and "fast-cooldown" procedure. For the hot-load procedure we kept the sample outside of the heated zone of the oven until the oven was hot. Only then the sample was moved into the heated zone and the gas flow set for the growth conditions, thus reducing the time it is exposed to heat. Once the growth process was finished, after 15 minutes in our case, we immediately removed the sample from the heated zone again resulting in a fast cooldown of the sample which further reduced the overall heatload.

The second major disadvantage of the top-growth process is the non-deterministic nature of the CNT integration. While it is comparably easy to achieve low-ohmic resistance between CNT and metal since no additional post-treatment is required to achieve a resistance of 50 kΩ or less, the complexity of the circuits is strongly limited. It is easy to imagine that circuits containing more than one functional CNT component are even harder to build as the likelihood of a successful growth (i.e. exactly one good CNT per junction) decreases exponentially with the number of devices. It is also necessary to protect other structures that are not supposed to be connected to a CNT from randomly growing CNTs or redeposited catalyst particles. Since even in our top-growth process CNTs could grow to significant lengths up to at least 30 µm on substrate, either big spatial separation or encapsulation in insulating materials is necessary. Because insulating materials almost always contain defects and two-level systems, the device performance, e.g. the lifetime of sensitive quantum states like qubits, can be negatively affected by this. The addition of an insulating layer also makes fabrication more complex as electrically contacting parts of the circuit is now more complicated.

Another part worth mentioning is that after the growth it is unclear what the growth yielded and the devices first need to be examined (cf. section 3.3.3). Thus, additional work is required where every individual junction needs to be tested in order to determine its quality and usability for experiments. Even though every individual junction is quick to precharacterise in terms of electronic transport properties, measuring hundreds is still time consuming. This characterisation is, for us, impossible to do in a clean environment without breaking the vacuum/inert gas atmosphere at some point after the growth resulting in unavoidable contamination of the devices.

While there are definitely some drawbacks to the top-growth techniques it also provides a few benefits. The biggest selling argument is that without additional effort, the contact resistance between CNT and metal is reliably quite low which, until recently, was not the case for other techniques like the stamping technique [57] discussed in section 3.3.4. This opens a broad range of experiments and physics [19, 26, 97, 175–177] as was shown in the past and in measurements shown in chapter 5.3.

Since the CNT growth is the last step in the nanofabrication it was considered to be "ultra-clean" [19, 178] in the past. By now a competing, reliable fabrication approach is established, our stamping approach, but the absence of additional fabrication steps afterwards, especially of lithographies, still greatly increases the cleanliness compared to top-down fabricated devices.

As the requirements on circuit geometry are not too strong and space consuming, it is easy to mass fabricate devices of this kind thereby compensating the non-deterministic nature of the process. If it is possible to fabricate hundreds of devices simultaneously even a yield rate of 5-10 % provides enough devices for plenty of measurements. As a consequence the throughput of devices can be made

quite large, so the time until a CNT-device with the desired properties after cooldown to cryogenic temperatures can potentially be found faster than for other techniques where every device needs to be designed by hand or requires lengthy treatment.

3.3.3 Room-temperature characterisation of top-growth devices

After fabricating top-growth devices for our desired experiments using the various techniques of nanofabrication as just described, we first have to pre-sort them at ambient temperatures before cooling them down in a mK-cryostat. This is quite apparent upon taking the statistical nature into account, where many of the devices are either not connected at all or possess more than a single CNT bridging the source and drain contacts. Cooling down a single chiplet with 48 devices would require 132 dc-lines (60 gates + 72 Source/Drain) inside the cryostat as well as an extremely complex and challenging microbonding pattern. Even when splitting this into reasonable numbers such as six devices per cooldown, this approach is very inefficient in terms of time and money. Therefore, we characterise the possible Source/Drain pairs in vacuum inside a probe station with the possibility to cool down to 4 K.

A photograph of the probestation we use is shown in figure 3.12. Here, four movable arms with triaxial connectors and rf-fitted needles made of tungsten or copper-beryllium attached to them enable the characterisation of individual Source/Drain pairs on the chip. The probing needles are located inside a vacuum chamber with a pumping unit consisting of a membrane pump and a turbomolecular pump able to reach pressures in the 10^{-5} mbar range.

To characterise a potential CNT connecting source and drain, the possibly most important parameter is the electric resistance. Since the resistance of the leads is negligible compared to the intrinsic resistance of the CNT plus the contact resistances at the CNT-metal interfaces, the measured resistance can be directly attributed to the latter contributions. Because a single carbon nanotube possesses four conduction channels, the maximum conductivity G is given by $G = 2G_0$ (two valley channels, G_0 takes two spin-states into account), where G_0 is the quantum of conductance defined as $G_0 = 2e^2/h$ =77.5 µS and is therefore $G = 2G_0$ =145 µS or a minimum resistance of 6.9 kΩ. This means that every resistance with a lower value than $\frac{1}{2G_0}$ can not be caused only by a single CNT but rather by either a bundle of CNTs or some on chip contamination like metallic dust and flakes, catalyst particles etc. At the same time, sections that show a high resistance of $R \geq$200 kΩ can be excluded as well, since this means that the coupling to the metallic leads is rather bad which limits the spectrum of performable experiments at cryogenic temperatures, since the resistance of these badly connected devices also more often diverges towards low temperatures [99].

If the resistance (or conductance) was neither too high nor too low , i.e. in the range between 15-100 kΩ, we measured the gate-dependence of the conductance using one of the five local gates. From the gate dependence we can infer even more properties of the device under test. Our procedure involved performing a lock-in measurement at a rather low frequency of about 91 Hz (we always tried to avoid multiples of 50 Hz and other commonly used frequencies) at 0 V applied dc-bias voltage V_{sd} and sweeping the applied gate voltage V_{g} in a range of a few volts symmetrically around 0 V. Figure 3.13 shows a compilation of gate dependences measured for different devices.

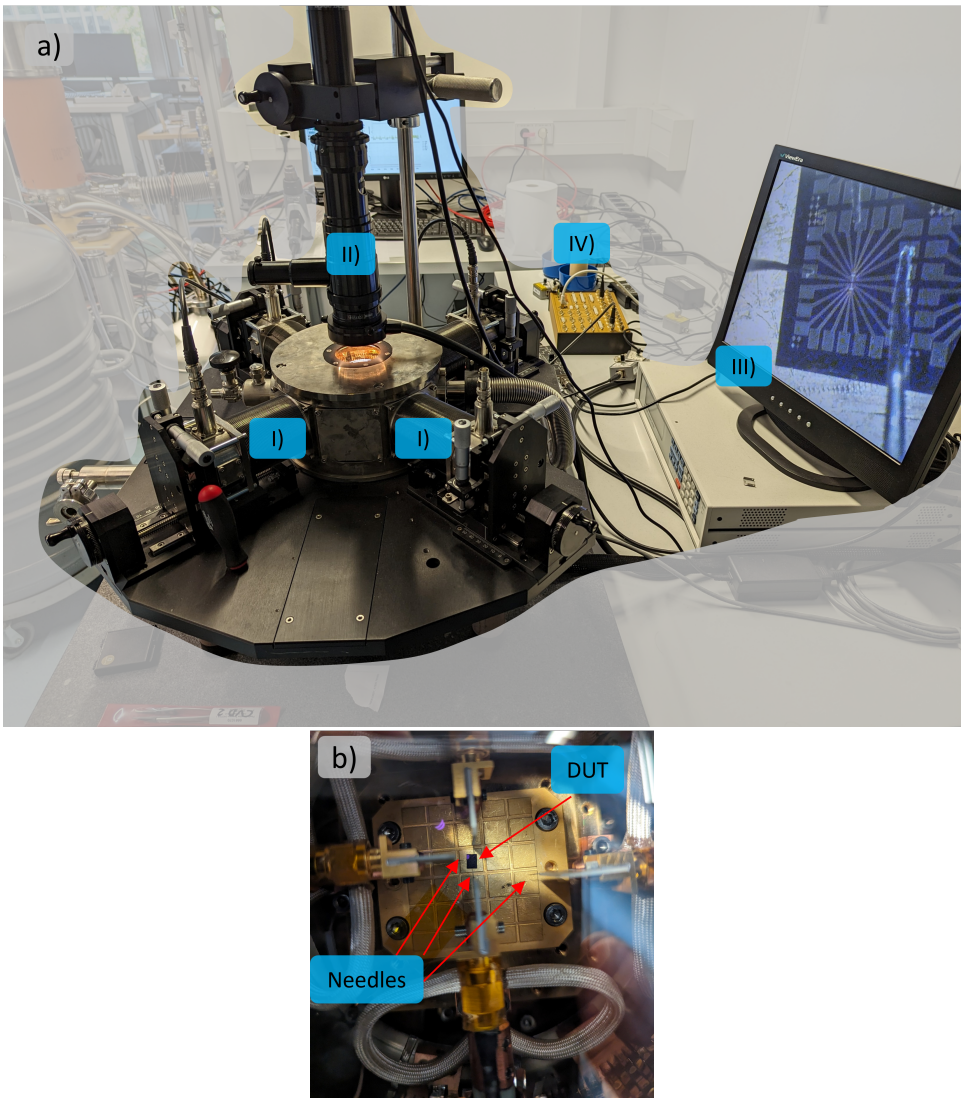

Figure 3.12: **Photographs of the probestation used for room temperature characterisation of the top-growth devices. a)** shows a full overview of the setup including the four movable needles (I), the camera (II) and screen(III) as well as our real-time measurement setup (IV). In **b)** a top-down photography of the samples and the four needles is shown. Navigation on the millimetre scale by eye is possible, for small movements the camera with tunable magnification and focus are needed.

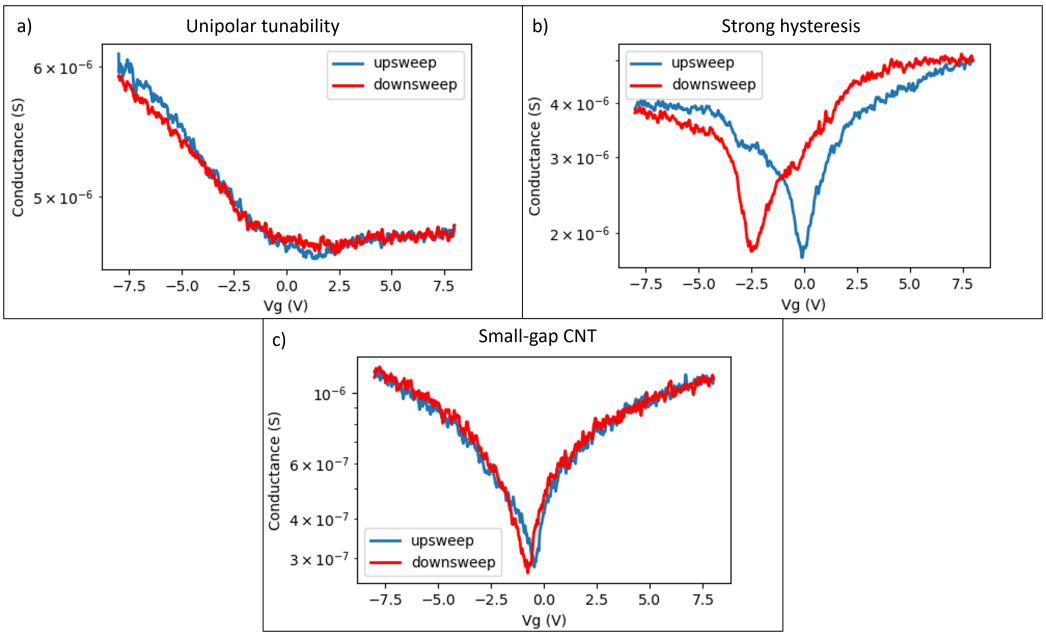

Figure 3.13: **Compilation of the gate-voltage ("Vg") dependent conductance for three different CNTs. a)** p-doped behaviour with larger conductance on the hole side G_{h^+} than on the electron side G_{e^-}. **b)** strong observable hysteresis between up- and downsweep of the gate voltage which indicates contamination. **c)** small bandgap CNT showing an ambipolar "v-shaped" gate-voltage dependence as well as little hysteresis.

An ideal, pure CNT shows ambipolar conduction behaviour [179] which is expressed in a symmetric behaviour for positive and negative gate-voltages. However, for real devices often a unipolar p-type conduction behaviour is measured (fig.3.13a)). This behaviour of a "polar" tube has been attributed to H_2O/O-redox couples that can lead to a strong suppression of the n-branch of conduction [179, 180] for non-suspended CNTs. Since the pure sp^2-hybridised surface of the CNTs is hydrophobic similar to graphene [181], clean and suspended CNTs should not express a unipolar behaviour but rather keep their intrinsic ambipolar conduction. Very generally, various adsorbates can influence the π-electrons responsible for electric conduction along the CNT axis and therefore polarise the conductance. Thus, devices that show a strong polarity at room temperature are not used for later experiments.
While no change of conductance with an applied gate voltage may also be considered to be ambipolar, devices that show no gate dependence were also ruled out since their origin can not be determined. This can occur, if the CNT is a metallic nanotube (i.e. $n = m$ in terms of CNT indices) with zero gap, if the gate electrode is not functional due to an interruption or if the device under test is not a CNT but rather something else like a metal flake.
Another indication of cleanliness can be accessed by measuring a trace and retrace of the gate-voltage dependence. Ideally, trace and retrace show the same behaviour and no hysteresis occurs. Due to adsorbates and dielectrics in the proximity of the CNT it is however possible to obtain hysteresis between upwards and downwards sweeps of the gate voltage as a result of charging effects. Close-by dielectrics that could cause a charge transfer from the CNT to the dielectric can be neglected for

suspended CNTs but hysteresis may still be explained with adsorbates that may polarise as well and screen parts of the applied field imhomogeneously from the CNT. Since we want the CNTs to be as clean as possible, for both electric and mechanical properties, CNTs that show a large hysteresis (fig. 3.13b)) are neglected.
If a device shows a symmetric and non-hysteretic "v-shape" behaviour with a dip in conductance (fig.3.13c)) that is sufficiently large we consider this a well connected and clean single CNT with a small bandgap which is what we are aiming for. If the gate-dependence expresses a "W-shaped" gate-dependence, i.e. two dips in conductance, a single CNT is not sufficient to explain the dependence and we assume to have at least two CNTs in the same junction. These devices are ruled out as well, since two tubes in parallel will result in much more complicated behaviour and interpretation of data for measurements at low temperatures.

3.3.4 The stamping technique

In contrast to the top-growth technique, when using the stamping technique the metal circuit is never exposed to the CNT growth conditions. As mentioned before, this increases the flexibility in terms of material choice, since no harmful effect of the CVD process is to be expected. However, the CNTs still need to be created and for this technique they are grown on a separate chip. This silicon-chip with a 3x4 mm^2 footprint is fabricated by *micromotive Mikrotechnik*[8] using a patented fabrication recipe and has an elevated flat part that ends in an array of cantilevers. Each cantilever has a length of 500 µm and a width of 30 µm. The spacing between individual cantilevers is 30 µm as well. The catalyst solution application onto this chip happens globally, so there are no lithographically defined areas, which simplifies the process since no lift-off is required. The application technique itself does not vary when compared to the top-growth. The growth parameters for this technique can be tuned more flexibly since there is no damage to functional structures to be expected. Thus, high temperatures are not an issue of their own. The parameter that qualifies growth conditions to be good or bad is the number of, ideally single-wall, CNTs close to the tip of the cantilevers that connect two neighbouring cantilevers in an approximately straight line. If there is another CNT in close proximity to the one that is supposed to be transferred it can become challenging to avoid transferring this one as well and creating a parallel circuit of CNTs. An overview image composition of a cantilever chip after CVD-growth is shown in figure 3.14
After the growth is finished and the cantilever chip is thermalised back to room temperature, it is transferred in a portable loadlock built by our mechanical workshop and transferred into a dedicated scanning electron microscope (SEM). The work of designing and assembling the vacuum transfer of the cantilever chip into the SEM and vacuum transfer of the finished sample from the SEM into our cryostat was performed by Dr. Tino Cubaynes[9]. Inside the SEM the cantilever chip can be manipulated by piezomotors with a precision down to ±10 nm. The five piezomotors used allow for movement in three spatial axes, and rotation by two angles: One angle that allows to lower the cantilevers with respect to the bulk of the chip and one angle rotating around the normal vector of the cantilever

[8] Micromotive GmbH, Carl Zeiss Str. 18-20,55129 Mainz
[9] Institute for Quantum Materials and Technologies, KIT, Karlsruhe, Germany

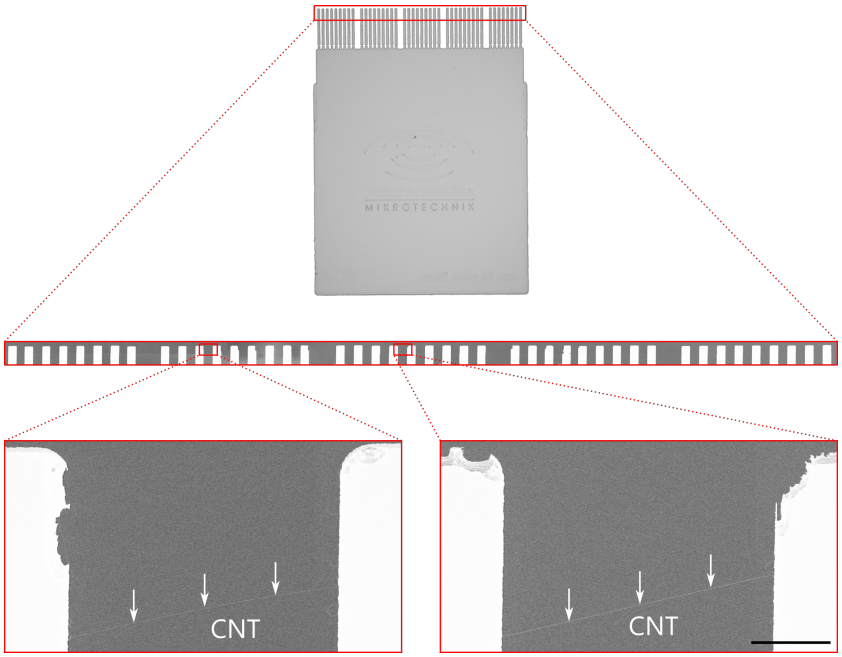

Figure 3.14: **Scanning electron microscope (SEM) image of a cantilever chip after the growth process.** Typically, only the topmost 50 µm are observed to spot the CNTs. The bottom inserts show CNTs suited for stamping and their respective position on the chip.

surface. The stack of piezomotors in the end allowed for a positioning accuracy of ±200 nm. Smaller values are feasible if a more sophisticated layout and approach are chosen.
The metal circuit chip is prepared by being glued to the sample-PCB (printed circuit board), microbonded and Ar-sputter cleaned using a Kaufman ion-gun before being transferred into the SEM. Inside the SEM the sample stage can be moved to the target position such that a transfer of the sample PCB from an attached loadlock is possible. Since it is possible to observe the sample inside the SEM using its given imaging features, potential shorts and disconnected lines can be detected by monitoring the contrast when applying a dc-voltage to the individual lines, since the static electric field affects the emitted secondary electrons that the SEM detects. If a bias of a few Volts does not lead to a change of contrast, typically a line is interrupted at some point.
For the actual stamping procedure itself where the CNT is placed on the metal circuit, the cantilevers are first aligned with the etched trenches of the chip so that they can be lowered into the created cavity. A photography of the inside of the SEM in the stamping configuration in the beginning of the approach of the cantilever chip towards the sample is presented in figure 3.15. While the cantilever chip is lowered onto the sample chip with a finite angle, a bias of a few Volts is applied between inner and outer electrodes to detect when the CNT is in contact with the electrodes. Once contact is established, a high current (often $\geq 10\,\mu A$) is driven between the outermost and second outermost electrode on each side such that the CNT is cut. A high current inside the CNT leads to a strong heating resulting in a cut [59, 182]. After the CNT is cut there is no longer a connection of the central sections with the electric circuit of interest to the cantilever chip which therefore can be safely retracted without the

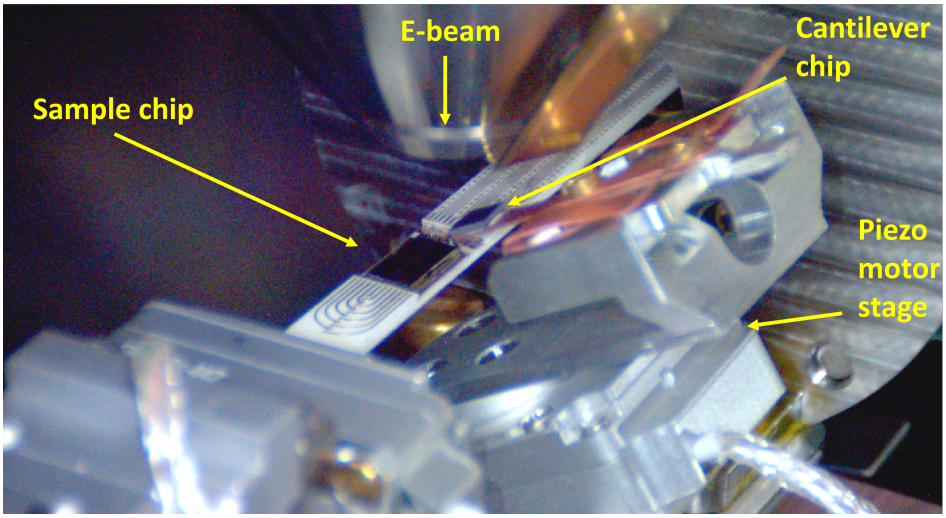

Figure 3.15: **Photography of the interior of the SEM in the Stamping configuration.** The five piezomotors enable a lateral movement in three dimensions and a rotation by two angles. Since the setup is located below the e-beam column imaging is possible simultaneously.

risk of removing the CNT again. At this point, the resistance between metal electrodes and CNT is still rather large and annealing methods that reduce it are required to increase the device quality.

Room-temperature preparation of stamping-devices

In this section the room-temperature treatment of CNT-devices created with the stamping technique will be presented. Here, the measures taken to ensure a high quality contact while maintaining a clean sample are introduced. The techniques presented can be found in more detail in [57].
Analogously to devices created with the top-growth procedure we aim for a low resistance, gate tunable single CNT that is suspended between two electrodes. However, the device resistance for stamped CNTs was mostly found to be in the order of 100 kΩ and more [59, 183, 184], while for devices created with a top-growth procedure or with electrodes evaporated onto the CNT much lower resistances could be observed [26, 162, 185]. At the same time, this high resistance also impedes superconductivity, as it is a coherent process that requires low barriers [185]. Therefore, it is intuitively clear that dirt and insulators which can lead to the formation of a barrier should be avoided as much as possible. As mentioned, we used palladium as the interface material due to its potentially low barrier to CNTs and because superconductivity in a CNT contacted by palladium (in a top-down process) has been shown in the past [24, 186]. However, palladium builds an oxygen rich layer at its surface in adsorption and oxidation processes at different timescales [187], which limits the quality of the contact. These processes are not an issue in a top-down fabrication as the contacting part of the palladium is buried and nicely envelops the CNT. In order to remove this contaminated layer we used a Kaufman-ion gun to sputter the uppermost 5-10 nm of the palladium using argon atoms. Starting from this point, the faster adsorption processes happen on the timescale of seconds and can hardly be avoided. We do the argon milling after microbonding the sample and the total air exposure time is in the order of few

minutes. Especially the oxidation of palladium takes hours [187]. For this purpose a special sample holder was built that avoids sputtering the aluminium bond wires which would be detrimental for the sample. This pre-treatment of the sample already led to a significant contact improvement (i.e. lowering) of the contact resistance [57].
The transferring procedure of the cantilever chip with the CNTs into the SEM has been described in 3.3.4 as well as the general procedure of transferring the CNT onto the chip inside the SEM. Once the CNT was transferred onto the sample-chip we apply a two-stage annealing process.
In the first stage, a high current in the range of a few μA is driven through the CNT. Since the CNT is resistive the current induces heating where the parts with the highest resistance are heated the most. Since this, in our case, is the non-improved contact to the metal electrode, the heating is the strongest in the proximity of this interface. Since a (too) high current through a CNT results in its destruction, typically a resistor of $\geq 100\,\mathrm{k\Omega}$ is put in series to the CNT to implement a threshold value for the current that supposedly does not cut a defect-free CNT upon reduction of the resistance. During this annealing abrupt current changes can be observed which might be explained by discrete events such as desorption of molecules or atomic rearrangement in the vicinity of the CNT-metal interface [57]. Besides decreasing the observed resistance, current annealing also led to a decrease of a plateau occurring in an *I-V*-curve at 0 V bias. This regime of reduced conductance can be explained by a potential barrier which could be caused by adsorbates between CNT and metal that may get removed during local heating. Since almost all measurements inside the cryostat and at mK-temperatures are performed at a bias voltage close to 0 V (as 1 meV corresponds to ≈11.6 K), ohmic behaviour for low bias voltages is highly desired.
In the second stage, a halogen lamp is used to globally heat the full sample-chip. Due to the manoeuvrability of the stage inside the SEM we are able to position the sample right below the halogen lamp with a distance of about 5 mm. During the parameter-testing phase we found that it is very much within reach to melt aluminium bonds connecting the sample PCB (Printed Circuit Board) to the sample chip, indicating that the temperatures reached surpassed the melting point of aluminium (≈ 670 °C). The parameters we used for the annealing later on involved a power that was only one third at maximum of the power used to melt the aluminium bond wires. Therefore, we expected the occurring temperatures to be well below 400 °C which is well below the melting point of all the metals used. Additionally, the used halogen lamp is shielded at every side but the one facing towards the sample to reduce the heating of the SEM chamber and the electron optics in particular. We split the actual radiative thermal annealing procedure into two parts with different power (≈ 5.5 W in step 1, ≈ 11 W in step 2) and applied each for 30-60 min. In contrast to the current annealing step, the conductance change was more continuous until reaching a plateau. We tested different metal stacks with the general principle of Ti-M-Pd (M = (Al, Nb, Mo, Ti, Pd)) and found that this annealing works better for metals with a lower thermal conductance and higher melting point (i.e. Nb and Mo). This could possibly be explained with the less efficient heat transfer away from the CNT-chip which might facilitate annealing effects at the CNT-metal interface.
The combination of the three presented techniques allowed us to reliably fabricate clean CNT-devices

with a rather low contact resistance down to ≈ 30 kΩ enabling us to explore a broader range of physical phenomena than previously accessible via the stamping approach.

3.4 Single-molecule magnet deposition

As the very last step of fabrication we want to functionalise the carbon nanotube by attaching a single-molecule magnet (SMM) to it. The obvious main criterion for this functionalisation is that both the SMM as well as the CNT-circuit need to be intact and maintain their properties. In the past, the deposition often has been done by dropcasting [99] a solution of single-molecule magnets dissolved in dichloromethane onto the chip with integrated carbon nanotubes. The sample was later rinsed in other solvents to remove weakly connected SMMs. This approach, however, inherently requires to eventually also remove the solvent again. If the solution simply would be blown away using nitrogen or evaporated by heating, the surface tension of the solution and occurring capillary forces will rip off the carbon nanotube or tear it apart [99]. Thus, a technique where no phase transition occurs has been used. For this so called 'supercritical point drying', the sample is placed in a temperature controllable pressure chamber and the solvent is replaced by liquid CO_2. Then the temperature is raised to bring the CO_2 into a supercritical phase followed by a transition into the vapour phase by reducing the pressure. This way the vapour-liquid phase transition is avoided and the CNT can sustain the drying process.
For our applications however, where we particularly care about the cleanliness of the devices, the supercritical point drying technique is a strong source of contamination that we want to avoid. In order to do so, we use thermal evaporation in a high vacuum chamber (photography and schematic in figure 3.16 with $p \approx 10^{-6}$ mbar) similarly to what has been used for STM and STS studies on film growth as well as structural and electrical properties [188–190] and to a previous attempt in our research group [173]. It was found that the previously introduced $TbPc_2$ tends to attach to the surface via van-der-Waals forces with the phthalocyanine planes parallel to the surface. If the film grows thicker, the angle between the phthalocyanine plane and the surface changes and approaches 90° indicating a strong surface influence [191]. Due to the for us desirable properties of $TbPc_2$ of a large anisotropy, an isolated spin and a potentially strong orbital overlap with a CNT due to the sp^2 hybridised surface we also decided to use $TbPc_2$ for our purposes. To perform the thermal evaporation of $TbPc_2$ without exposing our samples to air, we remodeled a pre-existing evaporation chamber that has been used for STM-sample preparation. A picture of the setup is shown in figure 3.16. The vacuum chamber is pumped by a mobile pump unit consisting of a dry scroll pump and a turbomolecular pump yielding a base pressure in the 10^{-7} mbar range. The pressure inside the chamber is determined by using a hot cathode vacuummeter measuring a pressure dependent ion current created by ionising atoms in the gas by electrons emitted from a cathode. We attached an additional airlock on one side of the evaporation chamber allowing us to perform a vacuum transfer of samples. We designed it to be compatible with the transfer arm used for the stamping technique (section 3.3.4) allowing for a clean and easy way to evaporate SMMs. The transfer arm can also host other sample PCBs allowing other group members to use this setup as well. The evaporation unit itself is placed with a 45° angle with respect to the

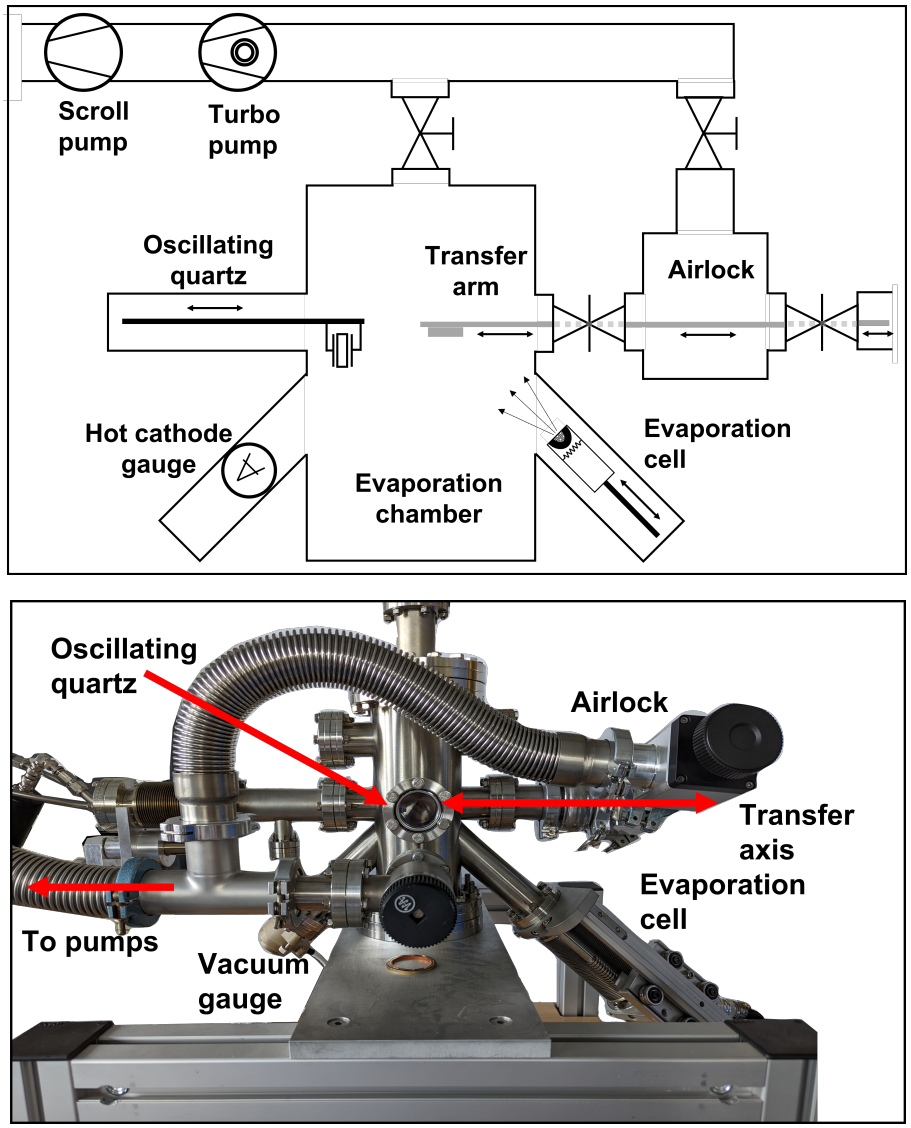

Figure 3.16: **Schematic and photography of the evaporation system used for the evaporation of single-molecule magnets.** The SMMs are sublimated from a powder stock in an evaporation cell with a 45° angle. The sample is located on the transfer arm that can be moved along the transfer axis. The evaporation rate can be calibrated by using an oscillating quartz which can be moved to the evaporation position. The pressure inside the chamber is monitored by a hot cathode gauge.

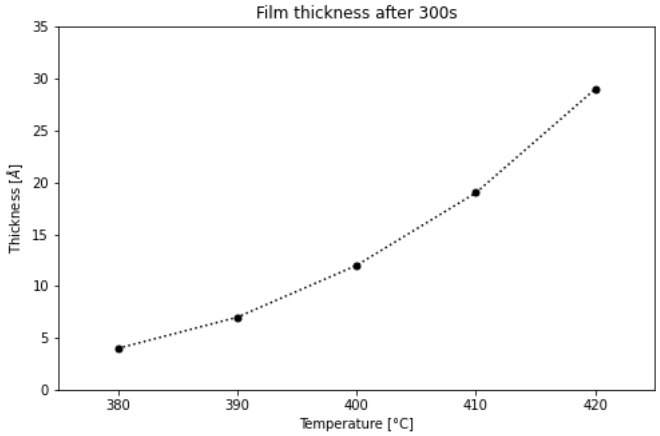

Figure 3.17: **Calibration of the $TbPc_2$ evaporation rate.** Plotted is the thickness measured with an oscillating quartz after 300 seconds of evaporation against the set temperature at the crucible after few minutes of thermalisation. The rate can be determined by dividing total thickness by the evaporation time.

sample manipulation axis. It contains three separate pockets that can be heated individually and is water cooled. A shutter is mounted on top of it to screen the chamber from the crucibles and vice versa. In a typical evaporation, while the sample is still outside of the chamber, a degassing step is performed at temperatures well below the sublimation point of the SMMs with an open shutter to avoid later contamination and pressure spikes. An oscillating quartz can be moved into the deposition position that will later be used for the sample in evaporation processes and thus allows a calibration of the evaporation rate for various temperatures. Since the desired amount of SMMs on the sample is quite low, because a single one attached to the CNT is the ideal case, a high evaporation rate is not desirable. A high rate would require very short shutter opening times resulting in large fluctuations as the shutter screening the sample from the evaporation crucible is manipulated by hand. Thus, we aimed for very low evaporation rates which also means that the oscillating quartz mostly shows a rate of zero. In order to compensate for this we evaporated for five minutes at different temperatures and measured the total thickness with the quartz to get an evaporation rate calibration (see figure 3.17). We tried to verify the thicknesses using an atomic force microscope (AFM) but could not receive a clear answer. In non-contact mode it was hard to find a clear step that is needed to identify changes in the sub-nm vertical range while in contact mode the AFM tip moved the weakly bound SMMs across the surface resulting in strong agglomerations (figure 3.18) making a precise and local thickness determination non-feasible.

To verify the structural integrity after evaporation we performed Raman spectroscopy on different samples with molecules evaporated onto them. An exemplary set of data is presented in figure 3.19. When comparing to a detailed Raman-study of (bis)phthalocyanine-lanthanides [192], many of the prominent peaks could be identified such as the G-Band/benzene stretching at $1600\,cm^{-1}$, a C=N (aza) stretching mode at $1525\,cm^{-1}$ and several more. However, not all peaks have a perfectly matching

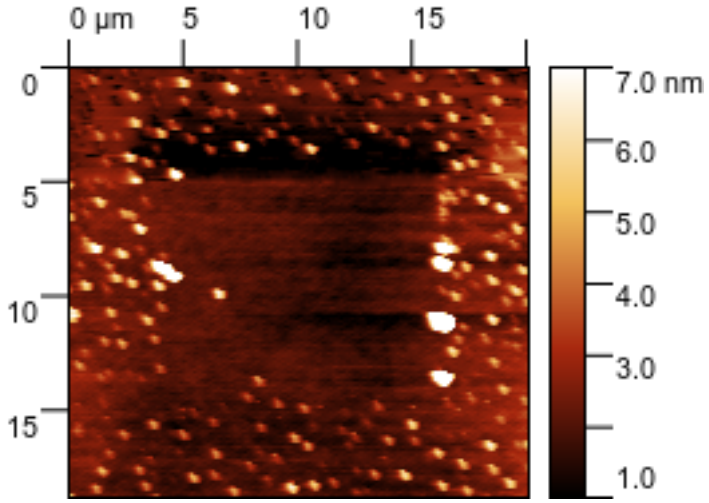

Figure 3.18: **Atomic force microscope image of an area with deposited molecules previously scanned in contact mode.** A square with very few particles is nicely visible with agglomerations at the edges.

counterpart in literature but deviate by up to $20\,\mathrm{cm}^{-1}$. In previous Raman-studies [173] a similar behaviour, but deviations at slightly different positions were observed. The deviations could either be caused by chemical degradation in the powder as a result of the heating in the crucible, some damage taken during the deposition (i.e. broken molecules) or the differing strain conditions in thin film on a SiO_2 surface compared to grains of a single crystal. The chemical integrity of the powder remains were later confirmed by S. Klyatskaya[9], indicating that overheating in the crucible did not occur.

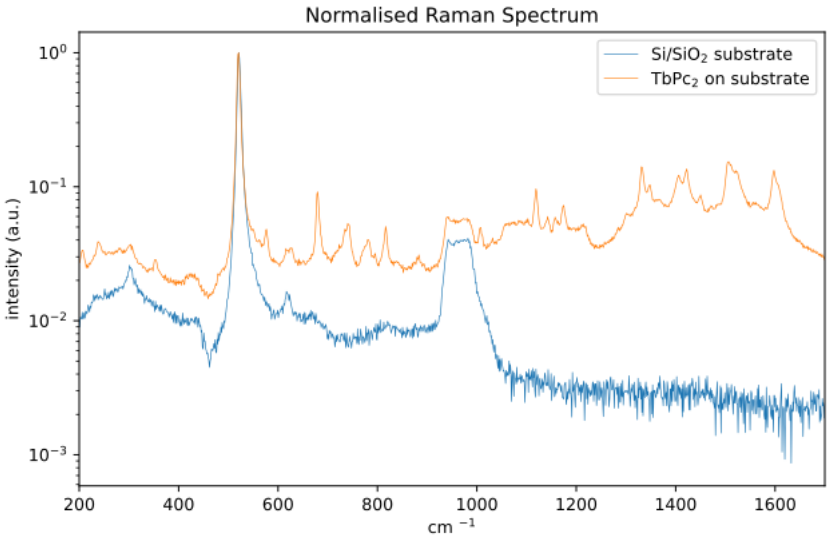

Figure 3.19: **Comparison of normalised Raman spectra of a blank Si/SiO_2 chip and a thin film of thermally evaporated $TbPc_2$ on a Si/SiO_2 sample.** The counts were normalised with respect to the main Si-peak. Several additional peaks occur in the $TbPc_2$-spectrum that can be attributed to various modes of the organic ligands indicating a still intact chemical structure.

4 Cryogenic experimental Setup

Within this chapter, an overview of our setup as well as some of the used experimental techniques is provided. Overall, this chapter is divided in two major parts. The first part of this chapter describes the cryogenic measurement setup with a home-built Sionludi cryostat achieving temperatures down to 30 mK (sections 4.1 - 4.4). The second section of this chapter describes the different measurement techniques and principles at our disposal inside the cryostat (section 4.5).

4.1 Modified Sionludi cryostat for fast sample exchange

In order to measure many phenomena in quantum physics a clean environment with few disturbances is needed. One major disturbance for many systems are thermal excitations that incoherently drive the studied system and limit the applicability of various measurement schemes. More generally, temperature also smears out energy resolution decreasing the sharpness of studied features. In order to reach the quantum regime and to coherently control single electrons, phonons, photons etc., it is beneficial to reduce the influence of thermal excitations. Therefore, it is common to cool down devices under test to the minimum feasible temperature, which in our case is about of 30 mK.
To cool down our devices we use a *Sionludi* (inversed sillable order of *Di-lu-sion*) ^{3}He/^{4}He dilution refrigerator which was developed at Neel Institute in Grenoble by Alain Benoit and coworkers for the Planck satellite project [99]. In this project, it was used to cool down the two microwave-frequency detectors to decrease the noise. One requirement for this application was to build the system in a way that works in a zero gravity environment which in the end led to the inverse design (i.e. the cold part is on the top whereas for most other cryostats it is at the very bottom) used in the Sionludi-cryostat today. A detailed description of features and working principle of the current generation Sionludis can be found in [193].
The following description of cooling methods follows [194]. To reach temperatures of 4 K liquid ^{4}He (lHe) can be used as a cooling agent, since its boiling point at ambient pressure is about 4.2 K. When part of the lHe evaporates, the enthalpy of evaporation is taken from the remaining liquid thereby cooling it. The temperature can be decreased further by pumping on the liquid until the equilibrium of vapour pressure and achieved pressure is reached again. Using a turbomolecular pump pressures below 1×10^{-6} mbar can be achieved which corresponds to a temperature of the lHe below 1.5 K. Using the same argument, the temperature can be decreased even further by using a cooling agent with a higher vapour pressure, which is liquid ^{3}He. Upon pumping on liquid ^{3}He, temperatures of about 300 mK can be achieved. In order to reach temperatures below this, a different type of cooling technique must to be used. Historically, a Pomeranchuk cell was used to reach temperatures down to

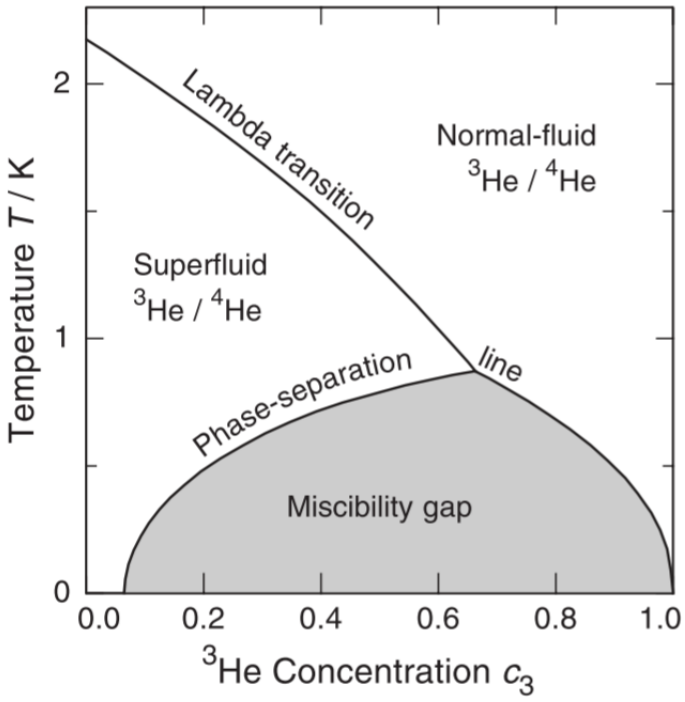

Figure 4.1: **Phase diagram of ^{3}He and ^{4}He in the liquid phase for temperatures below $\approx 2\,$K.** For very low ^{3}He-concentrations or higher temperatures a Fermi liquid of ^{3}He in superfluid ^{4}He occurs. For higher ^{4}He concentrations past the lambda transition a mixture of normal fluids forms. For low temperatures and ^{3}He concentrations $\geq$6.5 % (the grey shaded area) a separation of two phases occurs that are not miscible. Figure reproduced from [194]

$\approx$1 mK [194] which used the fact that the entropy of solid ^{3}He can be larger than the one of liquid ^{3}He [195] dominated by the spin. Interestingly, an analogous effect has been observed in twisted bilayer graphene for electrons when nearly filling a Moiré unit cell with one electron [196]. By solidifying ^{3}He by adiabatically applying pressure to a liquid/solid ^{3}He mixture the temperature of the system can be reduced. However, the implementation of this scheme is technically quite difficult as it requires moving pieces for a continuous operation. In order to continuously cool down to temperatures in the low mK regime a ^{3}He/^{4}He dilution cryostat makes use of the occurring phase separation in ^{3}He/^{4}He-mixtures (fig. 4.1) at temperatures below 850 mK and ^{3}He concentrations above 6.5 %. In these conditions, a separation of a ^{4}He-rich phase with a certain percentage of ^{3}He and a phase of almost pure ^{3}He is energetically beneficial. Due to the lower zero point energy of ^{4}He compared to ^{3}He, ^{3}He atoms are stronger bound to ^{4}He than to other ^{3}He atoms. In addition, the kinetic energy of ^{3}He increases with the number density since it follows Fermi statistics, which reduces the resulting binding energy. As a consequence, the binding energy approaches zero when a certain, temperature dependent, ^{3}He-concentration in ^{4}He is reached (see phase barrier in figure 4.1) creating two separate phases as the energetically preferred state. The cooling power is again a result of entropy changes: The ^{3}He atoms in the pure ^{3}He-phase possess a low entropy compared to the ^{3}He atoms dissolved in the superfluid ^{4}He-rich phase. Therefore, when ^{3}He atoms enter the ^{4}He-rich phase an energy $\Delta Q = T\Delta S = \alpha T^2$ with

$\alpha = -84\,\mathrm{J\,K^{-1}\,mol^{-1}}$ [194] is provided by the environment. By removing ^{3}He-atoms from the ^{4}He-rich phase (e.g. by pumping, because the vapour pressure of ^{3}He is higher by several orders of magnitude), a continuous cooling power can be achieved.
In the Sionludi-cryostat the two-phases of ^{3}He/^{4}He-mixture coexist in the *mixing chamber*. Here, the solution of ^{3}He in ^{4}He takes place and the mixing chamber is therefore the coldest element in the cryostat. A schematic overview of the cryostat can be seen in figure 4.2. The ^{4}He-rich phase is connected to the so called *still*, where ^{3}He is evaporated at elevated temperatures of 700-800 mK by pumping on the liquid with a turbomolecular pump, via a counterflow heat exchanger that is also used to cool down gaseous ^{3}He that is reintroduced into the mixing chamber to compensate for evaporated ^{3}He-atoms. Before being reintroduced, the ^{3}He is cleaned in a liquid N_2 cold-trap, pre-cooled by a first counterflow heat exchanger and H_2-filtered in a charcoal filter at temperatures below the liquefaction temperature of H_2 inside the cryostat. The cooling agent of the first heat exchanger is ^{4}He that is provided by an outside vessel with 100 L of lHe located next to the cryostat and typically lasts about six days. The lHe is also used to cool down the system from ambient temperature. A small pot (4K-pot) connected to the 4 K stage can collect some lHe and serves as a buffer.
The Sionludi has two main advantages over many other cryostats: Firstly, its tabletop design makes it easily accessible and the small dimensions result in rather lightweight components. Secondly, as a consequence of the lightweight design and well desgined heat-exchangers, typical cooldown times for us are in the order of 3 h which is well below the average of other systems. Systems with less components inside can achieve 100 mK in about half the time. When looking at the cross section of the two heat exchangers (figure 4.2), it is nicely visible that the diameter for the fast-injection line is much larger than for the regular injection line. This allows for a larger flow during the cooldown speeding up the process. The fast injection line is well thermalised to the turbo condenser which serves as a small pot with lHe that has a pump connected to it, i.e. it has a temeprature of about 1.5 K. This way, the mixture in the fast injection line is efficiently precooled and the condensation process facilitated which reduces the cooldown time. Further facilitation of the condensation is achieved by using a compressor to pressurise the mixture hence facilitating the condensation. During normal operation, the fast-injection line is closed and mixture may only enter the mixing chamber via the regular injection line and the heat exchanger connecting mixing chamber and still.

4.1.1 Top-load system for quick sample exchange

The cryostat used for our measurements possesses the peculiarity of being suited for loading a sample into the cryostat while the latter is already cooled down to cryogenic temperatures. In order to do so, all thermal radiation shields need to have an opening that can be sealed and reopened upon demand. The challenging part from an engineering point of view was to design the shields in a way that they are still nicely shielding radiation when closed, being movable by manipulation from the outside (since there is not much space and no fixation points to put any motors and cables) and to be readable from the outside i.e. it can be checked whether they are open or closed without disturbing them. This was solved by attaching a small magnet on a movable lid on top of the screens with the magnet of the

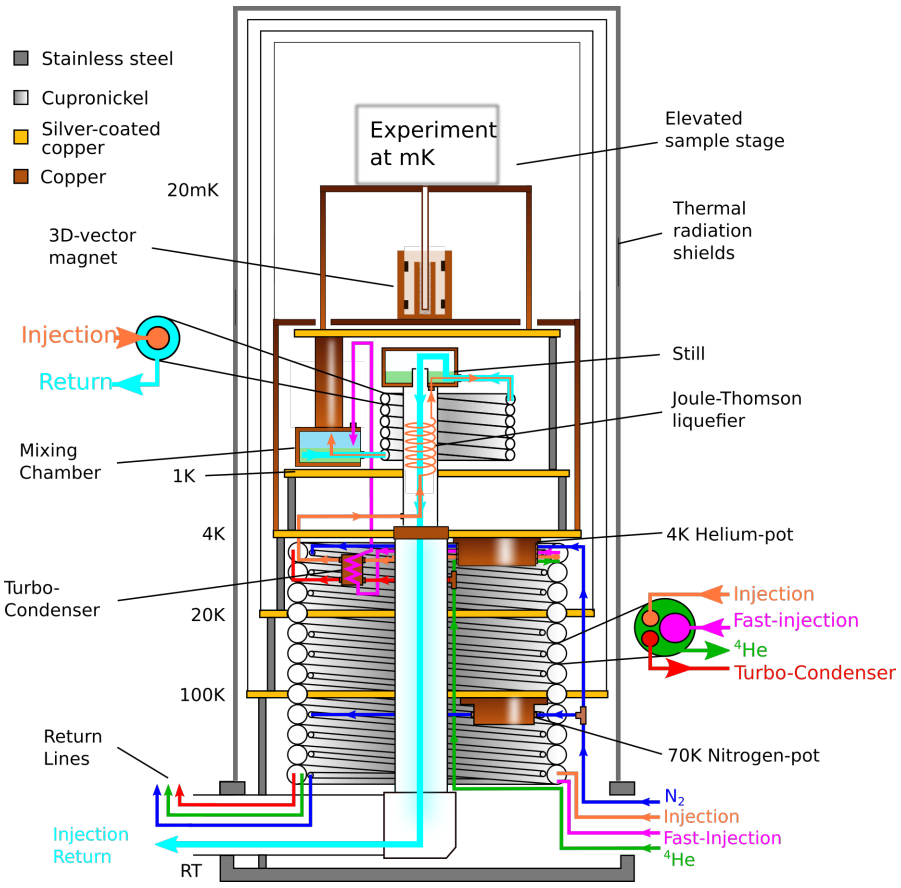

Figure 4.2: **Schematic drawing of the Sionludi cryostat used within this thesis.** The six different temperature stages, the heat exchanger as well as their cross section and the elevated experimental stage thermalised to the mixing chamber plate are shown. Adapted from [197].

20 K screen being on the opposite side of the 4 K and 100 K screen due to space constraints and to decrease the interaction between the magnets. Their respective position can easily be measured from the outside using any commercial magnetic field probe or even a smartphone application. The magnets can be manipulated by sliding a permanent magnet along the outermost thermal/vacuum shield. The latter has a loadlock attached to its top (see fig. 4.3a) which we use to transfer the samples into and out of the cryostat while maintaining vacuum conditions for the sample and avoiding too much absorption of gases into the fridge. The same transfer arm that we use to transfer samples into the SEM or the molecule evaporation unit is used for the transfer into the fridge as well. Since there are only two degrees of freedom (rotation and movement along the transfer axis), the cable connections need to be designed in a way that all connections are established in a single plugging motion, rendering connector types such as SMA impractical. How this interfacing is done is described in section 4.2.
As a result of the top loading, however, it was necessary to build an elevated experimental stage (ref. fig.4.2) which can receive the sample from the top and is thermalised to the mixing chamber stage in order to combine the sample with the 3D-vectormagnet (section 4.1.2). This results in a more complex and unorthodox layering of temperatures which requires particular care upon closing the cryostat and we achieved temperatures between 30-40 mK during experiments.
When transferring the sample into the cryostat, the circulation of mixture needs to be stopped during the transfer since the insertion of the sample holder, which is still at ambient temperatures at this point, introduces a large amount of heat into the system which cannot be instantly compensated. Hence, the mixture will evaporate and is stored in the tank for the duration of the transfer. If done well and quick, temperatures at the mixing chamber stage do not exceed ≈ 40 K. After removal of the transfer arm and closing of the shields, the cooldown can be restarted and the cryostat typically reaches its base temperature after 45-60 min, which is faster than a full warm-up and cooldown by a factor of four while still maintaining clean conditions.

4.1.2 3D-vector magnet

Since we want to do experiments using magnetic fields with different angles we used coils to build a 3D-electromagnet (see fig. 4.3b). A pair of Helmholtz coils is used for one in-plane (x-direction) and the out-of-plane direction (y-direction) and a cylindrical coil in-between the Helmholtz coils creates the second in-plane direction (z-direction) which is typically along the CNT-axis. The cables for the coils consist of thin threads of superconducting Nb-Ti, that connect to high-T_c cables which finally connect to copper cables that lead to the outside of the cryostat. The coils are thermalised at the 4 K stage to be superconducting but to not warm up the sample stage too much in case of quenching, i.e. breakdown of superconductivity, which provides a significant heat input due to the finite resistance. The coils can sustain currents up to 8 A before superconductivity breaks down. An overview of the values of the approximate magnetic field strength and the maximum sustained current is given in table 4.1. The current for the coils is provided by GS-Cs 4/10[1] current sources where the output current is

[1] Manufactured by Prof. Georg Schmidt, Martin-Luther-Universität Halle-Wittenberg

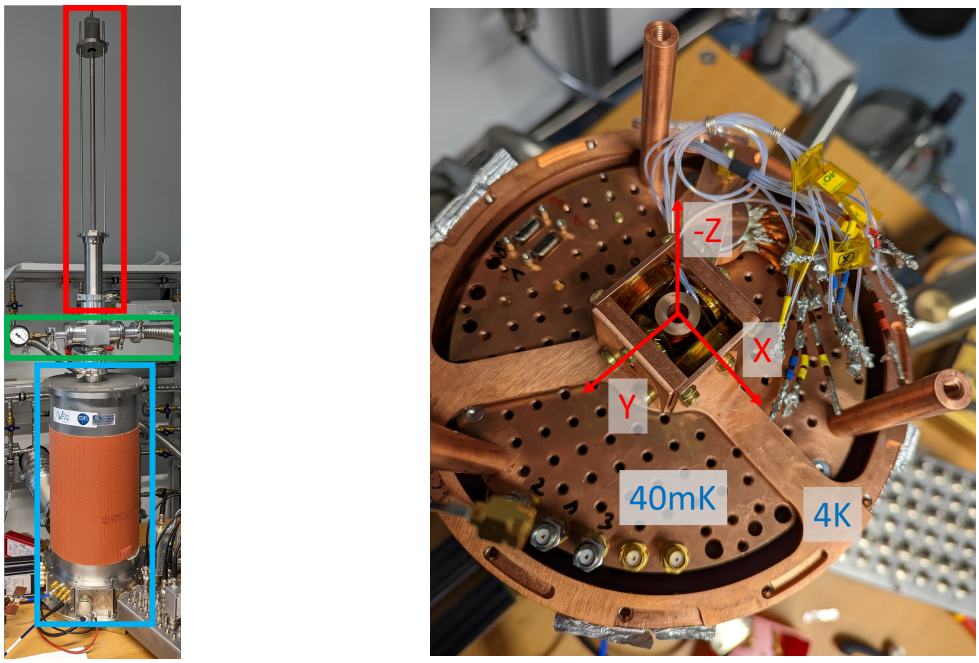

(a) Photography of the cryostat with attached loadlock.

(b) Top-down photography of the 3D vector-magnet inside our cryostat.

Figure 4.3: **Photographs of two aspects of the cryostat used for the experiments. a)** Photography of the Sionludi cryostat (blue) with the portable loadlock or transfer arm (red) connected to the outermost shield with loadlock (green). **b)** Photography of the 3D vector-magnet used to apply magnetic fields. The coils are thermalised to the 4 K stage via three copper beams while the sample is loaded from the top inside the cylindrical coil without touching to avoid a thermal short. The three vertical copper rods are used to fix the elevated experimental stage.

Field direction	**Current to field ratio**	**Maximum field strength**
X-coil	52 mT A^{-1}	395 mT
Y-coil	30 mT A^{-1}	240 mT
Z-coil	188 mT A^{-1}	1600 mT

Table 4.1: **Overview of the individual coils used for the 3D-vector magnet.** The values for the magnetic field strength are the result of simulations. The maximum field is determined by determining the maximum current before quenching occurs.

tunable by a DC input voltage. The current sources feature a quench protection to protect the cryostat from the worst heat spikes.

4.2 Sample holder, cabling and filtering

In this section, the sample holder with the sample PCB will be introduced. Since the sample holder is loaded into the cryostat using the top-load process described in section 4.1.1, the sample holder needs to fulfil special requirements discussed in the following.
In general, we have two types of electric lines inside the cryostat and on the sample PCB: lines for direct current or current with low frequencies (dc-lines) and lines that are suited for high frequencies (rf-lines). Our sample PCB features 24 dc-lines as well as three 50 Ω matched rf-lines (figure 4.4c) designed as coplanar waveguides made of gold-coated copper. The rf-lines' end on the PCB is located right between the sample and the end of half the DC lines and is suited for microbonding. The 24 dc-lines are equipped with an RC-filter with a time constant $\tau = RC$ of either 1 µs or 100 µs. Half the dc lines are guided in a lower layer of the PCB and resurface after passing the sample's location such that 12 dc-lines suited for microbonding face the sample on both sides. The sample can be glued (e.g. with PMMA) on a cut out part with a metalised bottom towards the tip of the PCB. Using our 3D-microbonder[2] we could connect all the lines nicely to the bondpads patterned on the sample chip with a 25 µm aluminium wire.

Bias-Tee

In later generations of the sample PCB we introduced two on-chip bias-tees allowing us to put both rf- and dc-signals on one line on the sample. In order to do so, a capacitor is put in-line on the rf-line effectively blocking all dc-components to protect the rf-source. To reduce leakage of the rf-signal into the dc-line a simple resistor is added in-line that attenuates the rf-signal sufficiently. Generally, an inductor could replace the resistor due to its generally large impedance at high frequencies and low dc-resistance but we found in simulations that the resulting pulse shape on the sample, especially for square pulses, deviates strongly from the one sent in and that a compensation for this deviation is a fair bit trickier than for a simple resistor. Also, every inductor possesses a self-resonance due to parasitic capacitance which further comlicates compensation and usage range. Even for a resistor, when sending a square pulse via the rf-line the capacitor will charge and discharge via the resistor (see figure 4.5) hence modifying the shape of the square or in an extreme case reduce the voltage amplitude at the sample to 0 V with a time constant $\tau = RC$.
To connect the PCB to the exterior, three SMP connectors as well as two sets of PCI connectors are included in the PCB. A short coaxial cable with one plug fixed at the copper sample holder (see fig. 4.4a) is used to connect the exterior with the SMP plugs on the PCB. The PCI plugs consist of two redundant sets of 24 individual lines each. The front set (pointing towards the sample) is used inside the SEM and inside the cryostat to connect to the sample, while the back set is mainly used inside

[2] WestBond Inc., Anaheim, Ca92806, USA

(a) The SMP-connectors lead to the rf-connectors on the sample PCB. The banana plugs are used for mechanical fixation, grounding and thermalisation. The visible PCI connectors are highlighted in **c)**.

(b) Photography of a partially disassembled sample holder. The connecting cables between sample holder and PCB as well as the copper rods stabilising the barrel are now visible.

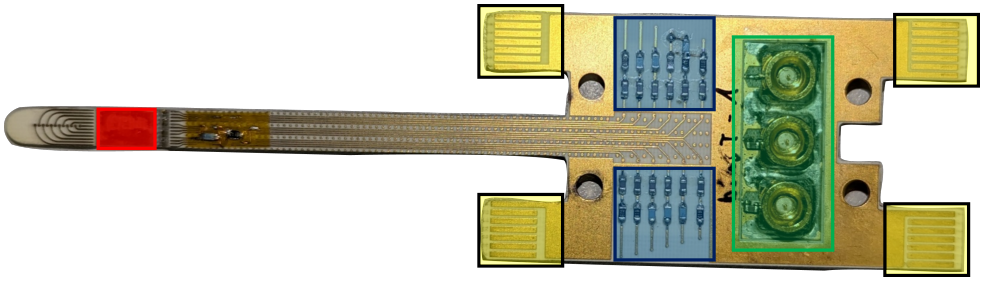

(c) Highlighted photography of the sample PCB used for most measurements. Highlighted in red is the position where the sample chip is glued, right next to the end of rf- and dc-lines. Highlighted in blue are the RC-filters on the dc-lines. Highlighted in green are the SMP-connectors used to connect the rf-lines on the PCB to outside rf-lines as well as an inline capacitor on the bottom two connections. Highlighted in yellow are two sets (one on the left, one on the right) of PCI-connectors that are used to connect the dc-lines to their counterpart inside the cryostat.

Figure 4.4: **Compilation of Photographies of sample holder and PCB in different stages of assembly.**

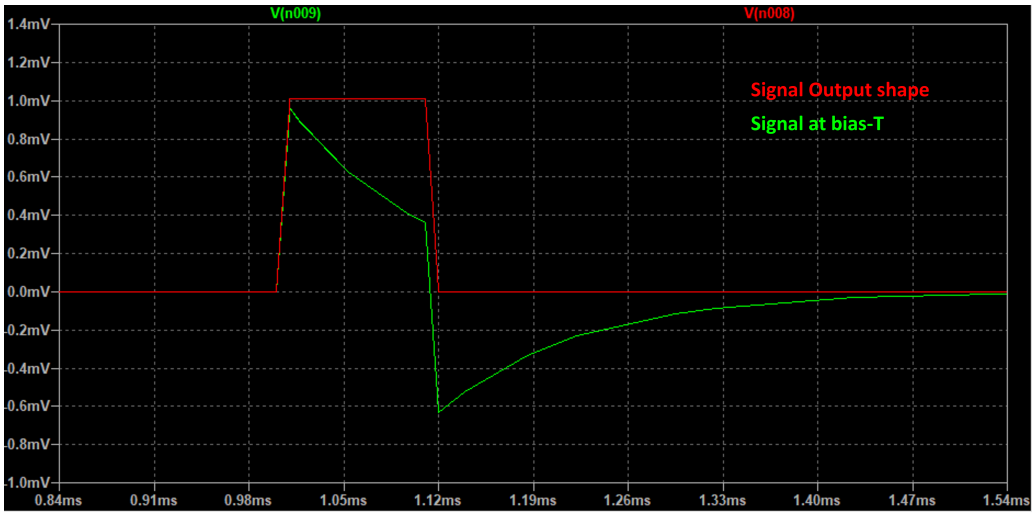

Figure 4.5: **Simulated response of a bias-T to an applied square pulse.** Plotted in red is the time behaviour of a square pulse before being fed into the bias-T, plotted in green is the time behaviour after the capacitor leading into the bias-T. The voltage signal is deviating from the square shape due to a discharging of the capacitor via the resistive part of the bias-T.

the transfer arm to electrically short all sections and connect them to ground via a 500 kΩ resistor thereby reducing the risk of electrostatic discharges. The mentioned copper sample holder consists of a copper barrel where the top and bottom lid contain the necessary electric and mechanical connections. Copper rods on the inside used to fix the banana plugs on the top lid are increasing the mechanical stability. The banana plugs themselves ensure a proper electric grounding and thermal connection when the sample holder is plugged and also fix the sample holder in place preventing a bending of the sensitive SMP plugs. The long arm of the PCB is sticking out of the sample holder by several cm which allows the sample to still be located inside the 3D-vector magnet described in section 4.1.2.

4.3 Dc-cabling of the measurement setup

The 24 dc-lines on the PCB are ending on a male PCI connector while the female counterpart of the PCI connector is located on another PCB on the mixing chamber stage. Starting from there, two cables with 12 dc-lines each, corresponding to one plug, first pass another RC-filter stage before exiting the fridge via a JAEGER-connector[3] at the bottom-side of the fridge (see figure 4.6). Inside the cryostat the dc-lines are put into a narrow capillary of about 500 µm diameter to mechanically protect them. To reduce thermal noise at the sample, the dc-lines are thermalised at the first filtering stage on the mixing chamber plate via a PCB in a copper box so the thermal noise reaching the sample is in the order of few tens of mK. On the outside part of the JAEGER-connector feedthrough, we installed one breakout box with 24 BNC-ports making every line adressable individually. Each port features a

[3] by HUMMEL AG, Lise-Meitner-Straße 2, D-79211 Denzlingen

three-position switch and we can either short the port to ground, connect it to ground via a 470 kΩ resistor or have it floating, i.e. a voltage/current can be applied.

4.4 Rf-cabling of the measurement setup

The rf-lines on the sample holder are ending in female SMP connectors. Their counter part of male SMP connectors passes through a hole in the dc-PCB and end in SMA connectors. Starting from here, superconducting coaxial Nb-Ti SMA-cables are used to carry the signal towards the output. A schematic overview of the rf-cabling described in the following can be seen in figure 4.7. At 4 K two HEMT amplifiers[6,7]are installed and thermalised. Before each cooldown we connect one of the two depending on the desired frequency range. The first HEMT is suited for a range of 1-7 MHz, the second one for a range of 0.3-14 GHz. On the output of the HEMT SMA cables lead to the feedthrough at the bottom-side of the fridge. On the rf-input side, the signal is attenuated by 60 dB by three attenuators located on 4 K, 800 mK and the mixing chamber plate. The attenuators as well as the cables are well thermalised by a thick copper/silver wire clamped to the fridge and glued to the cable with a compound of silver powder mixed with epoxy glue. At higher temperatures, tin soldering was used instead of gluing.

4.5 Electronic setup for cryogenic measurements

After introducing the cryostat and some of the inside components, this section introduces the experimental design as well as the electronic equipment used for the different measurements. For the majority of the measurements we performed transport measurements using a real-time dc measurement setup, mainly for charge stability diagrams, or a quasi-static but more versatile dc setup, especially for the combination of several devices like rf-sources, an AWG etc. During the last months of this thesis another type of measurement setup suited for time-domain measurements was implemented and will also be described here. The data acquisition was handled by different software environments which will be described first.

4.5.1 Measurement software

The software framework traditionally used in our group to do real-time low-frequency measurements is called *nanoqt* and was developed in the past in Grenoble, mainly by Dr. Edgar Bonet-Orozco[8]. It is well optimised for the work with ADwin Gold II[9] real-time computer controlled data-acquisition system (details on the equipment used in the experimental setup are presented in the next section). It already

[6] Cryo Amp A5-1 by CRYOHEMT, 6 Boulevard Dubreuil, 91400 Orsay, France
[7] LNF-LNC0.3_14A by Low Noise Factory, Nellickevägen 24, 412 63 Göteborg, Sweden
[8] Institut Néel, CNRS UPR2940, 25 rue des Martyrs BP 166, 38042 Grenoble cedex 9
[9] Jäger Computergesteuerte Messtechnik GmbH, Rheinstraße 2-4, D-64653 Lorsch

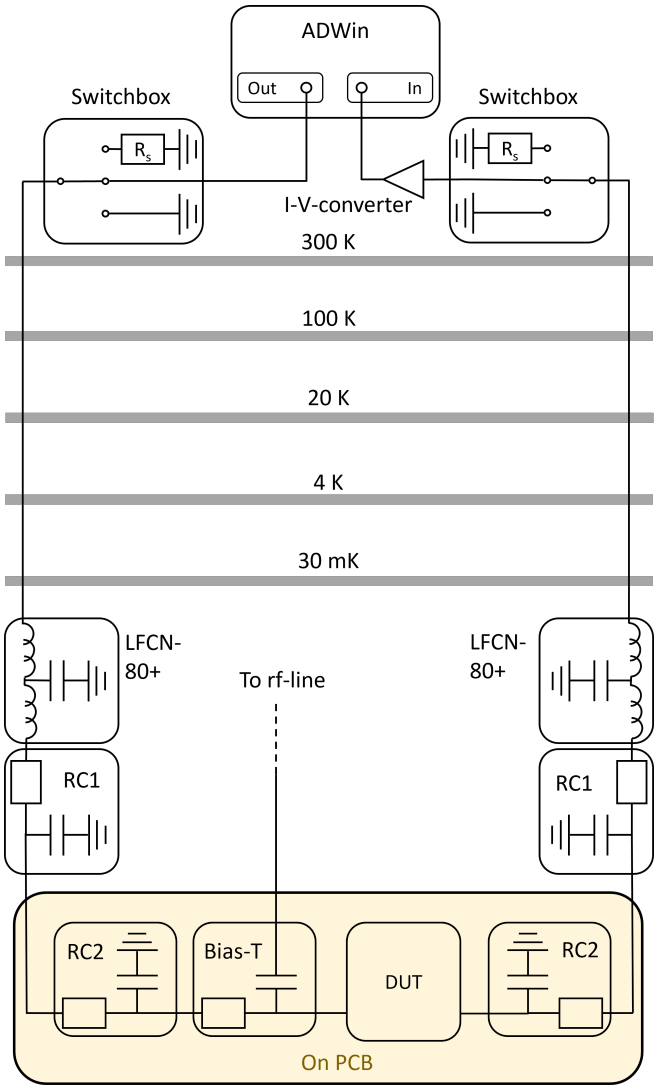

Figure 4.6: **Schematic overview of the path of a hypothetical dc-signal.** It is sent into the cryostat via a switchbox and thermalised on various stages. On the mixig chamber stage it is filtered by a commercial low-pass filter (LFCN-80+[4], components unknown to the author, representative circuit diagram, cut-off frequency 80 MHz) and the first stage of RC-low-pass-filters (RC1) with R=1 kΩ and C=25 nF. It then reaches the PCB and a second RC-filtering stage with R=1 kΩ and C=15 nF for bias-lines and R=100 kΩ and C=15 nF for gate lines. Some lines additionally feature a bias-T with R=1 kΩ and C=1 nF. On the output side, the signal passes the same filtering stages in the inverse order before leaving the cryostat via the switchbox. An I-V-converter amplifies the signal and converts it to a voltage. Both the excitation as well as the readout were typically done by an ADWin[5].

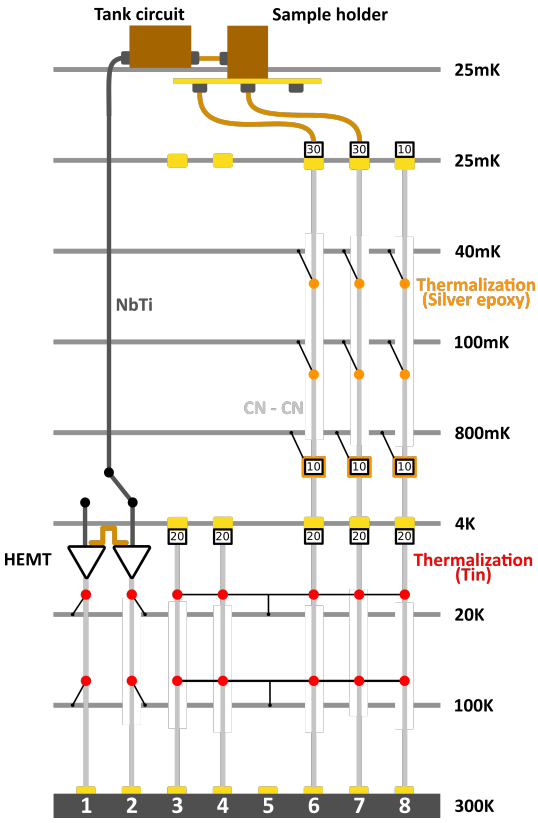

Figure 4.7: **Schematic drawing of the rf-cabling inside the fridge.** The red/orange circles represent thermalisation with points with tin/silver epoxy. The golden blocks on some stages represent feedthrough connectors that also serve as additional thermalisation points. Depending on the application, either of the two HEMT amplifiers can be connected. The small boxes with a grey frame represent attenuators with the number inside giving the attenuation in dB.

contains plenty of functions in a custom JavaScript environment such as a LockIn-procedure. The real time setup allows for measurements while sweeping one parameter resulting in fast acquisition times while still measuring accurately. In addition it does some minor data post-treatment and filters outliers, such as one-point spikes, that do not originate from the physical phenomena studied. The trade-off is made in the form of complexity when trying to integrate new pieces of equipments and measurement routines into this framework which is well possible but harder than for the python based software framework.

The second measurement software is based on the *qkit*[10] measurement framework developed here at KIT, which provides an easy possibility to integrate electronic devices, perform logging and is generally set up in a very modular way to give the user a lot of flexibility in designing their measurement scheme. It is savespace friendly since it stores data in the .h5 format which requires way less space than e.g. a .txt or .json file at the cost of being not human-readable. However, qkit provides a viewer to show and tweak line plots and colour maps. The measurement frameworks we used inside qkit were developed by

[10] open source - https://github.com/qkitgroup/qkit

Julian Ferrero[2]. The first one basically iteratively conducts a predefined measurement routine for every entry of a one-, two- or threedimensional array of measurement parameters defined in the beginning. Since there are no requirements on the physical quantity (voltage, current, frequency, averages...) of the array or how the specific measurement operation needs to look like, it is very flexible. The tradeoff is speed since the system "stands still" while measuring and proceeds to the next datapoint only after finishing the previous one which makes the acquisition of sweeps generally slower than a comparable measurement performed with nanoqt. The ease of integration of different devices still make it very attractive, hence all measurements where an rf-signal was applied were performed using qkit.
The two different measurement frameworks described previously are suited for dc-measurements but are not suited when it comes to actual time-precise measurements. In order to perform time domain measurements, a different measurement framework within qkit (again by Julian Ferrero) is used which basically creates a measurement protocol of known time span given by a sampling rate and a sequence of samples determining what is supposed to be happening. The sequence can be quite long, meaning that several iterations of the same measurement or with variations of individual parameters are possible. Since the full measurement routine is defined within one sequence, the difference in time between each individual point is well known. The obvious choice for a suitable piece of equipment is an Arbitrary waveform generator (AWG) that basically does exactly what the framework requires for precise sample and equipment manipulation. Since the integration of different pieces of equipment is similar to the first qkit-environment this framework is also flexible when it comes to the eqipment used.

4.5.2 Electronic equipment

The real-time dc-measurement setup mainly uses the aforementioned ADwin Gold II[11] real time computer controlled data acquisition system. It is controlled by a lab-PC via an ethernet connection and offers 8 analog outputs, 16 analog inputs, and several digital connections. The voltage range is $-10\,\mathrm{V}$ to $10\,\mathrm{V}$ with a resolution of 16 bit, i.e. $20\,\mathrm{V}/2^{16} = 305\,\mu\mathrm{V}$ for output parts and 18-bit, i.e. $305\,\mu\mathrm{V}/4 = 76\,\mu\mathrm{V}$, for input ports. The resolution is determined by the digital-analog converter and the analog-digital converter, respectively. It also features a real-time processor which can be used for feedback loops e.g. when measuring a μ-SQUID [198]. Our standard measurement protocol consists of sweeping (nanoqt) or stepping (qkit) a voltage on one of the analog outputs while at the same time measuring the voltage on one of the inputs. After a successful sweep, another voltage can automatically be changed before repeating the sweep hence creating a map. Since we mostly did transport measurements, an applied voltage results in a current response of the CNT which we reconvert into a voltage using an IV-converter[12] with a gain between 10^5 and 10^9 and very low noise. This amplifier can also be used when performing lock-in detection which improves the signal-to-noise ratio (SNR).
We generated rf-signals using either a Keysight 5183B[13] or a R&S 100SMA[14]. Both signal generators

[11] Jäger Computergesteuerte Messtechnik GmbH, Rheinstraße 2-4, D-64653 Lorsch
[12] SP983C with LSK-input by Basel Precision Instruments GmbH, c/o Universität Basel Physik Department, Klingelbergstrasse 82, 4056 Basel, Switzerland
[13] German representation: Keysight Technologies Deutschland GmbH, Herrenberger Straße 130, D-71034 Böblingen
[14] Rohde & Schwarz GmbH & Co. KG, Mühldorfstraße 15,D-81671 Munich

offer the possibility to perform frequency and pulse modulations which enable various measurement schemes. The R&S signal generator additionally offers the possibility to change frequencies within a certain window without changing the phase of the signal which might be very interesting when measuring bistable mechanical resonances.
As an AWG we used a ZI HDAWG4[15] for this purpose. Since the readout is ideally also precise in time, we use a dual-channel digitizer (ADQ14AC-2X[16]) with a sampling speed of 2 gigasamples per second. This allows for many different measurement schemes, such as pump-probe-, ringdown-, Rabi-oscillation-measurements and many more. To increase time accuracy between the devices we synchronised their clocks to the 10 MHz clock of the AWG. Most of the time, we performed measurements in the low MHz-regime and used two amplifiers to enhance the signal. On the 4 K stage we installed an HEMT amplifier[17] with a gain of 13 dB. Additionally, at room temperature another amplifier[18] of 46 dB was installed. If needed, an additional amplifier[19] at room temperature with 36 dB could be added. We installed two low-pass filters (LPF) within the amplification stage to filter higher frequency noise picked-up by the amplifiers. The first LPF between HEMT and first room-temperature amplifier consists of a 100 pF capacitor to ground. The second LPF between first and second room-temperature amplifier is a commercial filter[20] with a cut-off frequency of 5 MHz.

4.5.3 RLC-tank circuit

Classically, we measured the mechanical resonances of the CNT by measuring its conductance as a function of applied frequency and power. This, however, means that we always drive the mechanical resonance artificially by the ac-electric field's photons filling the vibrational state with phonons making it impossible to measure the actual phonon occupation of this resonance. In order to overcome this and to, for example, measure the thermal occupation of the resonance, we implemented another measurement technique similarly to what is described in [105, 199, 200]. A schematic illustration of this setup is given in figure 4.8.
The most notable feature is the addition of an additional RLC parallel-circuit to ground (figure 4.9) on one electrode connected to the CNT. This prohibits a current measurement with an IV-converter as described earlier since the circuit is shunted to ground via the low ohmic inductor[21]. We overcame this limitation by introducing an additional resistor in series of the CNT and performing a four-point voltage measurement on it. The voltage signal is then amplified by a voltage amplifier[22] before being measured at the input port of the ADwin. Another option we later used was to install a capacitor (1 nF) in-line between the RLC-circuit and the CNT effectively blocking dc-signals while still transmitting the MHz-signal which allowed us to apply all previously used measurement techniques. The RLC-circuit also behaves as a bandpass filter allowing only signals around $\omega = 1/\sqrt{LC}$ with a quality factor of

[15] Zurich Instruments AG, Technoparkstrasse 1, 8005 Zurich, Switzerland
[16] by SP Devices, Teknikringen 8D, SE-583 30, Linköping, Sweden
[17] Cryo Amp A5-1 by CRYOHEMT, 6 Boulevard Dubreuil, 91400 Orsay, France
[18] NF SA 200-F5, NF Corporation, 6-3-20 Tsunashima Higashi, Kohoku-ku, Yokohama 223-8508, Japan
[19] ZX60-100VH+, Mini-Circuits, 13 Neptune Ave Brooklyn, NY 11235, United States
[20] SLP-5+, Mini-Circuits
[21] 33.3 µH, 1812CS-333XJEC, Coilcraft, 1102 Silver Lake Road; Cary, Illinois; 60013, USA
[22] EPC1-D, differential amplifier, Groupe SPHEREL Systèmes,10bis, route d'Ax, 31120 Portet-sur-Garonne, France

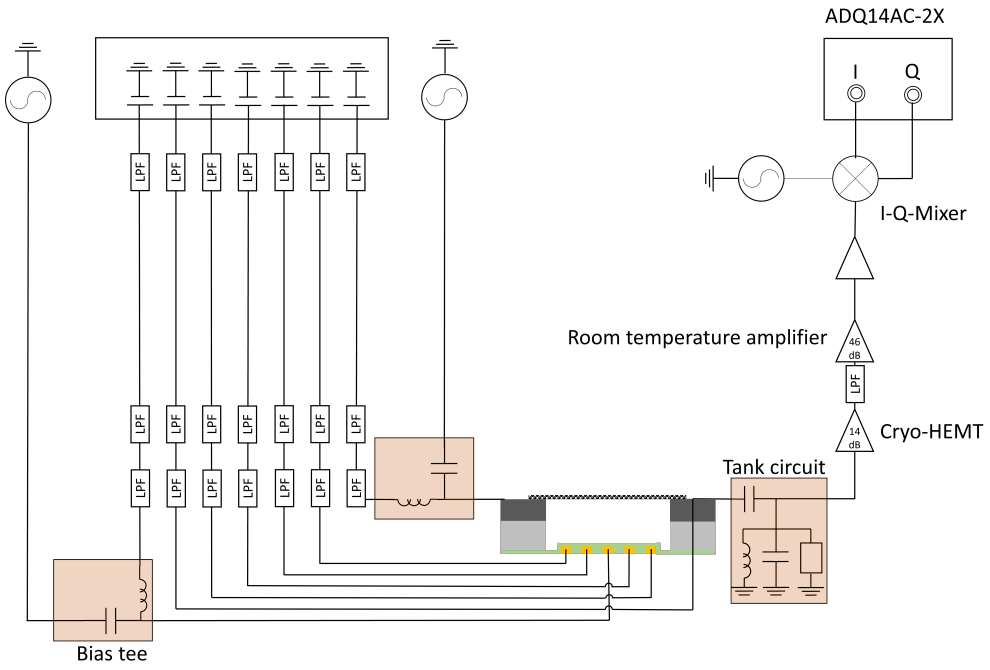

Figure 4.8: **Schematic drawing of the full cabling of our setup.** We connect seven DC-lines to the DUT with two of them being part of a bias-T. One bias-T is connected to the source-electrode, one bias-T is connected to one of the local gates. The rf-side of the bias-T is connected to an rf-source via three stages of attenuators. The drain-electrode is connected to one dc-line for transport measurements as well as to an RLC-tank circuit via a capacitor to measure in the MHz-range at the RLC-resonance frequency. Three stages of amplification amplify the signal, the additional low-pass-filter filters higher frequency noise. An acquisition card with 2 Gigasamples/s collects the signal.

the resonance following $Q = R\sqrt{C/L}$ to pass. In reality, parasitic capacity C_{par} adds on top to the capacitance soldered onto the PCB and can, as in our case, dominate. In our case, with $L = 33\,\mu\text{H}$, $C = C_1 + C_{\text{par}}$ ($C_1 = 10\,\text{pF}$, $C_{\text{par}} \approx 120\,\text{pF}$) and $R = 10\,\text{k}\Omega$, the resulting quality factor Q is about 20 and the resonance frequency about 2.1 MHz. The components are soldered onto a PCB manufactured in house by the electronic workshop. The PCB is glued into a copper box with silver epoxy glue to ensure proper grounding and thermalisation. The box can be closed with a copper lid that is fixed by four brass screws. Two additional brass screws on the ground plane as well as excess silver epoxy at the edges ensure a thermalisation and grounding of the large ground planes on the up facing parts of the PCB. By introducing an in-line capacitance at the marked position where the transmission line is interrupted the potential to perform DC-measurements might be restored but potential drawbacks such as a reduced signal via the RLC circuit, additional resonances or a modified RLC resonance are experimentally unexplored so far.

After determining the resonance frequency of the CNT via transport measurements with constant

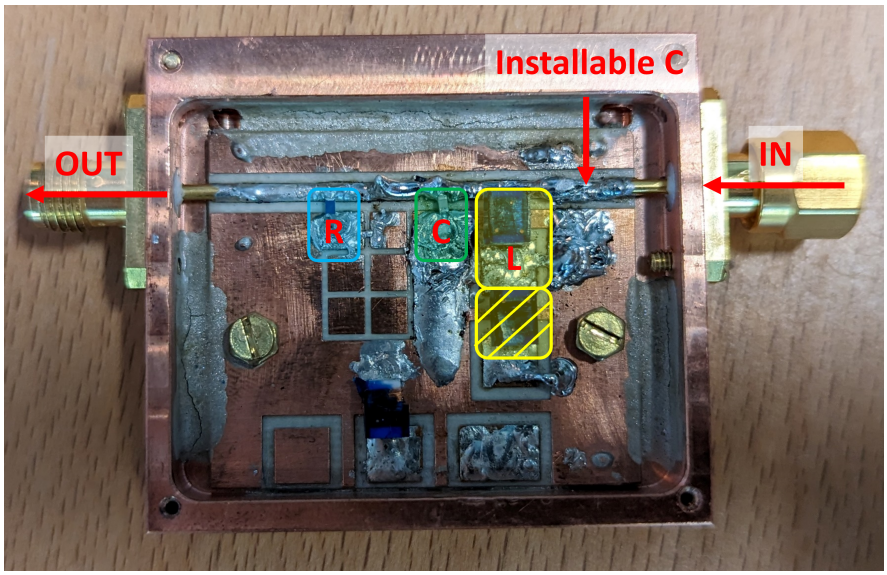

Figure 4.9: **Photography of the RLC tank circuit used.** The soldered resistance (blue), capacitance (green) and inductor (yellow) are highlighted. By removing the shunt to ground between the two inductors a second inductor (yellow striped box) can easily be added. The transmission line is interrupted and reconnected via solder and allows for the introduction of a capacitor at the highlighted spot.

rf-excitation, this setup allows us to readout the occupation of the mechanical resonance by driving the CNT off-resonance and using it as a mixer [102, 113, 114] by interaction of the electrons with the phonons of the vibrational state to downconvert the applied frequency to match the passing band of the RLC tank-circuit. This experimental technique potentially allows for cooling of the vibrational mode [201, 202], creation of mechanical cat states [92] or a mechanical qubit [72].

5 Experimental results

After introducing the physical background relevant for this thesis, the fabrication concepts applied to obtain functional devices and the experimental setup used, this chapter contains acquired measurements and potential explanations to the phenomena observed. The first section (section 5.1) focuses on the characterisation and optimisation of carbon nanotube growth as the last step towards functional 'top-growth devices'. Since this process exposes the device to rather violent conditions, a study to find the proper combination of good carbon nanotube yield while maintaining the integrity of the metal circuit is necessary.
The section 5.2 is dedicated to first attempts of devices fabricated with the stamping technique using molybdenum as the contact material. While most similar devices use platinum or palladium contacting layers, we tested molybdenum due to its carbide forming behaviour.
The bulk of this chapter is dedicated to transport measurements on carbon nanotube nanoelectromechanical systems at cryogenic temperatures. Among others, single and double quantum dot as well as mechanical resonances have been measured. During this thesis devices fabricated via the top-growth procedure (see sec. 3.3.1) as well as the stamping procedure (see sec. 3.3.4) have been studied and the results are presented in section 5.3 and section 5.4, respectively.
Unfortunately, the coupling to single-molecule magnets could not be achieved in this thesis and the measurements, showing mostly noise, are being omitted for the sake of clarity.

5.1 Carbon nanotube growth optimisation for the top-growth process

In section 3.3.1 the advantages and disadvantages of the top-growth procedure have been discussed. The issues can mostly be boiled down to the statistical nature (i.e. nondeterministic growth-result for each junction) and the damaging CVD-conditions of the carbon nanotube growth process. Therefore it was essential to determine growth conditions that provide a high yield of single-nanotube devices while at the same time inflict little damage on the metal-structures. These requirements are different than what is needed, e.g. for the comb-like cantilever chips, and therefore require a different trade-off between the growth parameters.
The higher the temperature and the longer the device is exposed to these temperatures the more nonbeneficial thermally activated changes are to be expected at the metal structures. At the same time, strong temperature gradients as well as fast heating rates can cause structural damage due to an inhomogeneous thermal expansion across the sample. In addition, the decomposition rate of the precursor hydrocarbon gases increases with temperature and gas flow rate which as a first approximation also means more formation of carbon nanotubes. Here, the focus will be on the growth

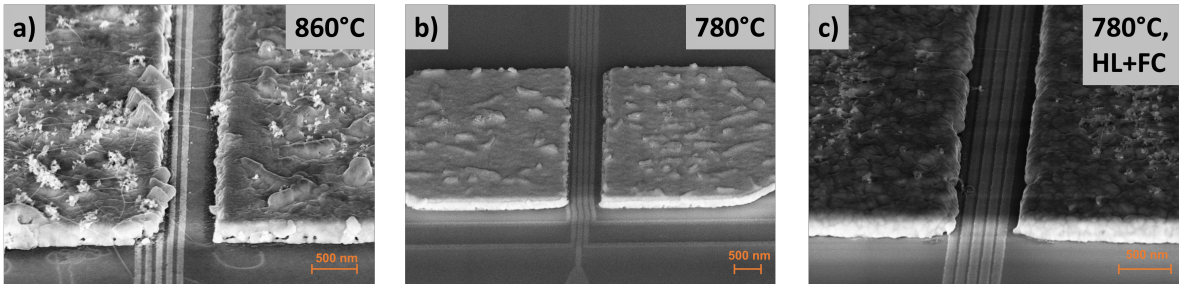

Figure 5.1: **SEM micrograph comparison of devices after CVD-growth process at different temperatures. a)** After CVD growth at 860 °C, a multitude of carbon nanotubes was found on a metal film that was clearly distorted. **b)** Number of tubes and damage to the metal circuit was reduced after normal growth at 780 °C though the metal film was still corrugated. **c)** The metal film shows very little bumps after a growth at 780 °C with the hot load (HL) and fast cooldown (FC) applied, emphasising their effect. The faint carbon nanotube in the background was device *8I18* that was measured at cryogenic temperatures.

temperature and heating cycle, which was done after fixing the other growth parameters discussed in the fabrication chapter.

Once other parameters were fixed we altered the growth temperature in a range between 780-860 °C. As parameters to determine whether a growth yielded 'good' results, we examined qualitatively damage to metal structures and quantitatively the yield of single-nanotube junctions for a chip with 48 junctions. The influence of temperature on the metal film can be analysed by SEM imaging. A comparison of two different growth temperatures and the application of the *hot load*, sliding the sample in the oven only when growth conditions are reached, and *fast cooldown* technique, removing sample directly after terminating growth conditions, [203] is given in figure 5.1. A clear trend emerges where higher temperatures and a longer exposure time lead to more deformation of the metal film, as expected. While deformation is not necessarily a disadvantage since it is unclear whether it is detrimental for the CNT-metal contact or even beneficial and it also could help to achieve suspended CNTs, the CVD-growth also made the metal-film more brittle thus strongly impeding the microbonding process. From these SEM observations it is also obvious that there are far too many carbon nanotubes growing and connecting the two electrodes making characterisation at room temperature (sec. 3.3.3) more challenging. Judging from the SEM images, it appears that temperatures above 800 °C cause strong alterations of the metal structure and should thus be avoided, if possible.

To quantify which percentage of junctions contained one CNT, we performed transport measurements between the two electrodes to see if a connection could be detected and looked at the electrodes using an SEM enabling us to count the number of CNTs per section. It should be noted that by doing so we cannot distinguish bundles from single CNTs. We performed this study for a temperature range between 780-860 °C and different catalyst densities with and without the hot load and fast cooldown procedure. The number of junctions measured per growth was between 30 and 100 and an excerpt showing the global trend is given in figure 5.2. As expected, the number of CNTs per junction is overall decreasing upon decreasing the growth temperature. The growth at 820 °C featured a reduced catalyst

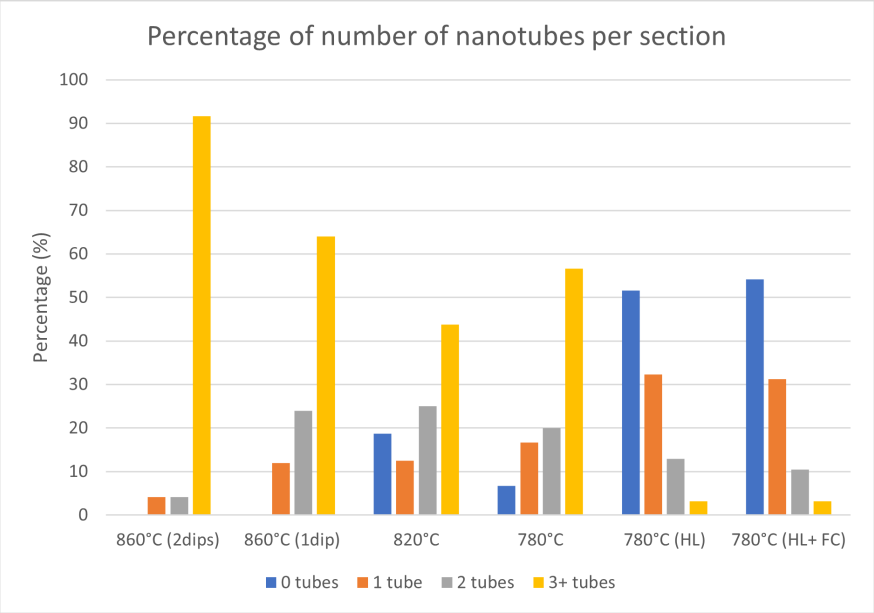

Figure 5.2: **Bar diagram showing the yield of nanotubes per junction for different growth parameters.** At 860 °C, both one and two dips into the catalyst solution, the growth yields a multitude of CNTs which is not suited for the characterisation of individual CNTs. Lowering the temperature overall results in a lower abundance of CNTs. Introducing the hot load (HL) technique [203] drastically reduced the yield of CNTs which strongly increased the chances of achieving a single CNT in a junction. The fast cooldown (FC) showed little effect overall.

density and is thus an outlier. The two growths at 860 °C received a different amount of catalyst showing that in our case more catalyst means more CNTs. Overall, the catalyst density used by us appears to be a lot smaller than in previous works [68, 99, 199] using top-growth. The biggest improvement in terms of single-nanotube-per-junction yield was achieved by using the hot load procedure which overall reduced the CNT yield by a lot making it likely that a connection measured at room temperature is actually caused by only a single CNT. The additional usage of the fast cooldown did not lead to any yield improvement but protected the metal film more than keeping the sample in the oven.

In summary, this small characterisation showed that we are able to perform a growth at rather low temperatures using a rather low catalyst density that on average had a yield of ≈ 30% single CNT devices at the time of these tests while maintaining the integrity of the nanofabricated metal structure.

5.2 Stamping devices with molybdenum-topped electrodes

Following the intriguing findings of low-ohmic CNT end-bonded contacts to molybdenum by Cao et al. [51] we tried to replicate similarly good contacts using our stamping technique. Therefore, devices were nanofabricated analogous to the process described for stamping devices in section 3.2.2 but with a molybdenum contacting layer instead of palladium. Cao et al. achieved the low resistance for CNTs with

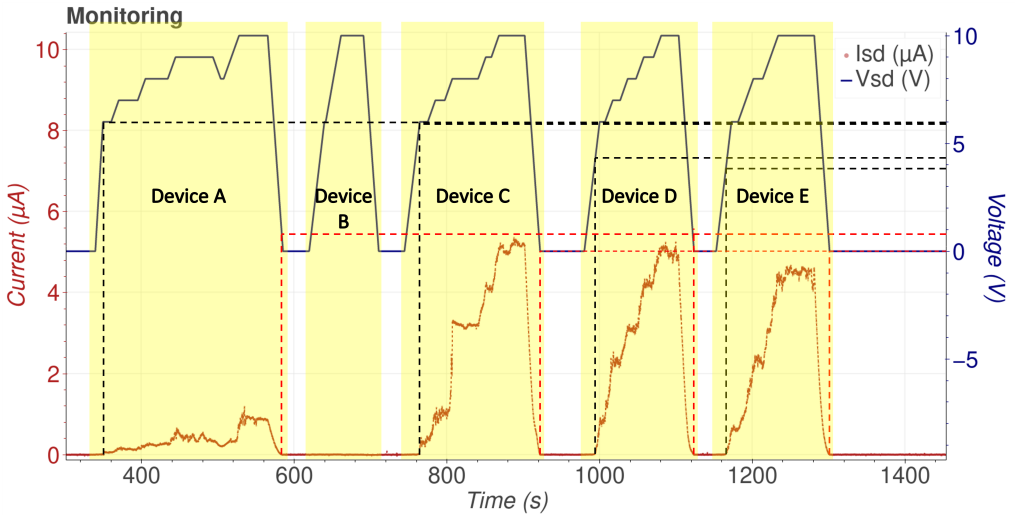

Figure 5.3: **Representative measurements of conductance directly after depositing the CNT.** The current through the CNT was measured with additional 1 MΩ in series for different devices. Between the yellow boxes, the outside cabling was adjusted. For device B no connection could be established, while the other sections showed a clear initial barrier requiring between 3.5-6 V to overcome highlighted by the black dashed lines. After overcoming this barrier and achieving a somewhat large current, the barrier is gone for most devices, though a non-ohmic deviation is observed towards low bias.

molybdenum evaporated on top of the CNT and subsequent annealing resulting in carbide formation with the molybdenum. Since they found the contact to be independent of the overlapping area and a device resistance below 40 kΩ it was worthwhile to try and reproduce the low resistance using the stamping technique. Using the stamping approach, their geometry of evaporating molybdenum on top could not be reproduced since CNTs were integrated on top of the metal as the last step of fabrication. Additionally, their annealing in an oven at more than 800 °C could not be applied without breaking the vacuum and removing the wirebonds. Therefore, current annealing was tested aiming to reproduce similarly high temperatures locally.

In order to perform the stamping, the CNTs have been vacuum transferred into the SEM after their growth and the chip with the metal circuit loaded after microbonding. These tests have been performed at an early stage when the radiative thermal annealing and argon-milling of the first few nanometres have not been introduced, yet. The stamping thus consisted of the CNT-transfer itself and current annealing. In the following an electrode pair connected by a CNT is called a device. The typical behaviour of a device featured initially large barrier, leading to a non detectable current (few nA or smaller) up to a few volts. After reaching voltage thresholds varying with the initial contact quality, a finite current is measured. Upon slowly increasing the voltage, the measured current becomes more unstable and can jump to larger values which we attribute to an improvement of the contact to the metal electrode, i.e. local rearrangements. Representative data for five different electrode pairs fabricated from one CNT, are shown in figure 5.3, showing the threshold values and also the annealing

behaviour, e.g. for device C. In this measurement, the barrier voltage is describing the threshold voltage at which a notable increase in current was detected. The barrier voltage was typically between 3-7 V for devices without O_2-plasma cleaning of the contacts and larger barriers of typically more than 10 V occurred for samples that were cleaned in an O_2-plasma. Application of the O_2 should have helped if the initially bad contact is the result of hydrocarbon remnants after nanofabrication processes by burning them in the plasma. The instead observed larger barriers indicate an enhancement of the native oxide layer at the molybdenum surface hampering a good connection.
Using Ohm's law $R = U/I$ we can determine some resistance values for large bias voltages. Taking the 1 MΩ resistor in series into account, the resistance is between ≈1 MΩ for devices C-E and about 10 MΩ for device A. This is, however, an optimistic estimation since transport measurements are typically performed at low bias voltages (mV or smaller) where the resistance is even larger as indicated by the change of slope when approaching zero voltage. Since the conductance of the CNT itself is not expected to be this low, these large resistance values are expected to be the result of strong interface barriers. As discussed in section 2.2, the barrier height strongly determines the transport behaviour and in this case will most likely block almost all tunnelling processes at small bias due to the low tunnelling probability.
Nonetheless during the several attempts there was one device that after annealing showed a linear current/voltage dependence down to few tens of mV (see figure 5.4). The measurement was performed with 100 kΩ in series. The CNT was most likely actually a bundle of CNTs as it could sustain quite large currents (≈ 30 µA) without cutting in a section of about 800 nm suspension length and showed a resistance of ≈ 160 kΩ after deduction of the inline resistance. When looking at the time course of the current for a fixed bias of 6 V, it can be seen that the behaviour is still volatile meaning that no stable position has been reached, yet. This implies that further treatment might still improve the resistance and potentially get closer to the 36 kΩ reported by Cao et al. [51].
At a later point we used externally fabricated chips with full molybdenum electrodes while applying the annealing recipe developed in our group [57]. This treatment contains cleaning of the surface by argon milling and a global heating of the chip inside the SEM, after locally heating it by driving a high current through the CNT. The cleaning supposedly removed thin oxidation layers present on the surfaces of the chip which should help establishing a good contact. However, upon stamping we found that there was again an initial barrier to overcome. At the stage when these tests where performed, the microbonding was done after Ar milling. This resulted in a timespan of 10+ minutes after argon milling, caused mainly by the need of microbonding, where the sample is exposed to air. During this time, a newly oxidised or otherwise altered surface may have formed. The radiative thermal annealing showed a small improvement of the resistance but could not achieve resistance values comparable to palladium contacts or Mo_2C end-bonded contacts. The resistance values obtained for these samples were about 250 kΩ or higher for a bias voltage of 100 mV. The temperatures typically achieved during the radiative thermal annealing are below 300 °C [57] which is well below the carbide formation temperature of 850 °C [51] making this an unlikely process to happen. Exposing the sample to more than 800 °C is not feasible as it will damage the microbonding (Al-bondwires) and can potentially damage the metal circuit, depending on the used materials (e.g. strong damage on Al and Au) nullifying one of the

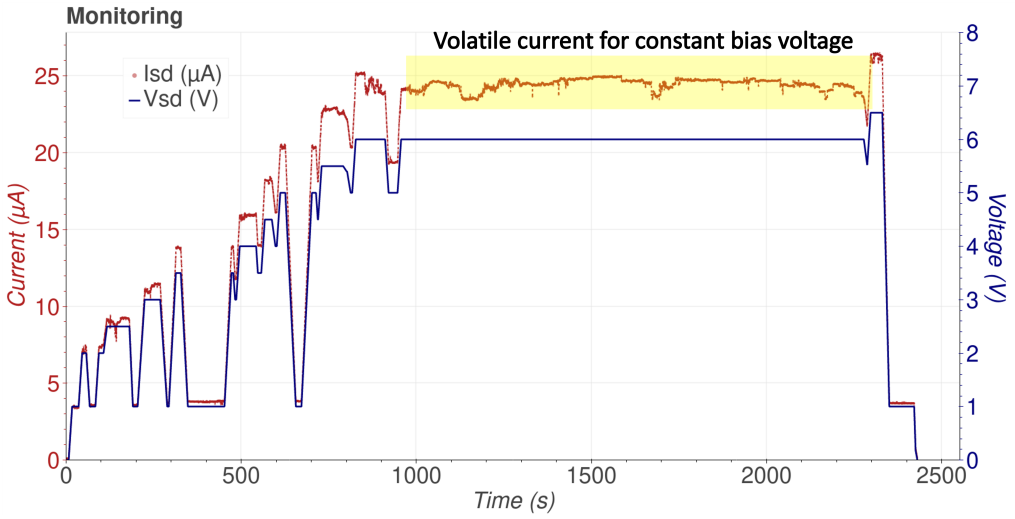

Figure 5.4: **Current and voltage monitoring for a low barrier voltage device** (additional inline resistance 100 kΩ. The device showed ohmic behaviour down to low applied bias voltages and a resistance of ≈160 kΩ at 1 V. For large bias voltages, the current showed instable behaviour, indicating that the local configuration at the interface was not stable, yet.

advantages the stamping technique has compared to the top-growth procedure. Additionally, creating these temperatures inside the SEM will almost certainly cause troubles for the equipment.
As a summary of these tests, it can be said that we successfully stamped CNTs onto electrodes using molybdenum as the contacting material and that an overall resistance in the hundreds of kΩ was detected. These values are an order of magnitude larger than what we found when using palladium as the contacting material, making the latter the preferred choice of material.

5.3 Transport measurements on top-growth multi-gate carbon nanotube devices

In this section, electronic transport measurements at cryogenic temperatures conducted on carbon nanotube devices fabricated via the top-growth process (see sec. 3.3.1) are presented. The data presented was mostly measured on four individual devices (*K47, I18, D67* and *I54*) and measurements will be attributed to these devices.

5.3.1 Room-temperature characterisation

The four devices featured a room-temperature resistance of R_{K47}= 257 kΩ, R_{I18}= 42 kΩ, R_{D67}= 110 kΩ and R_{I54}= 105 kΩ. Their respective gate dependence is plotted in figure 5.5. The devices I18 and K47 showed a clean, ambipolar gate dependence with little hysteresis, while I54 and D67 showed a deviation for negative gate voltages (hole conductance side). Their suspension length was between 650 and 750 nm as determined from SEM observations. Inside the cryostat we performed measurements

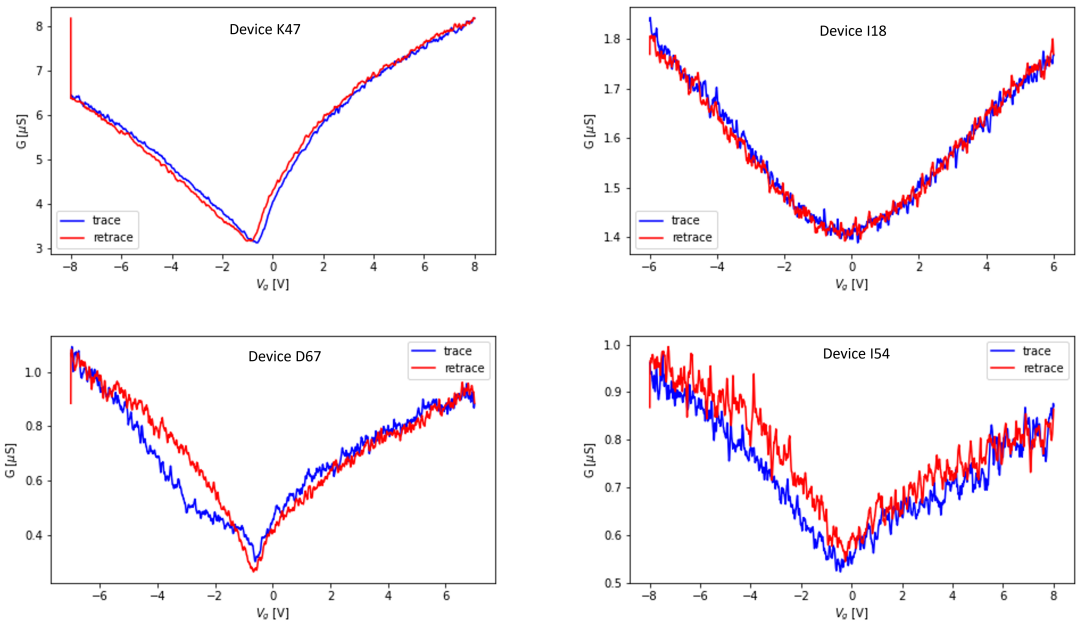

Figure 5.5: **Room-temperature gate dependence of four measured CNT devices.** The applied bias voltage was 10 mV. **Top left:** K47 with R_{K47}= 257 kΩ; **Top right:** I18 with R_{I18}= 42 kΩ; **Bottom left:** D67 with R_{D67}= 110 kΩ; **Bottom right:** I54 R_{I54}= 105 kΩ. Resistance was determined by fitting a line to an *I-V*-trace in the few tens of mV range. Overall, little hysteresis was detected for K47 and I18, while I54 and especially D67 showed some hysteresis.

on electronic transport across a single or a series double quantum dot and studied the mechanical resonance whenever we could detect it.

5.3.2 Single quantum dots

After cooling down a device, the characterisation routine typically starts by measuring a bias-gate map, i.e. measuring the electronic differential conductance as a function of applied bias voltage and gate voltage. This type of measurement is powerful in providing a general overview of obtainable transport regimes (see section 2.2), cleanliness and state spectroscopy. As a reoccurring feature, most of the devices showed much more expressed conductance for negative gate voltages indicating that hole conductance is stronger than electron conductance in these devices.

Bias-gate map of K47

An exemplary bias-gate map for a device (K47) showing unipolar p-conductance in the intermediate quantum dot regime is presented in figure 5.6. Areas in blue represent areas of constant conductance (not necessary zero) while red areas represent the availability of additional states. No electron conductance was observed up to a gate voltage of 5 V. A dominating hole conductance has been observed for many devices fabricated by top-growth or being exposed to air [53, 154, 176, 204]. One possible

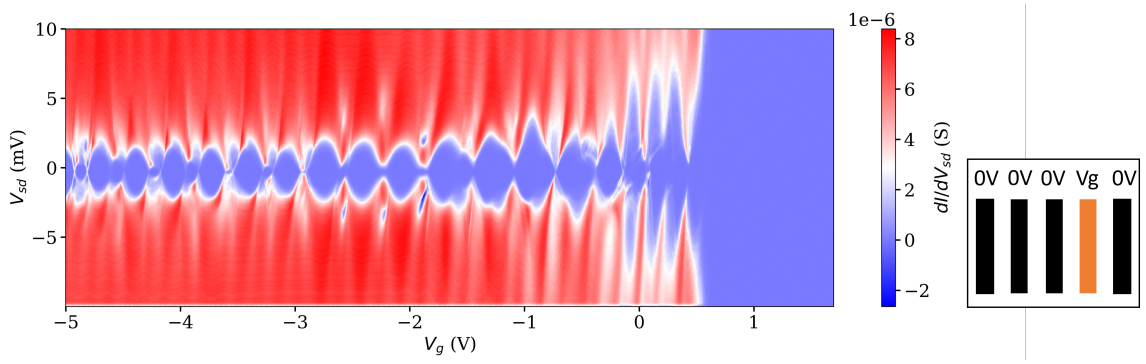

Figure 5.6: **Bias-gate-map of device K47.** Gate voltage applied on gate 4. For negative and slightly positive gate voltages, Coulomb diamonds are visible. For larger positive gate voltages, no conductance was measurable.

explanation is the surface coverage of CNTs with adsorbates or the influence of oxygen which is compensated at room-temperature due to the available thermal energy.

The appearing Coulomb-diamonds follow a regular pattern with a size that is slowly decreasing towards larger gate voltages hinting at a limitation of the constant interaction model, i.e. a dependence of the addition energy on the number of charge carriers in the quantum dot which contradicts the assumption of a constant interaction. An alternative explanation could be an effective size increase of the quantum dot caused by the gate voltage modifying the tunnelling barrier width. By measuring the width and height of a Coulomb diamond we can estimate the gate lever arm $\alpha = \frac{\Delta V_{sd}}{\Delta V_g}$ to be approximately $\alpha \approx 0.013$. A gate lever arm this small states that the coupling is rather weak which means that the CNT is far away from the local gate. In this case, the CNT must be suspended. Due to the geometry of the gap between the contact electrodes ($\approx 200\,\text{nm}$ high and $\approx 700\,\text{nm}$ wide) it can be ruled out that the CNT touches the substrate and is only partially suspended while being far away from the central gate (asymmetric v-shape). At the same time, the map shows few jumps and irregularities indicating that the device overall is clean. Nonetheless, conductance at low bias voltages is reduced which could have many reasons. The most probable one is that the contact is not perfect and some bias is necessary to establish measurable tunnelling rates. Another possibility are forbidden vibronic ground-state to ground-state transitions blocking transport at low bias, but since no clear vibronic sidebands (appearing as conduction bands parallel to the Coulomb diamond's edge) are visible, this seems implausible. [21]

Excited states

When looking at the shape of individual Coulomb diamonds it becomes apparent that they do not have a clear diamond-shape but are rounded towards higher bias voltages. A deviation like this could be caused by smeared out excited states that cause a rounding of the Coulomb diamond instead of a clear horizontal cut or cotunnelling processes. A zoom in on the small gate voltage region even shows transport within a Coulomb diamond (see figure 5.7). Indicated by the yellow arrows it is apparent that

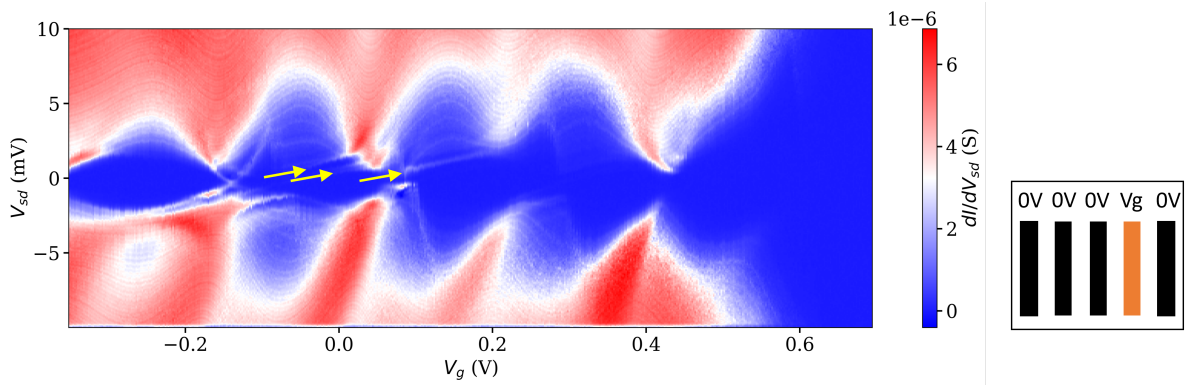

Figure 5.7: **Zoom-in on low gate voltage region of figure 5.6.** The Coulomb diamonds of the first electronic shell are about twice the height of higher shells. Inside the area of blocked transport, tilted lines of conduction, most likely caused by excited states, are visible of which some are highlighted by yellow arrows.

the excited states do not appear as horizontal lines but are tilted similar to what was shown in figure 2.9 [56]. This has been attributed to asymmetric tunnelling barriers in the past, an effect, that could already be explained by the top-growth mechanism itself where the CNT growth is initiated from a catalyst nanoparticle on a metal surface and terminated on a different electrode which is an intrinsic difference for the local contact. A further indication towards asymmetric tunnelling barriers is given by the asymmetry in the conduction areas separating the individual Coulomb diamonds. Looking at the conduction area at $\approx 0.4\,\mathrm{V}$, for negative bias it is well visible how the side facing more negative gate voltages is conducting stronger than its counterpart. This effect can also be seen at $-0.75\,\mathrm{V}$ and even a continuation at positive bias voltages, this time facing more positive gate voltages hinting at a common origin. Considering the energy level scheme introduced in the theory section (figure 2.6), in case of an applied bias voltage the energy barrier between the aligned levels has the stronger influence since there is no energy difference. In our data, it seems like the "right" barrier towards the drain is more transparent, though we have no means of linking it to the growth since start and end position of the latter are unknown.

Negative differential conductance

When paying close attention to figure 5.6 the colourbar showing negative values for the differential conductance raises questions. In figure 5.8 a zoom in on the features showing negative differential conductance is shown. In general, negative differential conductance hints at the availability of long-lived states that block the transport of charge carriers. When a long-lived state enters the bias window and gets occupied, transport is inhibited while this state is occupied due to a shift of the chemical potential. Thus, the appearance of a state like this can reduce the conductance. In the past, features of negative differential conductance have been attributed to coupling asymmetry caused by spin interaction with superconducting leads [205] which can be excluded due to our material choice. Another option could be an interaction between electron tunnelling and the mechanical motion [97, 206]. This feedback

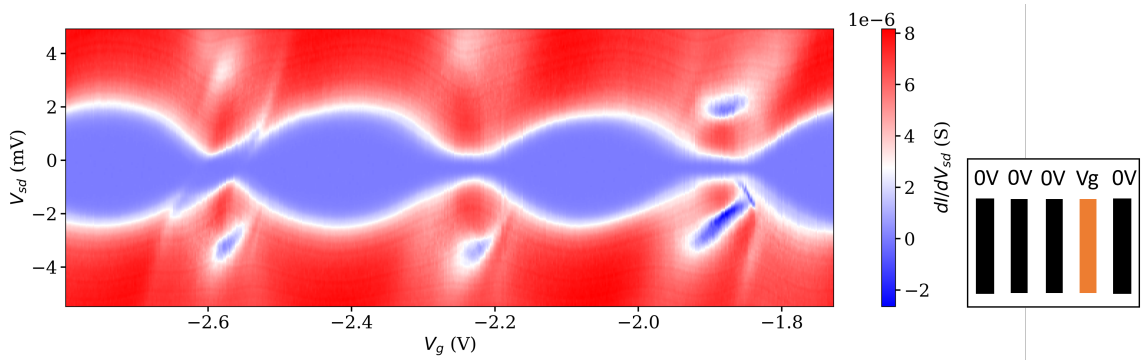

Figure 5.8: **Zoom in on regions with periodically arising negative differential conductance, appearing in dark blue, in figure 5.6.** We typically observed these features on conduction ridges in suspended samples

mechanism requires an electron tunnelling rate larger than the mechanical resonance frequency, an underdamped mechanical oscillator and a quantum dot with energy dependent tunnelling [206]. An underdamped mechanical oscillator can be driven to high amplitudes, even if the driving force is small and stochastic in nature [207] as is the case for electrons tunnelling in and out of a quantum dot which at the same time induces additional dissipation [208]. This dissipation can also become negative and in this case current spikes are to be expected [206].

Effects of current annealing

In contrast to the data shown so far, later devices partially also showed finite but clean electron conductance after 'annealing' the CNT inside the cryostat. In this case, annealing describes the process of driving a large dc-current through the CNT by applying a dc voltage of few Volts which causes local heating. The local heating is assumed to cause degassing of adsorbates and potentially also initiate minor local rearrangements especially at the CNT-metal interface. Since adsorbates can act as scattering centres and dopants, the transport properties are expected to improve. This technique proved to be successful for others groups as well [177, 209, 210]. For the determination of the current setpoint, we follow a similar procedure to the sample annealing during stamping. Using real-time monitoring we track the current while increasing the dc-voltage. Upon reaching a point of decreasing slope or even decreasing current caused by excitation of phonons [211] and additional scattering, we stay at this point for few tens of minutes before ramping the dc-voltage back to zero and giving the sample time to thermalise.

In figure 5.9 a bias-gate-map of sample D67 is presented which shows conductance on both electron and hole side. This data was acquired before and after thermal annealing and thermal cycling of the sample. Before these two steps, the sample showed predominantly hole transport and an overall much less regular behaviour (see upper panel of figure 5.9). After annealing, hole transport was still more expressed, but a very regular pattern of Coulomb diamonds is observable. Again, one pair of edges of the Coulomb diamonds is more expressed. For this map, the gates 2-4 were used for setting the gate voltage resulting in a larger lever arm. It also appears that there are two superposed periodic patterns

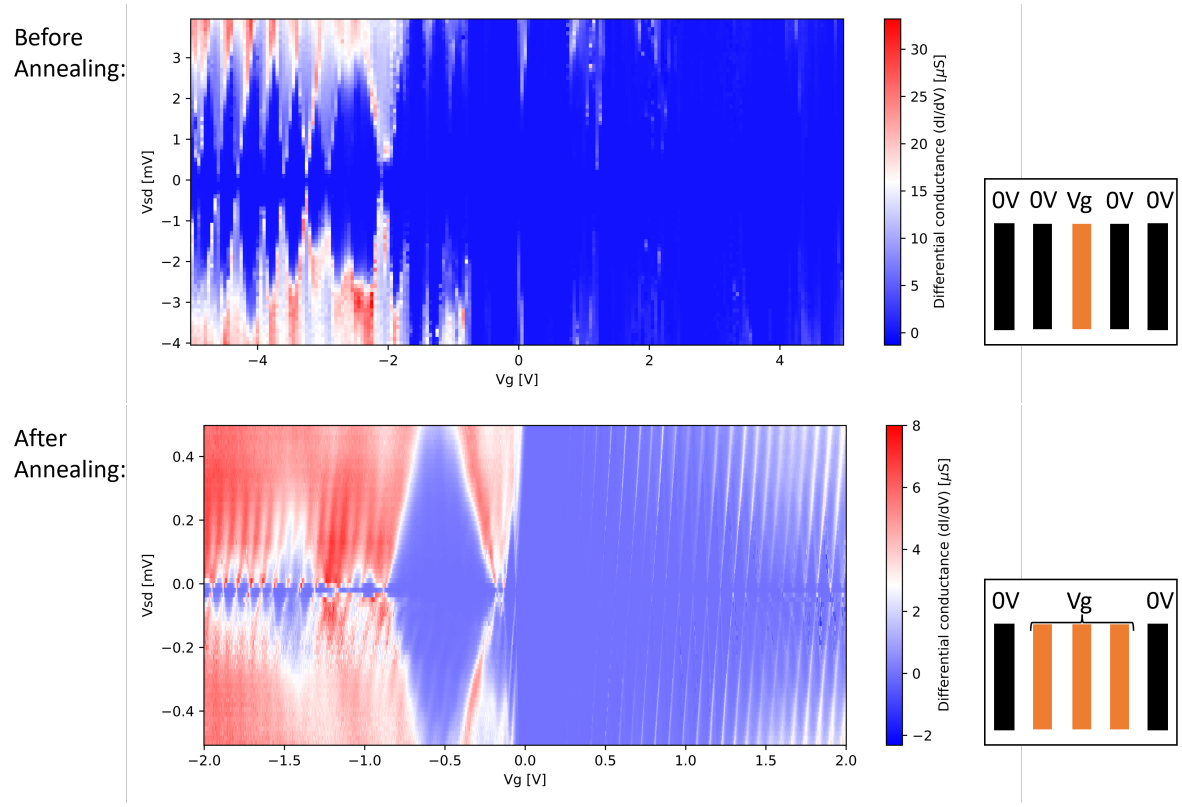

Figure 5.9: **Bias-gate-maps of device D67 showing the effect of current annealing on a sample with favoured hole-conductance but finite electron conductance. Upper panel:** Before annealing, the device showed hole dominated transport and noisy behaviour. Conduction on electron side exists but Coulomb diamond tips are spaced by > 1 mV. Gate voltage applied only on gate 3. **Lower panel:** The apparent superposition of two pattern with different periodicity hints at two parallel CNTs. A clear Coulomb blockade regime is visible for positive gate voltages (electron conductance) while negative gate voltages (hole conductance) seem to result in an intermediate regime. Gate voltage applied on gate 2,3 and 4, which causes the stronger coupling but not the cleaner data. Conductance partially saturated for visibility of electron side.

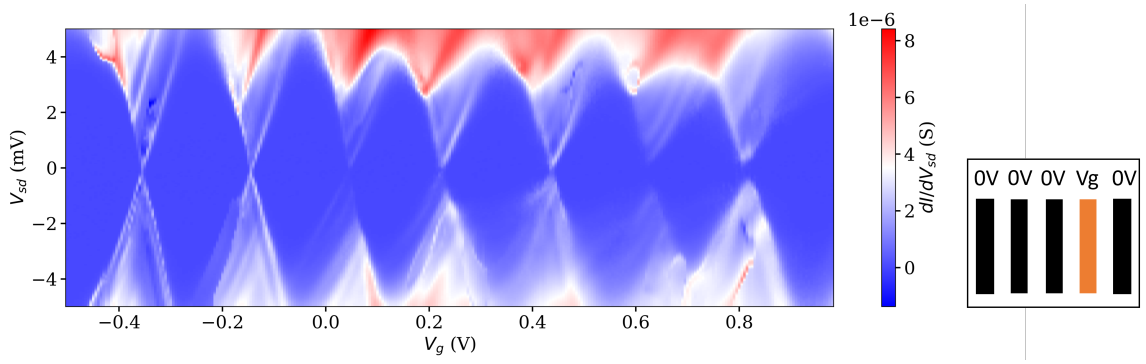

Figure 5.10: **Bias-gate4 map of device I54.** At the point of this measurement the device has survived four cooldowns to mK-temperatures, days in ambient conditions and two SMM evaporation processes while still showing rather clean Coulomb blockade behaviour, excited states and negative differential conductance.

which is a strong indication towards two parallel nanotubes and in consequence two parallel quantum dots. This is in agreement with the observed kink in the room-temperature gate-dependence (figure 5.5) that is not explicable with a single, pristine carbon nanotube. Why the conductance is reduced to almost zero in the region of the very large Coulomb diamond at −0.5 V is not obvious and requires both potential CNTs to be non-conductive over this parameter range. Why this apparently coincides for the two nanotubes is unclear to the author as it is unlikely that it is the same nanotube crossing the same junction twice (possible after doing a U-turn).

As an example for the robustness of CNT-devices fabricated in the presented top-growth process a bias-gate 4 map of device I54 is shown in figure 5.10. At the point of this measurement, this device has sustained two full cooldowns (i.e. from room temperature to mK-temperatures) and one molecule evaporation process while being not contacted with bond-wires and another two cooldowns with one molecule evaporation process after being microbonded. The bias-gate map in itself shows a regular Coulomb diamond pattern without fourfold periodicity. The lines parallel to the edges of Coulomb diamonds in the areas of higher conductance indicate the presence of transport via excited state cotunnelling. The spacing of the individual Coulomb diamonds represents a small gate lever arm which means that the nanotube was likely still suspended. However, no measurements on the nanomechanics were performed on this device to prove it, but small pockets of negative differential conductance also hint in the direction of a suspended nanotube. The fact that Coulomb diamonds are closing demonstrates the absence of a strong tunnelling barrier or electron-vibron coupling blocking transport at lower bias.

5.3.3 Double quantum dots in top-growth NEMS

So far the discussion was limited to the formation of a single quantum dot formed within the CNT. But since the devices cooled down typically possessed four or five functional local gates (sometimes losses due to alignment of lithography steps or damage during the CVD-growth made some gates unusable) it was possible to divide the large single quantum dot into two smaller quantum dots in

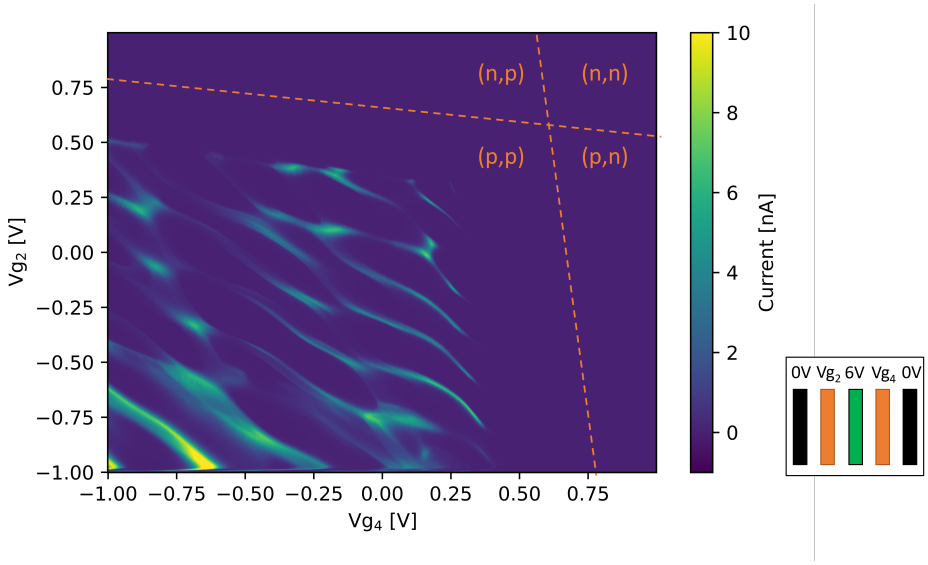

Figure 5.11: **Gate2-gate4 map of device K47 with an applied barrier voltage of** 6 V **and gate 1 and gate 5 on floating potential.** The inset on the bottom right shows the applied voltages to the gates, the bias voltage was 1 mV. Due to time constraints no lock-in measurement was performed. The dashed lines give an approximation to the four expected quadrants. No conductance is observable when either dot is tuned to an n-conducting state. The map shows weak coupling between the two dots between -0.5 to 0.4 volt which is slowly converting to strong coupling when the voltages approach −1 V.

series. Some theory for this and how to generally read gate-gate maps (charge stability diagrams) has been introduced in section 2.2.4. The data presented in the following was acquired using the devices K47 and I18, which unfortunately both showed strong unipolar hole conductance and gate-gate maps (charge stability diagrams) are thus focused on the (p,p) quadrant. Bias-gate maps study one cross-section of a gate-gate map as a function of bias and the latter is thus a complementary technique to understand transport behaviour of the device.

In our devices, typically three gates were needed in order to form a controllable double quantum dot. Two gates were used to tune their respective dot while the third gate placed between them was used to manipulate the interdot barrier. The confinement between the dots and their neighbouring electrode was given by the, albeit small, interface barrier. An exemplary map for device K47 where the gates 2 and 4 were tuned from −1 V to 1 V with an applied voltage at gate 3 of 6 V is shown in figure 5.11. Gate 1 and gate 5 were at a floating potential. In order to measure a current, a dc-bias voltage of 1 mV was applied. The charge stability diagram only shows conductance in the lower left quadrant where both dots are tuned to a p-conducting state. If either dot is tuned to an n-state, transport was blocked for this device. In the room-temperature measurements, conductance was measured for electrons and holes. From annealing of stamped devices it is known that the ratio of electron/hole conductance and the bandgap position can shift [57] which could have shifted the onset for electron conductance to higher gate voltages. An interesting question that arises is how much a third dot with n-conductance

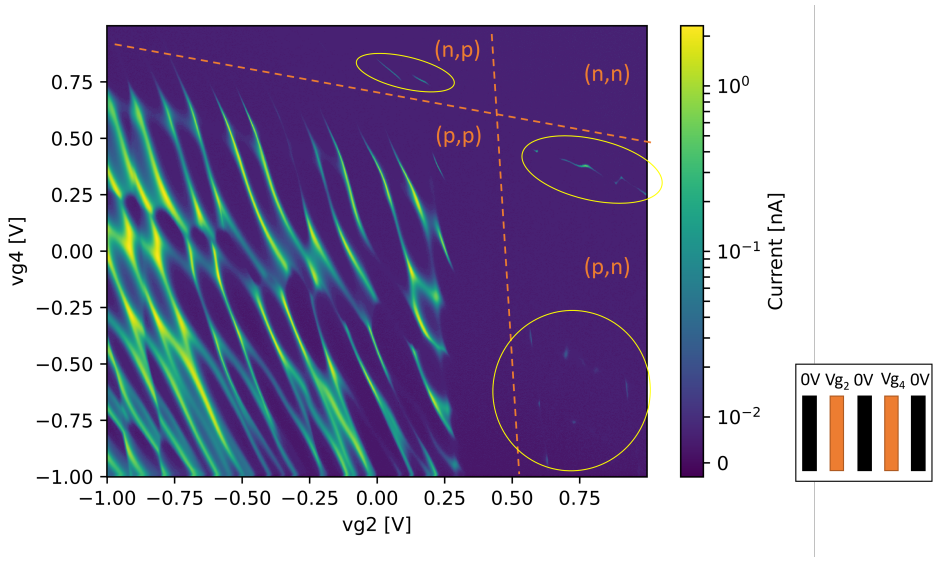

Figure 5.12: **Gate2-gate4 map of device I18** with an applied bias of 0 mV, which was offset by the setup at few hundred μV. The voltage at gate 3 was 0 V and the two outer gates were floating. The colourbar is plotted in a logarithmic scale to emphasise low conductance features at the cost of apparently broadened features in the (p,p)-quadrant. The two quantum dots are weakly coupled for the full range of applied gate voltages with suppressed conductance when gate voltages where $\geq$0 V. In the quadrants, where one of the quantum dots was tuned to electron conductance, very weak transport could be observed.

created in between the two p-dots will alter the transport. From this, information on the internal electron level structure and on the Schottky barriers could be inferred. Figure 5.11 shows two weakly coupled dots for the gate range of -0.5 to 0.4 V with a slow transition towards strongly coupled dots if gate voltages are more negative. Due to the applied bias voltage and large tunnelling rates, transport is not only observed at triple points, which in this case are appearing as roughly triangular areas of higher conductance, but also at the edges of the honeycomb shaped stable charge states. The two triple points at each avoided crossing are distinguishable in many cases, though the broadening sometimes results in a merging, effectively masking the avoided crossing.
Similar results were reproduced when studying device I18, which also primarily showed hole conductance with few, narrow and weak conductance ridges on the electron conductance side. For the most part, the charge stability diagram of I18 (see figure 5.12) behaved analogous to the one of K47, with the small distinction of little but finite transport (highlighted by yellow ellipses) if either of the two quantum dots, but not both, is tuned to an electron conducting state. It should be noted that the colourbar in this case is plotted in a logarithmic scale to make features with small current values more visible. At the same time this may cause misleadingly broad features in areas with larger conductance. Upon increasing the barrier voltage applied on gate 3, the four quadrants are shifted towards more negative gate voltages. An exemplary charge stability diagram for device I18 with an applied voltage on gate 3 of 3 V is shown in figure 5.13. In the top right corner transport is mostly suppressed as a result of the influence of the barrier gate on the quantum dots which basically shifts the quadrant boundaries.

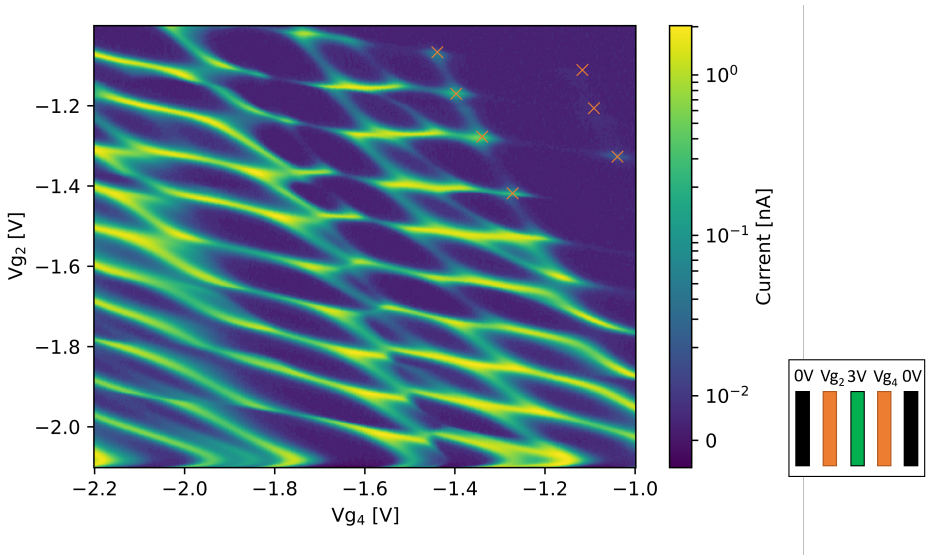

Figure 5.13: **Gate2-gate4-map of device I18** with an applied bias of 0 mV and a barrier voltage at gate 3 of 3 V. Plotted in logarithmic colourscale to make low conductance areas visible. Gate 1 and gate 5 were at floating potential. The two quantum dots are mostly in the intermediate coupling regime with the exception of the top-right quadrant where a progression into a weakly coupled regime, indicated by a more rectangular shape of constant charge areas and the absence of triple-point splitting.

Here, intermediate coupling with the typical honeycomb pattern is visible for most of the applied gate ranges. In the upper right quadrant of the figure, the interdot coupling is ever decreasing with increasing gate voltages (to positive values) represented by a slow transformation of the honeycomb pattern to a more rectangular shape. The triple points in this weakly coupled regime are further highlighted with orange crosses to increase their visibility. The splitting between electron and hole conduction processes caused by the interdot interaction seems to vanish complementing the argument for a decoupling of the dots by an increasing barrier voltage.

Our measurements show, that the top-growth technique presented in this thesis is suited to create double quantum dots with control over the interdot coupling using only three out of five possible gates. The usage of five gates would have given more freedom and therefore likely have given cleaner data or data at a wider parameter range. Even though transport in the devices tested was mostly limited to the (p,p)-quadrant, proper tuning of the barrier gate in the centre allows to vary the coupling from strong (single quantum dot) to weak (two almost independent quantum dots).

5.3.4 Nanoelectromechanics in top-growth suspended carbon nanotubes

Besides measuring electronic transport across one or two quantum dots inside the nanotube and tuning its conductance behaviour with varying gate voltages, we can make use of the nanotube being suspended and study mechanical resonances. The relevant theory has been introduced in section 2.4. This section presents data acquired on nanomechanical features, such as high quality bistable mechanical

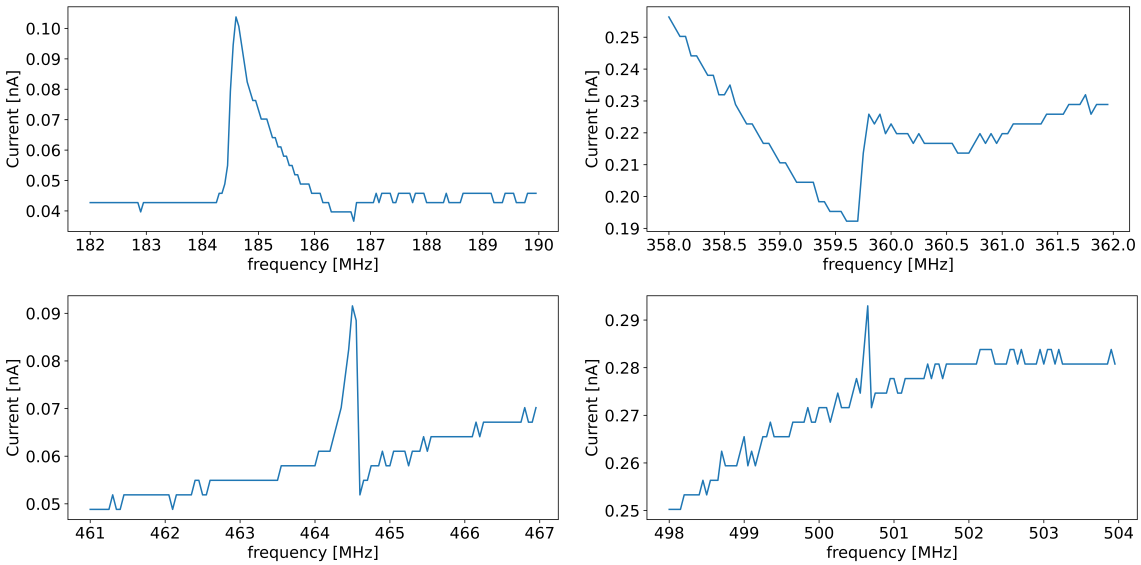

Figure 5.14: **Compilation of current measurements as a function of applied rf-frequency sent by an antenna.** The sweep was performed at V_{g3}=−2.95 V and V_{sd}=−200 µV. Further measurements on the device were performed on the resonance at ≈ 184-185 MHz, which was proven to be a CNT resonance. The sweep was performed from low to high frequencies. Due to time constraints only current was measured as lock-in measurements at this time took three to four times as long. The low current resolution is a (now resolved) binning artefact within the measurement software and not the physical resolution achieved.

resonances and tunnelling induced alterations, acquired on device K47. Similar measurements have been performed on other devices as well and followed the same trend.

As a short reminder: For top-growth devices we measured mechanical features by applying an oscillating voltage to an antenna in the vicinity of the CNT thereby emitting an oscillating electric field. Measurements performed this way mostly rely on current rectification to create a measurable signal induced by the mechanical resonator. Since this technique induces a change of conductance in the CNT depending on the local curvature of the conductance with respect to the gate voltage, it was necessary to determine a position in gate voltage with a large curvature $\frac{\partial^2 G}{\partial V_g^2}$. Since a larger bias voltage typically leads to a larger current and hence more tunnelling induced losses (see sec. 2.4.7) we initially try to keep the bias voltage small to observe the resonance with only small perturbation. Measurements on the mechanical bending modes were mostly performed on K47 and I18.

After choosing a proper electrostatic working point with a mechanically uncharacterised carbon nanotube, a first sweep performed covers a large frequency range in order to find mechanical resonance frequencies as well as harmonics. A small compilation of features that are caused by mechanical resonances of the carbon nanotube on device K47 are shown in figure 5.14. The clearest indicator pointing to the CNT as the cause of the resonance is a bifurcating resonance shape caused by the bistable behaviour of the resonator. The sign of the conductance change as well as the sign of the Duffing parameter are determined by the tuning point (see sec. 2.4.7). We identified the resonance at 184 MHz to be the

strongest resonance mode caused by the CNT and focused the analysis on this specific resonance mode.

Power dependence of the mechanical resonance

Since the shape of the bifurcating resonance strongly depends on the applied power a reasonable next step is to test the power dependence of the resonance. If the resonance follows the behaviour of a Duffing oscillator, as would be expected for a CNT bending mode, a strong broadening with increasing power in only one frequency direction will be observed. If the resonance has a Lorentzian shape power broadening will also occur but to a smaller extent. If the resonance is caused somewhere else in the measurement setup, the power broadening should not be as strongly expressed, symmetric in frequency and also no bifurcation should arise. In figure 5.15, the power dependence of the 185 MHz resonance is shown in a colour map. Two features are striking: First, the resonance width increases from left to right before reaching a stable state at the highest applied powers and second, every other trace features a much more narrow resonance. The first observed feature of increasing resonance broadening towards higher powers is rather straightforward and textbook behaviour for a bifurcating resonance. A comparison of four different driving powers extracted from 5.15a) is given in figure 5.15b). It is apparent that both the amplitude as well as the width are increasing and that the vertical signal jump at the resonance peak is shifted to ever higher frequencies while maintaining the same onset frequency. The onset frequency is expected to change as well due to power broadening, which could not clearly be observed hinting at a narrow resonator linewidth. The effect of every other trace featuring a more narrow resonance, apparent in the colour map, can be explained by looking at the measurement routine which included a meander-type frequency sweeping. Here, meander describes that one trace was measured with increasing frequency while the next trace was acquired with decreasing frequency. This is basically measuring trace and retrace and resembles hysteresis measurements. In figure 5.15c), trace and retrace of the resonance in a strongly bifurcating range is shown. Looking at the two curves it becomes apparent why every sweep going from low to high frequencies features a broad resonance and every sweep from high to low frequencies a narrower resonance shape. It is worth noting, that the bifurcation can be observed in both cases, though the signal jump is much more expressed in case of an upwards sweep. This type of hysteresis only vanishes, once the system reaches a linear regime and the resonance shape becomes Lorentzian again. At highest powers, the meandering behaviour disappears which is explained by an ever increasing resonance broadening up to a point, where the system always remains on the upper branch and the amplitude jump is outside the measurement window. This shows, that the system is rather stable on this upper branch as it could remain there for minutes during the frequency sweep without dropping to the lower branch.

On a sidenote, it is worthwhile mentioning that the frequency sweeps were performed by setting a frequency and then measuring the response of the system. When setting a new frequency, the phase of the outputted signal is not necessarily continuous which causes a jump in output amplitude. This phase shift caused by a high frequency component consequentially causes an additional uncontrolled phase shift between the applied rf-signal and the CNT oscillation. Given that the resonator is in a metastable state during the measurement, this phase-jump of the driving force could

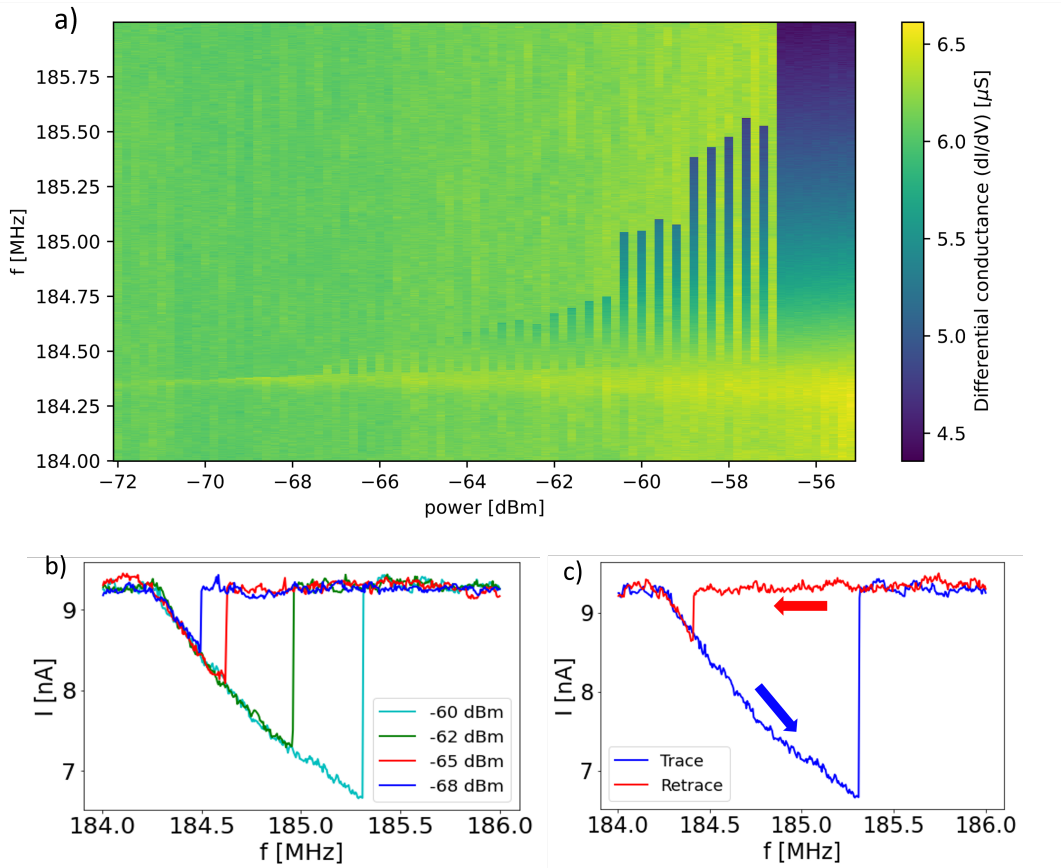

Figure 5.15: **Power dependence of the resonance at** ≈ 185 MHz**. a)** Colour map showing the differential conductance as a function of rf-power and rf-frequency. Vertical traces are acquired alternating between sweeping from low to high frequencies and high to low frequencies. For high powers, the resonance width reached a point at which no amplitude drop to the lower branch was observed anymore. **b)** Vertical cuts acquired for upwards sweeps only. The increasing broadening, but same onset frequency, with increasing power is clearly visible. **c)** Trace and retrace measurement at -60 dBm. The hysteretic behaviour observed is the result of the two branches expected for a Duffing oscillator.

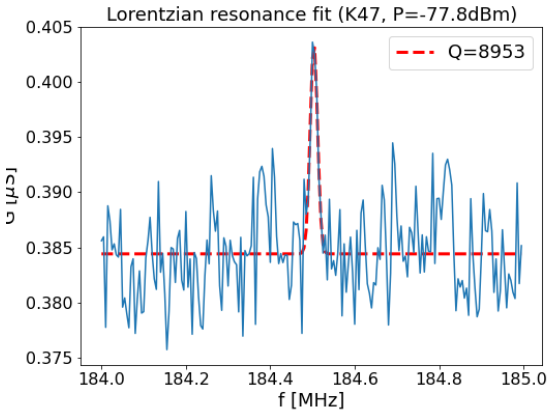

Figure 5.16: **Frequency sweep with a Lorentzian fit to determine the quality factor Q.** Acquired at a power of -77.8 dBm, bias voltage of $-200\,\mu V$ and a gate voltage of V_g=$-2.95\,V$.

induce additional and unwanted perturbations that could be detrimental for the resonator performance.

Determining the quality factor

The increasing broadening at higher powers also means that determining the true shape of the mechanical resonance becomes challenging. The broad slope of the resonance when measuring the trace is cloaking the actual width at the base of the resonance and while the retrace is giving a better approximation of the base width, it still does not give any clear information on the linewidth like the FWHM does. We can thus assume that when determining the width or FWHM of the resonance while in a power range with bifurcation, the estimated quality factor Q given by $Q = \frac{\omega}{\Delta\omega}$ is a lower boundary. Towards lower powers, the resonance shape should at some point revert back to a Lorentzian shape, which we could however not observe before the signal was vanishing in the noisefloor. We thus evaluated a measurement at low driving power and approximated the resonance with a Lorentzian (see figure 5.16). We determined a value of $Q \approx 8900$ with variations, depending on the quality of the fit, for similar applied powers between 5000-12000. As previously mentioned, this value only serves as a lower boundary. By properly tuning the working point, increasing signal-to-noise ratio, lowering the rf-power, decreasing the frequency step and sweeping the frequency in a phase-continuous way it is likely possible to increase the quality factor. Thus, these devices did not show a quality factor as high as reported for previous work [19, 103], but still show a reasonably large quality factor even for non-optimised parameters.

Tunnelling induced spring constant softening

In section 2.4.7, the interaction between single-electron tunnelling and mechanical bending modes has been introduced and described. Another possibility to verify the origin of the detected resonance while probing electron-phonon coupling is to measure the gate voltage dependence of the resonance.

Changing of gate voltage should not affect resonances caused somewhere in the cables or the cryostat. In figure 5.17, a measurement tracking the mechanical resonance across the Coulomb peak at a gate voltage of about −2.9 V, where previous measurements have been carried out, is presented for two different driving powers. At -66 dBm, i.e. the upper panel, the spring softening due to electron tunnelling manifesting as a dip of the resonance frequency is visible for the high Coulomb peak but also faintly for the weaker shoulder peak. The sign of the peak matches the expectation of a positive sign (yellow) at the flanks of the Coulomb peak and a negative sign (dark blue) close to the peak due to the dependence of the read-out technique proportional to the local curvature $\frac{\partial^2 G}{\partial V_g^2}$. When paying close attention, it can be noted that the negative peak values are arranged slightly asymmetric in terms of gate values with respect to the frequency minimum which cannot be explained by the local curvature only and the current rectification technique. However, when taking into account that our device under test is by no means an ideal device and crosstalk and crosscoupling can and will occur we can expect a finite amount of rf-signal being transmitted from the antenna into the source-drain lines. As a consequence, besides current rectification also frequency mixing will take place in the CNT causing an additional mechanical signal proportional to the first derivative $\frac{\partial G}{\partial V_g}$ or transconductance of the CNT. When this effect is weaker than the current rectification it perturbs the symmetry around the minimum and therefore nicely explains the measured data. Given that the signal was applied by a wirebond functioning as an antenna, this type of crosstalk is likely.
In the lower panel of figure 5.17, the same measurement is shown when using a higher rf-driving power. As was established in figure 5.15, an increasing driving power causes the resonance peak to extend further in the sweeping direction. This effect is again visible when comparing the resonance shape for the two different driving powers (note the same y-axes). At the same time, it is interesting that the onset frequency of the mechanical resonance peak shifts in the same fashion across the Coulomb peak as it does for the lower driving power, basically stating that the driving power has no influence on the observed spring constant softening. The asymmetry of the peak sign with respect to the frequency minimum could not be reproduced. For the more expressed Coulomb peak, the frequency at which the resonator leaves the higher amplitude branch of the bistable resonance and "falls" back to the baseline appears to be constant over a broad range. In general, this type of measurement offers a great opportunity to study the coupling between electron tunnelling and mechanical bending modes. In order to understand the behaviour of the device under test better, it would have been helpful to acquire the frequency-gate map in the same parameter range with additional different powers in order to increase nonlinear effects caused by the mechanical properties of the CNT and with different applied bias voltages which affect the tunnelling rate. In doing so, a better understanding of the system and the interactions could have been achieved.

5.4 Transport measurements on stamped multi-gate carbon nanotube devices

At about half-time through this thesis, the focus of our group shifted from devices fabricated with the top-growth technique towards devices, where the CNT is integrated via stamping. The Pros and Cons have been thoroughly discussed section 3.3 and the arguments will not be repeated here. The data

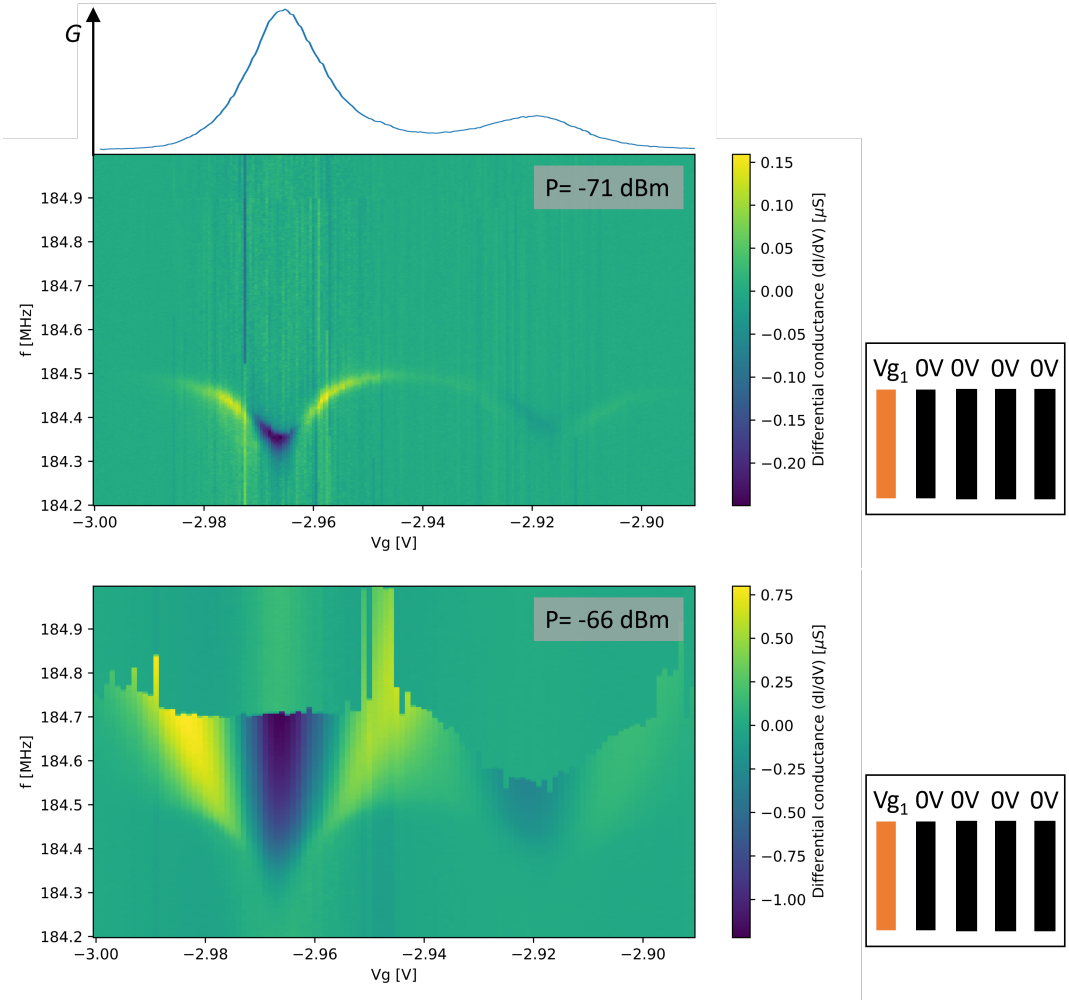

Figure 5.17: **Differential conductance of device K47 measured as a function of gate voltage and applied rf-frequency.** The plotted values for the differential conductance are plotted as the difference to the average of their respective vertical trace. Frequency sweeps were performed upwards at a bias voltage of −200 µV. Upper panel: Gate dependence at a driving power of -71 dBm. The dips of the resonance frequency occur, whenever a Coulomb peak is crossed, i.e. the conductance is maximum. The conductance showing a Coulomb peak with a weaker shoulder peak is given qualitatively on top of the resonance frequency-map was measured at a frequency of 183 MHz. Right: Gate dependence at a driving power of -66 dBm. The higher driving power increases the resonance width drastically while keeping the same onset frequency and causes the amplitude jumps of the resonance to occur roughly at the same frequency on a Coulomb peak.

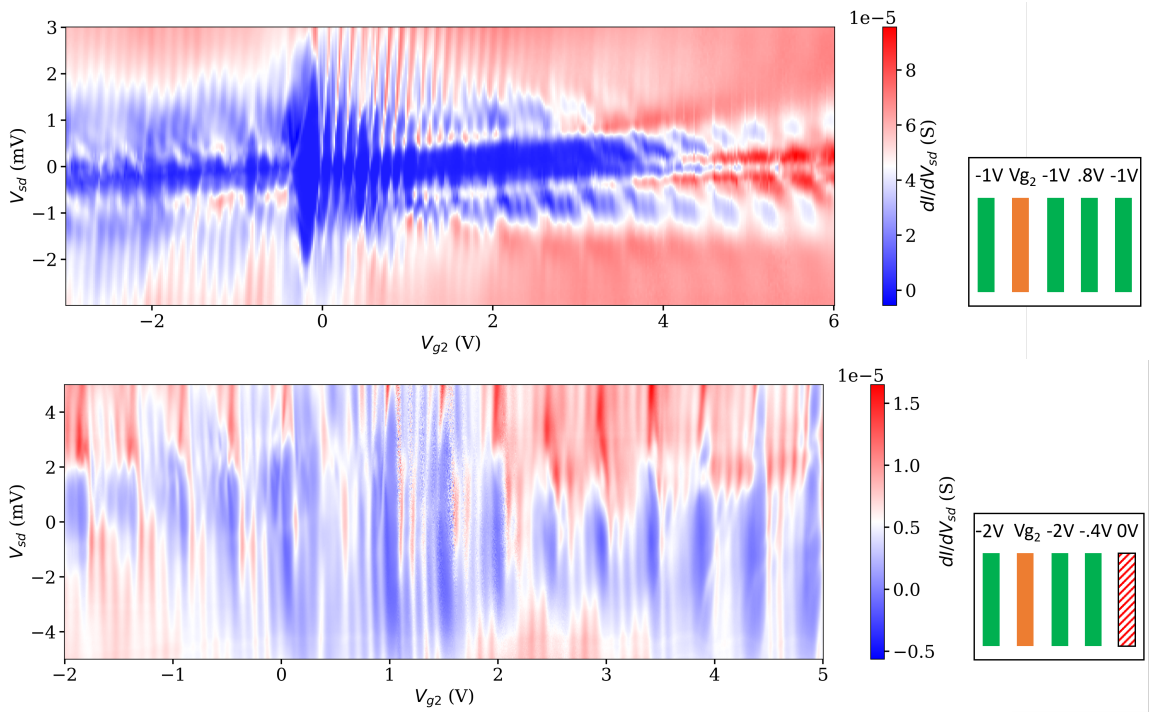

Figure 5.18: **Bias-gate maps for the two CNTs on chip EA5. Upper panel:** CNT EA5-1 showing Coulomb blockade behaviour in the few electron and hole conductance gate range before transitioning into a more irregular pattern at higher gate voltages. Stepped gate 2, gate 1,3,5 at −1 V, gate 4 at 0.7 V. **Lower panel:** CNT EA5-2 shows a more regular pattern of Coulomb diamonds for a large gate range. A fourfold periodicity or clustering of four conduction ridges is clearly visible for the full applied gate range. Between +1 and 2 V a region of instability emerges, most likely due to interaction with the environment.

presented in this section was acquired inside the cryostat at mK-temperatures after transferring the samples into the cold cryostat in vacuum. The data presented was measured on two different chips (*EA5* and *FA3*), both including two CNTs each that do not share any contact electrodes.

5.4.1 Measurements on single quantum dot

Bias-gate maps for device EA5

Analogous to the procedure on top-growth devices, it is instrumental to acquire a bias-gate voltage map in order to get an overview of the device, its cleanliness and integrity, the gate coupling, transport regimes, excited states etc. Interestingly enough, all four CNTs show quite different behaviour and could easily be distinguished by looking at these bias-gates map. Therefore, the data for all four CNTs is shown in this section.

A comparison of the bias-gate maps for the two CNTs (EA5-1 and EA5-2) stamped on EA5 is given figure 5.18. Since both measurements were taken on the same chip, no difference in the metal-circuit fabrication has occurred and all deviations necessarily include some interaction with the CNTs. In

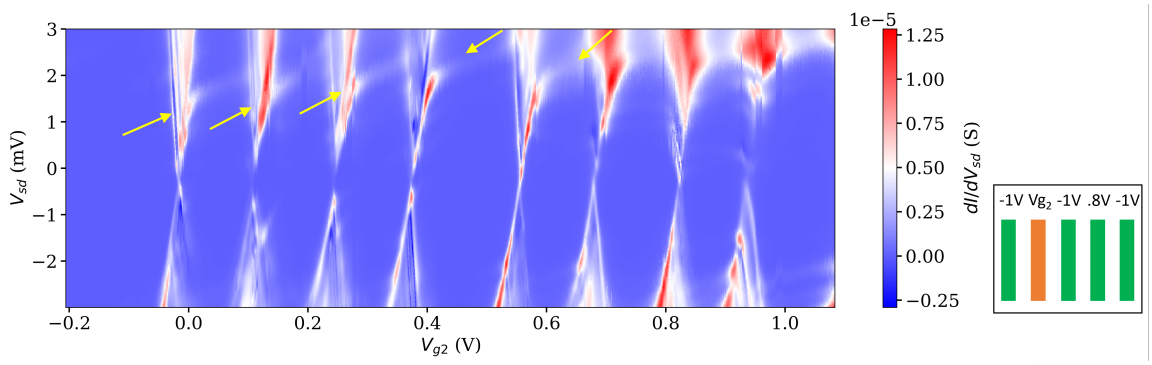

Figure 5.19: **Bias-gate map of CNT EA5-1 with focus on the Coulomb blockade regime.** The CNT shows tilted excited states caused by asymmetric tunnelling barriers (yellow arrows) inside the Coulomb diamonds as well as negative differential conductance, in particular on the Coulomb peak at about 0.38 V in combination with excited states parallel to the Coulomb diamond edge.

contrast to many devices fabricated with the top-growth technique, both maps show electron and hole-conductance as would be expected from very clean devices. Device EA5-1 (upper panel of fig. 5.18) shows rather clean Coulomb-diamonds for few charge carriers and fourfold periodicity arising from the spin and valley states of the CNT. In the hole-conductance side the CNT remains in a Coulomb blockade regime and apparently the first higher order Coulomb diamond is visible as well. Since differential conductance is plotted, the presence of extra Coulomb diamonds at higher bias hints at a low density of higher energy states. For positive gate voltages, i.e. the electron side of conductance the CNT remains in a regime of Coulomb blockade with progressively broadening features and fourfold periodicity until two shells are fully filled before converging to a much more irregular pattern with a band gap in the order of 0.5-1 mV that additionally slightly shifts with increasing gate voltage. The origin of this emerging gap is unclear to the author. For even higher gate voltages, Kondo ridges emerge in the low-bias range and the band gap fully vanishes. Overall, the device shows unexpected and irregular behaviour for gate voltages >1 V that cannot easily be explained and could hint to interaction with the environment.

When zooming in on the few electron regime (figure 5.19) where Coulomb diamonds have been observed the regular Coulomb diamond pattern for the first seven electrons added to the quantum dot becomes more obvious. Similarly to what has been observed for top-growth devices in figure 5.7, tilted excited states in the Coulomb blockade area as well as excited states parallel to the Coulomb diamond edge are visible and imply an intermediate coupling regime with coupling Γ comparable to the charging energy E_c ($\Gamma \simeq E_c$). Features of negative differential conductance, especially at a gate voltage of about 0.4 V may hint to a suspended CNT, an assumption which is supported by the gate voltage spacing of the individual diamonds.

For device EA5-2 (lower panel of figure 5.18) the bias-gate map shows a more regular behaviour. It appears that the CNT is always in a comparably well coupled Coulomb blockade regime featuring a fourfold-periodicity presenting itself as a clustering of conduction ridges for the majority of the gate

range. The device shows no bandgap as all Coulomb diamonds are separated. Between 1 V and 2 V of applied gate voltage, the measured signal became quite noisy for a certain bias window. Since this bias window was shifting with the gate voltage it appears that the CNT was coupling to some gate-tunable contamination which proved detrimental for the quality of the data without obscuring the features of the bias-gate map.

Bias-gate maps for device FA3

The bias-gate voltage maps for device FA3 are given in figure 5.20. The upper two panels show the behaviour of CNT FA3-1 before and after current annealing while the lower panel shows the behaviour of device FA3-2. Before annealing, CNT FA3-1 showed quite irregular behaviour in the hole side of conductance which appears for gate voltages <-1.2 V. A clear bandgap between electron and hole side is not visible but in this voltage range definitely a change of transport mechanism takes place. There is no clear periodicity but the differential conductance could reach rather high values up to 30 µS. On the electron side of conductance, the pattern appears to be far more regular with a fourfold periodicity arising with every third area of blocked conductance being more expressed as well. The shape of the features, resembling Kondo-features due to the two-fold periodicity, cannot be explained with Coulomb blockade or Fabry-Perot interference alone but rather some interaction, potentially also with the environment, must take place. In addition, the areas of blocked conductance become wider with an increasing number of electrons in the quantum dot. The assumed transition between electron and hole conductance still occurs at the same gate voltage after current annealing even though there is some conductance visible inside the bandgap which is a deviation from pristine behaviour and should be caused by some imperfection, like adsorbates, leakage or a parasitic parallel transport channel. Such a channel could be another CNT in a potential bundle. The electron side of conductance was cleaner after annealing indicated by the more regular pattern. The number of added electrons is increasing in the same gate range which either speaks for an increased gate lever-arm or smaller energy level splitting. The latter could be caused by an increased quantum dot size which is imaginable after current annealing and removal of 'dirt' on the CNT. The lever arm could potentially have also shifted, if the CNT is closer to the gates after current annealing which is unlikely, but possible, after local rearrangements at the CNT-metal contact. Additionally, this gate region at zero bias shows alternating occurence between three conduction peaks and 1 blocking area hinting at an SU(4)-Kondo effect. The overall appearance resembles more an interference pattern than a Coulomb-diamond shape indicating high tunnelling rate transport in the open quantum dot regime.
The bias-gate voltage map for device FA3-2 in the lower panel of figure 5.20 shows very regular behaviour of electronic transport in the Coulomb blockade regime for gate voltages >-2 V which should be caused by electrons. The Coulomb diamonds follow a strict periodicity, with observable fourfold periodicity. The diamonds are separated by conduction ridges which excludes a strong interface barrier necessitating a bias voltage to enable electronic transport. The conduction ridges show features of excited states and a small region of instability at about 1.3 V shifting with the bias voltage. The hole side of conductance is in the Coulomb blockade regime as well but featuring Coulomb diamonds of a larger height but with comparable width.

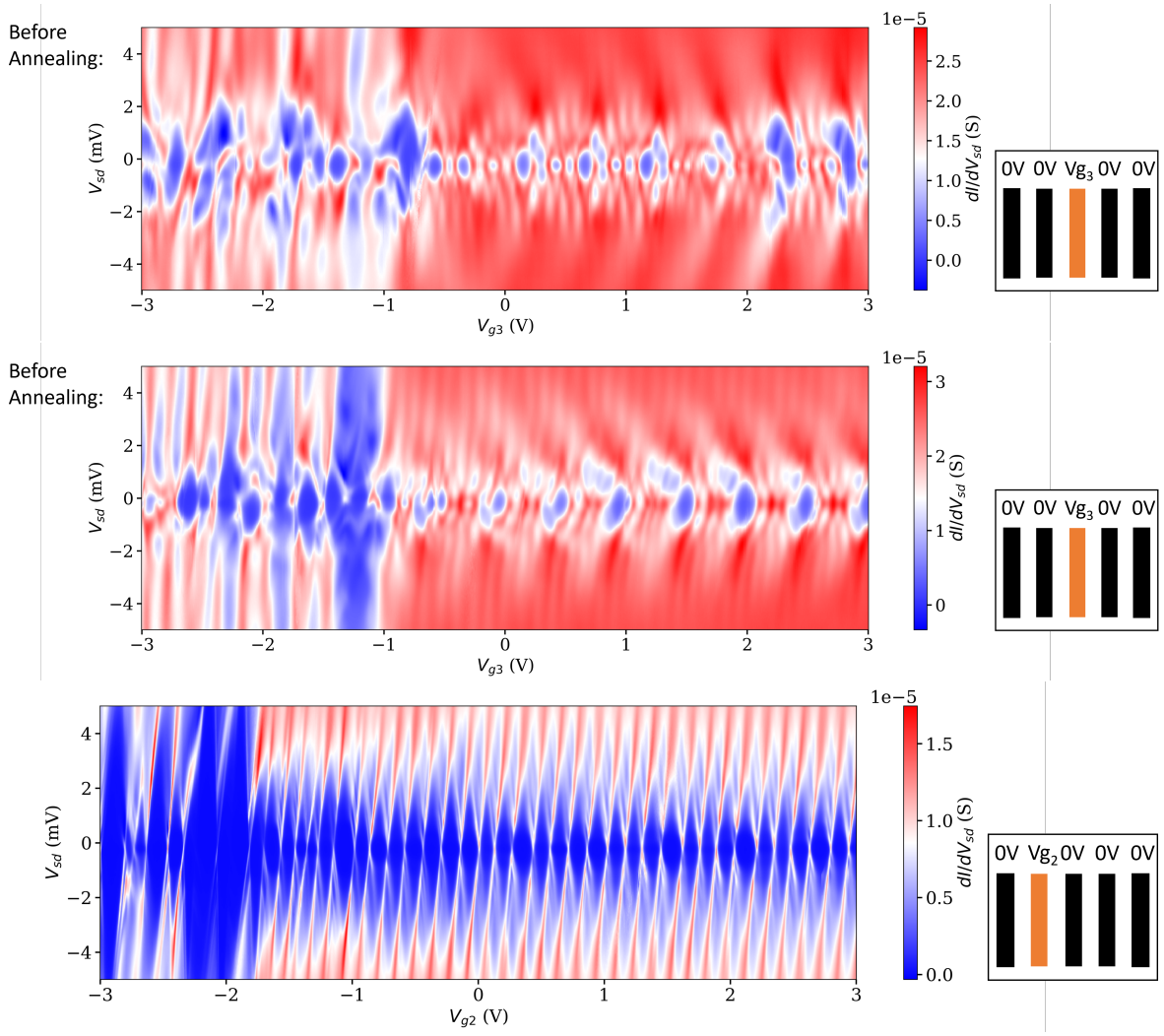

Figure 5.20: **Bias-gate maps of CNTs FA3-1 and FA3-2 on chip FA3. Upper and middle panel:** CNT FA3-1 before (upper) and after (middle) current annealing. The CNT shows irregular behaviour in the hole-conductance branch with many features of high conductance, also at vanishing bias voltage. The electron branch shows periodic features, resembling SU(4)-Kondo effect at larger electron numbers. **Lower panel:** CNT FA3-2 showing clean Coulomb blockade behaviour on the electron conductance side and less regular Coulomb blockade behaviour on the hole conducting side. Almost every Coulomb peak features excited states running parallel to the diamond edge.

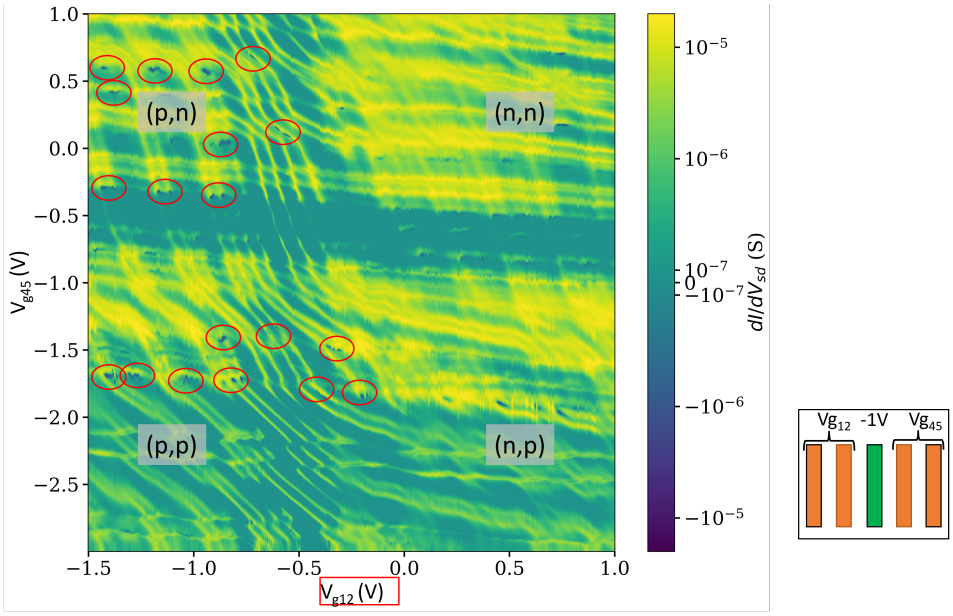

Figure 5.21: **Gate1,2-gate4,5 map measuring conductance (plotted in log-scale)** at zero bias voltage and the barrier gate 3 at −1 V. The band gap at about −0.5 V is reproduced only for gate 3,4. Several small areas of negative differential conductance are spread across the map in a rather regular pattern following the charge states. The four quadrants are highlighted and can be well distinguished, though their exact boundaries are not obvious and the shape of stable charge areas non-standard.

5.4.2 Double Quantum dots in stamped NEMS

Since all four devices had four to five functional local gates, we used the circuits to induce double quantum dots in series in the CNTs. In order to study double quantum dots, we acquire gate-gate maps that provide a charge-stability map for a fixed bias voltage. It can therefore be seen as a measurement of a horizontal cut in a bias-gate map as a function of another gate voltage probing the energy levels in both quantum dots as well as the coupling. Since the devices showed conductance for electron and hole side all four quadrants of a gate-gate map, i.e. the quantum dots are in (n,n), (n,p), (p,n) or (p,p) configuration, are expected to show some transport behaviour, though the maps will, judging from the bias-gate maps, show differences. All devices feature strong coupling between CNT and leads and thus show transport not only at triple points but also at boundaries between stable charge configurations.

Charge stability diagrams of EA5-1 and EA5-2

The bias-gate map of CNT EA5-1 showed several irregularities on the electron side of conductance which also show on a gate-gate map (figure 5.21). For this measurement, gates 1&2 as well as 4&5 were actuated in parallel, while the voltage at gate 3 was set to −1 V with zero set bias voltage (a finite offset from the IV-converter remained). The band gap that was visible in the bias gate map

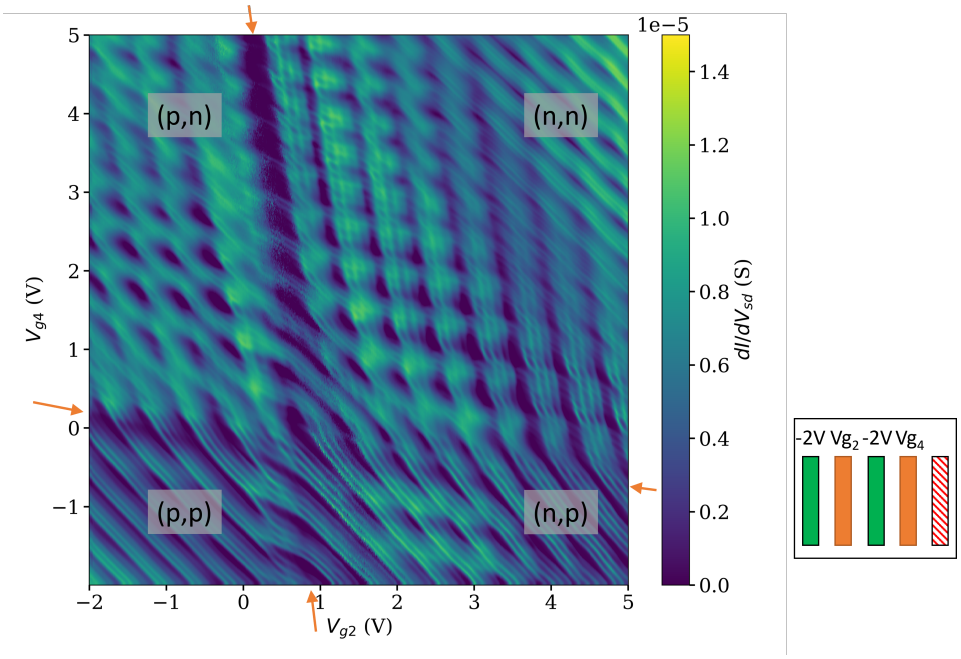

Figure 5.22: **Gate2-gate4 differential conductance map for device EA5-2** with gate 1 and gate 3 at −2 V at a bias of zero volt. The clear fourfold periodicity observed in the bias-gate map (5.18) is reproduced for both gate-axes. In the (n,n)-quadrant the interdot coupling changes from strongly to intermediate coupling with decreasing gate voltage. No bandgap between electrons and holes can be observed.

(figure 5.18) at ≈ −0.5 V is highlighted in the figure and separates differently doped areas of this charge stability diagram. Gate 3&4 seem to be able to suppress transport more efficiently than gate 1&2 as the horizontal manifestation of the gap is more expressed. Nonetheless, small areas of transport in the gap are observed. While many details of the map are non-trivial, noisy or indicate the presence of charge fluctuations in the vicinity, an interesting periodically reoccurring feature are pockets of negative differential conductance in regions with weak interdot coupling. These areas are mostly sharper for gate 3&4, meaning that these gates couple stronger and the origin is likely to be found in the right dot which is supported by the periodicity matching the Coulomb peak periodicity. The physical origin is, however, unexplored.

Device EA5-2 showed no clear bandgap in a bias-gate map (figure 5.18 b) and a clustering of Coulomb peaks to packs of four, giving fourfold periodicity. Both properties are reproduced when measuring the CNT while tuning two gates. The diagonal lines in packs of four in the (n,n) and (p,p) regime, for higher gate voltages, of the double dot signalise strong interdot coupling (i.e. the system is better described as one large quantum dot). In the (n,p) quadrant, the non-constant slope of conduction lines represents a weakened coupling and a transition to an intermediate coupling range. The same behaviour with even less interdot coupling can be observed in the (p,n)-regime. In the gate range of low positive gate voltages, the fourfold periodicity causes the formation of honeycomb-clusters close to the transition to weakly or uncoupled quantum dots. The noise band observed in the bias-gate map is detected again crossing the

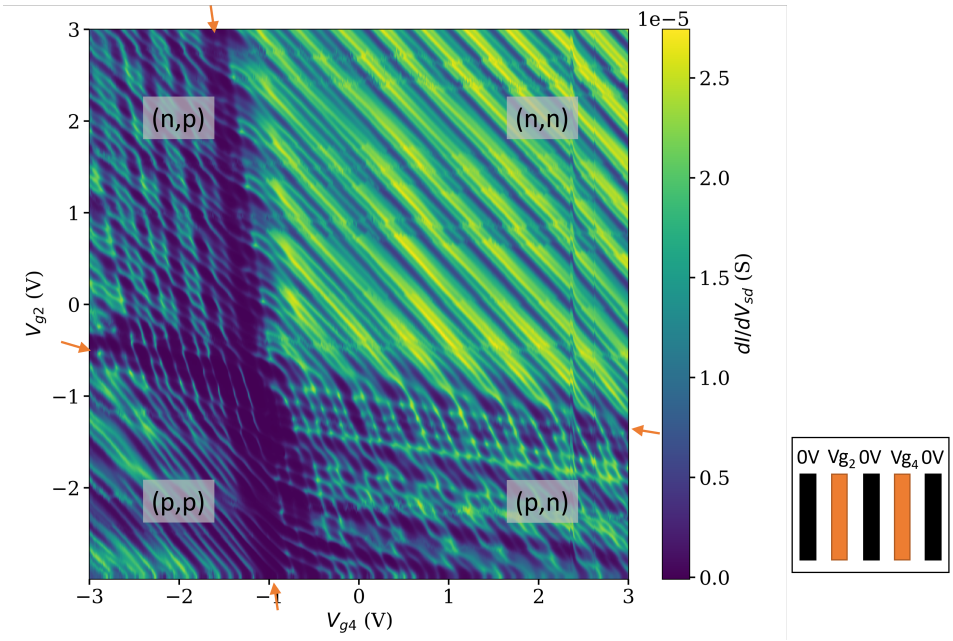

Figure 5.23: **Gate2-gate4 differential conductance map for device FA3-1 with gates 1,3 and 5 set to zero volt.** The map is visually separated in four quadrants with strongly coupled quantum dots for (p,p) and (n,n) tuning and intermediate coupling for (n,p) and (p,n) tuning. A clear gap separating electron and hole states can only be determined for tuning of gate4.

gate-gate map diagonally from (-2V,5V) to (1.5V,-2V) showing that the noise source is tunable by both gates with different strengths. Since gate 2 couples more strongly, the noise source must be located closer to gate 2 and could be e.g. a defect or surface contamination. Gate-gate maps can thus also serve as a tool to roughly localise noise sites enabling the experimenter to avoid them in future measurements.

Charge stability diagrams of FA3-1 and FA3-2

CNT FA3-1 showed a qualitatively similar behaviour to CNT EA5-2. The (p,p) and (n,n) quadrants show two strongly coupled quantum dots. The (p,n) and (n,p) quadrants contain sharp honeycomb features and a separation by eye of the four quadrants is intuitive. Yet, in the low occupation regime the stable charge configurations are not well distinguished and it remains challenging to determine the exact number of electrons/holes in the two respective dots.

The gate1-gate3 map of CNT FA3-2 showed a behaviour mostly analogous to FA3-1 and the regions of different coupling will thus not be explained again. However, this map is still interesting, as the behaviour around zero to small positive gate voltages hints at the formation of a third quantum dot in between the two original quantum dots. In this region, the quantum dots formed by gate 1 & gate 3 are tuned to an n-state and the barrier voltage applied at gate 2 (−3 V) is strong enough to form a p-doped quantum dot in between them. The arising pn-barrier between the quantum dots leads to a weaker

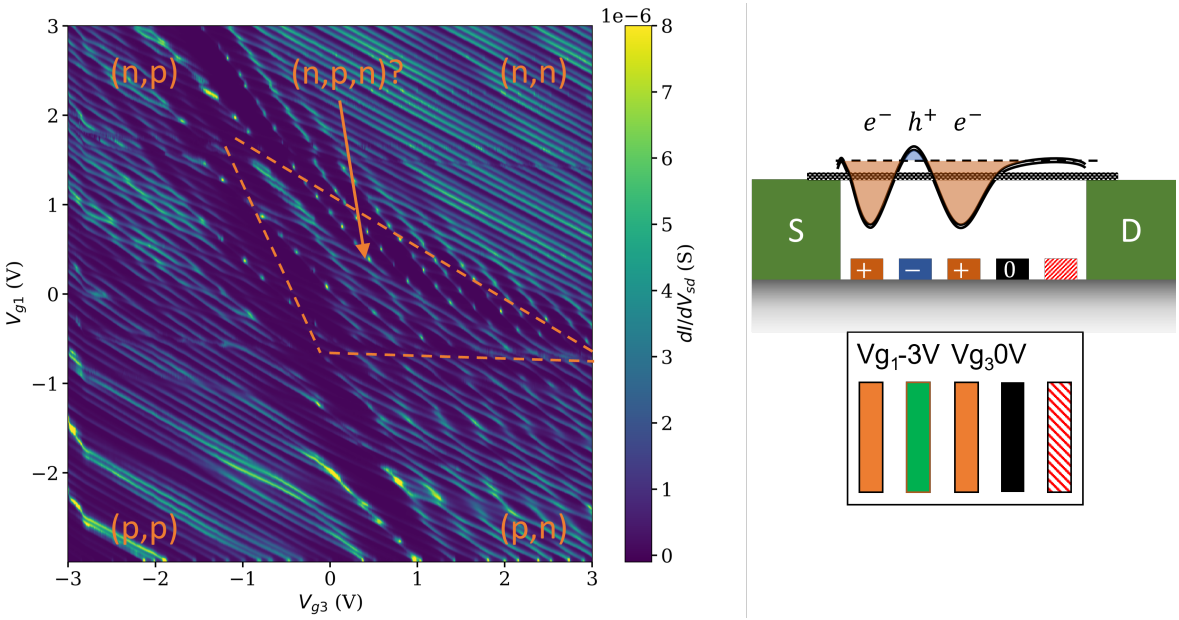

Figure 5.24: **Gate1-gate3 differential conductance map of device FA3-2**, with gate 2 at −3 V, gate 4 at 0 V and zero bias voltage. Strong coupling and single dot formation occurs in the (n,n) and (p,p) quadrants, while (p,n) and (n,p) show the honeycomb structure of intermediate coupling. At slightly positive gate voltages, it appears that a (n,p,n) triple dot is formed in the highlighted range. The scheme on the right side shows the energy structure of a triple quantum dot with (n,p,n) tuning.

coupling. Since the CNT has a vanishing bandgap, the separation between the triple dot configuration and different double-dot states is not as clearly expressed as for devices with a larger gap [212]. In order to form this triple-dot, only three of the five local gates were used. Therefore, a device with five functional gates should be even better suited and allow for more control over the triple dot.
Overall, this section showed that for all devices measured we could induce and measure double-quantum dots with, for the most part, clean behaviour suited for more advanced measurements. The good coupling to the leads, that is one of the key properties of these stamped CNT-devices, comes at the cost of more washed out features in these charge stability diagrams since it is easier for charges to tunnel into or out of the quantum dot. The vanishing bandgap between electrons and holes also complicates the identification of exact charge states which makes the usage of the double quantum dot (e.g. as a platform for a qubit) more challenging. Good coupling also implies, that any signal that could disturb a prepared quantum state in the double quantum dot is more likely to be transmitted from the leads into the CNT which causes state lifetimes to be shorter. With the larger number of local gates, we can, however, close the double quantum dot by properly tuning the barrier gates between the quantum dots and the leads.

5.4.3 Nanoelectromechanics in stamped carbon nanotubes

Since the contact electrodes fabricated for devices with CNTs integrated with the transfer technique were high enough to support suspended CNTs, measurements on nanoelectromechanical properties were performed and a selection is presented in the following. The measurement procedure is the same that was used for NEMS using CNTs integrated by a top-growth process and relies on current rectification in order to create a measurable modification to the electronic conductance.

Comparison of local rf-gate and antenna for mechanical resonance measurements for CNT EA5-1

The devices fabricated using the stamping technique were the first generation to include the bias-T on PCB and thus allowed us to apply an rf-signal not only via a wirebonded antenna but also by using one of the local gates (gate 4). Due to a limited number of rf-lines inside the cryostat only one CNT per chip (EA5-1 and FA3-1) was equipped with an rf-gate. As a proof of principle, CNT EA5-1 was cooled down with both redundant rf-application possibilities. In figure 5.25 a comparison measurement between a signal applied via the antenna and a signal applied via the local gate is shown. All other parameters were unchanged between measurements. The resonance detected when the rf-gate was used is both broader and larger in amplitude signalling a higher ac-field strength at the CNT. Though the working point apparently drifted slightly between measurements, identifiable by the conductance difference in the order of 3%, no drift can explain the broadening and thus the higher power acting on the CNT.
The effect of stronger coupling when using the local rf-gate can be even better visualised when measuring the power dependence of the mechanical resonance for both possibilities. In figure 5.26 the power dependence of the mechanical resonance is plotted for both the local rf-gate as well as the wirebonded antenna. The most striking difference is the lower power threshold at which the resonance, here manifesting as a drop in conductance, can be detected. For the antenna, the minimum power,

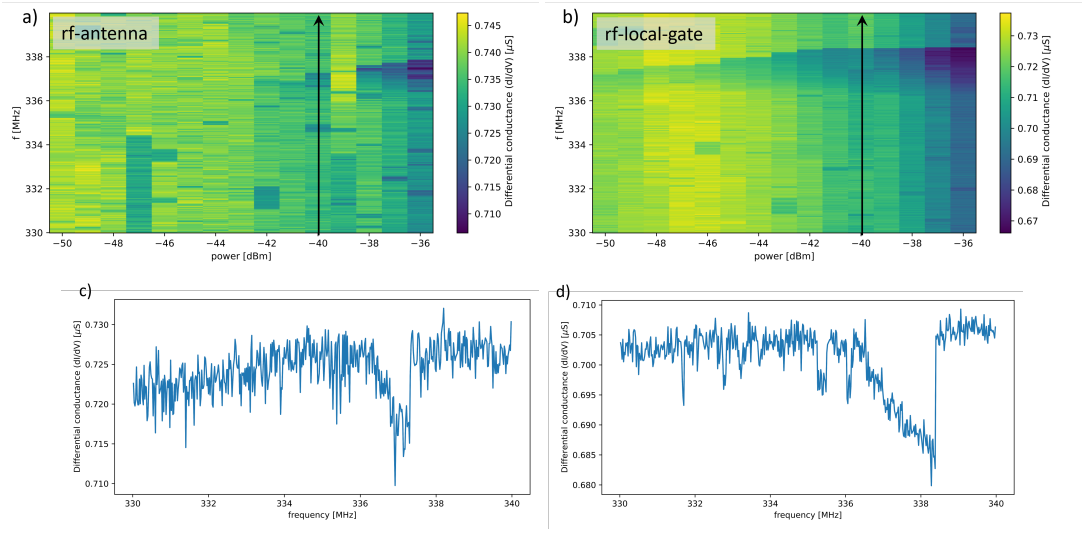

Figure 5.25: **Power dependence of resonance sweeps measuring differential conductance as a function of applied rf-frequency via a wirebonded antenna a) or a local gate b).** The resonance can be detected for signals that are at least 10 dB smaller when sending the signal via the local gate. **c) and d)**: Resonance sweeps measuring differential conductance as a function of applied rf-frequency at −40 dBm when applied via a wirebonded antenna **c)** or a local gate **d)** show a clear difference in terms of amplitude and resonance width.

at this working point, at which the resonance could be detected was −41 dBm while the resonance was still visible at the lowest values of this measurement −50 dBm when using the local gate. When extending the power range to lower values (not shown) the resonance soon vanishes in the noise. Therefore, it is reasonable to assume that the power of the rf-signal arriving at the CNT is at least a factor ten higher when compared to using an rf-antenna. While this difference in measured signal could be compensated by using different attenuators to achieve the same effective power, for the cryogenic environment it is beneficial to send less overall power since less power causes less heating and less disturbance. In our setup, powers upwards of ≈ −40 dBm arriving at the attenuators at the mixing chamber stage result in a measurable temperature increase of hundreds of microkelvin with increased heating for increased rf-power. In order to keep the device and the cryostat well thermalised to base temperature, having to send less power is thus favourable.

Mechanical resonance spectrum of CNT EA5-1

In the following section we explore the rich spectrum of bending modes of the CNT (see section 2.4.5. To measure the different harmonics of the bending modes we performed a frequency sweep over a large range of frequencies. In order to identify resonances as modes of the CNT and not the setup, we performed such a sweep for several gate voltages in a range spanning across one Coulomb peak. For the following measurements, only the local rf-gate has been used. If a peak/dip is caused by a physical system and not just noise, the resonance will appear as a sharp feature visible for several gate voltages. Since gate resolution needed to be sacrificed as a trade-off for the increased frequency

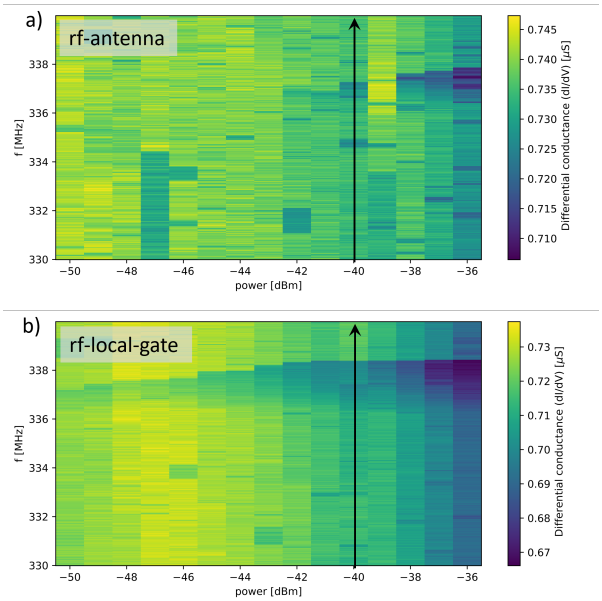

Figure 5.26: **Power dependence of resonance sweeps measuring differential conductance as a function of applied rf-frequency via a wirebonded antenna a) or a local gate b).** The resonance can be detected for signals that are at least 10 dB smaller when sending the signal via the local gate.

span, this method only serves to give a rough idea of spring softening etc. Figure 5.27a) presents such a two-dimensional measurement where the visible horizontal lines show the positions of the stronger resonance signals detected. A full overview of the frequencies where a resonance feature was found is given in table 5.1. It is apparent that some frequencies are multiples of another hinting at harmonics of one fundamental mode. Nevertheless, harmonic frequencies do not have to be at the exact multiple of the fundamental mode, e.g. caused by the differing influence of slack [81], which makes the identification of the mode delicate. Since the rf-signal was applied asymmetrically beneath the CNT on gate 4, it is easier to excite higher modes compared to a symmetric application on the central gate or a far away antenna.

When zooming in on the gate-dependence of the different resonances and plotting the difference to the average of a trace for the zoom, some intriguing details can be noted. All selected resonances feature a weak but finite change of spring constant and are therefore resonances caused by the CNT and no standing waves or LC-modes in the setup. For the resonances at 124 MHz and 232 MHz the motion amplitude was large enough that the induced conductance signal changed sign. Comparing the resonances at 95 MHz and 247 MHz, it becomes apparent that the bifurcation direction is opposite, which is visualised by the sudden colour change in a vertical trace. This is unexpected and cannot be explained by a tunnelling induced modification of the Duffing parameter as this would be identical in both cases. It is therefore more likely that this behaviour is caused by the mechanical properties of the CNT, i.e. that different vibration modes possess different Duffing parameters or that there was a second unidentified CNT.

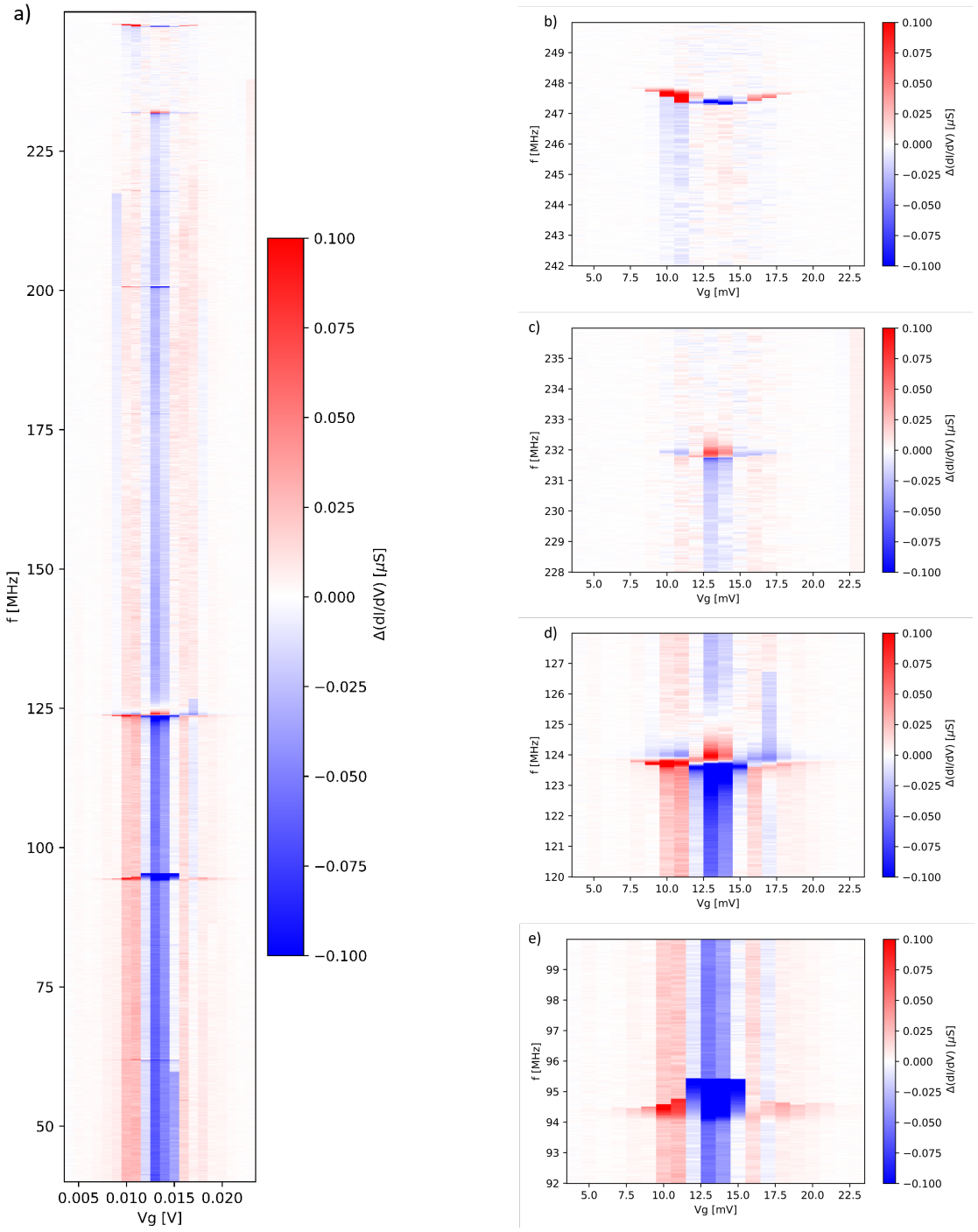

Figure 5.27: **Conductivity response to applied rf-frequencies as function of gate voltage.** The colour code plots the difference to the average of each vertical trace. The left panel **a)** shows the full measured frequency range with a multitude of resonances summarised in table 5.1. The four right panels **b)-e)** show a zoom-in on the most prominent resonance features. The resonance at 94 MHz shows a bifurcation in the opposite direction to the other resonances. The resonance at 124 MHz has a large amplitude jump in the centre of the resonance resembling the behaviour of the phase of a harmonic oscillator at resonance.

Frequency	signal strength	notable properties
41 MHz	weak	-
62 MHz	medium	≃ 3/2 of 41 MHz
82.5 MHz	weak	-
95 MHz	very strong	bifurcating towards high frequencies
100 MHz	very weak	-
109 MHz	very weak	-
116 MHz	weak	-
124 MHz	very strong	≃3x 41 MHz, odd resonance shape
178 MHz	weak	-
200.5 MHz	medium	≃ 2x 100 MHz
218 MHz	weak	≃ 2x 109 MHz
232 MHz	strong	≃ 2x 116 MHz
248 MHz	strong	≃ 6x 41 MHz

Table 5.1: **List of the resonances detected in figure 5.27.** Some of the resonances appear to be more or less multiples hinting at the presence of harmonics.

Besides measuring the spring constant softening occurring when crossing Coulomb peaks, measuring the resonance frequency as a function of a broader gate range provides additional insights on the internal mechanical stress. As introduced in the theory section 2.4.3, the dependence of the resonance frequency on the gate voltage over a broad range gives an estimation on the ratio of flexural and axial rigidity. In figure 5.28 the gate dependence of a resonance of CNT FA3-1 is shown for an applied gate voltage between -3 and 0 V. The resonance frequency change has the shape of a half-parabola which locates the CNT in the bending limit where the flexural rigidity dominates over internal tension. Since the signal strength depends on the curvature of the conductance $\frac{\partial^2 G}{\partial V_g^2}$, the resonance cannot be measured at arbitrary positions and some traces thus show no signal. The frequency changed from about 80 MHz to almost 120 MHz, so about 50 %, which could easily be extended by increasing the gate voltage. This possibility to tune the resonance frequency by such a large amount might prove beneficial for future applications, e.g. when matching the CNT mechanical mode to a resonator of fixed frequency or to fit a band-pass filter.

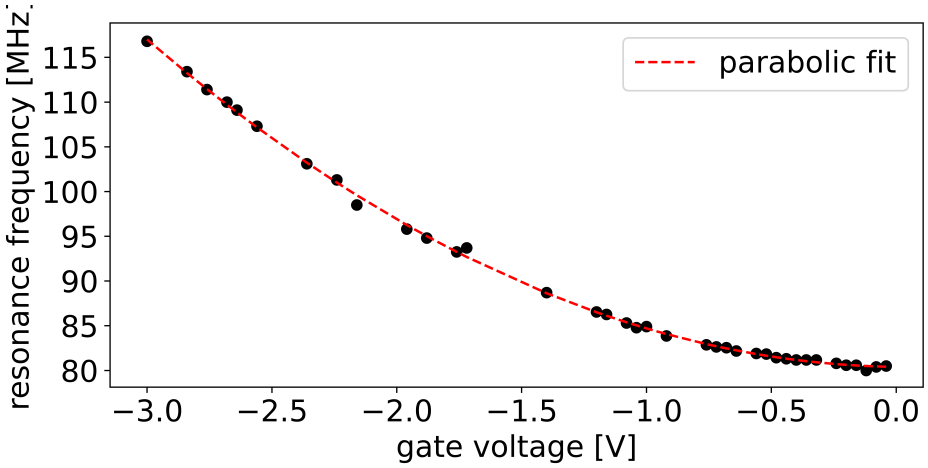

Figure 5.28: **Resonance frequency as a function of applied gate voltage**. The applied rf-power was −50 dBm. The resonance frequency shows quadratic dependence, emphasised by the well matching quadratic fit, on the applied dc-gate voltage indicating behaviour in the bending limit.

6 Conclusion and Outlook

This thesis was originally aimed at coupling a suspended CNT to a single-molecule magnet making it a sensitive magnetometre while also being suited to read out the molecular spin states. During the years, while never abandoning this original target, the focus of this work shifted towards the more controlled fabrication of carbon nanotube nanoelectromechanical systems (NEMS) as well as experiments on them studying their intrinsically rich physics.

In order to study a suspended CNT, the first step is to obtain a suspended CNT and therefore large parts of the work went into the nanofabrication of such devices and the growth of the CNTs in a chemical vapour deposition process. To achieve this, the project branched into two possibilities: The growth of CNTs directly on the metal contact electrodes and a growth on a second chip with later integration via a 'stamping' process transferring the CNT onto the metal electrodes.
The growth on the metal electrodes, or 'top-growth', forced constraints on the nanofabrication in terms of usable materials and circuit design, due to the high temperatures and reactive gases used during the growth process as well as the non-deterministic growth process. Molybdenum, platinum and titanium were used as resilient, high melting point materials suited to form the metallic circuit of the chip. The evaporation of molybdenum proved to be delicate as it needs to be heated to very high temperatures to establish a reasonable evaporation rate which caused a destructive heating of the resist mask on the chip. This heating problem could be mitigated by cooling both the chamber walls and the sample holder using liquid nitrogen and a slow, stepwise evaporation procedure. The devices fabricated this way were successfully used for top-growth processes and, while they may change their texture during the chemical vapour deposition, they did not fail in their functionality and provided four to five local gates as well as high contact electrodes to support suspension.
As a consequence of the non-deterministic nature of the CNT growth process, an additional insulating layer covering the local gate electrodes was introduced in an atomic layer deposition process in order to screen the gates from randomly growing CNTs and displaced catalyst nanoparticles. Earlier tests using evaporated aluminium oxide showed leakage after the CNT growth, most likely due to an annealing process forming conductive channels. The aluminium oxide grown in the atomic layer deposition proved to be more resilient and no leakage was detected if not for metal-circuit misalignments
The chemical vapour deposition used to grow CNTs was optimised. By tuning the parameters of the growth process, the damage inflicted to the metal circuit was reduced and a reasonable yield of devices with a single CNT per junction achieved. Essential for this was the introduction of short heating and cooldown times by quick loading and removal of the sample. This way, less damage was inflicted to the metal circuit and the overall CNT yield was reduced, pushing the process more in the limit of zero or one CNT per junction. This resulted in an easier room-temperature analysis, since resistance

measurements are simplified to a binary question where a finite resistance was most of the time caused by a single CNT and no resistance showed the absence of CNTs. The contact resistance between the CNTs and the platinum film at the contacts was very small, comparable to other state-of-the-art devices fabricated at different groups.

The devices created with the top-growth technique were analysed in a dilution cryostat at mK-temperatures and their electronic transport properties measured. They showed a trend towards favoured hole-conductance and sometimes even fully suppressed electron-conductance. The measured differential conductance maps showed features of Coulomb blockade, cotunnelling effects and negative differential conductance indicating a suspended CNT with good contact quality. By tuning two or more gates, double quantum dots were induced in the CNT and the interdot coupling could be tuned by using dc electric fields created by the local gates.
Using a wirebonded antenna, rf-signals were sent to the CNT to induce mechanical motion and detect mechanical bending modes. The CNTs showed mechanical resonances at frequencies between 100-450 MHz with quality factors up to 10000. By tuning the dc-gate voltage, spring softening due to electronic conductance was detected resulting in a measurable electron-phonon coupling. The resonance shape followed the bifurcating behaviour of a Duffing oscillator down to lowest powers at which the resonance was still visible. Using a setup with better filtering and less noise, the devices could have been studied at lower driving powers and the maximum quality factor enhanced, due to less power broadening.

The second branch of devices investigated consisted of CNT NEMS where the CNT was grown on a second comb-like chip and integrated into the metal circuit with a stamping procedure inside a scanning electron microscope. This approach was implemented in the group during the course of this thesis and offered the two benefits of not exposing the metal circuit to the high temperatures of the CNT growth and giving us the opportunity to not expose the CNT to air at the cost of spatial constraints on the circuit chip due to the space requirements of the nano-assembly and limited mass-fabrication capabilities.
The assembly setup used inside the electron microscope provides the opportunity to anneal the CNT-metal contact in-situ and without the need to transfer it into another piece of equipment. The low contact resistances achieved are very low and can match the values obtained for top-growth processes or top-down fabrication approaches. This enables experiments in the open quantum dot regime. From the vacuum chamber of the electron microscope, devices could be transported to the cryostat without breaking vacuum where they were transferred into the already cold environment. This way, the CNTs were never exposed to air and contaminations reduced to a minimum.
The devices produced with the stamping technique overall showed cleaner conductance measurements with more regular features and often a higher conductance value. Whereas top-growth devices favoured hole-conductance, devices with stamped CNTs showed stronger electron conductance - an effect that arises during the annealing procedure. Due to the four to five working gate electrodes, double quantum dots could be induced as well with complete tuning capabilities for the interdot coupling providing clean charge stability diagrams. The CNTs showed a rich mechanical resonance spectrum, again

with the expected bifurcations, dc gate tunability of the resonance frequency by more than 50 % and comparable quality factors.

In order to accomplish the deposition of single-molecule magnets onto CNTs and to provide an alternative to the previously used dropcasting method which exposes the CNT to organic solvents, an existing evaporation chamber was remodeled. The evaporation system was equipped with a vacuum load-lock to enable the functionalisation of the CNT without unnecessary air exposure and up to three crucibles with different materials to evaporate. $TbPc_2$ molecules were evaporated on each of the measured devices top-growth devices and several stamped devices, and the response analysed in the cryostat. However, none of the devices showed a signature that could clearly be attributed to a single-molecule magnet. The most probable reason for this lies in the statistical nature of this process where a single molecule needs to collide with the few nanometre wide suspended CNT with a fitting velocity, angle and orientation in order to stick to it at a position where it influences the electronic transport properties.

This functionalisation of a CNT with a single-molecule magnet is a non-deterministic process that requires larger numbers of samples in order to yield a reasonable number of devices that couple to one or two single-molecule magnets in a clean and controllable fashion. Using the large sensitivity of CNTs, the non-deterministic could be turned deterministic in the future. Since the mechanical resonance frequency and the conductance of CNTs will shift if additional molecules attach to it, an in-situ monitoring of these properties would provide greater control over the deposition process. In order to measure the CNT as a mechanical resonator with a large quality factor, low temperatures are needed that are not obtainable in the currently used evaporation chamber. The ideal solution is an evaporation system integrated into the dilution cryostat that is later used for cryogenic measurements on the device since this way, the least possible number of steps is needed between sample preparation and measurement yielding the cleanest devices. The implementation of such a setup is non-trivial and requires smart engineering, given the constraints of space caused by shielding, lines and the metal backbone of the cryostat and given the heat produced in the thermal evaporation of the single-molecule magnets used in this thesis ($\approx 400\,^{\circ}\mathrm{C}$) which does not really suit a cryogenic environment. Nonetheless, there might be an intermediate solution possible when using the vacuum-transfer setup developed in our group.

While a reliably working nanofabrication process for top-growth CNT NEMS was established, there is always room for improvements. Due to the growth process behaviour drifting over time, readjustments might be necessary in the future. By optimising the insulating oxide height or using a high κ dielectric like hafnium oxide, the gate coupling could be enhanced. The atomic layer deposition process in itself was not optimised with respect to other parameters than insulation and the defect density is probably far above the minimum of what is possible, inducing electric field jittering which causes noise in the measurement. The choice of different contacting materials could improve the device behaviour or cause new phenomena like superconductivity, e.g. in case of Mo-Re [176].

With the deterministic approach of the stamping technique more complex device geometries could be explored. Due to the precise positioning capabilities, experiments using the CNT as a charge sensor measuring e.g. the charge configuration of a double quantum dot in a nearby circuit, can be imagined.

It also allows to imagine hybrid-systems where a CNT couples to e.g. a single-photon emitter in the vicinity or acts as a one-dimensional gate electrode for graphene. Generally, the option of combining the nanoassembly techniques of two-dimensional van-der Waals materials and one-dimensional carbon nanotubes allows to envision new, complex device geometries.

Overall, during this thesis CNT NEMS were fabricated and measured at cryogenic temperatures. The devices showed rather clean and textbook behaviour and allowed the measurement of double quantum dots as well as the mechanical resonances of the suspended CNT. The coupling to single-molecule magnets could not be shown, which could potentially be fixed by measuring larger number of devices at the cost of other measurements. Adding the experimental setup improvements, all building blocks are now in place to perform more advanced experiments such as a cooling of the mechanical oscillator to the ground state [201, 202], forming mechanical cat states [92], inducing a spin qubit in the CNT [4], building a CNT magnetometre and more.

Bibliography

[1] Morten Kjaergaard et al. “Superconducting Qubits: Current State of Play”. In: (2020). DOI: 10.1146/annurev-conmatphys. URL: https://doi.org/10.1146/annurev-conmatphys-.

[2] Guido Burkard et al. “Semiconductor spin qubits”. In: *Reviews of Modern Physics* 95 (2023). ISSN: 15390756. DOI: 10.1103/RevModPhys.95.025003.

[3] Z. V. Penfold-Fitch, F. Sfigakis, and M. R. Buitelaar. “Microwave Spectroscopy of a Carbon Nanotube Charge Qubit”. In: *Physical Review Applied* 7 (2017). ISSN: 23317019. DOI: 10.1103/PhysRevApplied.7.054017.

[4] E. A. Laird, F. Pei, and L. P. Kouwenhoven. “A valley-spin qubit in a carbon nanotube”. In: *Nature Nanotechnology* 8 (2013), pp. 565–568. ISSN: 17483395. DOI: 10.1038/nnano.2013.140.

[5] Eufemio Moreno-Pineda and Wolfgang Wernsdorfer. *Measuring molecular magnets for quantum technologies*. 2021. DOI: 10.1038/s42254-021-00340-3.

[6] Sébastien Pezzagna and Jan Meijer. *Quantum computer based on color centers in diamond*. 2021. DOI: 10.1063/5.0007444.

[7] Colin D. Bruzewicz et al. “Trapped-ion quantum computing: Progress and challenges”. In: *Applied Physics Reviews* 6 (2019). ISSN: 19319401. DOI: 10.1063/1.5088164.

[8] George Christou et al. “Single-Molecule Magnets”. In: *MRS Bulletin* 25 (2000), pp. 66–71. ISSN: 0883-7694. DOI: 10.1557/mrs2000.226. URL: http://link.springer.com/10.1557/mrs2000.226.

[9] S. Thiele et al. “Electrical readout of individual nuclear spin trajectories in a single-molecule magnet spin transistor”. In: *Physical Review Letters* 111 (2013). ISSN: 00319007. DOI: 10.1103/PhysRevLett.111.037203.

[10] Stefan Thiele et al. “Electrically driven nuclear spin resonance in single-molecule magnets”. In: *Science* 344 (2014), pp. 1135–1138. ISSN: 0036-8075. DOI: 10.1126/science.1249802. URL: https://www.science.org/doi/10.1126/science.1249802.

[11] M. Urdampilleta et al. “Supramolecular spin valves”. In: *Nature Materials* 10 (2011), pp. 502–506. ISSN: 14764660. DOI: 10.1038/nmat3050.

[12] M. Urdampilleta et al. “Landau-Zener tunneling of a single Tb3+ magnetic moment allowing the electronic read-out of a nuclear spin”. In: *Physical Review B - Condensed Matter and Materials Physics* 87 (2013). ISSN: 10980121. DOI: 10.1103/PhysRevB.87.195412.

[13] Matias Urdampilleta et al. “Magnetic interaction between a radical spin and a single-molecule magnet in a molecular spin-valve”. In: *ACS Nano* 9 (2015), pp. 4458–4464. ISSN: 1936086X. DOI: 10.1021/acsnano.5b01056.

[14] Marc Ganzhorn et al. “Strong spin-phonon coupling between a single-molecule magnet and a carbon nanotube nanoelectromechanical system”. In: *Nature Nanotechnology* 8 (2013), pp. 165–169. ISSN: 17483395. DOI: 10.1038/nnano.2012.258.

[15] Marc Ganzhorn et al. “Carbon Nanotube Nanoelectromechanical Systems as Magnetometers for Single-Molecule Magnets”. In: *ACS Nano* 7 (2013), pp. 6225–6236. ISSN: 1936-0851. DOI: 10.1021/nn402968k. URL: https://pubs.acs.org/doi/10.1021/nn402968k.

[16] Marc Ganzhorn et al. “Quantum Einstein-de Haas effect”. In: *Nature Communications* 7 (2016), p. 11443. ISSN: 2041-1723. DOI: 10.1038/ncomms11443. URL: https://www.nature.com/articles/ncomms11443.

[17] C. Godfrin et al. “Operating Quantum States in Single Magnetic Molecules: Implementation of Grover’s Quantum Algorithm”. In: *Physical Review Letters* 119 (2017). ISSN: 10797114. DOI: 10.1103/PhysRevLett.119.187702.

[18] Jia-Shiang Chen et al. “Long-lived electronic spin qubits in single-walled carbon nanotubes”. In: *Nature Communications* 14 (2023), p. 848. ISSN: 2041-1723. DOI: 10.1038/s41467-023-36031-z. URL: https://www.nature.com/articles/s41467-023-36031-z.

[19] J. Moser et al. “Nanotube mechanical resonators with quality factors of up to 5 million”. In: *Nature Nanotechnology* 9 (2014), pp. 1007–1011. ISSN: 17483395. DOI: 10.1038/nnano.2014.234.

[20] I Shapir et al. “Imaging the electronic Wigner crystal in one dimension”. In: *Science* 364 (2019), pp. 870–875. ISSN: 10959203. DOI: 10.1126/science.aat090.

[21] Renaud Leturcq et al. “Franck-Condon blockade in suspended carbon nanotube quantum dots”. In: *Nature Physics* 5 (2009), pp. 327–331. ISSN: 17452481. DOI: 10.1038/nphys1234.

[22] Mukul Kumar and Yoshinori Ando. “Chemical Vapor Deposition of Carbon Nanotubes: A Review on Growth Mechanism and Mass Production”. In: *Journal of Nanoscience and Nanotechnology* 10 (2010), pp. 3739–3758. ISSN: 15334880. DOI: 10.1166/jnn.2010.2939.

[23] Wenjie Liang et al. “Fabry - Perot interference in a nanotube electron waveguide”. In: *Nature* 411 (2001), pp. 665–669. ISSN: 0028-0836. DOI: 10.1038/35079517. URL: https://www.nature.com/articles/35079517.

[24] J.-P. Cleuziou et al. “Carbon nanotube superconducting quantum interference device”. In: *Nature Nanotechnology* 1 (2006), pp. 53–59. ISSN: 1748-3387. DOI: 10.1038/nnano.2006.54. URL: https://www.nature.com/articles/nnano.2006.54.

[25] Nathan R. Franklin et al. “Integration of suspended carbon nanotube arrays into electronic devices and electromechanical systems”. In: *Applied Physics Letters* 81 (2002), pp. 913–915. ISSN: 0003-6951. DOI: 10.1063/1.1497710. URL: https://pubs.aip.org/apl/article/81/5/913/531967/Integration-of-suspended-carbon-nanotube-arrays.

[26] Jien Cao, Qian Wang, and Hongjie Dai. “Electron transport in very clean, as-grown suspended carbon nanotubes”. In: *Nature Materials* 4 (2005), pp. 745–749. ISSN: 1476-1122. DOI: 10.1038/nmat1478. URL: https://www.nature.com/articles/nmat1478.

[27] J. J. Viennot, J. Palomo, and T. Kontos. “Stamping single wall nanotubes for circuit quantum electrodynamics”. In: *Applied Physics Letters* 104 (2014). ISSN: 0003-6951. DOI: 10.1063/1.4868868. URL: https://pubs.aip.org/apl/article/104/11/113108/25319/Stamping-single-wall-nanotubes-for-circuit-quantum.

[28] Romain Maurand et al. “First-Order 0-π Quantum Phase Transition in the Kondo Regime of a Superconducting Carbon-Nanotube Quantum Dot”. In: *Physical Review X* 2 (2012), p. 011009. ISSN: 2160-3308. DOI: 10.1103/PhysRevX.2.011009. URL: https://link.aps.org/doi/10.1103/PhysRevX.2.011009.

[29] H. W.Ch Postma et al. “Dynamic range of nanotube- and nanowire-based electromechanical systems”. In: *Applied Physics Letters* 86 (2005), pp. 1–3. ISSN: 00036951. DOI: 10.1063/1.1929098.

[30] Sumio Iijima. “Direct observation of the tetrahedral bonding in graphitized carbon black by high resolution electron microscopy”. In: *Journal of Crystal Growth* 50 (1980), pp. 675–683. ISSN: 00220248. DOI: 10.1016/0022-0248(80)90013-5.

[31] Sumio Iijima. “Helical microtubules of graphitic carbon”. In: *Nature* 354 (1991), pp. 56–58. ISSN: 0028-0836. DOI: 10.1038/354056a0.

[32] K. S. Novoselov et al. “Electric Field Effect in Atomically Thin Carbon Films”. In: *Science* 306 (2004), pp. 666–669. ISSN: 0036-8075. DOI: 10.1126/science.1102896.

[33] D. H. Choi et al. “Fabrication and Characterization of Fully Flattened Carbon Nanotubes: A New Graphene Nanoribbon Analogue”. In: *Scientific Reports* 3 (2013), p. 1617. ISSN: 2045-2322. DOI: 10.1038/srep01617.

[34] L. Forro et al. “Electronic and Mechanical Properties of Carbon Nanotubes”. In: Kluwer Academic Publishers, pp. 297–320. DOI: 10.1007/0-306-47098-5_22. URL: http://link.springer.com/10.1007/0-306-47098-5_22.

[35] Y. H. Yang and W. Z. Li. “Radial elasticity of single-walled carbon nanotube measured by atomic force microscopy”. In: *Applied Physics Letters* 98 (2011). ISSN: 0003-6951. DOI: 10.1063/1.3546170.

[36] A. H. Castro Neto et al. “The electronic properties of graphene”. In: *Reviews of Modern Physics* 81 (2009), pp. 109–162. ISSN: 0034-6861. DOI: 10.1103/RevModPhys.81.109.

[37] P. R. Wallace. “The Band Theory of Graphite”. In: *Physical Review* 71 (1947), pp. 622–634. ISSN: 0031-899X. DOI: 10.1103/PhysRev.71.622.

[38] R. Saito et al. “Electronic structure of chiral graphene tubules”. In: *Applied Physics Letters* 60 (1992), pp. 2204–2206. ISSN: 0003-6951. DOI: 10.1063/1.107080.

[39] Noriaki Hamada, Shin-ichi Sawada, and Atsushi Oshiyama. “New one-dimensional conductors: Graphitic microtubules”. In: *Physical Review Letters* 68 (1992), pp. 1579–1581. ISSN: 0031-9007. DOI: 10.1103/PhysRevLett.68.1579.

[40] C. L. Kane and E. J. Mele. "Size, Shape, and Low Energy Electronic Structure of Carbon Nanotubes". In: *Physical Review Letters* 78 (1997), pp. 1932–1935. ISSN: 0031-9007. DOI: 10.1103/PhysRevLett.78.1932.

[41] E. D. Minot et al. "Tuning Carbon Nanotube Band Gaps with Strain". In: *Physical Review Letters* 90 (2003), p. 156401. ISSN: 0031-9007. DOI: 10.1103/PhysRevLett.90.156401.

[42] Edward A. Laird et al. "Quantum transport in carbon nanotubes". In: *Reviews of Modern Physics* 87 (2015), pp. 703–764. ISSN: 0034-6861. DOI: 10.1103/RevModPhys.87.703. URL: https://link.aps.org/doi/10.1103/RevModPhys.87.703.

[43] Rolf Landauer. "Electrical resistance of disordered one-dimensional lattices". In: *Philosophical Magazine* 21 (1970), pp. 863–867. ISSN: 0031-8086. DOI: 10.1080/14786437008238472.

[44] Paul L. McEuen and Ji-Yong Park. "Electron Transport in Single-Walled Carbon Nanotubes". In: *MRS Bulletin* 29 (2004), pp. 272–275. ISSN: 0883-7694. DOI: 10.1557/mrs2004.79.

[45] Sander J. Tans et al. "Individual single-wall carbon nanotubes as quantum wires". In: *Nature* 386 (1997), pp. 474–477. ISSN: 0028-0836. DOI: 10.1038/386474a0. URL: https://www.nature.com/articles/386474a0.

[46] Sander J. Tans, Alwin R. M. Verschueren, and Cees Dekker. "Room-temperature transistor based on a single carbon nanotube". In: *Nature* 393 (1998), pp. 49–52. ISSN: 0028-0836. DOI: 10.1038/29954. URL: https://www.nature.com/articles/29954.

[47] Peng Liu et al. "Measuring the Work Function of Carbon Nanotubes with Thermionic Method". In: *Nano Letters* 8 (2008), pp. 647–651. ISSN: 1530-6984. DOI: 10.1021/nl0730817.

[48] Florian Banhart. *Interactions between metals and carbon nanotubes: At the interface between old and new materials*. 2009. DOI: 10.1039/b9nr00127a.

[49] Aaron D. Franklin, Damon B. Farmer, and Wilfried Haensch. "Defining and overcoming the contact resistance challenge in scaled carbon nanotube transistors". In: *ACS Nano* 8 (2014), pp. 7333–7339. ISSN: 1936086X. DOI: 10.1021/nn5024363.

[50] Saraswati Behera. "Pure edge-contact devices on single-layer-CVD-graphene integrated into a single chip". In: *Scientific Reports* 13 (2023). ISSN: 20452322. DOI: 10.1038/s41598-023-37487-1.

[51] Qing Cao et al. "End-bonded contacts for carbon nanotube transistors with low, size-independent resistance". In: *Science* 350 (2015), pp. 68–72. ISSN: 0036-8075. DOI: 10.1126/science.aac8006. URL: https://www.science.org/doi/10.1126/science.aac8006.

[52] F. Pelayo García de Arquer et al. "Semiconductor quantum dots: Technological progress and future challenges". In: *Science* 373 (2021). ISSN: 0036-8075. DOI: 10.1126/science.aaz8541.

[53] Jien Cao et al. "Suspended carbon nanotube quantum wires with two gates". In: *Small* 1 (2005), pp. 138–141. ISSN: 16136810. DOI: 10.1002/smll.200400015.

[54] R. Hanson et al. "Spins in few-electron quantum dots". In: *Reviews of Modern Physics* 79 (2007), pp. 1217–1265. ISSN: 0034-6861. DOI: 10.1103/RevModPhys.79.1217. URL: https://link.aps.org/doi/10.1103/RevModPhys.79.1217.

[55] J. M. Thijssen and H. S.J. Van Der Zant. *Charge transport and single-electron effects in nanoscale systems*. 2008. DOI: 10.1002/pssb.200743470.

[56] J. V. Holm et al. "Gate-dependent tunneling-induced level shifts observed in carbon nanotube quantum dots". In: *Physical Review B - Condensed Matter and Materials Physics* 77 (2008). ISSN: 10980121. DOI: 10.1103/PhysRevB.77.161406.

[57] Tim Althuon et al. "Nano-assembled open quantum dot nanotube devices". In: *Communications Materials* 5 (2024), p. 5. ISSN: 2662-4443. DOI: 10.1038/s43246-023-00439-3. URL: https://www.nature.com/articles/s43246-023-00439-3.

[58] J. R. Petta et al. "Coherent Manipulation of Coupled Electron Spins in Semiconductor Quantum Dots". In: *Science* 309 (2005), pp. 2180–2184. ISSN: 0036-8075. DOI: 10.1126/science.1116955. URL: https://www.science.org/doi/10.1126/science.1116955.

[59] J. Waissman et al. "Realization of pristine and locally tunable one-dimensional electron systems in carbon nanotubes". In: *Nature Nanotechnology* 8 (2013), pp. 569–574. ISSN: 17483395. DOI: 10.1038/nnano.2013.143.

[60] W. G. van der Wiel et al. "Electron transport through double quantum dots". In: *Reviews of Modern Physics* 75 (2002), pp. 1–22. ISSN: 0034-6861. DOI: 10.1103/RevModPhys.75.1. URL: https://link.aps.org/doi/10.1103/RevModPhys.75.1.

[61] Sami Sapmaz et al. "Excited state spectroscopy in carbon nanotube double quantum dots". In: *Nano Letters* 6 (2006), pp. 1350–1355. ISSN: 15306984. DOI: 10.1021/nl052498e.

[62] G. A. Steele, G. Gotz, and L. P. Kouwenhoven. "Tunable few-electron double quantum dots and Klein tunnelling in ultraclean carbon nanotubes". In: *Nature Nanotechnology* 4 (2009), pp. 363–367. ISSN: 17483395. DOI: 10.1038/nnano.2009.71.

[63] Xing Lan Liu, Dorothee Hug, and Lieven M.K. Vandersypen. "Gate-defined graphene double quantum dot and excited state spectroscopy". In: *Nano Letters* 10 (2010), pp. 1623–1627. ISSN: 15306984. DOI: 10.1021/nl9040912.

[64] C Schönenberger. "Charge and spin transport in carbon nanotubes". In: *Semiconductor Science and Technology* 21 (2006), S1–S9. ISSN: 0268-1242. DOI: 10.1088/0268-1242/21/11/S01. URL: https://iopscience.iop.org/article/10.1088/0268-1242/21/11/S01.

[65] A. Avsar et al. "Colloquium: Spintronics in graphene and other two-dimensional materials". In: *Reviews of Modern Physics* 92 (2020). ISSN: 15390756. DOI: 10.1103/REVMODPHYS.92.021003.

[66] Tsuneya Ando. "Spin-Orbit Interaction in Carbon Nanotubes". In: *Journal of the Physical Society of Japan* 69 (2000), pp. 1757–1763. ISSN: 0031-9015. DOI: 10.1143/JPSJ.69.1757. URL: http://journals.jps.jp/doi/10.1143/JPSJ.69.1757.

[67] G.A. Steele et al. "Large spin-orbit coupling in carbon nanotubes". In: *Nature Communications* 4 (2013), p. 1573. ISSN: 2041-1723. DOI: 10.1038/ncomms2584. URL: https://www.nature.com/articles/ncomms2584.

[68] Joachim Schönle. "Quantum transport studies for spintronics implementation: from supramolecular carbon nanotube systems to topological crystalline insulator". PhD thesis. Université Grenoble Alpes, 2018. URL: https://theses.hal.science/tel-01895425.

[69] Wataru Izumida, Kentaro Sato, and Riichiro Saito. "Spin-orbit interaction in single wall carbon nanotubes: symmetry adapted tight-binding calculation and effective model analysis". In: *Journal of the Physical Society of Japan* 78 (2009). ISSN: 00319015. DOI: 10.1143/JPSJ.78.074707.

[70] T. S. Jespersen et al. "Gate-dependent spin-orbit coupling in multielectron carbon nanotubes". In: *Nature Physics* 7 (2011), pp. 348–353. ISSN: 17452481. DOI: 10.1038/nphys1880.

[71] I. Khivrich and S. Ilani. "Atomic-like charge qubit in a carbon nanotube enabling electric and magnetic field nano-sensing". In: *Nature Communications* 11 (2020). ISSN: 20411723. DOI: 10.1038/s41467-020-16001-5.

[72] F. Pistolesi, A. N. Cleland, and A. Bachtold. "Proposal for a Nanomechanical Qubit". In: *Physical Review X* 11 (2021). ISSN: 21603308. DOI: 10.1103/PhysRevX.11.031027.

[73] Hans Andreas Engel et al. "Measurement efficiency and n-shot readout of spin qubits". In: *Physical Review Letters* 93 (2004). ISSN: 00319007. DOI: 10.1103/PhysRevLett.93.106804.

[74] J. M. Taylor et al. "Fault-tolerant architecture for quantum computation using electrically controlled semiconductor spins". In: *Nature Physics* 1 (2005), pp. 177–183. ISSN: 17452481. DOI: 10.1038/nphys174.

[75] Keiji Ono and Seigo Tarucha. "Nuclear-spin-induced oscillatory current in spin-blockaded quantum dots". In: *Physical Review Letters* 92 (2004). ISSN: 00319007. DOI: 10.1103/PhysRevLett.92.256803.

[76] A. C. Johnson et al. "Singlet-triplet spin blockade and charge sensing in a few-electron double quantum dot". In: *Physical Review B - Condensed Matter and Materials Physics* 72 (2005). ISSN: 10980121. DOI: 10.1103/PhysRevB.72.165308.

[77] András Pályi and Guido Burkard. "Spin-valley blockade in carbon nanotube double quantum dots". In: *Physical Review B - Condensed Matter and Materials Physics* 82 (2010). ISSN: 10980121. DOI: 10.1103/PhysRevB.82.155424.

[78] A. M.J. Zwerver et al. "Qubits made by advanced semiconductor manufacturing". In: *Nature Electronics* 5 (2022), pp. 184–190. ISSN: 25201131. DOI: 10.1038/s41928-022-00727-9.

[79] M. L. Roukes. "Nanoelectromechanical Systems". In: (2000), p. 376. URL: http://arxiv.org/abs/cond-mat/0008187.

[80] K. L. Ekinci and M. L. Roukes. "Nanoelectromechanical systems". In: *Review of Scientific Instruments* 76 (2005). ISSN: 00346748. DOI: 10.1063/1.1927327.

[81] Vera A Sazonova. "A tunable carbon nanotube resonator". PhD thesis. Cornell University, 2006. URL: https://hdl.handle.net/1813/3205.

[82] Yang Xiao et al. *A Review on Graphene-Based Nano-Electromechanical Resonators: Fabrication, Performance, and Applications*. 2022. DOI: 10.3390/mi13020215.

[83] Antoine Reserbat-Plantey et al. “Electromechanical control of nitrogen-vacancy defect emission using graphene NEMS”. In: *Nature Communications* 7 (2016). ISSN: 20411723. DOI: 10.1038/ncomms10218.

[84] Max C. Lemme et al. “Nanoelectromechanical Sensors Based on Suspended 2D Materials”. In: *Research* 2020 (2020). ISSN: 26395274. DOI: 10.34133/2020/8748602.

[85] Sajedeh Manzeli et al. “Self-sensing, tunable monolayer MoS2 nanoelectromechanical resonators”. In: *Nature Communications* 10 (2019). ISSN: 20411723. DOI: 10.1038/s41467-019-12795-1.

[86] Eric Sage et al. “Single-particle mass spectrometry with arrays of frequency-addressed nanomechanical resonators”. In: *Nature Communications* 9 (2018). ISSN: 20411723. DOI: 10.1038/s41467-018-05783-4.

[87] X. L. Feng et al. “A self-sustaining ultrahigh-frequency nanoelectromechanical oscillator”. In: *Nature Nanotechnology* 3 (2008), pp. 342–346. ISSN: 17483395. DOI: 10.1038/nnano.2008.125.

[88] D. I. Bradley et al. “Operating Nanobeams in a Quantum Fluid”. In: *Scientific Reports* 7 (2017). ISSN: 20452322. DOI: 10.1038/s41598-017-04842-y.

[89] Mingwei Li et al. “Bottom-up assembly of large-area nanowire resonator arrays”. In: *Nature Nanotechnology* 3 (2008), pp. 88–92. ISSN: 17483395. DOI: 10.1038/nnano.2008.26.

[90] Kwanoh Kim et al. “Ultrahigh-speed rotating nanoelectromechanical system devices assembled from nanoscale building blocks”. In: *Nature Communications* 5 (2014). ISSN: 20411723. DOI: 10.1038/ncomms4632.

[91] Stefano Stassi et al. “Reaching silicon-based NEMS performances with 3D printed nanomechanical resonators”. In: *Nature Communications* 12 (2021). ISSN: 20411723. DOI: 10.1038/s41467-021-26353-1.

[92] Marius Bild et al. “Schrödinger cat states of a 16-microgram mechanical oscillator”. In: *Science* 380 (2023), pp. 274–278. ISSN: 0036-8075. DOI: 10.1126/science.adf7553.

[93] C. Samanta et al. “Nonlinear nanomechanical resonators approaching the quantum ground state”. In: *Nature Physics* 19 (2023), pp. 1340–1344. ISSN: 17452481. DOI: 10.1038/s41567-023-02065-9.

[94] Jeremy Q. Broughton et al. “Direct atomistic simulation of quartz crystal oscillators: Bulk properties and nanoscale devices”. In: *Physical Review B* 56 (1997), pp. 611–618. ISSN: 0163-1829. DOI: 10.1103/PhysRevB.56.611. URL: https://link.aps.org/doi/10.1103/PhysRevB.56.611.

[95] Rob Phillips. *Crystals, Defects and Microstructures*. Cambridge University Press, 2001. ISBN: 9780521790055. DOI: 10.1017/CBO9780511606236.

[96] S. Sapmaz et al. “Tunneling in suspended carbon nanotubes assisted by longitudinal phonons”. In: *Physical Review Letters* 96 (2006). ISSN: 10797114. DOI: 10.1103/PhysRevLett.96.026801.

[97] G. A. Steele et al. “Strong Coupling Between Single-Electron Tunneling and Nanomechanical Motion”. In: *Science* 325 (2009), pp. 1103–1107. ISSN: 0036-8075. DOI: 10.1126/science.1176076. URL: https://www.science.org/doi/10.1126/science.1176076.

[98] L. D. Landau et al. *Theory of Elasticity*. Elsevier, 1986. ISBN: 9780080570693. DOI: 10.1016/C2009-0-25521-8.

[99] Marc Ganzhorn. "Coupling Magnetism and Mechanics at a molecular scale". PhD thesis. Université Grenoble Alpes, 2013. URL: https://theses.hal.science/tel-00950769.

[100] S. Sapmaz et al. "Carbon nanotubes as nanoelectromechanical systems". In: *Physical Review B - Condensed Matter and Materials Physics* 67 (2003), pp. 2354141–2354147. ISSN: 01631829. DOI: 10.1103/PhysRevB.67.235414.

[101] Tobias Zengerle et al. "Using the nonlinear duffing effect of piezoelectric micro-oscillators for wide-range pressure sensing". In: *Actuators* 10 (2021). ISSN: 20760825. DOI: 10.3390/act10080172.

[102] Vera Sazonova et al. "A tunable carbon nanotube electromechanical oscillator". In: *Nature* 431 (2004), pp. 284–287. ISSN: 0028-0836. DOI: 10.1038/nature02905. URL: https://www.nature.com/articles/nature02905.

[103] Andreas K. Hüttel et al. "Carbon Nanotubes as Ultrahigh Quality Factor Mechanical Resonators". In: *Nano Letters* 9 (2009), pp. 2547–2552. ISSN: 1530-6984. DOI: 10.1021/nl900612h. URL: https://pubs.acs.org/doi/10.1021/nl900612h.

[104] Benjamin Lassagne et al. "Coupling Mechanics to Charge Transport in Carbon Nanotube Mechanical Resonators". In: *Science* 325 (2009), pp. 1107–1110. ISSN: 0036-8075. DOI: 10.1126/science.1174290. URL: https://www.science.org/doi/10.1126/science.1174290.

[105] Ilya Khivrich, Aashish A. Clerk, and Shahal Ilani. "Nanomechanical pump–probe measurements of insulating electronic states in a carbon nanotube". In: *Nature Nanotechnology* 14 (2019), pp. 161–167. ISSN: 17483395. DOI: 10.1038/s41565-018-0341-6.

[106] C. Urgell et al. *Cooling and self-oscillation in a nanotube electromechanical resonator*. 2020. DOI: 10.1038/s41567-019-0682-6.

[107] B. Lassagne et al. "Ultrasensitive mass sensing with a nanotube electromechanical resonator". In: *Nano Letters* 8 (2008), pp. 3735–3738. ISSN: 15306984. DOI: 10.1021/nl801982v.

[108] Hsin Ying Chiu et al. "Atomic-scale mass sensing using carbon nanotube resonators". In: *Nano Letters* 8 (2008), pp. 4342–4346. ISSN: 15306984. DOI: 10.1021/nl802181c.

[109] Masato Hamada, Takehito Yokoyama, and Shuichi Murakami. "Spin current generation and magnetic response in carbon nanotubes by the twisting phonon mode". In: *Physical Review B - Condensed Matter and Materials Physics* 92 (2015). ISSN: 1550235X. DOI: 10.1103/PhysRevB.92.060409.

[110] M.S. Dresselhaus et al. "Raman spectroscopy of carbon nanotubes". In: *Physics Reports* 409 (2005), pp. 47–99. ISSN: 03701573. DOI: 10.1016/j.physrep.2004.10.006. URL: https://linkinghub.elsevier.com/retrieve/pii/S0370157304004570.

[111] Feng Yang et al. "Chirality Pure Carbon Nanotubes: Growth, Sorting, and Characterization". In: *Chemical Reviews* 120 (2020), pp. 2693–2758. ISSN: 0009-2665. DOI: 10.1021/acs.chemrev.9b00835. URL: https://pubs.acs.org/doi/10.1021/acs.chemrev.9b00835.

[112] R. Knobel, C. S. Yung, and A. N. Cleland. “Single-electron transistor as a radio-frequency mixer”. In: *Applied Physics Letters* 81 (2002), pp. 532–534. ISSN: 00036951. DOI: 10.1063/1.1493221.

[113] R. Knobel and A. N. Cleland. “Piezoelectric displacement sensing with a single-electron transistor”. In: *Applied Physics Letters* 81 (2002), pp. 2258–2260. ISSN: 00036951. DOI: 10.1063/1.1507616.

[114] Robert G. Knobel and Andrew N. Cleland. “Nanometre-scale displacement sensing using a single electron transistor”. In: *Nature* 424 (2003), pp. 291–293. ISSN: 00280836. DOI: 10.1038/nature01773.

[115] C. Samanta et al. “Nanomechanical vibrational response from electrical mixing measurements”. In: *Applied Physics Letters* 123 (2023). ISSN: 00036951. DOI: 10.1063/5.0184931.

[116] S. L. De Bonis et al. “Ultrasensitive Displacement Noise Measurement of Carbon Nanotube Mechanical Resonators”. In: *Nano Letters* 18 (2018), pp. 5324–5328. ISSN: 15306992. DOI: 10.1021/acs.nanolett.8b02437.

[117] S. Jezouin et al. “Quantum Limit of Heat Flow Across a Single Electronic Channel”. In: *Science* 342 (2013), pp. 601–604. ISSN: 0036-8075. DOI: 10.1126/science.1241912. URL: https://www.science.org/doi/10.1126/science.1241912.

[118] T. Jullien et al. “Quantum tomography of an electron”. In: *Nature* 514 (2014), pp. 603–607. ISSN: 14764687. DOI: 10.1038/nature13821.

[119] R. J. Schoelkopf et al. “The Radio-Frequency Single-Electron Transistor (RF-SET): A Fast and Ultrasensitive Electrometer”. In: *Science* 280 (1998), pp. 1238–1242. ISSN: 0036-8075. DOI: 10.1126/science.280.5367.1238. URL: https://www.science.org/doi/10.1126/science.280.5367.1238.

[120] C. W. J. Beenakker. “Theory of Coulomb-blockade oscillations in the conductance of a quantum dot”. In: *Physical Review B* 44 (1991), pp. 1646–1656. ISSN: 0163-1829. DOI: 10.1103/PhysRevB.44.1646. URL: https://link.aps.org/doi/10.1103/PhysRevB.44.1646.

[121] J. Franck and E. G. Dymond. “Elementary processes of photochemical reactions”. In: *Transactions of the Faraday Society* 21 (1926), p. 536. ISSN: 0014-7672. DOI: 10.1039/tf9262100536. URL: http://xlink.rsc.org/?DOI=tf9262100536.

[122] Edward Condon. “A Theory of Intensity Distribution in Band Systems”. In: *Physical Review* 28 (1926), pp. 1182–1201. ISSN: 0031-899X. DOI: 10.1103/PhysRev.28.1182. URL: https://link.aps.org/doi/10.1103/PhysRev.28.1182.

[123] Eros Mariani and Felix von Oppen. “Electron-vibron coupling in suspended carbon nanotube quantum dots”. In: *Physical Review B - Condensed Matter and Materials Physics* 80 (2009). ISSN: 10980121. DOI: 10.1103/PhysRevB.80.155411.

[124] L P Kouwenhoven, D G Austing, and S Tarucha. “Few-electron quantum dots”. In: *Reports on Progress in Physics* 64 (2001), pp. 701–736. ISSN: 0034-4885. DOI: 10.1088/0034-4885/64/6/201. URL: https://iopscience.iop.org/article/10.1088/0034-4885/64/6/201.

[125] Juan Bartolomé, Fernando Luis, and Julio Fernández. *Molecular Magnets*. Ed. by Juan Bartolomé, Fernando Luis, and Julio F. Fernández. Springer Berlin Heidelberg, 2014. ISBN: 978-3-642-40608-9. DOI: 10.1007/978-3-642-40609-6. URL: https://link.springer.com/10.1007/978-3-642-40609-6.

[126] B. Barbara et al. "Macroscopic quantum tunneling in molecular magnets". In: *Journal of Magnetism and Magnetic Materials* 200 (1999), pp. 167–181. ISSN: 03048853. DOI: 10.1016/S0304-8853(99)00409-6. URL: https://linkinghub.elsevier.com/retrieve/pii/S0304885399004096.

[127] T. Lis. "Preparation, structure, and magnetic properties of a dodecanuclear mixed-valence manganese carboxylate". In: *Acta Crystallographica Section B Structural Crystallography and Crystal Chemistry* 36 (1980), pp. 2042–2046. ISSN: 0567-7408. DOI: 10.1107/S0567740880007893. URL: https://scripts.iucr.org/cgi-bin/paper?S0567740880007893.

[128] R Sessoli et al. *Magnetic bistability in a metal-ion cluster*. 1993.

[129] J Villain et al. "Magnetic Relaxation in Big Magnetic Molecules". In: *Europhysics Letters (EPL)* 27 (1994), pp. 159–164. ISSN: 0295-5075. DOI: 10.1209/0295-5075/27/2/014. URL: https://iopscience.iop.org/article/10.1209/0295-5075/27/2/014.

[130] H. B. Heersche et al. "Electron Transport through Single <math display="inline"> <msub> <mi>Mn</mi> <mn>12</mn> </msub> </math> Molecular Magnets". In: *Physical Review Letters* 96 (2006), p. 206801. ISSN: 0031-9007. DOI: 10.1103/PhysRevLett.96.206801. URL: https://link.aps.org/doi/10.1103/PhysRevLett.96.206801.

[131] Dante Gatteschi et al. "EPR of molecular nanomagnets". In: *Coordination Chemistry Reviews* 250 (2006), pp. 1514–1529. ISSN: 00108545. DOI: 10.1016/j.ccr.2006.02.006.

[132] Rashmi Bagai and George Christou. "The drosophila of single-molecule magnetism: [Mn12O12(O2CR)16(H2O)4]". In: *Chemical Society Reviews* 38 (2009), pp. 1011–1026. ISSN: 14604744. DOI: 10.1039/b811963e.

[133] G. S. Ofelt. "Structure of the f6 configuration with application to rare-earth ions". In: *The Journal of Chemical Physics* 38 (1963), pp. 2171–2180. ISSN: 00219606. DOI: 10.1063/1.1733947.

[134] K. S. Thomas, S. Singh, and G. H. Dieke. "Energy levels of Tb3+ in LaCl3 and other chlorides". In: *The Journal of Chemical Physics* 38 (1963), pp. 2180–2190. ISSN: 00219606. DOI: 10.1063/1.1733948.

[135] Naoto Ishikawa et al. "Determination of ligand-field parameters and f-electronic structures of double-decker bis(phthalocyaninato)lanthanide complexes". In: *Inorganic Chemistry* 42 (2003), pp. 2440–2446. ISSN: 00201669. DOI: 10.1021/ic026295u.

[136] Naoto Ishikawa, Miki Sugita, and Wolfgang Wernsdorfer. "Quantum tunneling of magnetization in lanthanide single-molecule magnets: Bis(phthalocyaninato)terbium and bis(phthalocyaninato)dysprosium anions". In: *Angewandte Chemie - International Edition* 44 (2005), pp. 2931–2935. ISSN: 14337851. DOI: 10.1002/anie.200462638.

[137] Daniel N. Woodruff, Richard E. P. Winpenny, and Richard A. Layfield. "Lanthanide Single-Molecule Magnets". In: *Chemical Reviews* 113 (2013), pp. 5110–5148. ISSN: 0009-2665. DOI: 10.1021/cr400018q. URL: https://pubs.acs.org/doi/10.1021/cr400018q.

[138] Jonathan R. Friedman et al. “Steps in the hysteresis loops of a high-spin molecule”. In: *Journal of Applied Physics* 79 (1996), pp. 6031–6033. ISSN: 00218979. DOI: 10.1063/1.361837.

[139] J. M Hernández et al. “Field tuning of thermally activated magnetic quantum tunnelling in Mn ₁₂ - Ac molecules”. In: *Europhysics Letters (EPL)* 35 (1996), pp. 301–306. ISSN: 0295-5075. DOI: 10.1209/epl/i1996-00570-7. URL: https://iopscience.iop.org/article/10.1209/epl/i1996-00570-7.

[140] L. Thomas et al. “Macroscopic quantum tunnelling of magnetization in a single crystal of nanomagnets”. In: *Nature* 383 (1996), pp. 145–147. ISSN: 0028-0836. DOI: 10.1038/383145a0. URL: https://www.nature.com/articles/383145a0.

[141] C. Sangregorio et al. “Quantum Tunneling of the Magnetization in an Iron Cluster Nanomagnet”. In: *Physical Review Letters* 78 (1997), pp. 4645–4648. ISSN: 0031-9007. DOI: 10.1103/PhysRevLett.78.4645. URL: https://link.aps.org/doi/10.1103/PhysRevLett.78.4645.

[142] Anatole Abragam and Brebis Bleney. *Electron Paramagnetic Resonance of Transition Ions*. Oxford University Press, 1970. ISBN: 9780199651528.

[143] Lapo Bogani and Wolfgang Wernsdorfer. “Molecular spintronics using single-molecule magnets”. In: *Nature Materials* 7 (2008), pp. 179–186. ISSN: 1476-1122. DOI: 10.1038/nmat2133. URL: https://www.nature.com/articles/nmat2133.

[144] Lev Davidovich Landau. “Zur Theorie der Energieübertragung. II”. In: *Physics of the Soviet Union* 2 (1932), pp. 46–51.

[145] Clarence Zener. “Non-adiabatic crossing of energy levels”. In: *Proceedings of the Royal Society of London. Series A, Containing Papers of a Mathematical and Physical Character* 137 (1932), pp. 696–702. ISSN: 0950-1207. DOI: 10.1098/rspa.1932.0165. URL: https://royalsocietypublishing.org/doi/10.1098/rspa.1932.0165.

[146] Ernst Carl Gerlach Stueckelberg. “Theorie der unelastischen Stösse zwischen Atomen”. In: *Helvetica Physica Acta* 5 (1932), pp. 370–422. DOI: https://doi.org/10.5169/seals-110177. URL: https://doi.org/10.5169/seals-110177.

[147] Ettore Majorana. “Atomi orientati in campo magnetico variabile”. In: *Il Nuovo Cimento* 9 (1932), pp. 43–50. ISSN: 0029-6341. DOI: 10.1007/BF02960953. URL: http://link.springer.com/10.1007/BF02960953.

[148] Romain Vincent et al. “Electronic read-out of a single nuclear spin using a molecular spin transistor”. In: *Nature* 488 (2012), pp. 357–360. ISSN: 0028-0836. DOI: 10.1038/nature11341. URL: https://www.nature.com/articles/nature11341.

[149] B. Lassagne, D. Ugnati, and M. Respaud. “Ultrasensitive Magnetometers Based on Carbon-Nanotube Mechanical Resonators”. In: *Physical Review Letters* 107 (2011), p. 130801. ISSN: 0031-9007. DOI: 10.1103/PhysRevLett.107.130801. URL: https://link.aps.org/doi/10.1103/PhysRevLett.107.130801.

[150] K. L. Ekinci, Y. T. Yang, and M. L. Roukes. "Ultimate limits to inertial mass sensing based upon nanoelectromechanical systems". In: *Journal of Applied Physics* 95 (2004), pp. 2682–2689. ISSN: 0021-8979. DOI: 10.1063/1.1642738. URL: https://pubs.aip.org/jap/article/95/5/2682/483239/Ultimate-limits-to-inertial-mass-sensing-based.

[151] Reinhard Boehler and Marvin Ross. "Melting curve of aluminum in a diamond cell to 0.8 Mbar: implications for iron". In: *Earth and Planetary Science Letters* 153 (1997), pp. 223–227. ISSN: 0012821X. DOI: 10.1016/S0012-821X(97)00188-X. URL: https://linkinghub.elsevier.com/retrieve/pii/S0012821X9700188X.

[152] Harsha Reddy et al. "Temperature-dependent optical properties of gold thin films". In: *Optical Materials Express* 6 (2016), p. 2776. ISSN: 2159-3930. DOI: 10.1364/OME.6.002776. URL: https://opg.optica.org/abstract.cfm?URI=ome-6-9-2776.

[153] W. M. Albrecht, W. D. Goode, and M. W. Mallett. "Reactions in the Niobium-Hydrogen System". In: *Journal of The Electrochemical Society* 106 (1959), p. 981. ISSN: 00134651. DOI: 10.1149/1.2427194. URL: https://iopscience.iop.org/article/10.1149/1.2427194.

[154] Ali Javey et al. "Ballistic carbon nanotube field-effect transistors". In: *Nature* 424 (2003), pp. 654–657. ISSN: 00280836. DOI: 10.1038/nature01797.

[155] W. H. Teh et al. "Cross-linked PMMA as a low-dimensional dielectric sacrificial layer". In: *Journal of Microelectromechanical Systems* 12 (2003), pp. 641–648. ISSN: 10577157. DOI: 10.1109/JMEMS.2003.817891.

[156] Daniel J. Carbaugh et al. "Combination photo and electron beam lithography with polymethyl methacrylate (PMMA) resist". In: *Nanotechnology* 28 (2017). ISSN: 13616528. DOI: 10.1088/1361-6528/aa8bd5.

[157] M. Hatzakis. "PMMA copolymers as high sensitivity electron resists". In: *Journal of Vacuum Science and Technology* 16 (1979), pp. 1984–1988. ISSN: 0022-5355. DOI: 10.1116/1.570372.

[158] W.Y. Kwong and W.Y. Zhang. "Electron-beam assisted platinum deposition as a protective layer for FIB and TEM applications". In: IEEE, 2005, pp. 469–471. ISBN: 0-7803-9143-8. DOI: 10.1109/ISSM.2005.1513408.

[159] Kyle J. Blakeney and Charles H. Winter. "Atomic Layer Deposition of Aluminum Metal Films Using a Thermally Stable Aluminum Hydride Reducing Agent". In: *Chemistry of Materials* 30 (2018), pp. 1844–1848. ISSN: 0897-4756. DOI: 10.1021/acs.chemmater.8b00445.

[160] L. B. Freund and S. Suresh. *Thin Film Materials*. Cambridge University Press, 2004. ISBN: 9780521822817. DOI: 10.1017/CBO9780511754715. URL: https://www.cambridge.org/core/product/identifier/9780511754715/type/book.

[161] Eunmi Park et al. "Stress and microstructure evolution in Mo thin films without or with cover layers during thermal-cycling". In: *Materials* 13 (2020). ISSN: 19961944. DOI: 10.3390/MA13183926.

[162] F. Kuemmeth et al. "Coupling of spin and orbital motion of electrons in carbon nanotubes". In: *Nature* 452 (2008), pp. 448–452. ISSN: 0028-0836. DOI: 10.1038/nature06822. URL: http://www.nature.com/articles/nature06822.

[163] Guy K. White and C. Andrikidis. “Thermal expansion of chromium at high temperature”. In: *Physical Review B* 53 (1996), pp. 8145–8147. ISSN: 0163-1829. DOI: 10.1103/PhysRevB.53.8145. URL: https://link.aps.org/doi/10.1103/PhysRevB.53.8145.

[164] Binghui Deng, Ying Shi, and Fenglin Yuan. “Investigation on the structural origin of low thermal expansion coefficient of fused silica”. In: *Materialia* 12 (2020), p. 100752. ISSN: 25891529. DOI: 10.1016/j.mtla.2020.100752.

[165] H. Ibach. “Thermal Expansion of Silicon and Zinc Oxide (I)”. In: *physica status solidi (b)* 31 (1969), pp. 625–634. ISSN: 15213951. DOI: 10.1002/pssb.19690310224.

[166] Glen A. Slack and S. F. Bartram. “Thermal expansion of some diamondlike crystals”. In: *Journal of Applied Physics* 46 (1975), pp. 89–98. ISSN: 00218979. DOI: 10.1063/1.321373.

[167] M. D. Groner et al. “Electrical characterization of thin Al2O3 films grown by atomic layer deposition on silicon and various metal substrates”. In: *Thin Solid Films* 413 (2002), pp. 186–197. ISSN: 00406090. DOI: 10.1016/S0040-6090(02)00438-8.

[168] M. A. Martínez-Puente et al. “ALD and PEALD deposition of HfO2 and its effects on the nature of oxygen vacancies”. In: *Materials Science and Engineering B: Solid-State Materials for Advanced Technology* 285 (2022). ISSN: 09215107. DOI: 10.1016/j.mseb.2022.115964.

[169] Andreas Thess et al. “Crystalline Ropes of Metallic Carbon Nanotubes”. In: *Science* 273 (1996), pp. 483–487. ISSN: 0036-8075. DOI: 10.1126/science.273.5274.483. URL: https://www.science.org/doi/10.1126/science.273.5274.483.

[170] T. W. Ebbesen and P. M. Ajayan. “Large-scale synthesis of carbon nanotubes”. In: *Nature* 358 (1992), pp. 220–222. ISSN: 0028-0836. DOI: 10.1038/358220a0. URL: https://www.nature.com/articles/358220a0.

[171] Jing Kong et al. “Synthesis of individual single-walled carbon nanotubes on patterned silicon wafers”. In: *Nature* 395 (1998), pp. 878–881. ISSN: 0028-0836. DOI: 10.1038/27632. URL: https://www.nature.com/articles/27632.

[172] Alan M. Cassell et al. “Large Scale CVD Synthesis of Single-Walled Carbon Nanotubes”. In: *The Journal of Physical Chemistry B* 103 (1999), pp. 6484–6492. ISSN: 1520-6106. DOI: 10.1021/jp990957s. URL: https://pubs.acs.org/doi/10.1021/jp990957s.

[173] Ngoc Viet Nguyen. “{Synth{è}se et transport {é}lectronique dans des nanotubes de carbone ultra-propres}”. PhD thesis. {Universit{é} de Grenoble}, 2012. URL: https://theses.hal.science/tel-00859807.

[174] Brock Lumbers et al. “Mathematical modelling and simulation of the thermo-catalytic decomposition of methane for economically improved hydrogen production”. In: *International Journal of Hydrogen Energy* 47 (2022), pp. 4265–4283. ISSN: 03603199. DOI: 10.1016/j.ijhydene.2021.11.057.

[175] Adrian Bachtold et al. “Aharonov–Bohm oscillations in carbon nanotubes”. In: *Nature* 397 (1999), pp. 673–675. ISSN: 0028-0836. DOI: 10.1038/17755. URL: https://www.nature.com/articles/17755.

[176] B. H. Schneider et al. “Coupling carbon nanotube mechanics to a superconducting circuit”. In: *Scientific Reports* 2 (2012), p. 599. ISSN: 2045-2322. DOI: 10.1038/srep00599. URL: https://www.nature.com/articles/srep00599.

[177] W. Yang et al. “Fabry-Pérot Oscillations in Correlated Carbon Nanotubes”. In: *Physical Review Letters* 125 (2020). ISSN: 10797114. DOI: 10.1103/PhysRevLett.125.187701.

[178] Minkyung Jung et al. “Ultraclean single, double, and triple carbon nanotube quantum dots with recessed re bottom gates”. In: *Nano Letters* 13 (2013), pp. 4522–4526. ISSN: 15306984. DOI: 10.1021/nl402455n.

[179] Ali Javey, Moonsub Shim, and Hongjie Dai. “Electrical properties and devices of large-diameter single-walled carbon nanotubes”. In: *Applied Physics Letters* 80 (2002), pp. 1064–1066. ISSN: 0003-6951. DOI: 10.1063/1.1448850. URL: https://pubs.aip.org/apl/article/80/6/1064/115705/Electrical-properties-and-devices-of-large.

[180] Carla M. Aguirre et al. “The Role of the Oxygen/Water Redox Couple in Suppressing Electron Conduction in Field-Effect Transistors”. In: *Advanced Materials* 21 (2009), pp. 3087–3091. ISSN: 0935-9648. DOI: 10.1002/adma.200900550. URL: https://onlinelibrary.wiley.com/doi/10.1002/adma.200900550.

[181] J. H. Walther et al. “Carbon Nanotubes in Water: Structural Characteristics and Energetics”. In: *The Journal of Physical Chemistry B* 105 (2001), pp. 9980–9987. ISSN: 1520-6106. DOI: 10.1021/jp011344u. URL: https://pubs.acs.org/doi/10.1021/jp011344u.

[182] Philip G. Collins et al. “Current Saturation and Electrical Breakdown in Multiwalled Carbon Nanotubes”. In: *Physical Review Letters* 86 (2001), pp. 3128–3131. ISSN: 0031-9007. DOI: 10.1103/PhysRevLett.86.3128. URL: https://link.aps.org/doi/10.1103/PhysRevLett.86.3128.

[183] Stefan Blien et al. “Quartz Tuning-Fork Based Carbon Nanotube Transfer into Quantum Device Geometries”. In: *Physica Status Solidi (B) Basic Research* 255 (2018). ISSN: 15213951. DOI: 10.1002/pssb.201800118.

[184] T. Cubaynes et al. “Nanoassembly technique of carbon nanotubes for hybrid circuit-QED”. In: *Applied Physics Letters* 117 (2020). ISSN: 0003-6951. DOI: 10.1063/5.0021838. URL: https://pubs.aip.org/apl/article/117/11/114001/1022212/Nanoassembly-technique-of-carbon-nanotubes-for.

[185] Pablo Jarillo-Herrero, Jorden A. van Dam, and Leo P. Kouwenhoven. “Quantum supercurrent transistors in carbon nanotubes”. In: *Nature* 439 (2006), pp. 953–956. ISSN: 0028-0836. DOI: 10.1038/nature04550. URL: https://www.nature.com/articles/nature04550.

[186] Matthias Mergenthaler et al. “Circuit Quantum Electrodynamics with Carbon-Nanotube-Based Superconducting Quantum Circuits”. In: *Physical Review Applied* 15 (2021), p. 064050. ISSN: 2331-7019. DOI: 10.1103/PhysRevApplied.15.064050. URL: https://link.aps.org/doi/10.1103/PhysRevApplied.15.064050.

[187] Seoho Jung et al. “Understanding and improving carbon nanotube-electrode contact in bottom-contacted nanotube gas sensors”. In: *Sensors and Actuators B: Chemical* 331 (2021), p. 129406. ISSN: 09254005. DOI: 10.1016/j.snb.2020.129406.

[188] Zhitao Deng et al. “Self-assembly of bis(phthalocyaninato)terbium on metal surfaces”. In: *Physica Scripta* 90 (2015), p. 098003. ISSN: 0031-8949. DOI: 10.1088/0031-8949/90/9/098003. URL: https://iopscience.iop.org/article/10.1088/0031-8949/90/9/098003.

[189] Ferdous Ara et al. “A scanning tunneling microscopy study of the electronic and spin states of bis(phthalocyaninato)terbium(III) (TbPc2) molecules on Ag(111)”. In: *Dalton Transactions* 45 (2016), pp. 16644–16652. ISSN: 14779234. DOI: 10.1039/c6dt01967f.

[190] Patrick Lawes et al. “Hierarchical Self-Assembly and Conformation of Tb Double-Decker Molecular Magnets: Experiment and Molecular Dynamics”. In: *Nanomaterials* 13 (2023), p. 2232. ISSN: 2079-4991. DOI: 10.3390/nano13152232. URL: https://www.mdpi.com/2079-4991/13/15/2232.

[191] Ludovica Margheriti et al. “X-Ray Detected Magnetic Hysteresis of Thermally Evaporated Terbium Double-Decker Oriented Films”. In: *Advanced Materials* 22 (2010), pp. 5488–5493. ISSN: 0935-9648. DOI: 10.1002/adma.201003275. URL: https://onlinelibrary.wiley.com/doi/10.1002/adma.201003275.

[192] Fanli Lu et al. “Infra-red and Raman spectroscopic study of tetra-substituted bis(phthalocyaninato) rare earth complexes peripherally substituted with tert-butyl derivatives”. In: *Spectrochimica Acta - Part A: Molecular and Biomolecular Spectroscopy* 65 (2006), pp. 221–228. ISSN: 13861425. DOI: 10.1016/j.saa.2005.10.035.

[193] Péter Fejes. *Optimierung der Operation der Sionludi-Cryostaten (Optimization of the Operation of the Sionludi Cryostats)*. 2020.

[194] Christian Enss and Siegfried Hunklinger. *Low-Temperature Physics*. Springer-Verlag, 2005. ISBN: 3-540-23164-1. DOI: 10.1007/b137878.

[195] Isaak Pomeranchuk. “On the theory of ^{3}He”. In: *Zh. Eksp. Teor. Fiz* 20 (1950).

[196] Asaf Rozen et al. “Entropic evidence for a Pomeranchuk effect in magic-angle graphene”. In: *Nature* 592 (2021), pp. 214–219. ISSN: 0028-0836. DOI: 10.1038/s41586-021-03319-3.

[197] Alexander Zilz. *Investigation of the Rarefied Gas Flow in the Pumping Tube of a 3 He/ 4 He Dilution Refrigerator*. 2022.

[198] Michael Schulze. “Improvements in Superconducting Magnetometry”. PhD thesis. Karlsruhe Institute of Technology, 2023. DOI: 10.5445/IR/1000160388.

[199] Carlos Urgell Flores and Adrian Bachtold. “New phenomena in high-quality suspended nanotube devices”. In: (2021). URL: http://hdl.handle.net/10803/672093.

[200] Sergio Lucio De Bonis. “Polaron physics in carbon nanotube electro-mechanical resonators”. In: (2019). URL: http://hdl.handle.net/10803/668846.

[201] Stefano Zippilli, Giovanna Morigi, and Adrian Bachtold. “Cooling Carbon Nanotubes to the Phononic Ground State with a Constant Electron Current”. In: *Physical Review Letters* 102 (2009), p. 096804. ISSN: 0031-9007. DOI: 10.1103/PhysRevLett.102.096804.

[202] Stefano Zippilli, Adrian Bachtold, and Giovanna Morigi. “Ground-state-cooling vibrations of suspended carbon nanotubes with constant electron current”. In: *Physical Review B* 81 (2010), p. 205408. ISSN: 1098-0121. DOI: 10.1103/PhysRevB.81.205408.

[203] Shaoming Huang et al. “Growth mechanism of oriented long single walled carbon nanotubes using "fast-heating" chemical vapor deposition process”. In: *Nano Letters* 4 (2004), pp. 1025–1028. ISSN: 15306984. DOI: 10.1021/nl049691d.

[204] Jiwoong Park and Paul L. McEuen. “Formation of a p-type quantum dot at the end of an n-type carbon nanotube”. In: *Applied Physics Letters* 79 (2001), pp. 1363–1365. ISSN: 00036951. DOI: 10.1063/1.1396318.

[205] B. M. Andersen et al. “Nonequilibrium Transport through a Spinful Quantum Dot with Superconducting Leads”. In: *Physical Review Letters* 107 (2011), p. 256802. ISSN: 0031-9007. DOI: 10.1103/PhysRevLett.107.256802. URL: https://link.aps.org/doi/10.1103/PhysRevLett.107.256802.

[206] O. Usmani, Ya. M. Blanter, and Yu. V. Nazarov. “Strong feedback and current noise in nanoelectromechanical systems”. In: *Physical Review B* 75 (2007), p. 195312. ISSN: 1098-0121. DOI: 10.1103/PhysRevB.75.195312. URL: https://link.aps.org/doi/10.1103/PhysRevB.75.195312.

[207] Ya. M. Blanter, O. Usmani, and Yu. V. Nazarov. “Single-Electron Tunneling with Strong Mechanical Feedback”. In: *Physical Review Letters* 93 (2004), p. 136802. ISSN: 0031-9007. DOI: 10.1103/PhysRevLett.93.136802. URL: https://link.aps.org/doi/10.1103/PhysRevLett.93.136802.

[208] Ya. M. Blanter, O. Usmani, and Yu. V. Nazarov. “Erratum: Single-Electron Tunneling with Strong Mechanical Feedback [Phys. Rev. Lett. 93 , 136802 (2004)]”. In: *Physical Review Letters* 94 (2005), p. 049904. ISSN: 0031-9007. DOI: 10.1103/PhysRevLett.94.049904. URL: https://link.aps.org/doi/10.1103/PhysRevLett.94.049904.

[209] Hideyuki Maki, Masaki Suzuki, and Koji Ishibashi. “Local change of carbon nanotube-metal contacts by current flow through electrodes”. In: vol. 43. Japan Society of Applied Physics, 2004, pp. 2027–2030. DOI: 10.1143/JJAP.43.2027.

[210] Yunsung Woo, Georg S. Duesberg, and Siegmar Roth. “Reduced contact resistance between an individual single-walled carbon nanotube and a metal electrode by a local point annealing”. In: *Nanotechnology* 18 (2007). ISSN: 09574484. DOI: 10.1088/0957-4484/18/9/095203.

[211] Jingqi Li and Qing Zhang. “Room-temperature negative differential conductance in carbon nanotubes”. In: *Carbon* 43 (2005), pp. 667–670. ISSN: 00086223. DOI: 10.1016/j.carbon.2004.10.019. URL: https://linkinghub.elsevier.com/retrieve/pii/S0008622304006001.

[212] R. Tormo-Queralt et al. “Novel Nanotube Multiquantum Dot Devices”. In: *Nano Letters* 22 (2022), pp. 8541–8549. ISSN: 15306992. DOI: 10.1021/acs.nanolett.2c03034.

Appendix A

In this appendix, the parameters used for the nanofabrication process of the devices are being presented for both top-growth as well as stamping devices.

Fabrication Recipe for top-growth devices

In this section, the nanofabrication recipe up to the point of the CNT growth is being presented.

Chip-preparation

- Spincoating p-doped Si-wafer using S1818[1] as protective resist layer. Spincoating parameters: 4000 rpm, 500 rpm/s, bakeout @ 80 °C for 300 s
- Dicing wafer in pieces of 15x15 mm^2
- Removing resist using acetone in high-power ultrasonic bath for 5 min
- Removing acetone with isopropanole (IPA) in high-power ultrasonic bath for 5 min, blow drying using pressurised N_2
- Removing solvent residues in O_2 plasma asher, 5 min, 200 W, 25 sccm.

Alignment markers

- Spincoating of S1805 (4500rpm 70s, bakeout 70s @ 115°C)
- Exposure 4s, 356 nm, Intensity 13 mW cm^{-2}
- Development 40s in AZ MIF 726[2], stop 30s in destilled water
- Evaporation 5nm Ti (rate: ≈ 0.2 nm s^{-1}), 40nm Au (rate idem)
- Lift-off in hot 1-ethyl-2-pyrrolidone (NEP) or dimethyl sulfoxide (DMSO) for >1h @90 °C
- Acetone for 4-5 minutes, medium power in ultrasonic bath
- IPA for 2-3 minutes, medium power in ultrasonic bath, blow drying using N2

[1] URL: https://www.microresist.de/en/produkt/microposit-s1800-g2-series/, last access: 07/04/24
[2] URL: https://www.microchemicals.com/products/developers/azr_726_mif_developer.html, last access: 07/04/24

Local gates

- Spincoating:
  Bottom layer: PMMA 600K 2%[3], 4000rpm, bakeout 150s @ 150°C, 60nm thickness
  Top layer: PMMA 950K 2.25%[4], 2000rpm, bakeout 150s @ 150°C, 60nm thickness
- E-beam exposure: 600 µC cm^{-2}, 50 kV
- Developing: 45s in AR 600-56[5] or methyl isobutyl ketone(MIBK):IPA (1:3), stopping in IPA
- Evaporation: 2 nm Ti (rate: ≈ 0.2 nm s^{-1}), 8 nm Mo (rate: ≈ 0.1 nm s^{-1})
- Lift-off in hot NEP or DMSO for >1h @ 90°C
- Acetone for 4-5 minutes, medium power in ultrasonic bath
- IPA for 2-3 minutes, medium power in ultrasonic bath, blow drying using N2

Gate bondpads

- Spincoating of S1805[1] (4500rpm 70s, bakeout 70s @ 115°C)
- Exposure 4s, 356 nm, Intensity 13 mW cm^{-2}
- Development 40s in AZ MIF 726[2], stop 30s in destilled water
- Evaporation 5nm Ti (rate: ≈ 0.2 nm s^{-1}), 70nm Pt (rate 0.1-0.2 nm s^{-1})
- Lift-off in hot 1-ethyl-2-pyrrolidone (NEP) or dimethyl sulfoxide (DMSO) for >1h @ 90 °C
- Acetone for 4-5 minutes, medium power in ultrasonic bath
- IPA for 2-3 minutes, medium power in ultrasonic bath, blow drying using N2

Insulating oxide

- Atomic layer deposition, using 150-250 cycles to reach ≈ 15-25 nm @ 250 °C
- using ozone or O_2-plasma for surface cleaning during process initialisation
- used process gases for Al_2O_3: H_2O and trimethylalumium

[3] URL: https://www.allresist.com/portfolio-item/e-beam-resist-ar-p-662-series/, last access: 07/04/24
[4] URL: https://www.allresist.com/portfolio-item/e-beam-resist-ar-p-672-series/, last access: 07/04/24
[5] URL: https://www.allresist.com/portfolio-item/developer-ar-600-56/, last access: 07/04/24

Contact electrodes

- Spincoating:
  MMA/PMMA copolymer[6]; 2000 rpm 60s, 180s @ 185°C baking
  PMMA 950K 4.5%[4] ; 6000rpm 60s, 150s @ 150°C baking
- Exposure: E-beam 50 kV, 400 µC cm^{-2}
- Exposure: Deep-UV (no filter), 2100 s, 500 W
- Developing 45s in AR 600-56[5] or MIBK:IPA (1:3), stopping in IPA **or** 90s in IPA:water (3:1) @6°C for 90s, stop in water
- Evaporation @ −80 °C sample holder temperature, cooled chamber walls: 5nm Ti (rate: ≈ 0.2 nm s^{-1}), 70nm Mo, 70 nm Pt (rate 0.1-0.2 nm s^{-1})
- Molybdenum evaporation: two times 35 nm with pause to cool down to base temperature. 35 nm split into 7 times 5 nm (rate 0.07 nm s^{-1}) with 90 s break with closed sample shutter in between.
- Lift-off in hot NEP or DMSO for >1h @ 90°C
- Acetone for 4-5 minutes, medium power in ultrasonic bath
- IPA for 2-3 minutes, medium power in ultrasonic bath, blow drying using N2

Catalyst islands

- Spincoating: Bottom layer: PMMA 950K[4] (1000rpm, 150s @ 150°C)
  Top layer: PMMA 950K[4] (1000rpm, 150s @ 150°C)
- Exposure e-beam lithography, 50 kV , 400 µC cm^{-2}
- Developing 45s AR 600-56[5], stop in IPA
- Dropcasting catalyst solution or dipping into solution
- Carefully removing the PMMA in acetone (no ultrasonics), using three beakers. 5 s in first, 5 s in second and 360 s in third.
- rinsing in IPA for 30 s, blow drying using N2
- O_2-plasma asher, 2 min, 25 sccm, 45 W

Fabrication Recipe for stamping devices

In this section, the nanofabrication recipe up to the point of wirebonding for stamping is presented.

[6] https://www.allresist.com/portfolio-item/e-beam-resist-ar-p-617-series/, last access: 07/04/24

Chip-preparation

- Spincoating p-doped Si-wafer using S1818[1] as protective resist layer. Spincoating parameters: 4000 rpm, 500 rpm/s, bakeout @ 80 °C for 300 s
- Dicing wafer in pieces of 20x20 mm^2
- Removing resist using acetone in high-power ultrasonic bath for 5 min
- Removing acetone with isopropanole (IPA) in high-power ultrasonic bath for 5 min, blow drying using pressurised N_2
- Removing solvent residues in O_2 plasma asher, 5 min, 200 W, 25 sccm.

Alignment markers

- Spincoating of S1805 (4500rpm 70s, bakeout 70s @ 115°C)
- Exposure 4s, 356 nm, Intensity 13 mW cm^{-2}
- Development 40s in AZ MIF 726[2], stop 30s in destilled water
- Evaporation 5nm Ti (rate: ≈ 0.2 nm s^{-1}), 40nm Au (rate idem)
- Lift-off in hot 1-ethyl-2-pyrrolidone (NEP) or dimethyl sulfoxide (DMSO) for >1h @90 °C
- Acetone for 4-5 minutes, medium power in ultrasonic bath
- IPA for 2-3 minutes, medium power in ultrasonic bath, blow drying using N2

Local gates

- Spincoating:
  Bottom layer: PMMA 600K 2%[3], 4000rpm, bakeout 150s @ 150°C, 60nm thickness
  Top layer: PMMA 950K 2.25%[4], 2000rpm, bakeout 150s @ 150°C, 60nm thickness
- E-beam exposure: 600 µC cm^{-2}, 50 kV
- Developing: 45s in AR 600-56[5] or methyl isobutyl ketone(MIBK):IPA (1:3), stopping in IPA
- exemplary Evaporation: 3 nm Ti (rate: ≈ 0.2 nm s^{-1}), 10 nm Al (rate: ≈ 0.5 nm s^{-1})
- Lift-off in hot NEP or DMSO for >1h @ 90°C
- Acetone for 4-5 minutes, medium power in ultrasonic bath
- IPA for 2-3 minutes, medium power in ultrasonic bath, blow drying using N2

Contact electrodes

The exact metal stack composition and resist stack used varied. One example is given here:

- Spincoating:
  MMA/PMMA copolymer[6]; 2000 rpm 60s, 180s @ 185°C baking
  PMMA 950K 4.5%[4] ; 6000rpm 60s, 150s @ 150°C baking
- Exposure: E-beam 50 kV, 400 $\mu C\,cm^{-2}$
- Developing 45s in AR 600-56[5] or MIBK:IPA (1:3), stopping in IPA **or** 90s in IPA:water (3:1) @6°C for 90s, stop in water
- Evaporation @ −80 °C sample holder temperature, cooled chamber walls: 5nm Ti (rate: $\approx 0.2\,nm\,s^{-1}$), 100nm Nb (rate: $\approx 0.3\,nm\,s^{-1}$), 10 nm P (rate $0.4\,nm\,s^{-1}$) with 90 s break with closed sample shutter in between.
- Lift-off in hot NEP or DMSO for >1h @ 90°C
- Acetone for 4-5 minutes, medium power in ultrasonic bath
- IPA for 2-3 minutes, medium power in ultrasonic bath, blow drying using N2

Chip-dicing

- Spincoating using S1818[1] as protective resist layer. Spincoating parameters:
  4000 rpm, 500 rpm/s, bakeout @ 80 °C for 300 s
- Dicing wafer
- Removing resist using acetone in high-power ultrasonic bath for 5 min
- Removing acetone with isopropanole (IPA) in high-power ultrasonic bath for 5 min, blow drying using pressurised N_2

Acknowledgements

Of course this thesis would not have been possible without the many people involved at KIT and outside and their contribution should not go unrecognised. I therefore want to thank

- Wolfgang Wernsdorfer, for giving me the possibility to join his research group and to get the opportunity to work in this fascinating, diverse research field. I felt welcome from the moment of my interview due to his friendly down-to-earth character, giving off-topics like proper preparation for an ultra-marathon a similar weight to upside-down cryostats and state-of-the-art physics. His work ethics is unrivaled, and even though he never has spare time, he always finds a way to free some time to discuss science whether the data is promising or not. I was deeply impressed by his ability to look at the foundations of presented data or ideas, quickly figuring out whether following up on this is feasible and promising or not, which proved to be a valuable learning experience for me.

- Ralph Krupke, for agreeing to be the second reviewer of this thesis. When discussing the results of this work with him, I realised that his different approach to carbon nanotubes could have proven fruitful for a deeper understanding of our devices and the design of new experiments. I hope, that the scientific exchange between the research groups is extended in the future likely benefiting everyone.

- Tino Cubaynes, for being my main scientific supervisor guiding me through this thesis. With his patience, widespread scientific knowledge and unwavering confidence in the project, he provided the needed support when the N-th sample died and fabrication needed to be restarted all over again. His creativity, friendly demeanour and sometimes unorthodox, yet efficient, problem-solving were inspiring and probably shaped my future work more than I would like to admit. I wish him all the best for his surely long and successful scientific career.

- Tim Althuon, for being my friendly and helpful partner in crime for the majority of this work. It was very helpful, to have someone fighting similar obstacles in nanofabrication, carbon nanotube growth or administration and especially, when performing surgery on a blocked SEM... not to mention all the discussions about life, physics and how to interpret what we see in both nanofabrication and experimental data.

- Christoph Sürgers, for helping me understanding how thin films work, being the (involuntary) expert for everything Physikalisches-Institut and infrastructure-related and the helping hand, when our machines did not want to work the way we wanted them to. Most importantly, however,

for creating a friendly and joyful atmosphere in the third floor by friendly chatter or the occasional singing and whistling in the evening when the labs were emptying.

- Svenja Müller, for joining forces for one year during her master's thesis in tackling the many small and large obstacles we encountered along the way.
- Sophie Klingel, for joining this project in the last months and hopefully continuing it. Also, for the entertaining discussions on all kinds of sports.
- The members of the nanostructure service laboratory. In particular Aina Quintilla, for guiding me through fabricating my first sample; Silvia Diewald, for performing countless e-beam lithographies and helping us to debug this crucial process; Lucas Radtke, for all the help regarding clean-room work in general and in particular with the laser-writer and its... peculiarities.
- the members of the mechanical and electronics workshop, in particular Michael Meyer for converting my sketches into meaningful CAD-files; Jannis Ret, for all the help regarding the building of filter of all sorts, PCB fabrication and the pleasant chats. I hope he is having a great time at his new position.
- Michael Pfirrmann, for maintaining the helium liquefaction plant. Without him, all scientific work in our group would come to a standstill.
- Julian and Thomas, for all the help regarding the measurement software and the AWG.
- All the current and previous unmentioned members of the Nanospin group for creating such a pleasant working environment of mutual help and friendly banter.
- My dear friends. In particular Max, for being such a rock-solid, good-tempered guy and the trip to Zermatt; Kevin, for the ever entertaining though sometimes weirdly deep-diving discussions about seemingly random topics.
- My family, especially my sister, parents and grandmas for being supportive in every way from the very beginning of my studies to the organisation of the defense party.
- Susi, for being you, for all the support you've given me and the glee you bring into my life. I can't imagine my life without you.